1S–2S Spectroscopy of Trapped Hydrogen: The Cold Collision Frequency Shift and Studies of BEC

by

Thomas Charles Killian

Submitted to the Department of Physics
in partial fulfillment of the requirements for the degree of

Doctor of Philosophy

at the

MASSACHUSETTS INSTITUTE OF TECHNOLOGY

February 1999

Author .....
Department of Physics
January 11, 1999

Certified by .....
Thomas J. Greytak
Professor of Physics
Thesis Supervisor

Certified by .....
Daniel Kleppner
Lester Wolfe Professor of Physics
Thesis Supervisor

Accepted by .....
Thomas J. Greytak
Chairman, Department of Physics Graduate Committee

1S–2S Spectroscopy of Trapped Hydrogen: The Cold Collision Frequency Shift and Studies of BEC

by

Thomas Charles Killian

Submitted to the Department of Physics
on January 11, 1999, in partial fulfillment of the
requirements for the degree of
Doctor of Philosophy

Abstract

The cold collision frequency shift of the $1S$-$2S$ two-photon transition is studied in trapped spin-polarized atomic hydrogen at submillikelvin temperatures. This effect is the low temperature manifestation of the pressure shift and broadening familiar from spectroscopy at normal temperatures and pressures. We find the shift is given by $\Delta\nu_{1S-2S} = -3.8 \pm 0.8 \times 10^{-10}\ n$ Hz cm^3, where n is the sample density.

Theory is developed to express the shift in terms of the mean field interaction energy due to collisions and thus relate it to the s-wave triplet scattering lengths, a_{1S-1S} and a_{1S-2S}. From this we derive $a_{1S-2S} = -1.4 \pm 0.3$ nm, which is in fair agreement with a recent calculation.

$1S$-$2S$ spectroscopy is a valuable probe of the density, temperature, and atom-atom interactions in the trapped sample, especially in the regime of Bose-Einstein condensation (BEC). We describe properties of the condensate and how they are determined from the $1S$-$2S$ spectrum.

Thesis Supervisor: Thomas J. Greytak
Title: Professor of Physics

Thesis Supervisor: Daniel Kleppner
Title: Lester Wolfe Professor of Physics

Acknowledgments

Graduate school has been the best time of my life and I owe that to Amy Salzhauer. She always shares my excitement when things go well and is ready with a reassuring smile when progress seems slow or nonexistent. She has a talent for getting me out of the lab to enjoy the rest of life, and my experience at MIT has been richer because I have had someone with which to share it.

For as long as I can remember my parents have encouraged me to ask questions, take risks, and explore the world around me, and those lessons have served me well. My family may not have understood why I spent the last five years staying up all night working in the lab, but they were always supportive. Thanks!

I couldn't have asked for better advisors than Tom Greytak and Dan Kleppner. They give their students the freedom to grow and take on challenges, and manage to encourage hard work without forgetting that above all, physics is fun.

In an experiment like this one, nothing gets done unless people can work together as a team, and this thesis wouldn't exist without the help of others in the lab.

I have learned a tremendous amount from working with Dale Fried, and I feel safe in saying that with him more than anyone else, I share feelings of great satisfaction and joy (and relief!) from finally seeing the experiment deliver on its promises.

Lorenz Willmann brought experience, a good sense of humor, and a passion for rigorous data analysis to the experiment – all of which were desperately needed. It is always a pleasure to work with him, even when learning about the subtleties of chi-squared.

I am envious of the younger graduate students, Dave Landhuis and Stephen Moss, because I am sure they will accomplish and learn amazing things in the next few years. It is hard to leave something that has absorbed so much of my sweat and tears, but it is made much easier by the talent and remarkable good nature of the people who will take care of it.

I would have been lost in the lab if Claudio Cesar hadn't been here when I arrived. He taught me all that I know about laser physics, and we had a great time in the

process.

It has been a privilege to work and share an office with Adam Polcyn. I have never met anyone with a better disposition or more patience, and with all the phone messages he took for me, I am sure I tested the latter!

Some of the most rewarding experiences I had at MIT have been working with undergraduates. In particular I value my friendships with Jonathan Goldman and Sourav Mandal and the chance I had to watch them learn about physics.

I also thank Ian Applebaum for help with numerical computations and Professors Wolfgang Ketterle and Leonya Levitov for many useful discussions.

Contents

List of Figures

List of Tables

Chapter 1

Introduction

Spectroscopy of atomic hydrogen has contributed to some of the major advances in physics in the twentieth century. Bohr's model to explain the hydrogenic electronic spectrum [1] was the bridge from classical to quantum mechanics. The fine structure splitting of the Balmer-alpha $2P$-$3S$,$3D$ transition led Sommerfeld to incorporate relativity in the description of the atom [2], a program which was continued by Dirac with his relativistic quantum theory [3]. Rabi's measurement of the ground state hyperfine structure [4, 5] suggested the existence of the anomalous electron magnetic moment. That work, along with Lamb's discovery of the $2S$ Lamb shift [6, 7], spurred the development of quantum electro-dynamics.

Today, hydrogen spectroscopy continues to occupy a prominent position in physics research, and there is particular interest in the two-photon $1S$-$2S$ transition because of its narrow natural linewidth, 1.31 Hz, at a resonance frequency of 2.46×10^{15} Hz. The $1S$-$2S$ transition, excited in an atomic beam, is part of the most precise measurement of the $1S$ Lamb shift, which now stretches our understanding of the structure of the proton and quantum chromodynamics[8]. The transition is also important for metrology and fundamental physical measurements. It has been suggested as a frequency reference[9], and is used in the most precise determination of the Rydberg constant[9].

This thesis describes new applications for $1S$-$2S$ hydrogen spectroscopy. We study H-H interactions in submillikelvin, magnetically trapped hydrogen[10] through the

cold collision frequency shift of the transition frequency [11, 12]. In addition, we show how $1S$-$2S$ spectroscopy and the cold collision frequency shift can be used to investigate Bose-Einstein condensation (BEC) in hydrogen[13].

The cold collision frequency shift is the low temperature manifestation of the pressure shift and broadening familiar from spectroscopy at normal temperatures and pressures [14]. In cold collisions, the temperature is so low that only a single partial wave contributes to atom-atom scattering. Collisional frequency shifts in this regime have been studied in the microwave region because they limit the accuracy of the cryogenic hydrogen maser [15] and atomic fountain clocks based on cesium[16, 17, 18]. The $1S$-$2S$ observations described here extend this research from the microwave to the optical region.

In hydrogen, the shift can be related to the s-wave elastic triplet scattering lengths for $1S$-$2S$ and $1S$-$1S$ collisions, a_{1S-2S} and a_{1S-1S}. The $1S$-$1S$ scattering length is known accurately from theory. To our knowledge these results constitute the first measurement of a scattering length involving an excited state, and it tests the understanding of H-H molecular potentials.

The theory for the cold collision frequency shift in masers and fountain clocks has been thoroughly developed [15], but this theory strictly applies only to a homogeneous noncondensed system. The extension to an inhomogeneous gas, and to BEC, is not trivial. The frequency shift is sensitive to atom-atom spatial correlations, and raises interesting new questions about the state of the system after excitation.

The study of dilute degenerate quantum gases has captured the attention of the physics community and the popular press since the condensation of rubidium [19], sodium [20], and lithium [21, 22] in 1995. The observation of BEC in hydrogen capped a 22-year research effort, and $1S$-$2S$ spectroscopy was an essential tool for detecting the phase transition. High resolution spectroscopy is a new method for studying BEC and it opens another window into this exciting phenomenon.

The techniques for magnetically trapping and cooling hydrogen are discussed in Chap. 2. The experimental details of $1S$-$2S$ spectroscopy are described in Chap. 3. Chapter 4 provides a theoretical description of two-photon excitation in a trap and

presents spectra observed under various experimental conditions.

Chapter 5 describes the data and analysis for the cold collision frequency shift measurements, and Chap. 6 discusses the theory for the shift, which is necessary for relating the shift to the s-wave scattering lengths. Chapter 7 discusses some of the BEC measurements that can be extracted from the $1S$-$2S$ spectrum, and Chap. 8 describes future prospects for the experiment.

Appendix A describes the current limitations and future potential of high resolution $1S$-$2S$ spectroscopy in the magnetic trap. Appendices B-D provide detailed derivations of many of the calculated results presented in the bulk of the thesis, and App. E describes the $^{130}Te_2$ reference spectrometer used to locate the frequency of the $1S$-$2S$ transition.

This work should be viewed as a companion to D. Fried's Ph.D. thesis [23], "Bose-Einstein Condensation of Atomic Hydrogen," which discusses the condensate data and properties in much greater detail. This experiment is a group effort, and the emphasis here is on describing how the $1S - 2S$ transition is used to study the trapped gas, and on pointing out new spectroscopic effects.

Chapter 2

Overview of Cryogenic Trapping and Cooling of Atomic Hydrogen

The study of magnetically trapped atomic hydrogen has been motivated by the pursuit of BEC, a phase transition to a state in which a macroscopic number of atoms occupies the lowest energy level of the system. The transition occurs at low temperatures and high densities when $n_0\lambda_T^3 \simeq 2.612$, where n_0 is the peak sample density, $\lambda_T = h/\sqrt{2\pi m k_B T}$ is the thermal de Broglie wavelength, and $n_0\lambda_T^3$ is the peak phase space density in the sample.

The techniques for trapping and cooling hydrogen have been discussed extensively in the literature (references given below), and also in the Ph.D. thesis of J. Doyle [24]. This chapter gives an overview of this aspect of the experiment and a bit of historical background.

2.1 Background

The study of gaseous atomic hydrogen in the quantum regime can be traced back to Hecht[25], who in 1959 pointed out that in a strong magnetic field the system would remain a gas to $T = 0$ and, at low enough temperatures, might display the effects of quantum degeneracy and superfluidity. There was little initial interest, but experimental work started in earnest in the 1970's after further details were worked

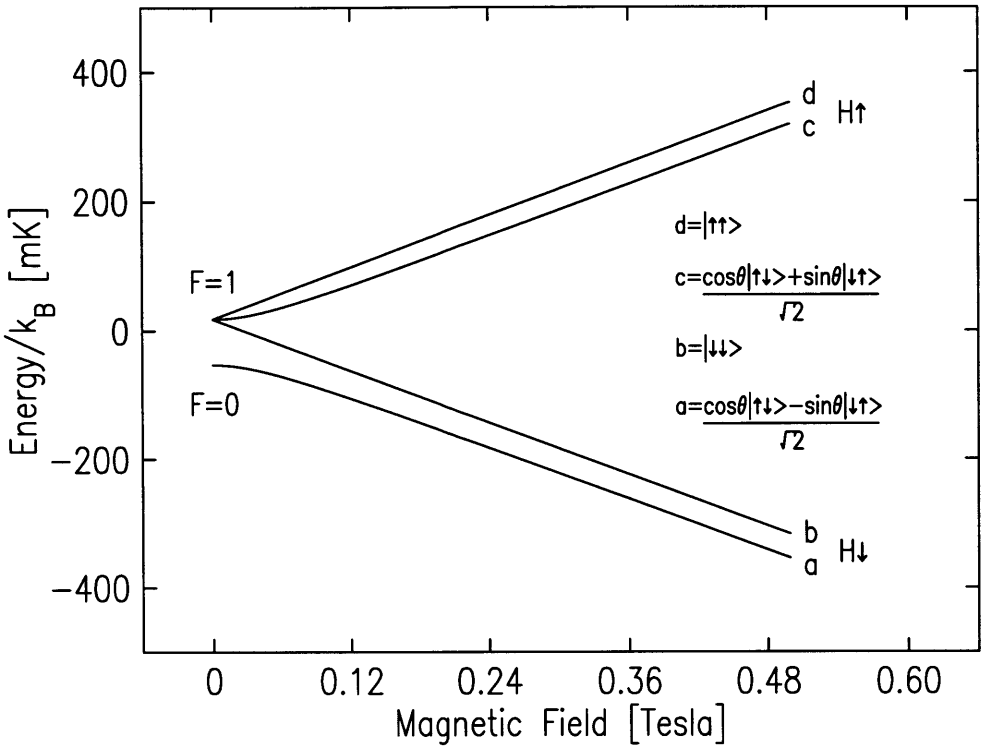

Figure 2-1: Hyperfine structure of the $1S$ ground state of hydrogen in a magnetic field. The symbol $|\uparrow\uparrow\rangle$ denotes the state with the electron spin up, $m_e = +1/2$, and the proton spin up, $m_p = +1/2$, *etc.* The mixing angle is defined by $\tan(2\theta) = A/h(\gamma_e + \gamma_p)B = .0506/B$, where A/h is the zero field hyperfine splitting, and γ_e are γ_p are the electron and proton gyromagnetic ratios, respectively. In high field ($B > 0.05$ T), the electron and proton spins couple to the magnetic field; in low field the hyperfine coupling dominates. Electron spin up atoms ($H\uparrow$) are pulled towards the magnetic field minimum, while the electron spin down atoms ($H\downarrow$) are pulled towards the maximum of the field. According to convention, states are labelled a through d in order of increasing energy.

out by Stwalley and Nosanow[26] and others [27]. To stabilize the system against molecular recombination, a magnetic field is required to spatially separate atoms with different electron spins. This greatly suppresses the exothermic reaction H + H $\Rightarrow$ H_2 + 4.6 eV, because electron spin-polarized atoms interact through the repulsive triplet molecular potential[28, 29].

Atomic hydrogen interacts with a magnetic field through the well known Zeeman effect [30]. The orientation of an atom's spin tends to follow the field adiabatically due to the spin angular momentum, so the magnetic potential, $U = -\mu \cdot \mathbf{B}$, reduces to a function of the magnitude of the field, as shown in Fig. 2-1. Atoms with their

electron spin down ($H\downarrow$, states a and b) are pulled towards a magnetic field maximum. Atoms with their electron spin up ($H\uparrow$, states c and d) are pulled towards a magnetic field minimum.

$H\downarrow$ atoms were magnetically stabilized by Silvera and Walraven [31] in 1979. The sample was confined at 300 mK in a liquid ^{4}He coated cell in fields of up to 7 T. In a similar apparatus, nuclear polarization was demonstrated in 1981 when the group of Greytak and Kleppner produced a sample of b state atoms [32].

Bose condensing high field seeking atoms proved impossible in these experiments because the trapped $H\downarrow$ atoms were always in thermal and diffusive contact with containment walls. This limited the temperature to greater than about 100 mK and three body recombination limited the sample densities to less than $\sim 10^{18}$ cm^{-3} [33], below the BEC critical density. Containment walls were essential because Maxwell's equations forbid the existence of a static magnetic field maximum in free space.

Hess [34] suggested wall free confinement of low field seekers in a magnetic field minimum, and evaporative cooling, as a path towards BEC. This led to the development of the current MIT hydrogen experiment.

2.2 Trapping Low Field Seeking Hydrogen Atoms

2.2.1 Magnetic Trap

For the experiments described in this thesis, a Ioffe-Pritchard [35] magnetic trap for $H\uparrow$ atoms is produced by superconducting magnets[24]. Large solenoids provide axial confinement, and radial confinement is provided by a quadrupole magnetic field whose magnitude increases linearly with r, the distance from the center axis, with gradient B'. The field profile on axis is shown in Fig. 2-2. The potential seen by d state atoms near the field minimum is $U(\mathbf{r}) \approx \mu_B\sqrt{B_0^2(1+z^2/z_0^2)+(rB')^2}$, where μ_B is the Bohr magneton ($\mu_B/h = 14$ GHz/T, $\mu_B/k_B = 0.67$ K/T). The minimum field in the trap is denoted B_0. It is important for future discussions to note that the curvature along the z axis is weak ($B_0/z_0 \ll B'$).

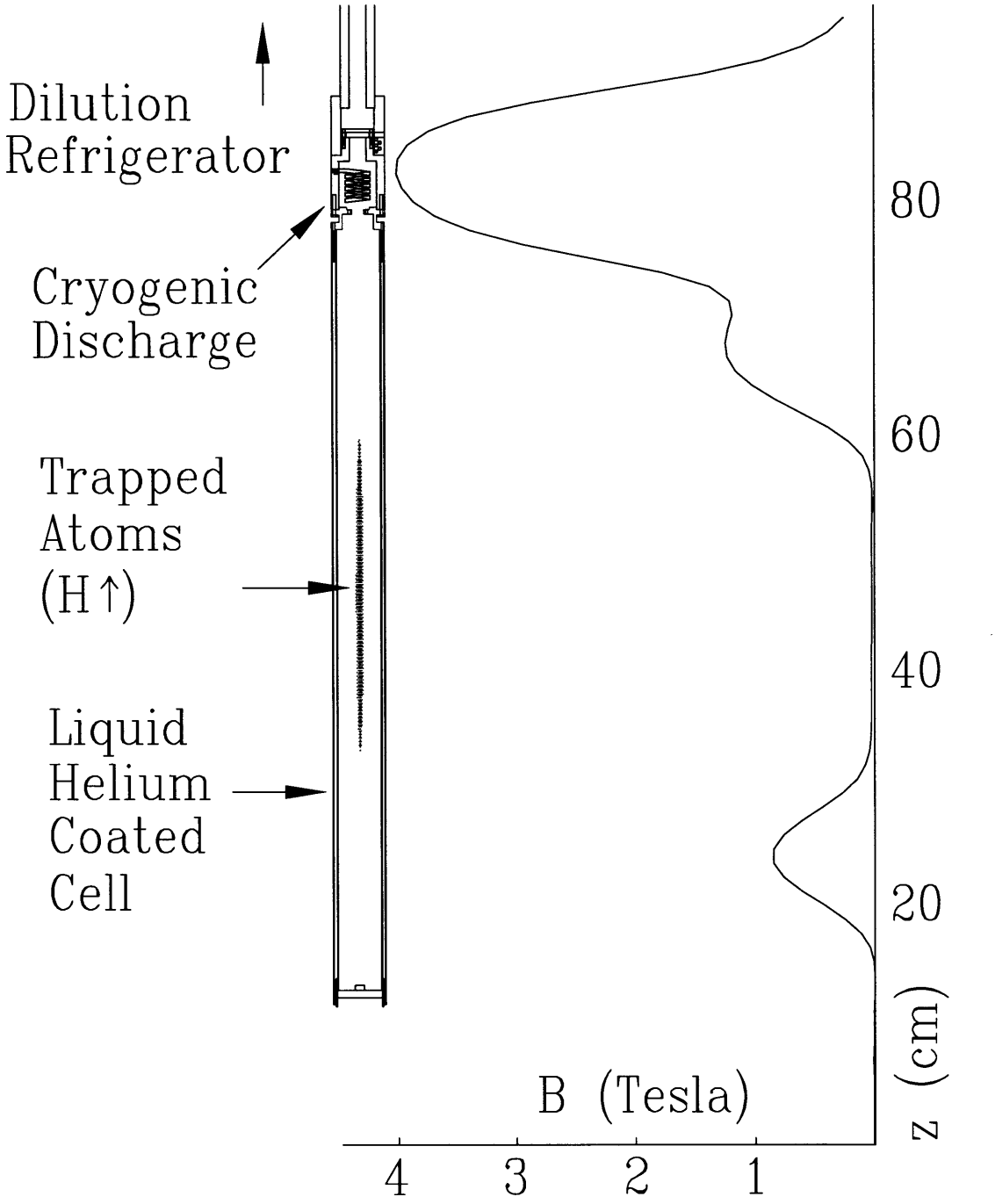

Figure 2-2: Overview of the trapping apparatus. The cylindrically symmetric trapping cell is thermally connected to a dilution refrigerator and can be cooled to 60 mK. Atoms are produced in a cryogenic discharge, thermalize through collisions with each other and with the liquid ^{4}He coated cell walls, and settle into the minimum of the trapping magnetic field. (The field profile on axis is shown.)

When loading the trap, the maximum trap depth is employed, $\varepsilon_{trap}/k_B \approx 0.5$ K. To load a 0.5 K deep trap, atoms must be precooled to $T \approx 0.5$ K or below. Laser cooling is a common method for cooling atoms, but it not feasible for hydrogen because an adequate light source does not exist for driving the $1S$-$2P$ fundamental transition at 121.6 nm[1]. Instead, the atoms are precooled through thermalizing collisions with a 250 mK liquid ^{4}He coated surface. A ^{3}He-^{4}He dilution refrigerator is used to cool the apparatus. The binding energy of hydrogen on liquid ^{4}He ($\epsilon_B/k_B \approx 1\ K$)[37] is low enough to allow the existence of an appreciable gas phase in thermal contact with the cold surface. This method for loading paramagnetic atoms into a trap appears to be limited to hydrogen because other atoms have too high a binding energy on liquid ^{4}He or any other surface one could imagine.

2.2.2 Forming Atomic Hydrogen in a Radio Frequency Discharge

To form atoms, a cryogenic radio frequency (RF) discharge dissociates molecules which were initially loaded through a small capillary and frozen on the walls in the discharge region. The discharge is located at the top of the trapping volume, in the highest magnetic field in the apparatus (4 T) as shown in Fig. 2-2. The discharge is simple in design (Fig. 2-3) and essentially unchanged from the first such discharges studied [38, 39] and the discharges which have been used in the MIT hydrogen experiment for the past 10 years [40]. It is a $\lambda/4$ coaxial resonator with a helical inner conductor, designed [41] to resonate at 300 MHz. The coil is tapped so as to impedance match at low temperature (< 2 K) the 50 Ω coaxial cable which carries the RF. This allows good coupling of the RF power into the dissociator ($> 90\%$). Care was taken to thermally anchor all discharge surfaces and avoid the formation of hot, liquid ^{4}He bare regions during loading which could serve as sights of enhanced recombination.

[1]The Amsterdam hydrogen trapping group had some success with a hybrid of laser cooling and magnetic trapping [36].

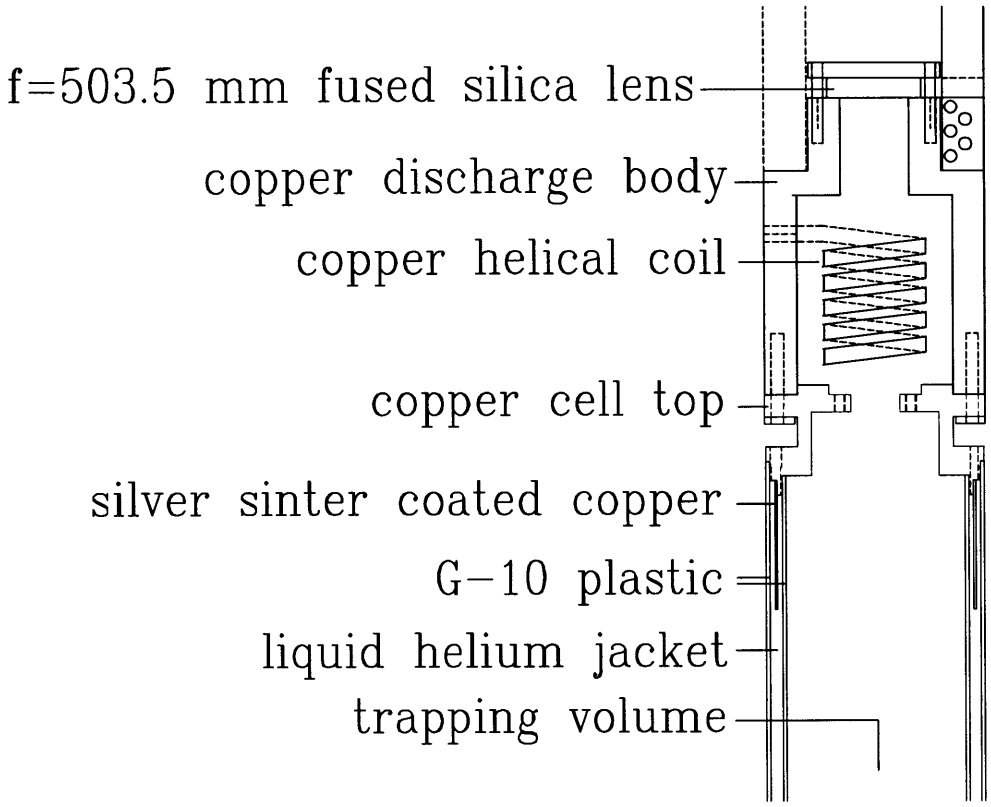

Figure 2-3: Diagram of the discharge and cell top. The discharge body and helical inner conductor form a $\lambda/4$ coaxial resonator for 300 MHz. When resonantly driven, the radio frequency field sparks a discharge which dissociates molecular hydrogen and forms atoms which stream into the trapping volume. The inner surface of the cell is coated with liquid ^{4}He to reduce the binding energy of hydrogen atoms to the walls. The walls of the trapping volume are made of G-10 plastic and a cylindrical space is filled with liquid ^{4}He to provide thermal conductivity. Silver sinter coated copper sheets provide a large surface area for heat transport across the ^{4}He–copper boundary.

When loading atoms into the trap, the discharge and cell are maintained at about 250 mK and the discharge is fired for about 30 seconds in pulsed mode, with 50 Hz repetition rate and 100 μs pulses with peak power of 10-30 W. The hydrogen flux is at least 10^{13} s^{-1}.

2.2.3 Spin Polarization

Atoms are produced in all four $1S$ hyperfine states and carried into the trapping cell in a puff of gaseous helium. After dissipating energy through collisions with the walls, high field seeking $H\downarrow$ atoms are pulled back to the discharge by the magnetic

field gradient. $H\uparrow$ atoms remain in the trapping volume and settle into the minimum of the magnetic field through atom-atom collisions. Atoms in the c state are lost from the trap very rapidly due to spin-exchange collisions which change the atoms to untrapped $H\downarrow$ [42]. This creates a doubly spin-polarized sample [43, 44] of typically a few times 10^{14} d state atoms.

2.2.4 Loss Processes and Gas-Surface Equilibrium

Two loss processes on the surface and one in the gas are important in the loading of d-state atoms into the trap. Magnetic impurities on the wall can flip the electron spin of a surface d state atom, causing it to be quickly expelled from the trapping region [45]. Also, in thermal equilibrium there is a small surface density of $H\downarrow$ atoms on the wall in the trapping region. While on the surface, a d state atom can readily recombine with a $H\downarrow$ atom since the interaction is through the singlet potential and the wall serves to conserve energy and momentum [46].

The hydrogen sample and wall are well thermally connected at the loading temperature of 250 mK because the H-^{4}He binding energy is low enough that atoms spend a short time on the wall compared to the characteristic recombination time with residual $H\downarrow$ or the spin flip time due to magnetic impurities. Atoms can thus hit the wall, stick, exchange energy with the wall, and return to the trap. The constant flux of energetic $H\uparrow$ atoms over the magnetic barrier to the wall, and off the wall into the trapped sample, maintains thermal equilibrium.

In the gas, weak dipole-dipole collisions[42, 44] can flip the spin of a d state atom, causing it to be lost from the trap. This process obeys the local two-body equation

$$\dot{n}_{dip} = -gn^2, \tag{2.1}$$

where n is the local density. The loss rate constant, $g = 2(G_{dd\to ac} + G_{dd\to aa} + G_{dd\to ad})$ is the sum of the dominant decay event rates for collisions between two d state atoms in the doubly spin-polarized sample. The event rates have been calculated[42] as a function of the magnetic field and temperature. For temperatures below 500 μK and

magnetic fields below 10^{-2} T, the rate constants change by less than a few percent from the zero temperature and field values. For this experiment, when the trap depth is less than half the hyperfine energy liberated in the inelastic processes (68 mK), atoms ending in the c and d states after a spin flip are lost from the trap, which explains the factor of two in the expression for g. For $B = 0$ and $T = 0$, the theoretical rate constant is $g = 1.1 \times 10^{-15}$ cm^3/s. At $n = 10^{13}$ cm^{-3}, this implies a 100 second sample lifetime. The theory quotes no uncertainties.

There is an experimental measurement of g [44] which agrees with theory with a 17% uncertainty. It is important to note that in that experiment [44], there was no way for d or c atoms to escape the trap besides flipping their electron spin. Hence the d and c atoms in the exit channels of spin flip collisions remained trapped and were not counted in the loss rate. The expression for g in [44] differs accordingly.

Since dipolar decay preferentially removes atoms from the low energy, high density region at the bottom of the trap, it is a heating mechanism for the sample.

A final loss process worth noting is three-body recombination in the gas. When three hydrogen atoms collide, two can recombine while the third serves to conserve energy and momentum. This is governed by the rate equation

$$\dot{n}_{3-body} = -Ln^3. \tag{2.2}$$

The decay constant is $L \approx 10^{-38}$ cm^6/s [33]. The process is negligible in the MIT hydrogen experiment, but it is often the density-limiting effect in alkali metal trapping experiments. [47].

2.3 Evaporative Cooling

After the trap is loaded the wall temperature is quickly lowered, and when it reaches about 150 mK, the wall residence time becomes so long that atoms which reach the wall and stick[48] are lost due to spin flip or recombination. The sample thermally disconnects from the wall and energetic atoms are quickly removed from the sample as

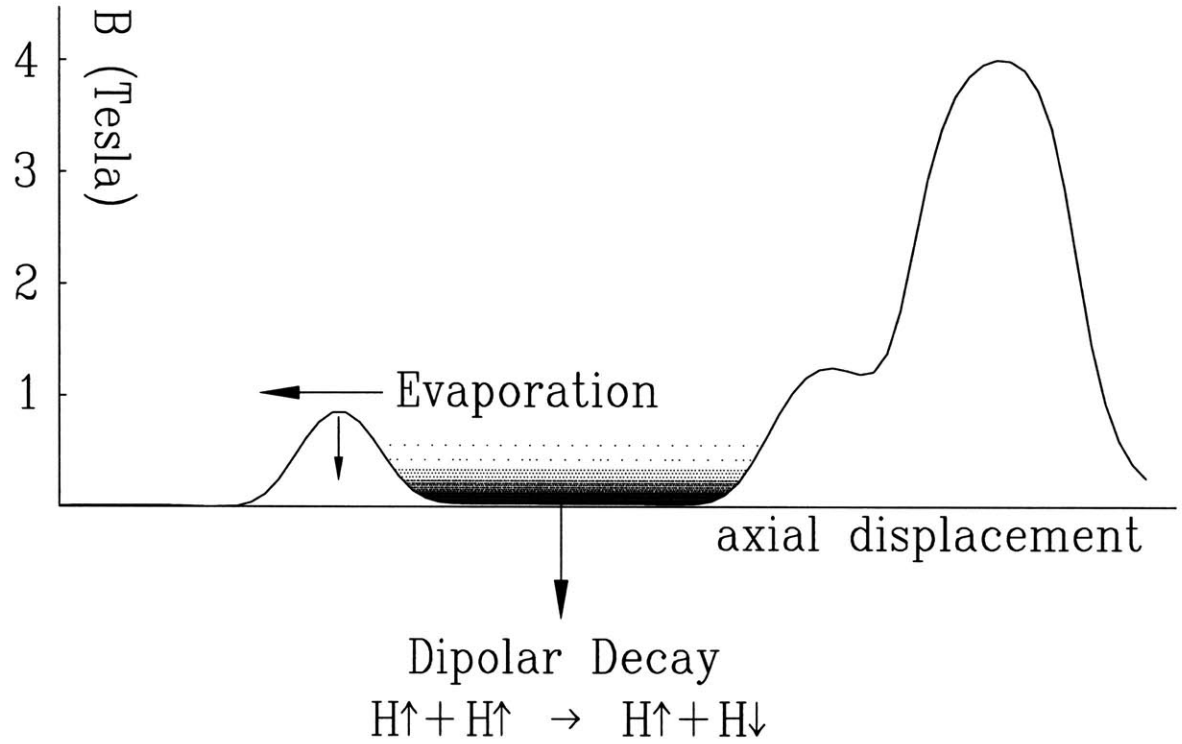

Figure 2-4: Schematic of the magnetic trap and hydrogen cloud shortly after loading the trap. Energetic atoms escape over a saddlepoint in the magnetic field, evaporatively cooling the sample. Dipolar decay removes atoms preferentially from the highest density region at the bottom of the trap, heating the sample. Heating and cooling balance when the sample temperature is about one thirteenth of the trap depth. By lowering the confining magnetic field, the sample can be further cooled through forced evaporation.

they evaporate over the magnetic barrier (Fig. 2-4). The temperature of the remaining sample drops until a balance is reached between the cooling due to evaporation and heating due to dipolar decay. A useful quantity to define is $\eta = \varepsilon_{trap}/k_B T$, the ratio of trap depth to equilibrium sample temperature, which, to a good approximation, depends only on the trap depth[24]. In the 0.5 K deep trap, $\eta \approx 13$. After the sample thermally disconnects from the wall and cools, there are about 10^{14} atoms at $T = 40$ mK, and the density distribution is given by $n(\mathbf{r}) = n_0 \exp(-U(\mathbf{r})/k_B T)$, where $n_0 \approx 10^{13}$ cm^{-3} is the peak density found at the magnetic field minimum.

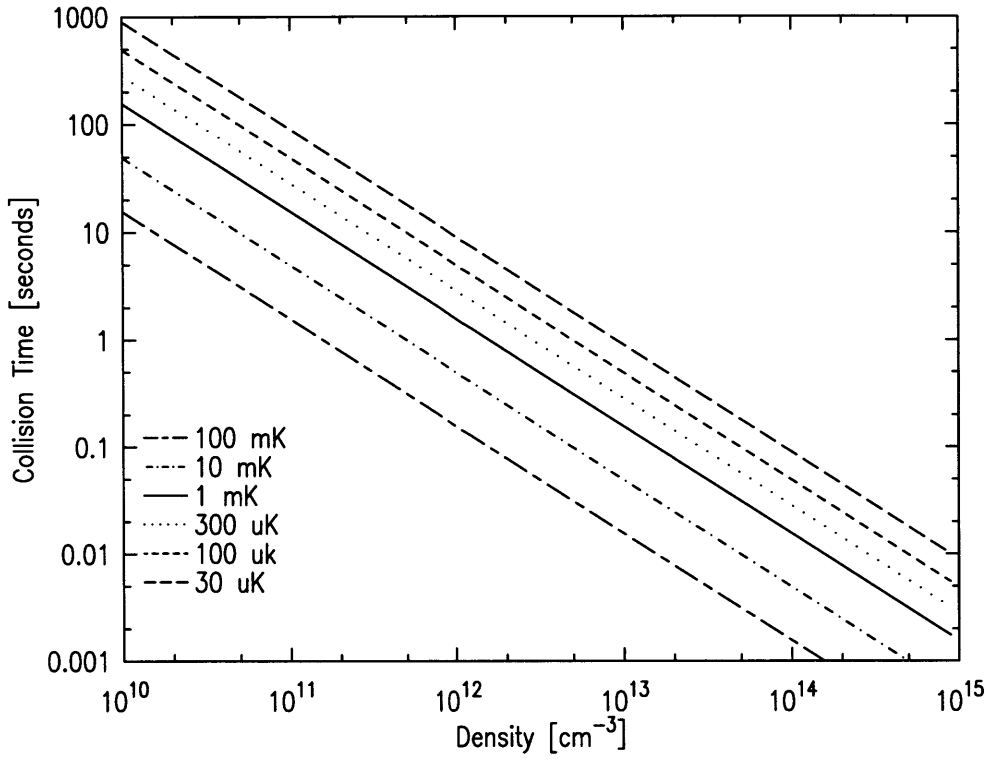

Figure 2-5: Time between collisions, $\tau = 1/n\sigma\bar{v}\sqrt{2}$ for various hydrogen densities and temperatures. The collision cross section is $\sigma = 8\pi a^2 = 1.06 \times 10^{-15}$ cm^2 and $\bar{v}\sqrt{2} = \sqrt{16k_BT/\pi m}$ is the thermal average relative velocity between two atoms. The thermalization time for a sample out of equilibrium has been estimated to be a few collision times[49, 47].

2.4 Forced Evaporative Cooling

H. Hess, while working on the MIT hydrogen experiment, first suggested that because the sample equilibrates at a fraction of the trap depth, one could force the evaporation and further cool the sample by gradually lowering the confinement barrier [34]. If the trap depth is lowered slowly enough for the sample to remain in equilibrium through elastic collisions (Fig. 2-5), but fast enough so that dipolar decay does not remove too many of the atoms, n_0 increases as well [47]. The peak phase space density increases even though atoms are lost from the trap.

The cooling power of evaporation is proportional to the rate at which energetic atoms are created in binary collisions and removed from the sample. For ideal evaporation, all atoms which attain energy greater than the trap depth leave immediately

and the cooling power per atom varies as a constant times the collision rate per atom, $n\sigma\bar{v}\sqrt{2} \propto \sqrt{T}$, where σ is the elastic collision cross section.

Since the dipolar heating rate goes as the loss rate per atom, gn, and is independent of temperature, the ratio of cooling power to heating decreases with temperature. Thus, η decreases with temperature as well. Evaporative cooling of hydrogen becomes difficult below about 1 μK [47, 50]. It was predicted that BEC in hydrogen could be realized at about 30 μK [34] where $\eta \approx 7$.

2.4.1 Magnetic Field Saddlepoint Evaporation

Forced evaporative cooling was first realized in the current experiment [51] by lowering a magnetic field saddlepoint which forms the lower axial confinement barrier and defines ε_{trap}, as shown in Fig. 2-4. If the barrier field is lowered from the starting height of about 0.8 T, to a final height of 15-20 $\times 10^{-4}$ T in about 5 minutes, the peak density increases to nearly 10^{14} cm^{-3} while the temperature drops to about 120 μK [52]. Over 10^{11} atoms remain in the trap.

Further evaporative phase space compression proves to be impossible in the current apparatus using this method to define the trap depth and remove energetic atoms. This was explained by the Amsterdam hydrogen trapping group [53] in the context of a similar experiment. Evaporating over the magnetic saddlepoint only removes atoms with high energy in the axial degree of freedom. This is not a problem when the density of atoms is relatively low and the temperature is high because all atoms which acquire energy greater than ε_{trap} still escape from the trap and evaporation is essentially ideal. This happens because the low density implies that the mean free path between collisions is long, and at a high temperature, atoms access anharmonic regions of the trap. Energy is exchanged between the three motional degrees of freedom quickly and the time required for atoms to explore the entire trap and escape is short compared to the time between collisions.

However, when the density increases, the mean free path decreases, and when the sample temperature drops, atoms settle into the harmonic region of the trap and the coupling between the degrees of freedom decreases. It becomes more likely for atoms

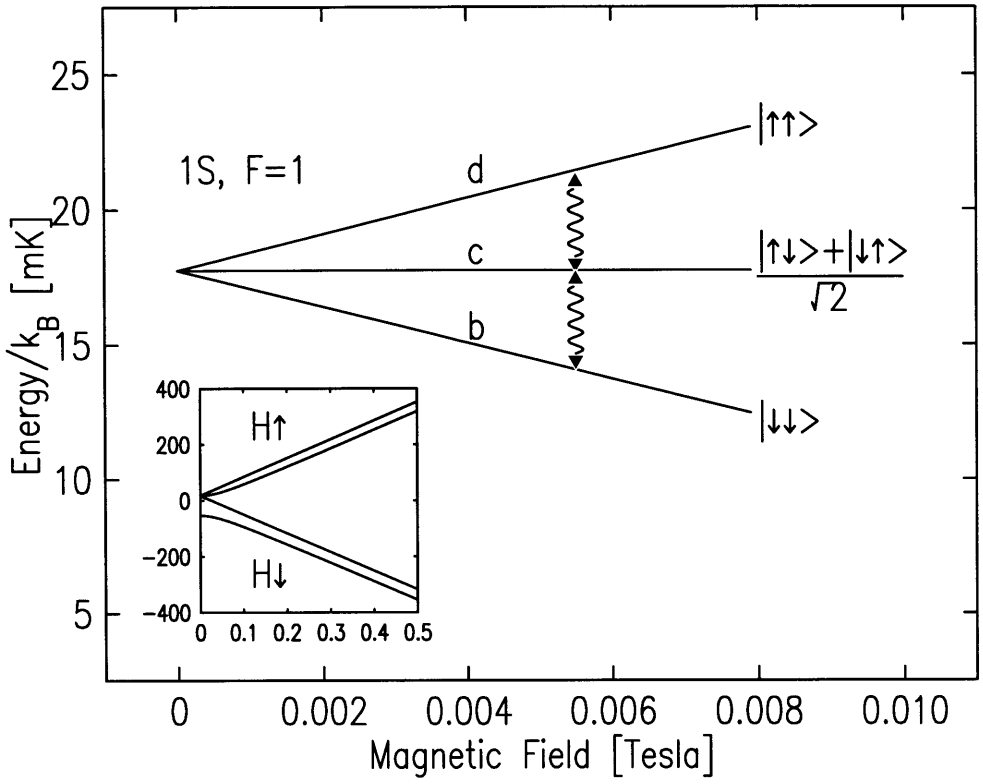

Figure 2-6: Zeeman diagram of $1S$ $F = 1$ states in low magnetic fields showing the transitions driven for RF evaporation. A trapped atom is in the d state. When it climbs the magnetic potential and passes a region where the field brings its levels into resonance with the RF frequency, the electronic spin can flip, changing the atom to a c state atom which feels a much weaker confining potential. If the c state atom does not escape the trap, in ensuing passes through resonance, it can be changed to an anti-trapped b state atom and be expelled from the trap. The inset shows the complete $1S$ Zeeman diagram.

with radial energy above ε_{trap} to suffer a collision before the energy is transferred into the axial degree of freedom. The additional collision is most likely to redistribute the energy so that neither the energetic atom, nor the atom with which it collides, has enough energy to escape. The probability for an energetic atom to escape drops significantly and the evaporation becomes nonideal, increasingly "one-dimensional," and inefficient [47].

2.4.2 Radio-Frequency Evaporation

To overcome this problem, an alternative method of defining the trap depth and removing energetic atoms is used. A d state atom's spin can be flipped by an RF field which is resonant with the magnetic sublevel spacing as shown in Fig. 2-6. (This is reminiscent of electron spin resonance spectroscopy.) In an inhomogeneous magnetic field such as the trap, the RF frequency, ν, defines a resonance surface where the magnetic field has constant magnitude, $B \approx h\nu/\mu_B$. Atoms with enough energy in any motional degree of freedom can climb the magnetic potential and pass this surface and be ejected from the trap. Lowering the RF frequency forces the evaporation. This method for ejecting atoms from a magnetic trap was introduced by Pritchard *et al.* [54] and has been used to evaporatively cool Rb [19], Na[20] and Li[21, 22] atoms into the quantum degenerate regime.

In this experiment, the RF evaporation typically starts at a trap depth of 1.1 mK, corresponding to a frequency of 23 MHz and sample temperature of 120 μK. In about 25 seconds the trap depth can be lowered to 100 μK, producing atoms with a temperature below 30 μK.

Implementing RF evaporation in the current experiment required major modifications of the trapping apparatus to reduce RF eddy current heating[23]. Virtually all metal in the trapping region had to be removed because more than $\sim$ 100 μW of RF heating in resistive conductors would cause the cell temperature to rise enough to create a significant vapor pressure of He in the cell which would greatly diminish the sample lifetime. Thermal transport along the trapping cell, which was previously supplied by copper wires, is now provided by a jacket of liquid ^{4}He (Fig. 2-3).

2.5 Probing the Trapped Gas

Many common methods for alkali atom detection, such as hot wire ionization for example, do not work for hydrogen because of its large electron binding energy. When hydrogen atoms leave the trap, however, they can recombine on the walls, and in a cryogenic environment, the liberated recombination energy can be recorded on a sensi-

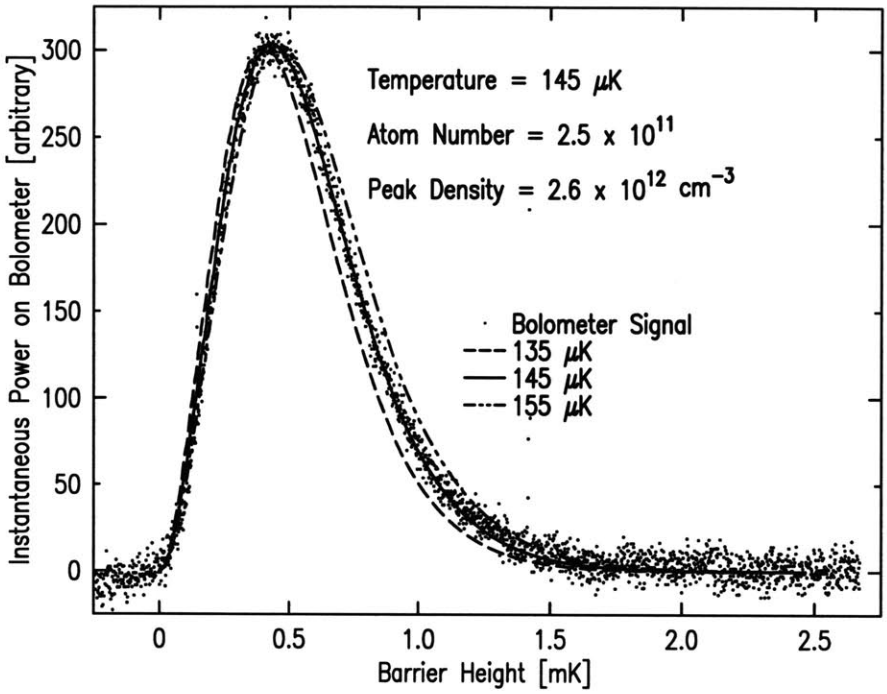

Figure 2-7: Bolometric determination of the sample temperature. The power deposited on the bolometer is recorded as a trap confinement barrier is lowered. The power measures the number of atoms with energy equal to the barrier height. The smooth curves are the expected distributions for various sample temperatures.

tive bolometer[24, 55]. A robust and reliable method of measuring the temperature[56] and density[51] of the hydrogen sample is to record the recombination energy while lowering the magnetic barrier and releasing the atoms from the trap.

2.5.1 Bolometric Temperature Measurement

If the barrier is lowered slowly compared to the time for atoms to escape, recombine, and deposit energy on the bolometer, the power deposited is proportional to the number of atoms in the sample at the energy of the barrier. Provided the release time is shorter than the collisional rethermalization time, the thermal distribution of atoms in the trap will not change during the dump, and from the bolometric data and a knowledge of the magnetic field, one can find the sample temperature (Fig. 2-7).

Considering the time scale constraints mentioned above and experimental details such as signal to noise of the measurement and inductive time constants of the magnets, the bolometric determination of temperature is only reliable for samples

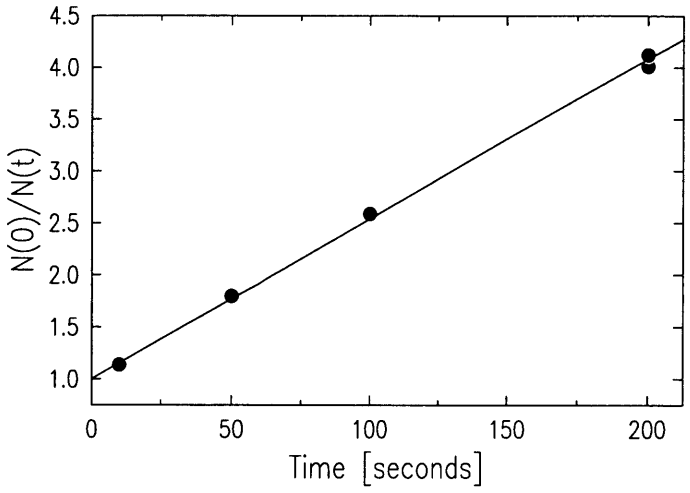

Figure 2-8: Decay of a trapped hydrogen sample. The sample density is found from the slope of $N(0)/N(t)$, the inverse of the normalized total number of atoms remaining in the trap. The data shown indicates a density of 6.0×10^{13} cm^{-3}.

temperatures between 100 μK and 5 mK and densities below 10^{14} cm^{-3}.

2.5.2 Bolometric Density Measurement

One can measure the sample density by releasing the atoms from the trap after holding them for different times following the forced evaporation. The total recombination energy deposited on the bolometer by a sample held for a time t is proportional to $N(t)$, the number of atoms remaining in the trap at time t. $N(t)$ decreases with time due to dipolar decay and evaporation, as shown in Fig. 2-8.

By integrating the local dipolar decay loss rate (Eq. 2.1) over the trap volume, one finds

$$\dot{N}_{dip} = -g\frac{V_2(T)}{V_1^2(T)}N^2(t), \tag{2.3}$$

where $\dot{N}_{dip}$ is the atom loss rate due to dipolar decay, and $V_m(T) = \int d^3r\ \mathrm{e}^{-mU(\mathbf{r})/k_BT}$ is an effective volume.

While measuring the decay, atoms are also lost due to evaporation. To maintain thermal equilibrium, for every $\eta - 2$ atoms lost due to dipolar decay, 1 atom must

evaporate[51]. Thus $\dot{N} = \dot{N}_{dip} + \dot{N}_{evap} = \dot{N}_{dip}(\eta - 1)/(\eta - 2)$, and

$$\frac{N(0)}{N(t)} = 1 + \left(\frac{\eta - 1}{\eta - 2}\right) \frac{V_2(T)}{V_1(T)}\, g n_0(0) t \tag{2.4}$$

where $n_0(t)$ is the peak density in the trap at time t, The value of $V_2(T)/V_1(T)$ is found numerically for each trap configuration, but to a good approximation, one can describe the potential by the potential energy density of states exponent, δ: $d^3r \propto U^{\delta-1}dU$. In a linear quadrupole trap, $\delta = 2$ and $V_2(T)/V_1(T) \approx (1/2)^\delta \approx .25$. For cold samples, which have settled nearer the bottom of the trap, the potential is harmonic in the radial direction, not linear, and δ can be significantly different.

From the relative number of atoms measured with the bolometer, and a knowledge of the trap shape, one can extract the initial peak density. The number of atoms in the sample and the absolute sensitivity of the bolometer can then be found from $N(0) = V_1(T)n_0(0)$.

The slope of the sample decay curve is reproducible to a few percent for identically prepared samples. The dominant uncertainty in this measurement, however, is systematic, arising from imperfect knowledge of our trapping fields. This limits the accuracy of the measurement of $n_0(0)$ to about 10-20%. Any error in the calculation of g would also be reflected in the inferred densities.

At temperatures below about 100 μK the trapping magnetic fields are so low that additional contributions from magnetic materials and trapped fluxes in the superconducting magnets become significant and the trap is not well known. The bolometric method for measuring n_0 then becomes unreliable.

Probing the trapped gas with bolometric techniques is limited by the escape time of the atoms and it also necessitates the destruction of the sample. Spectroscopic methods offer the possibility of monitoring the gas *in situ*. The Amsterdam hydrogen trapping group implemented Lyman-alpha $1S$-$2P$ spectroscopy of the sample [57], and then, to overcome the limitations imposed by the large natural linewidth of the $1S$-$2P$ transition, they developed resonance enhanced two-photon spectroscopy (RETS). In RETS, two-photon excitation to a relatively long-lived $3S$ or $3D$ state

is enhanced by tuning one laser frequency near resonance with an intermediate $2P$ state [58]. The MIT hydrogen trapping group chose an alternative path and pursued two-photon $1S$-$2S$ spectroscopy as a probe of the trapped gas.

Chapter 3

Overview of $1S$-$2S$ Spectroscopy in a Trap

This chapter gives an overview of the $1S$-$2S$ spectroscopy component of the experiment, as well as a bit of historical perspective. The laser system was designed and built by J. Sandberg and C. Cesar, and more details are available in their Ph.D. theses [59, 60].

High resolution spectroscopy is a useful probe of the trapped hydrogen gas, but the observations reported here also show that the physics of the excitation is of interest by itself. The two-photon spectrum is novel, and the long coherence time of the laser-atom interaction makes the atomic motion much more important than it is for normal one-photon transitions. The excitation also probes atom-atom interactions and correlations in ways which are not yet completely understood.

3.1 Background

The two-photon $1S$-$2S$ transition was first observed in 1975 in a gas cell[61], and the experimental linewidth was limited to about 100 MHz by the pulsed laser source. Improvements in nonlinear optical frequency generation made CW experiments possible, first in a gas cell at about 0.2 torr [62] where the linewidth was collisionally limited to a few MHz, and then in a liquid nitrogen temperature atomic beam [63]

where the linewidth of 50 kHz was due to the second order Doppler-shift and finite interaction time of the atoms with the laser. By cooling the atomic beam to about 5 K, and selecting the signal from only the coldest atoms, the resolution has reached about 2 kHz[64].

By comparing the $1S$-$2S$ transition frequency to that of another electronic hydrogen transition, one can determine the Rydberg constant and Lamb shift [8, 9], and the deuteron radius can be determined by comparing the $1S$-$2S$ frequency in hydrogen and deuterium [8, 65]. The $1S$-$2S$ frequency in hydrogen is $f_{1S-2S} = 2,466,061,413,187.34(84)$ kHz [9], and this is the most accurately known frequency in the UV or optical region.

In the late 1980's the MIT $H\uparrow$ trapping group, in the quest for BEC, set out to excite the $1S$-$2S$ transition in a trapped sample in order to study the gas *in situ*. A secondary goal was high resolution spectroscopy of the cold atoms. In a trap the possible interaction time is long, and at the low thermal velocities, the second order Doppler-shift is negligible.

3.2 Two-Photon Excitation

Figure 3-1 shows a sketch of the levels involved in $1S$-$2S$ spectroscopy of trapped hydrogen. The angular momentum is zero for both the $1S$ and $2S$ states, so the transition cannot be driven by one photon. An atom can absorb two 243 nm photons, however, and be excited to the $2S$ state through an intermediate virtual P level. For a transition to occur, an atom must absorb two photons in a time less than $\hbar/\Delta$, where $\Delta = (E_P - h\nu)$ is the laser detuning from E_P, the energy of the P level. The excitation rate varies as the square of the laser intensity, and for a given intensity, the rate is much lower than for a one photon transition. The $2S$ state is metastable ($\tau_{1S} = 122$ ms) because an unperturbed $2S$ atom can only radiatively decay to ground through emission of two photons[66].

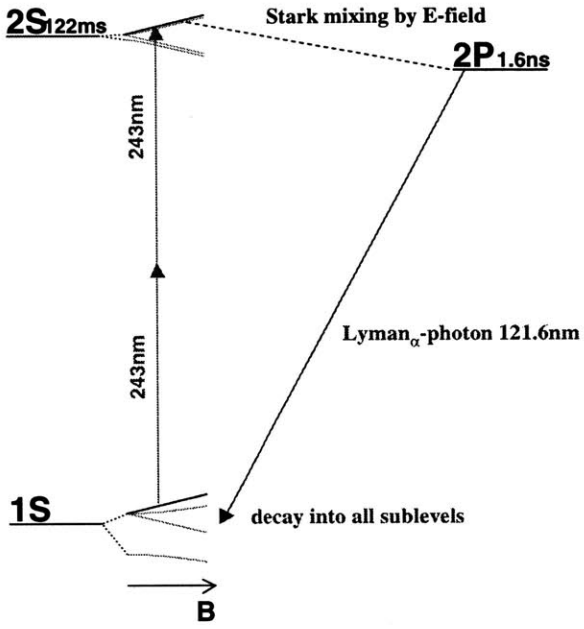

Figure 3-1: Level scheme for $1S$-$2S$ spectroscopy of magnetically trapped atomic hydrogen. Trapped $F = 1$, $m_F = 1$, $1S$ atoms are excited to the metastable $F = 1$, $m_F = 1$, $2S$ state by absorption of two 243 nm photons. An applied electric field Stark mixes some $2P$ character into the excited state wavefunction and causes prompt radiative decay to the ground state through emission of a single Lyman-alpha photon (121.6 nm). $1S$ and $2S$ $F = 1, m_F = 1$ atoms see the same magnetic trapping potential.

3.3 Detection Scheme

The sample is optically thin to the laser radiation, even on resonance, so it is not feasible to monitor the excitation rate by measuring direct absorption of the laser. However, photoexcitation can be detected by monitoring fluorescence from the excited state. The signal to noise ratio can be greatly enhanced by using a pulsed scheme (Fig. 3-2), in which each excitation pulse is followed by the application of a short electric field pulse ($\sim$ 10 V/cm). This Stark mixes some $2P$ character into the excited state wave function (See Sec. 4.4.3), and causes $2S$ atoms to promptly decay to the ground state through emission of a single Lyman-alpha photon (121.6 nm) which can be detected by a microchannel plate (MCP) [67, 68].

A typical timing sequence for excitation and detection is shown in Fig. 3-3. A

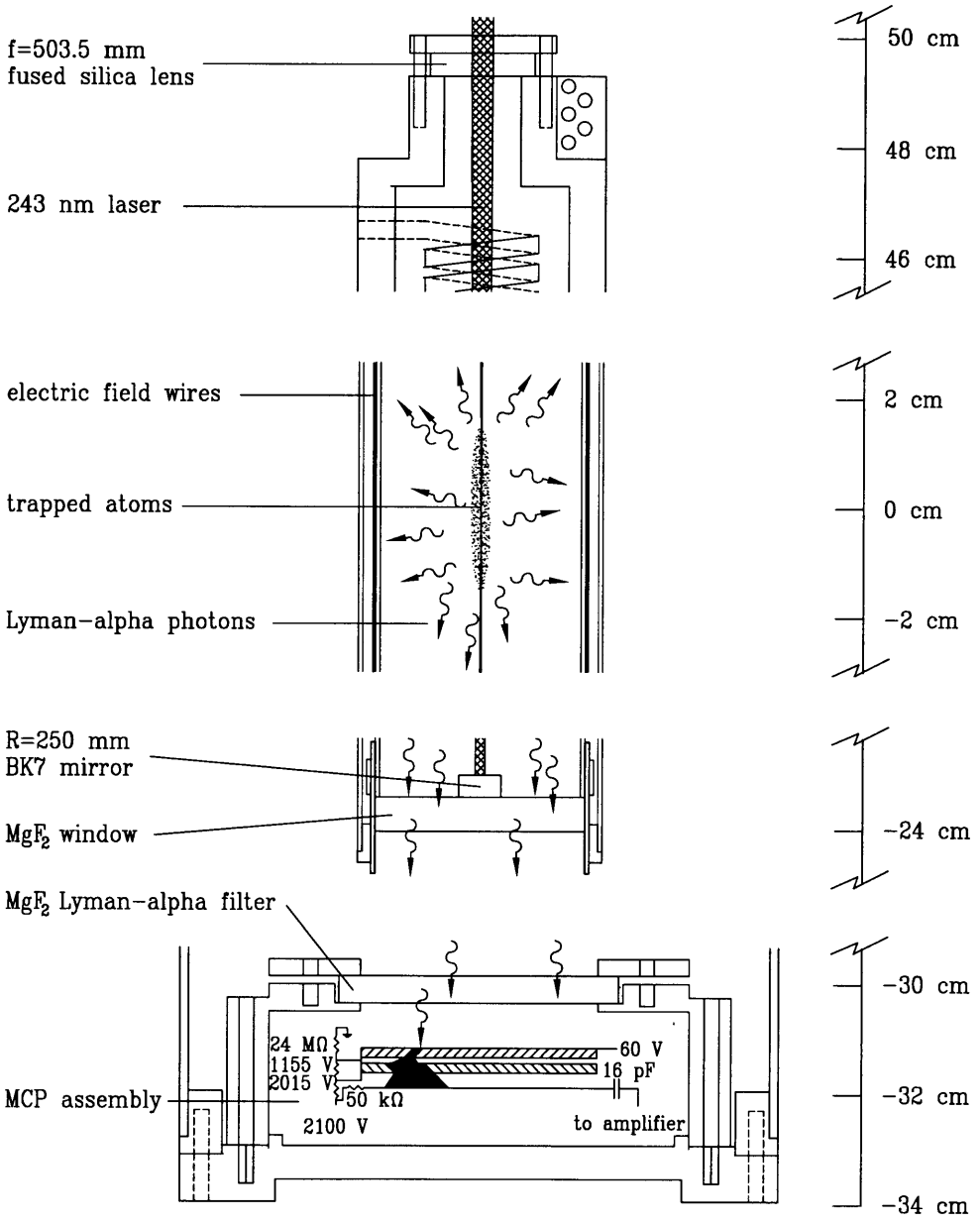

Figure 3-2: Excitation and detection. Trapped atoms are excited to the $2S$ state by the 243 nm standing wave laser field which passes on axis. The laser is blocked, and ± 100 V is applied across the electric field wires, producing a 10 V/cm field in the cell. This causes the $2S$ atoms to rapidly decay through emission of 121.6 nm Lyman-alpha photons. Approximately 10^{-5} of these photons are detected with a microchannel plate assembly. The aspect ratio of the figure is 1:1

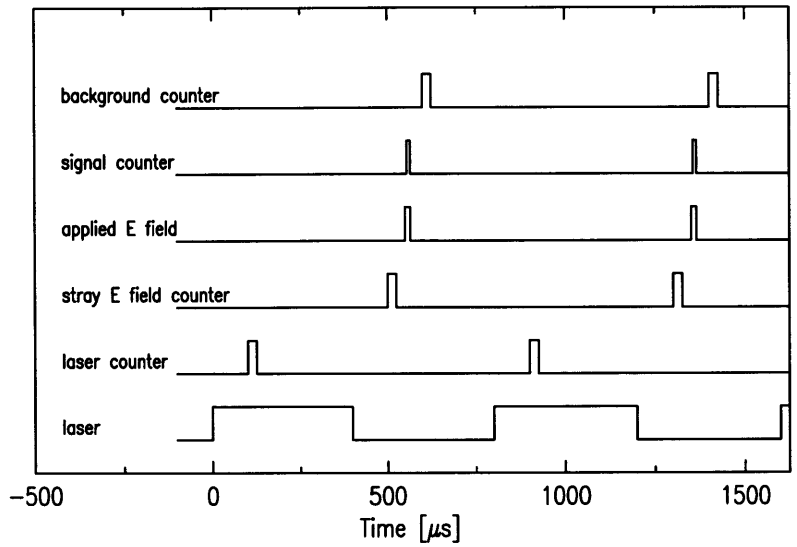

Figure 3-3: Typical timing sequence for $1S$-$2S$ excitation and detection.

mechanical chopper modulates the laser beam with 50% duty cycle and 400 μs pulse length. The electric field pulse is typically 12 μs long, and the resulting signal pulses are recorded by a counter enabled during this time. During this Stark quench the peak count rate can exceed 10 MHz. The number of signal Lyman-alpha counts recorded as a function of laser frequency is the photoexcitation spectrum.

Additional counters during each timing sequence are used for diagnostic purposes. The laser power can vary 10-20% during the recording of one spectrum, and its level is monitored by a counter gated open for 25 μs during the laser pulse. The count rate from scattered laser photons, which can exceed 100 kHz, is proportional to laser power. Following the laser pulse, but before the Stark quench, a counter enabled for 25 μs monitors the Lyman-alpha fluorescence caused by stray electric fields. The count rate can be used to measure the value of the field. Typical stray fields in the cell are on the order of a half volt per centimeter or less, and give the $2S$ state a lifetime of milliseconds (Sec. 4.4.3). A counter after the quench records dark counts ($\sim$ 200 Hz) for 25 μs. These counts arise chiefly from long lived fluorescence from organic materials in the cell which were excited by the laser, and the measured rate can be used to establish the background count rate, which can be subtracted when measuring very weak $1S$-$2S$ signals.

This sequence is repeated for typically 10-100 laser pulses for each laser frequency.

3.4 Microchannel Plate Photon Counter

The MCP assembly is shown in Fig. 3-2. The top plate is a 50 mm diameter, 0.6 mm thick lead glass disk with 60% open area in the form of an array of 10 μm diameter channels[68]. Each channel has a length to diameter ratio of 60:1. The top surface is coated with CsI to decrease the work function for efficient production of electrons by impinging vacuum ultraviolet photons. The top surface is positively biased by 60 volts with respect to the surrounding housing to guide electrons into the channels. Approximately 1000 volts is applied across the channels to accelerate the electrons. Collisions with the channel walls eject more electrons and create an electron shower. Each channel acts as an electron multiplier with a gain of about 10^4.

The bottom plate is similar in structure to the top, but it has a length to diameter ratio of 40:1[1] for its channels and is uncoated. With 2 plates, the gain is about 10^6 so that a single photon results in a 1 mV, 5 ns pulse into 50 Ω which is capacitively coupled to a high bandwidth video amplifier ($\times$100). Amplified pulses are discriminated and turned into logic pulses which are counted at rates up to 100 MHz. The quantum efficiency of the assembly for 121 nm photons was calibrated against a Hamamatsu R972 photomultiplier tube [69] and found to be 25%. Due to a small solid angle ($\sim 10^{-2}$ sr), absorption of Lyman-alpha in optical elements, and MCP quantum efficiency, only 10^{-5} of the emitted photons are detected.

To be close to the atoms, the MCP is mounted inside the cryostat. At low temperature, the replenishment of the charge in a single channel after it fires can take seconds. During the recovery time, that channel is effectively blind to photons. When a significant fraction of the channels fire during one recharging time, the quantum efficiency of the MCP drops. This implies a maximum sustainable counting rate which is about 20 kHz at 20 K, 200 kHz at 80 K, and greater than a MHz at room temperature. If precautions were not taken, counts due to scatter from the laser would

[1] 60:1 plates are newly available and are superior in gain and mechanical strength.

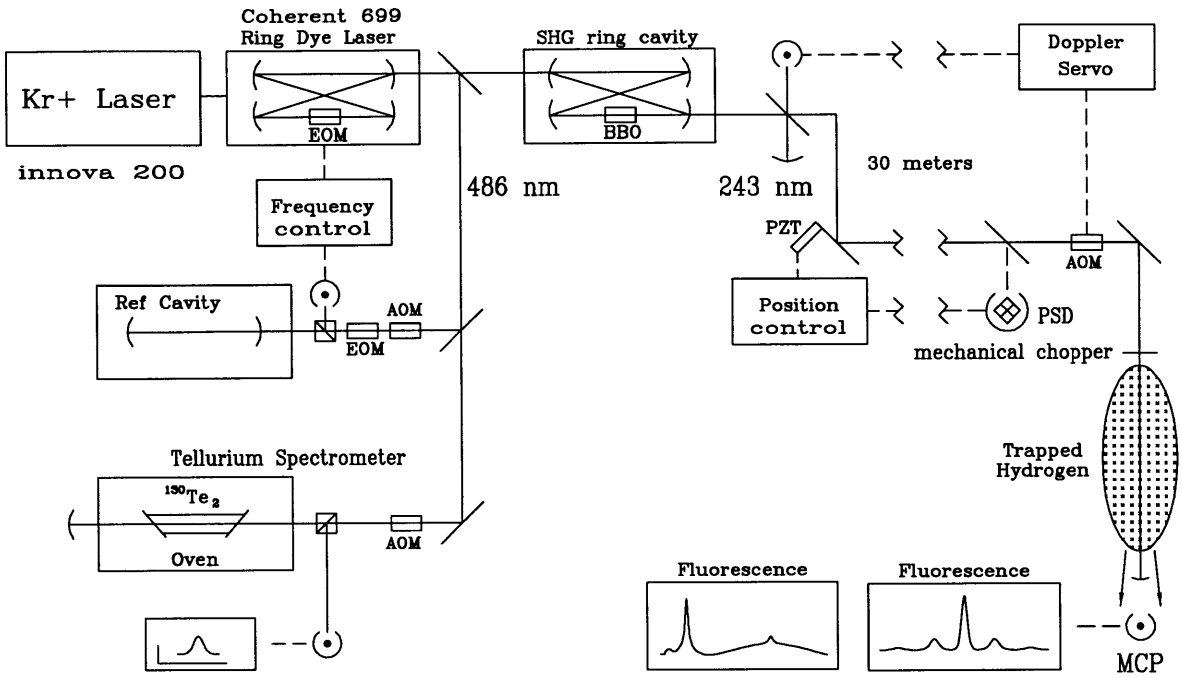

Figure 3-4: Laser system for $1S$-$2S$ spectroscopy of trapped atomic hydrogen. Components are explained in the text.

saturate the MCP even though the sensitivity to 243 nm photons, according to the manufacturer, is at least 4 orders of magnitude lower than to 122 nm photons. The MCP would be left blind during the Stark quench since the recovery time is longer than the time between laser pulses. The MCP assembly is weakly anchored to 4 K, but it is normally heated to 70 K or higher during operation. In addition, a Lyman-alpha filter[70] above the MCP cuts the 243 nm light by a factor of 500 and drops the laser scatter count rate below the saturation level. Unfortunately, the filter also cuts Lyman-alpha transmission by 90%.

3.5 Laser System

The laser system used for spectroscopy of atomic hydrogen (Fig. 3-4) was based on a design from the group of T. Hänsch in Munich [71]. We briefly point out the important features here. (For further details on some of the optical devices discussed below, see [72].)

A Coherent 699 ring dye laser, pumped by a krypton ion laser, produces about 450

mW of linearly polarized 486 nm radiation in a single longitudinal TEM_{00} mode. Due to acoustic vibrations of the laser support structure and fluctuations in the thickness of the dye lasing medium, active stabilization is required to maintain a narrow laser frequency spectrum. An intracavity electro-optic modulator, piezo-mounted mirror, and galvo-mounted brewster plate are used to control the optical path length in the laser cavity and lock the frequency to the center of a transmission fringe of a stable Fabry-Perot optical resonator. The error signal for the frequency control electronics is generated using the Pound-Drever-Hall locking scheme [73]. Using the hydrogen spectrum as a reference, the resulting spectral linewidth has been shown to be below 500 Hz for times of a few seconds (See App. A). The frequency of the laser can be tuned with respect to the fixed transmission fringe by changing the RF drive frequency of an acousto-optic modulator (AOM) which is in the light path to the the optical resonator.

Absolute frequency calibration to within a few hundred kHz is determined with Doppler-free saturated absorption spectroscopy of a transition in molecular $^{130}Te_2$. Appendix E provides more details on this important component of the experiment.

The 243 nm radiation necessary to drive the $1S$-$2S$ transition is generated by frequency doubling the 486 nm light in a beta barium borate crystal (BBO)[74]. To increase the nonlinear efficiency, the blue power is enhanced in an optical build-up cavity place around the crystal. The Hänsch-Couillaud locking scheme[75] is used to maintain the cavity on resonance with the 486 nm laser light. With 450 mW of 486 nm light from the laser, about 20 mW of linearly polarized 243 nm light can be produced. The 243 nm beam is highly astigmatic due to the large double refraction angle of BBO, and, even with astigmatism compensation, only about 10 mW of power is in a useful TEM_{00} mode.

The laser and hydrogen trap are in separate rooms, 30 meters apart, so the 243 nm beam is collimated and sent through air to the cryostat. The pointing stability is servo controlled using piezo-mounted mirrors, quadrant photodiodes, and a feedback system designed by C. Cesar [60]. Optics inside the cryostat (Fig. 3-2) focus the beam to a waist radius of 20-50 μm in the atom cloud to produce the high intensity

necessary to excite atoms to the $2S$ state. The beam is retro-reflected back on itself by a mirror below the atoms to create a standing wave in the trap region. The return beam is monitored on the optics table to ensure proper overlap with the outgoing beam. Continuous manual adjustment is required to maintain the overlap. This is a serious limitation for the experiment because it can take up to a second to acquire proper alignment when the laser beam is first let into the cryostat.

The laser can be modulated by a mechanical chopper at frequencies up to 2 kHz. An AOM can be inserted in the 243 nm beam path to allow faster chopping and active control of the excitation power at the expense of a 50% reduction in power. In these experiments, the AOM was only used when testing the limits of the spectral resolution of the $1S$-$2S$ signal as discussed in App. A.

3.6 Photoexcitation Spectrum

The metastability of the $2S$ state results in the narrow natural linewidth of the $1S$-$2S$ transition (1.31 Hz at 121 nm). This makes the spectrum extremely sensitive to potentially interesting broadening and shift mechanisms which provide valuable information about the sample. These effects are small in the cold, dilute gas, and they would be hidden by the natural linewidth of a one-photon transition. (The $1S$-$2P$ single-photon transition linewidth, for example, is 100 MHz, and, as will be described later, the maximum shifts we see are about 1 MHz.) In addition, the narrow linewidth can be exploited for ultrahigh resolution spectroscopy and fundamental measurements [10, 9].

The transition energy for a trapped $1S$ atom with momentum $\mathbf{p}_{1S}$, which absorbs two photons with momenta $\hbar\mathbf{k}_1$ and $\hbar\mathbf{k}_2$ and goes to the $2S$ state, is given by

$$\begin{aligned} 2h\nu_{laser} &= \sqrt{p_{2S}^2c^2 + (mc^2 + E_{1S-2S}^0)^2} - \sqrt{p_{1S}^2c^2 + (mc^2)^2} \\ &\approx E_{1S-2S}^0 + \frac{\mathbf{p}_{1S}\cdot(\hbar\mathbf{k}_1 + \hbar\mathbf{k}_2)}{m} + \frac{|\hbar\mathbf{k}_1 + \hbar\mathbf{k}_2|^2}{2m} - \frac{|\mathbf{p}_{1S} + \hbar\mathbf{k}_1 + \hbar\mathbf{k}_2|^2}{2m}\frac{E_{1S-2S}^0}{mc^2}. \end{aligned} \tag{3.1}$$

(We have used the fact that the atom must take up the momentum of the photons so $\mathbf{p}_{2S} = \mathbf{p}_{1S} + \hbar\mathbf{k}_1 + \hbar\mathbf{k}_2$.) The second and third terms represent the first order Doppler-shift and the photon momentum recoil shift respectively. The last term in Eq. 3.1 is the second order Doppler-shift. This effect often limits the resolution for $1S$-$2S$ spectroscopy in an atomic beam, but it is completely negligible for trapped hydrogen. (At 100 μK, $v^2/c^2 \approx 10^{-17}$, and the shift is 10^{-2} Hz.)

Since the excitation occurs in a standing wave, atoms can absorb photons in two ways. Absorption of two co-propagating photons ($\mathbf{k}_1 = \mathbf{k}_2$) gives rise to a recoil shifted ($\Delta\nu_{\text{recoil}} = 6.7$ MHz) and Doppler-broadened feature, and is called Doppler-sensitive excitation. The Doppler-width of this feature (RMS width $\Delta\nu_{\text{Dopper}} = 0.374 \times 10^9\sqrt{T}$ Hz $\text{K}^{-1/2}$) is a valuable absolute measure of the temperature of the sample (Fig. 3-5).

Doppler-free excitation results from the absorption of two counter-propagating photons ($\mathbf{k}_1 = -\mathbf{k}_2$). There is no recoil shift or Doppler-broadening in this case and the resulting spectral feature can be very narrow. The dominant broadening for low density samples usually comes from the finite interaction time of an atom with a laser (time-of-flight)[10, 76, 77]. In high density samples, the resonance is red-shifted and the feature is inhomogeneously broadened by atom-atom interactions [11]. This effect is often called the cold collision frequency shift [15, 42, 16, 17, 12, 18]. The lineshapes observed under different experimental conditions are discussed in Chap. 4.

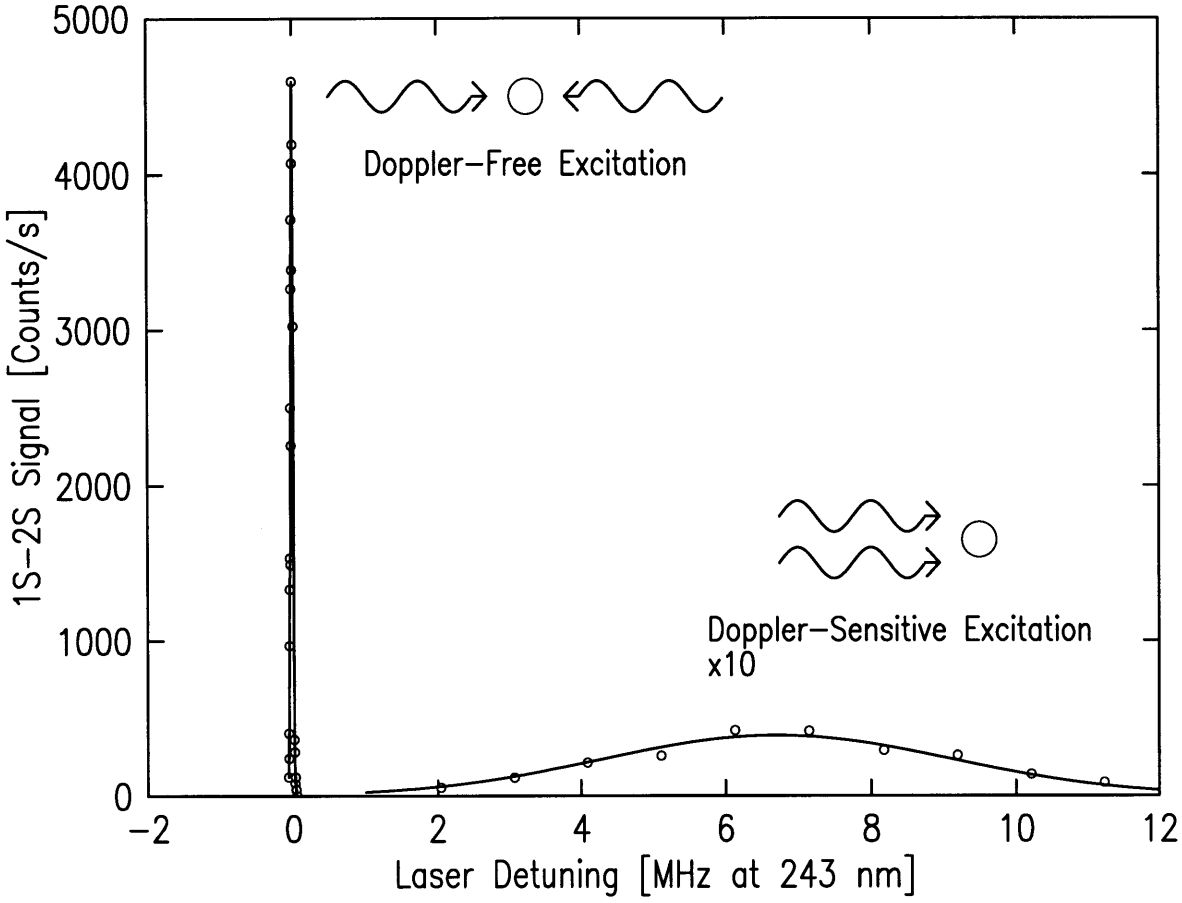

Figure 3-5: Composite $1S$-$2S$ two-photon spectrum of trapped hydrogen. The intense, narrow peak arises from Doppler-free absorption of counter-propagating photons. The wide, low feature on the right is from Doppler-sensitive absorption of co-propagating photons. The width of the Gaussian fit to the Doppler-broadened lineshape implies a sample temperature of 40 μK. Zero detuning is taken for unperturbed atoms excited Doppler-free. The Doppler-sensitive feature is shifted by 6.7 MHz due to momentum recoil. All frequencies refer to the 243 nm excitation radiation.

Chapter 4

Formal Description of $1S$-$2S$ Two-Photon Spectroscopy

In order to interpret the observed $1S$-$2S$ spectra, we present the formalism describing two-photon Doppler-free and Doppler-sensitive excitation. An effective Hamiltonian is constructed with which one can derive lineshapes and transition rates using formalism that is familiar from one-photon transition calculations. Perturbations such as the cold collision frequency shift can be added to the Hamiltonian. Experimental data is presented.

4.1 $1S$-$2S$ Two-Photon Transition Theory

4.1.1 Physical System and Interaction

The ground state for the transition is the $F = 1, m_F = 1$, $1S$ state, and the excited state is the $F = 1, m_F = 1$, $2S$ state (Fig. 3-1). The transition must proceed through intermediate P states. The two-photon $1S$-$2S$ selection rules preclude any change in hyperfine state during the excitation – the electronic and nuclear spins are essentially along for the ride. For our purposes, the analysis must incorporate atomic motion. The translational state wave functions are described by plane-wave states with periodic boundary conditions and normalization in a box of volume V. The $1S$ and $2S$

states have momentum $\mathbf{p}_1$ and $\mathbf{p}_2$ respectively, and the intermediate nP state has momentum $\mathbf{p}'_n$.

The important atomic energies are

$$\begin{aligned} E_{1S,\mathbf{p}_1} &= \frac{{\mathbf{p}_1}^2}{2m} \\ E_{2S,\mathbf{p}_2} &= \hbar\omega_{1S-2S} + \frac{{\mathbf{p}_2}^2}{2m} \\ E_{nP,\mathbf{p}'_n} &= \hbar\omega_{1S-nP} + \frac{{\mathbf{p}'_n}^2}{2m}. \end{aligned} \tag{4.1}$$

We define

$$\hbar\omega_{1S,\mathbf{p}_1-2S,\mathbf{p}_2} = (E_{2S,\mathbf{p}_2} - E_{1S,\mathbf{p}_1}) = \hbar\omega_{1S-2S} + \frac{{\mathbf{p}_2}^2}{2m} - \frac{{\mathbf{p}_1}^2}{2m}. \tag{4.2}$$

The first order Doppler shift of the transition frequency will arise naturally from momentum conservation. This treatment neglects the second order Doppler shift, but this effect could be recovered by considering energy and momentum relativistically.

The atoms actually move in a trap and do not simply occupy plane wave states. Our treatment will preserve all the relevant effects of the atomic motion so long as the trap level spacing is small compared with the motional energy of the atoms. This condition is not fulfilled for atoms in a Bose-condensate, and the discussion of the $1S$-$2S$ spectrum of BEC is deferred to Chap. 7. Cesar [60] developed a two-photon transition formalism in which the atomic motion in the trap is quantized, and it is a useful alternative picture.

4.1.2 Excitation Hamiltonian

The derivation of the photo-excitation spectrum begins with time-dependent perturbation theory[78], with the perturbing Hamiltonian

$$H' = -e\tilde{\mathbf{r}} \cdot \mathbf{E}(\tilde{\mathbf{R}}, \tilde{\mathbf{r}}, t). \tag{4.3}$$

The operators are $\tilde{\mathbf{R}}$, the center of mass of the atom, and $\tilde{\mathbf{r}}$, the position of the electron with respect to the nucleus[1]. The charge of the electron is $e < 0$, and we represent the standing wave laser as a classical monochromatic electric field of the the form

$$\mathbf{E}(\tilde{\mathbf{R}}, \tilde{\mathbf{r}}, t) = \frac{1}{2}\hat{\epsilon}_1 E_1(\tilde{\mathbf{R}}) e^{i\mathbf{k}_1\cdot(\tilde{\mathbf{R}}+\tilde{\mathbf{r}})-i\omega_1 t} + \frac{1}{2}\hat{\epsilon}_2 E_2(\tilde{\mathbf{R}}) e^{i\mathbf{k}_2\cdot(\tilde{\mathbf{R}}+\tilde{\mathbf{r}})-i\omega_2 t} + c.c. \tag{4.4}$$

E_1 and E_2 are taken to be real and they contain the slow spatial variations of the beam profiles. The laser is applied at time t_0.

The intensity of beam i is $I_i = \frac{1}{2}\varepsilon_0 c|E_i(\mathbf{R})|^2$. For the experimental situation, we have approximately a TEM_{00} Gaussian mode,

$$I(\mathbf{R}) = \frac{2P}{\pi w^2(z)} \exp\left[-\frac{2(x^2+y^2)}{w^2(z)}\right]. \tag{4.5}$$

Here, P is the power in the laser beam (4-8 mW), and $w(z) = w_0\sqrt{1+z^2/z_0^2}$ is the beam radius at position z. w_0 is the beam waist (20-50 μm), and $z_0 = \pi w_0^2/\lambda$ is the divergence length or Rayleigh length (0.5-3 cm). A typical peak intensity in the laser focus is about 200 W/cm^2.

As is well known, $\langle 2S, \mathbf{p}_2 \mid H'(t'') \mid 1S, \mathbf{p}_1\rangle = 0$, because parity conservation forbids a one-photon $\Delta l = 0$ transition, so the first order transition probability vanishes. We find the transition rate from the second order coefficient of the $2S$ state,

$$\begin{aligned} C^{(2)}_{2S,\mathbf{p}_2}(t) &= -\frac{1}{\hbar^2}\int_{t_0}^{t} dt'' \int_{t_0}^{t''} dt' \sum_{n,\mathbf{p}'_n} \langle 2S, \mathbf{p}_2 \mid H'(t'') \mid nP, \mathbf{p}'_n\rangle e^{-i\omega_{nP,\mathbf{p}n-2S,\mathbf{p}_2}(t''-t_0)} \\ &\quad \times \langle nP, \mathbf{p}'_n \mid H'(t') \mid 1S, \mathbf{p}_1\rangle e^{-i\omega_{1S,\mathbf{p}_1-nP,\mathbf{p}n}(t'-t_0)}. \end{aligned} \tag{4.6}$$

The sum extends over all P states, including the continuum. By making appropriate assumptions, we can recast this expression in the form of a first order transition

[1]To be explicit, when a position variable is an operator, it will have a tilde.

coefficient,

$$C^{(2)}_{2S,\mathbf{p}_2}(t) = -\frac{i}{\hbar}\int_{t_0}^{t} dt'' V_{2S,\mathbf{p}_2;1S,\mathbf{p}_1}(t'') e^{-i\omega_{1S,\mathbf{p}_1-2S,\mathbf{p}_2}(t''-t_0)}. \tag{4.7}$$

$V_{2S,\mathbf{p}_2;1S,\mathbf{p}_1}(t'')$ is the off diagonal element of the effective two-level Hamiltonian.[2]

To calculate $V_{2S,\mathbf{p}_2;1S,\mathbf{p}_1}(t)$, we make the rotating wave approximation and the adiabatic approximation [79] ($|\mathrm{d}E_i(\mathbf{R})/\mathrm{dt}| \ll |\omega_i E_i(\mathbf{R})|$). Using the electric dipole approximation, we set $e^{i\mathbf{k_i}\cdot\tilde{\mathbf{r}}}$ to one, but leave $e^{i\mathbf{k_i}\cdot\tilde{\mathbf{R}}}$ since it contains important information on momentum exchange during the excitation. We specialize to a standing wave laser field, for which $\mathbf{k}_1 = -\mathbf{k}_2 \equiv \mathbf{k}$ and $\omega_1 = \omega_2 \equiv \omega$; also, $\hbar|\omega + \omega_{1S,nP}| \gg |\frac{\mathbf{p}_1^2}{2m} - \frac{\mathbf{p}_n^2}{2m}|$

Appendix B gives more details of the calculation, but we present the result here,

$$\begin{aligned} V_{2S,\mathbf{p}_2;1S,\mathbf{p}_1}(t) &= \hbar\left(\frac{\alpha}{2R_\infty}\right)^3 \frac{1}{3\pi^2\hbar c}\{[I_1(\mathbf{R})\delta_{\mathbf{p}_2,\mathbf{p}_1+2\hbar\mathbf{k}} + I_2(\mathbf{R})\delta_{\mathbf{p}_2,\mathbf{p}_1-2\hbar\mathbf{k}}]M^{11}_{2S,1S}/2 \\ &\quad + \sqrt{I_1(\mathbf{R})I_2(\mathbf{R})}\delta_{\mathbf{p}_2,\mathbf{p}_1} M^{12}_{2S,1S}\} e^{2i\omega t}. \end{aligned} \tag{4.8}$$

Sums over dipole matrix elements, $\mathbf{r}_{\alpha,\beta}$, have been reduced to

$$\begin{aligned} &M^{ij}_{2S,1S} = \\ &\left(\frac{2R_\infty}{\alpha}\right)^3 \frac{3\pi^3 e^2}{\varepsilon_0 2h} \sum_n \frac{1}{(\omega + \omega_{1S-nP})} (\mathbf{r}_{2S,nP}\cdot\hat{\epsilon}_i\ \mathbf{r}_{nP,1S}\cdot\hat{\epsilon}_j + \mathbf{r}_{2S,nP}\cdot\hat{\epsilon}_j\ \mathbf{r}_{nP,1S}\cdot\hat{\epsilon}_i). \end{aligned} \tag{4.9}$$

The term proportional to $M^{12}_{2S,1S}$ in Eq. 4.8 gives rise to Doppler-free absorption of two counter-propagating photons, for which there is no momentum transfer and thus no recoil shift. The term proportional to $M^{11}_{2S,1S}$ gives rise to recoil-shifted Doppler-sensitive absorption of two co-propagating photons, for which the photons can come from either of the two laser beams. In our particular experimental arrangement, the polarization is linear and $\hat{\epsilon}_1 = \hat{\epsilon}_2$, $\omega \approx \omega_{1S-2S}/2$, and $M^{12}_{2S,1S} = M^{11}_{2S,1S} = 11.78$ [80].

Using Eq. 4.8 alone one can calculate the $1S$-$2S$ spectrum in the absence of any

[2] V is called the "effective two-level Hamiltonian" because only reference to the initial and final levels remains.

additional perturbations. Experimentally, this is often a good approximation, so we discuss this situation before including additional spectral shifts and broadenings.

4.2 Doppler-Sensitive Excitation

Theoretical Description

Doppler-sensitive excitation results in a spectral feature with a linewidth much larger than the inverse of the time of excitation. It is thus valid to define the Doppler-sensitive excitation rate for a single atom through Fermi's Golden Rule [78],

$$W_{1S,\mathbf{p}_1\to 2S}(2\hbar\omega) = \sum_{\mathbf{p}_2} W_{1S,\mathbf{p}_1\to 2S,\mathbf{p}_2} = \sum_{\mathbf{p}_2} \frac{2\pi}{\hbar} |V_{2S,\mathbf{p}_2;1S,\mathbf{p}_1}|^2 \delta(E_{2S,\mathbf{p}_2} - E_{1S,\mathbf{p}_1} - 2\hbar\omega). \tag{4.10}$$

We substitute the Doppler-sensitive excitation terms of Eq. 4.8 for $V_{2S,\mathbf{p}_2;1S,\mathbf{p}_1}$. The interaction vanishes unless the excited state has $\mathbf{p}_2 = \mathbf{p}_1 \pm 2\hbar\mathbf{k}$, so the sum over final momentum states is trivial. It yields the Doppler-sensitive excitation rate to the $2S$ level

$$\begin{aligned} W_{1S,\mathbf{p}_1\to 2S}(2\hbar\omega) &= \frac{\pi\hbar}{2}\left[\Omega_1^2(\mathbf{R})\delta\left(2\hbar\omega - \hbar\omega_{1S-2S} - \frac{2\hbar^2k^2}{m} - \frac{2\hbar\mathbf{k}\cdot\mathbf{p}_1}{m}\right)\right. \\ &\quad \left. + \Omega_2^2(\mathbf{R})\delta\left(2\hbar\omega - \hbar\omega_{1S-2S} - \frac{2\hbar^2k^2}{m} + \frac{2\hbar\mathbf{k}\cdot\mathbf{p}_1}{m}\right)\right]. \end{aligned} \tag{4.11}$$

We have defined the Rabi frequency for Doppler-sensitive excitation by a single laser beam,

$$\Omega_i(\mathbf{R}) = \frac{2|V_{2S,\mathbf{p}_1+2\hbar\mathbf{k};1S,\mathbf{p}_1}|}{\hbar} = M^{11}_{2S,1S}\left(\frac{\alpha}{2R_\infty}\right)^3 \frac{1}{3\pi^2\hbar c} I_i(\mathbf{R}) = 4.632\, I_i(\mathbf{R})\,\mathrm{s}^{-1}\,\mathrm{cm}^2\,\mathrm{W}^{-1}. \tag{4.12}$$

Note that because the final states ($\mathbf{p}_2 = \mathbf{p}_1 \pm 2\hbar\mathbf{k}$) are not the same, we must add the probabilities of being excited by I_1 and I_2. We do not coherently add the $2S$ amplitudes arising from each process.

When the transition is resonantly driven by the Doppler-sensitive term in Eq. 4.8,

the laser frequency must satisfy

$$2\hbar\omega = E_{2S,\mathbf{p}_2} - E_{1S,\mathbf{p}_1} = \hbar\omega_{1S-2S} \pm \frac{2\hbar\mathbf{k}\cdot\mathbf{p}_1}{m} + \frac{2\hbar^2k^2}{m}. \tag{4.13}$$

The recoil shift is given by the term which is quadratic in k. The $\mathbf{k}\cdot\mathbf{p}_1$ term is what is normally added in an *ad hoc* fashion as the Doppler-shift. The usual description of a photo-excitation spectrum does not mention the momentum recoil, and thus cannot arrive at Doppler-broadening in this way. The Doppler-broadening arises naturally if momentum transfer is correctly considered as is done here. Because of the small hydrogen mass, large transition frequency, and low sample temperature, the $1S$-$2S$ transition in trapped hydrogen is unique in that the magnitude of the recoil shift is greater than the Doppler width.

The experimentally observed excitation rate at a given frequency is found by integrating Eq. 4.11 over the sample density distribution and momentum distribution. We define the z axis along the laser beams. Note that Eq. 4.11 is independent of p_x and p_y and the spectrum maps the axial momentum distribution. Assuming a Maxwell-Boltzmann distribution of p_z, after a little algebra, one arrives at the Doppler-free spectrum,

$$\begin{aligned} S(\nu) &= \frac{1}{\sqrt{\pi}}\left(\frac{1}{2}\frac{mc^2}{k_BT}\frac{1}{\nu^2}\right)^{1/2}\exp\left[-\frac{1}{2}\frac{mc^2}{k_BT}\left(\frac{\nu - \frac{\nu_{1S-2S}}{2} - \frac{\hbar k^2}{2\pi m}}{\nu}\right)^2\right] \\ &\quad \times \int d^3R\; n(\mathbf{R})[\Omega_1^2(\mathbf{R}) + \Omega_2^2(\mathbf{R})]. \end{aligned} \tag{4.14}$$

This gives the number of 2S excitations per second and the frequency has been expressed in Hz. The spectrum is centered at

$$\nu = \frac{\nu_{1S-2S}}{2} + \frac{\hbar k^2}{2\pi m} = \frac{\nu_{1S-2S}}{2} + 6.70\text{ MHz}, \tag{4.15}$$

and has an RMS width of $\Delta\nu = \nu_{1S-2S}\sqrt{\frac{k_BT}{mc^2}} = 0.374\times10^9\sqrt{T}$ Hz $\mathrm{K}^{-1/2}$. The full width at half maximum is $2\sqrt{-2\ln(1/2)}\Delta\nu$. The integral over position in Eq. 4.14 accounts for the geometric overlap of the atom cloud and laser beams.

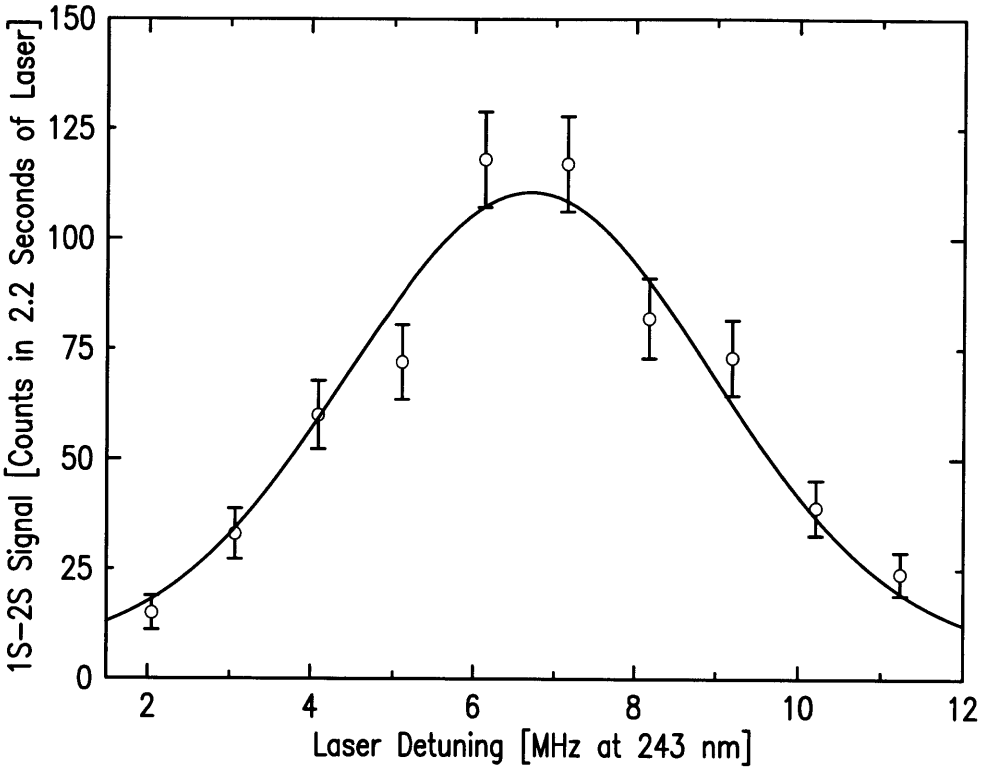

Figure 4-1: Doppler-sensitive excitation spectrum of a sample held at a trap depth of 280 μK. Zero detuning is the unperturbed $1S$-$2S$ frequency. The smooth curve is a Gaussian fit to the data which gives a RMS width of 2.3 ± 0.4 MHz, indicating $T = 37 \pm 12$ μK.

Experimental Observation

The Doppler sensitive spectrum is an important diagnostic of the temperature of the trapped sample. An example is shown in Fig. 4-1 for a 37 μK sample.

A calculation of the expected peak excitation rate is instructive. The laser power was about 5 mW and the beam focus was about 45 μm, which implies a peak laser intensity of 150 mW/cm^2 and a Rabi frequency of 700 s^{-1}. On resonance this gives a peak excitation rate of 0.17 s^{-1} per atom in the laser. The cloud is larger than the laser excitation region, however, and numerical simulations predict that one effectively accesses one sixth of the atoms. This implies that the lifetime of the sample due to laser excitation is about 35 s. This is long compared to the observed $\sim$ 10 s lifetime when the laser illuminates the gas. The lifetime seems to be reduced by collisions with helium atoms which the laser boils off the retroreflecting mirror.

There were about 5×10^9 atoms in this sample. Assuming the laser was well aligned with the atom cloud, the observed count rate implies a detection efficiency for the fluorescence photons of about $\alpha = 10^{-6}$. This is reasonably consistent with our estimate of $\alpha = 10^{-5}$ (Sec. 3.4) considering the crudeness of all the assumptions.

4.3 Doppler-Free Excitation: Simple Lineshapes

For Doppler-free excitation, the interaction vanishes unless initial and final momenta are equal, and there is no recoil shift or Doppler-broadening. The observed linewidth can arise from several different processes and we discuss the lineshape resulting from each.

4.3.1 Atoms Nearly at Rest

Theoretical Description

For an atom nearly at rest, which is in the laser beam for a long time compared to the shortest decoherence time in the system, it is useful to use Fermi's Golden Rule to find the excitation rate.

$$W_{1S,\mathbf{p}_1 \to 2S,\mathbf{p}_1}(2\hbar\omega) = \frac{\pi\hbar}{2}\Omega_0^2(\mathbf{R})\delta(2\hbar\omega - \hbar\omega_{1S-2S}). \tag{4.16}$$

The Rabi frequency for Doppler-free excitation in a standing wave, identified from Eq. 4.8, is

$$\Omega_0(\mathbf{R}) = 2M^{12}_{2S,1S}\left(\frac{\alpha}{2R_\infty}\right)^3 \frac{1}{3\pi^2\hbar c}\sqrt{I_1(\mathbf{R})I_2(\mathbf{R})} = 9.264\ \sqrt{I_1(\mathbf{R})I_2(\mathbf{R})}\ \mathrm{s}^{-1}\ \mathrm{cm}^2\ \mathrm{W}^{-1}. \tag{4.17}$$

To derive the spectrum, one convolves Eq. 4.16 with the spectrum of whatever sets the decoherence time, and then integrates the transition rate over the velocity and momentum distribution in the sample. For example, if the natural linewidth of the transition, $\gamma = 8.2\ \mathrm{s}^{-1}$, sets the decoherence time, one must convolve Eq. 4.16 with

the Lorentzian distribution of transition frequencies, ω'_{1S-2S},

$$G(\omega'_{1S-2S} - \omega_{1S-2S}) = \frac{\gamma/2\pi}{(\omega'_{1S-2S} - \omega_{1S-2S})^2 + \gamma^2/4}. \tag{4.18}$$

This yields

$$\begin{aligned} & S(\omega) = \\ = & \int d^3R\, d^3p_1\, n(\mathbf{R}, \mathbf{p}_1) \frac{\pi}{2} \Omega_0^2(\mathbf{R}) \int d\omega'_{1S-2S} G(\omega'_{1S-2S} - \omega_{1S-2S}) \delta(2\omega - \omega'_{1S-2S}) \\ = & \int d^3R\, d^3p_1\, n(\mathbf{R}, \mathbf{p}_1) \frac{\pi}{2} \Omega_0^2(\mathbf{R}) \frac{\gamma/2\pi}{(\omega_{1S-2S} - 2\omega)^2 + \gamma^2/4}. \end{aligned} \tag{4.19}$$

On resonance, for N atoms in the laser focus,

$$S\left(\frac{\omega_{1S-2S}}{2}\right) = N \frac{85.8 I_1 I_2}{\gamma} \mathrm{s}^{-1}\ \mathrm{cm}^2\ \mathrm{W}^{-1}. \tag{4.20}$$

As pointed out by Sandberg [59], for $I = 0.89$ W cm^{-2}, $S/N = \gamma$ and the transition is saturated for an atom in the laser beam for more than a natural lifetime.

The treatment is similar if the observed linewidth is dominated by the laser frequency spectrum.

4.3.2 Atoms in Motion: Time-of-Flight Lineshape

Theoretical Description

If an atom is in the laser beam for a time which is short compared to any decoherence time, such as the inverse of the laser linewidth, then the photoexcitation spectral linewidth is determined by the finite interaction time of the atom with the laser, as one would expect from the energy-time uncertainty relation $\Delta E \Delta t \approx \hbar$. One cannot resort to Fermi's Golden Rule; instead we compute the probability that a single atom is excited during its pass through the laser beam. Each trajectory corresponds to a different probability of excitation. The observed spectrum is found by adding the contributions from all trajectories which pass through the beam in a given time.

Figure 4-2, which is taken from [77], shows cross sections of the laser beam and

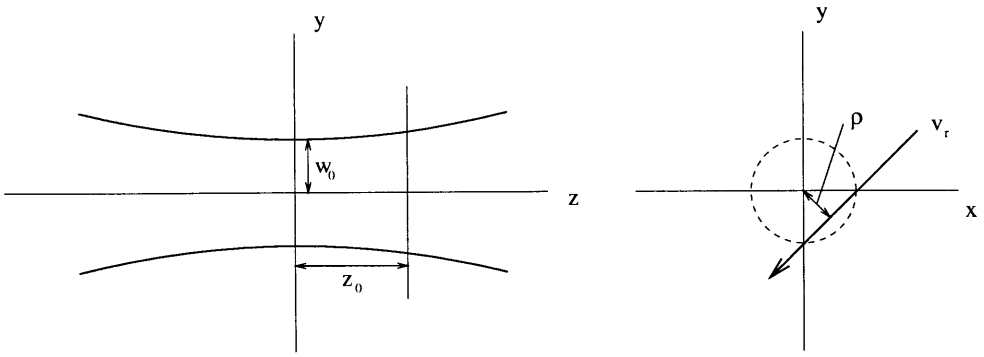

Figure 4-2: Cross sections of the laser beam and the trajectory of an atom in the $x-y$ plane. The atom's motion is given by $x^2+y^2=\rho^2+v_t^2t^2$, where v_t is the atom's velocity in the x-y plane, and the atom passes within a distance ρ of the focus at $t=0$. At $t=-\infty$ the atom is well outside the laser and as it enters the beam, the strength of the interaction with the light field grows and then diminishes as the atom moves away.

the atom trajectory in the $x-y$ plane. We make the approximation $I_1(\mathbf{R})=I_2(\mathbf{R})\equiv I(\mathbf{R})$, and the laser beam profile is given in Eq. 4.5.

In the experiment, the axial length scales of the laser profile and the atom cloud are typically a few centimeters. This is about 100 times greater than the radial length scale set by the laser radius, w_0. So very few atoms move any significant distance along z while they move radially through the laser beam. Thus, we can neglect axial motion. We also neglect the presence of the trap, and assume atoms pass once through the laser along a straight path. This is a good approximation when the radius of the thermal cloud is much larger than the laser radius, and the trap oscillation frequencies are much smaller than the spectral resolution of the experiment. If these conditions do not hold, then the spectrum will be motionally narrowed (See Sec. 4.4.5).

When an atom passes through the laser beam, the probability that it is excited to the $2S$ state is given by the square of the coefficient

$$C_{2S}^{(2)}(\infty)=-\frac{i}{\hbar}\int_{-\infty}^{\infty}dt''V_{2S,1S}(t'')e^{-i\omega_{1S-2S}(t'')}. \tag{4.21}$$

For $V_{2S,1S}$ we take the Doppler-free term in Eq. 4.8. If we substitute the details of

the trajectory into this expression, we find

$$C_{2S}^{(2)}(\infty,\rho,v_t,\omega) = -\frac{i}{\hbar}\int_{-\infty}^{\infty} dt'' \frac{\hbar\Omega_0(0)}{2\left(1+\frac{z^2}{z_0^2}\right)} \exp\left[-\frac{2(\rho^2+v_t^2t^2)}{w^2(z)}\right] e^{-i(\omega_{1S-2S}-2\omega)(t'')}. \tag{4.22}$$

This expression shows that the excitation amplitude is the Fourier transform of the time profile of the perturbation. The excitation probability has a Gaussian lineshape,

$$P(\infty,\rho,v_t,\omega) = |C^{(2)}|^2 = \frac{\pi}{8}\frac{\Omega_0^2(0)}{\left(1+\frac{z^2}{z_0^2}\right)}\frac{w_0^2}{v_t^2} e^{-\frac{4\rho^2}{w^2(z)}} \exp\left[-\frac{(2\omega-\omega_{1S-2S})^2 w^2(z)}{4v_t^2}\right]. \tag{4.23}$$

The spectral width is given by the inverse of the time the atom is in the laser beam. On resonance, the probability of being excited goes as the inverse of v_t^2, or the inverse of the kinetic energy.

To calculate the number of excitations per second in the entire sample, one must find the flux of atoms with a given v_t crossing the beam, which is $f(v_t)v_t n(z)$, where $f(v_t)$ is the relative probability for an atom to have velocity v_t. We can take f as the two dimensional Maxwell-Boltzmann distribution function, $2v_t/u^2 \exp(-v_t^2/u^2)$, and the density, $n(z)$ varies along z. Here, $u = \sqrt{2k_BT/m}$ is the most probable atomic speed. The integral over z, ρ, and v_t of the flux times the probability for the atom to be excited during the trajectory yields the excitation spectrum. One finds [77]

$$\begin{aligned} S(\nu) &= \int_{-\infty}^{\infty} d\rho \int_{-\infty}^{\infty} dz \int_0^{\infty} dv_t \; 2\frac{v_t}{u^2} e^{-\frac{v_t^2}{u^2}} \; v_t n(z) \; P(\infty,\rho,v_t,\omega) \\ &= \frac{\pi^2}{16}\frac{\Omega_0^2(0)w_0^4}{u}\int_{-\infty}^{\infty} dz \; \frac{n(z)}{w(z)} \exp\left[-\frac{|\nu-\frac{\nu_{1S-2S}}{2}|4\pi w(z)}{u}\right]. \end{aligned} \tag{4.24}$$

If the sample is confined to a region of length $L \ll z_0$, in which the beam radius is constant, the spectrum is given by

$$S(\nu) = \underbrace{\frac{\Omega_0^2(0)\pi w_0}{4u}}_{\text{excitation rate per atom}} \overbrace{\frac{\pi w_0^2}{4}\int dz \; n(z)}^{\text{number of atoms}} \exp\left[-\frac{|\nu-\frac{\nu_{1S-2S}}{2}|4\pi w_0}{u}\right]. \tag{4.25}$$

This double exponential is the time-of-flight lineshape which is also observed in

Doppler-free two-photon spectroscopy in an atomic beam [76, 77]. The $1/e$ half width is

$$\Delta\nu = \sqrt{\frac{2k_{\mathrm{B}}T}{m}}\frac{1}{4\pi w_0} \approx 10\sqrt{T}/w_0 \text{ Hz m K}^{-1/2}. \tag{4.26}$$

Assuming that the laser beam waist is known, the $1/e$ half width is a measure of the sample temperature.

If the sample extends beyond a divergence length from the focus, the lineshape given by Eq. 4.24 will still approximate a double exponential, $\sim \exp(-|\Delta\nu|4\pi w_{eff}/u)$, but the effective beam waist of the spectrum, w_{eff}, will be greater than w_0 due to the divergence of the laser beam.

Experimental Observation

It was experimentally shown [10] that Eq. 4.26 is valid for the trapped sample, but for the studies reported in this thesis, the laser waist profile is not well known. The optical alignment was drastically changed after the vacuum system and cryostat were assembled around the apparatus, making it impossible to observe the laser geometry in the region of the trap. In addition, in order to produce a standing wave in the trapping region, the beam fell near the edge of a lens and a mirror in the cryostat, so the beam was most likely highly astigmatic. The spectra still exhibit a time-of-flight lineshape, but the effective beam waist must be calibrated with independent determination of the sample temperature. The temperature can be found from bolometric measurement of the energy distribution (Sec. 2.5), the width of the Doppler-sensitive spectrum (Sec. 4.2), or a thermodynamic model of heating and cooling in the sample[24].

The optical layout was designed to produce a 47 μm beam waist, but the observed value of the effective waist ranged between 20 and 50 μm. It would remain stable as long as the laser alignment was not changed.

Figure 4-3 shows typical time-of-flight spectra recorded in the course of one evening. For samples with temperatures between 100 μK and 1 mK, the temperature is found with the bolometric technique. This implies an effective beam waist of 20 μm. To find the effective beam waist for warmer samples, the bolometric technique

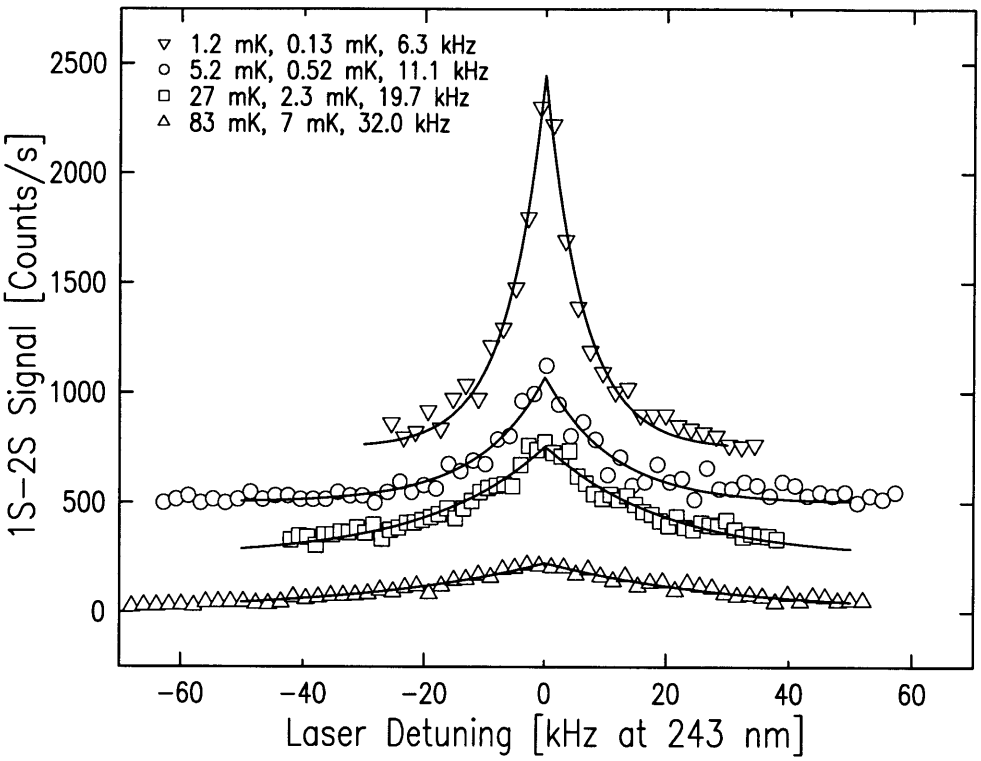

Figure 4-3: Typical Doppler-free spectra showing the dependence of linewidth on sample temperature. The trap depth, sample temperature, and $1/e$ halfwidth are given. The laser power in the trap region was about 7 mW and samples densities were 10^{12}-10^{13} cm^{-3}. The baseline of each spectrum is offset for clarity.

is not reliable. One can calculate the temperature with the thermodynamic model, however, and the inferred waists are substantially larger than 20 μm. This is reasonable since the warmer samples extend well beyond a divergence length from the beam focus. If the beam shape were better known, this hypothesis could be quantitatively verified by simulating the lineshape through numerical integration of Eq. 4.24.

Once the waist is calibrated, the time-of-flight spectrum is a valuable relative measure of sample temperature because the $\sqrt{T}$ linewidth dependence and high signal to noise ratio extend to temperatures which are both lower and higher than the useful regimes of other techniques.

The usefulness of the time-of-flight spectrum for determining the sample temperature is demonstrated in Fig. 4-4. The effective beam waist for this data set was determined to be 20 μm, and it is possible to measure temperatures down to 20 μK. This data set was not recorded for the purpose of measuring time-of-flight linewidths

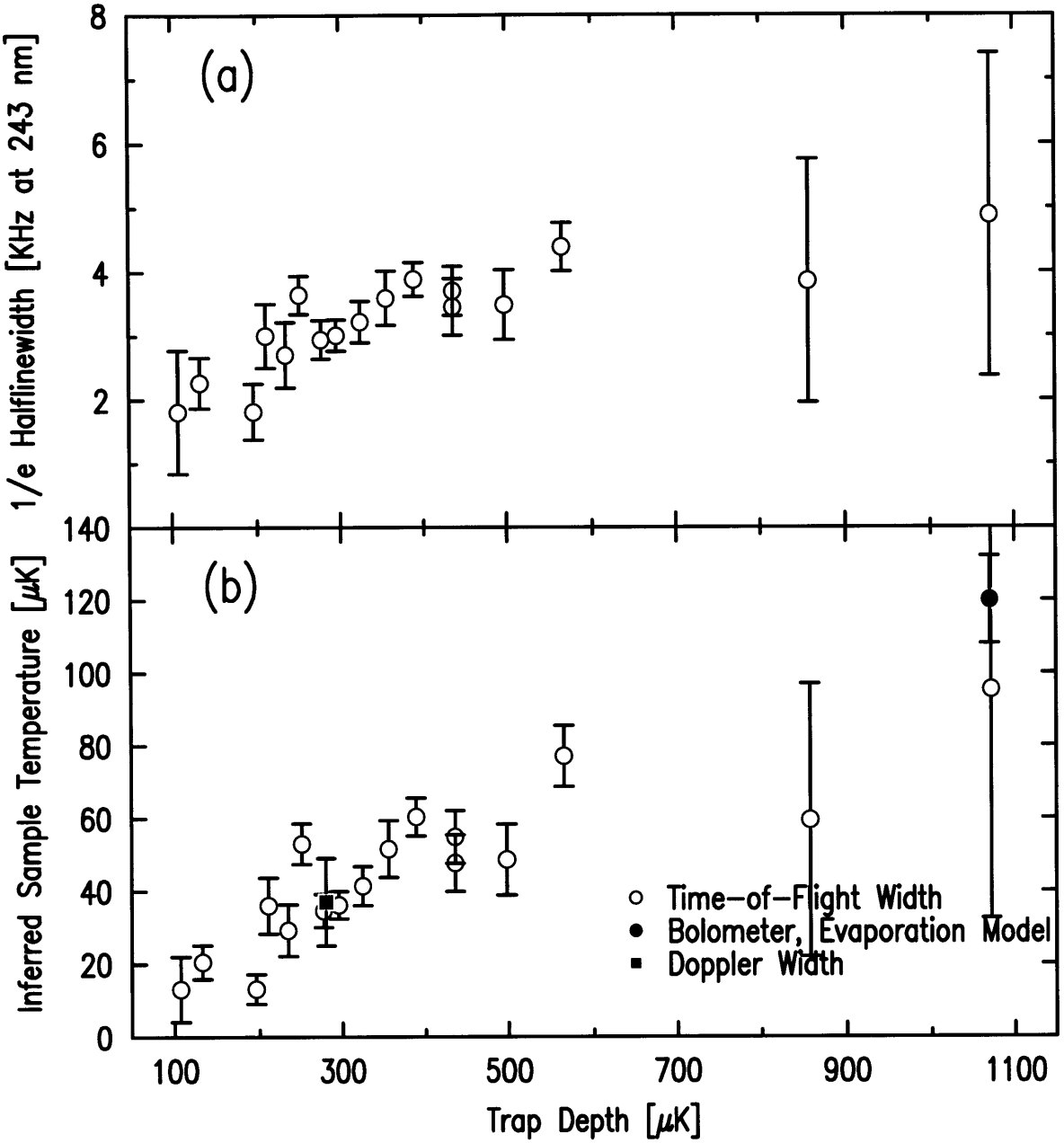

Figure 4-4: Plot (a) shows the 1/e halflinewidths of Doppler-free spectra from cold, low density samples ($< 10^{13}$ cm^{-3}). Each data point represents a different load of the magnetic trap and evaporation sequence. Plot (b) shows the temperatures implied by the linewidths and Eq. 4.26, assuming a 20 μm beam waist. This value of the beam waist was set by independent determination of the sample temperature using the bolometric dump method, a thermodynamic model of the sample [24], and the Doppler-sensitive spectrum linewidth. It is possible to infer the sample temperature down to around 20 μK.

and much improved data could be attained with the current apparatus. Also, more detailed modeling of the lineshape and study of the laser spectrum is required to better understand the very low temperature lineshapes.

For cold enough samples, as the atoms settle into the bottom of the trap, the sample radius will become smaller than the laser radius. In this case the motional broadening is suppressed. This is the two-photon analogue of Dicke narrowing [81] and the Mössbauer effect [82] in one-photon spectroscopy. In this limit, the atomic motion is negligible and the excitation spectrum linewidth is determined by the laser spectrum (Sec. 4.3.1), independent of the sample temperature. The data shows no evidence that this limit has been reached since the linewidth continues to drop as the trap depth decreases.

On the Doppler-free resonance, peak signal count rates can approach 30 counts per 400 μs laser pulse. Assuming a 10^{-5} detection efficiency, this implies about 3 million $2S$ atoms per pulse. These peak rates are seen for cold samples with high density, but low atom number ($\sim 10^{10}$). On resonance, for such a sample the lifetime due to laser excitation is about 1 s, which can be short on the time scale of the experiment. For most data discussed in this thesis, however, the excitation rate is lower and the number of atoms in the cloud is higher, and the loss due to excitation is not a significant factor.

4.4 Doppler-Free Excitation: Numerical Simulation of Complicated Lineshapes

When the time-of-flight linewidth is small, other processes can be important to the Doppler-free lineshape. The actual atomic trajectories in the trap can affect the spectrum, especially when the atoms maintain coherence with the light field over many passes through the laser. As will be described in Chap. 5 and 6, atomic collisions shift the energy levels so that the transition frequency depends on density. In these experiments the axial length scale for variation of the sample density profile and

the laser divergence length are roughly equal, so the spectrum normally reflects the inhomogeneous axial density and beam profile. Also, the AC Stark shift, photoionization, residual Zeeman shift, and saturation of the transition sometimes need to be considered. This section describes a semiclassical numerical calculation of the photoexcitation spectrum, based on the evolution of the single-particle density matrix, which can take all these effects into account.

4.4.1 Effective Two-Level Hamiltonian and Evolution of the Single Atom Density Matrix

We define an effective two-level Hamiltonian for spectroscopy of the $1S$-$2S$ system, which includes the unperturbed energies, any local level shifts ($\Delta E(\mathbf{r})$), and the interaction which gives rise to Doppler-free two-photon excitation (Sec. 4.1.2),

$$H = \frac{\hbar}{2}\begin{bmatrix} \omega_{1S-2S} + \Delta E(\mathbf{r}) & \Omega_0(\mathbf{r})e^{2i\omega t} \\ . & -\omega_{1S-2S} - \Delta E(\mathbf{r}) \end{bmatrix}, \tag{4.27}$$

The equation of motion for the density matrix, ρ, is

$$\dot{\rho} = \frac{1}{i\hbar}[H, \rho] + \frac{d}{dt}\rho\,|_{rel}\,. \tag{4.28}$$

We define

$$\rho = \begin{bmatrix} \rho_{2S,2S} & \rho_{2S,1S} \\ \rho_{1S,2S} & \rho_{1S,1S} \end{bmatrix}, \tag{4.29}$$

and the relaxation term reflects the laser linewidth, radiative decay, and photoionization of the 2S state, and is given by

$$\frac{d}{dt}\rho\,|_{rel} = \begin{bmatrix} -(\gamma_{2S} + \gamma_{photo}(\mathbf{r}))\rho_{2S,2S} & -(\gamma_{laser} + \gamma_{2S} + \gamma_{photo}(\mathbf{r}))\rho_{2S,1S}/2 \\ . & 0 \end{bmatrix}. \tag{4.30}$$

We assign the system a peak density, n_0, a well defined temperature, T, and a

trapping potential, $U(\mathbf{r})$. These imply a position and velocity distribution for the sample, $f(\mathbf{r}, \mathbf{v})$. ($\int d^3r\ d^3v\ f(\mathbf{r}, \mathbf{v}) = N$ is the number of atoms in the trap.)

For a given laser frequency, ν, we calculate the contribution to the spectrum from an atom initially in the $1S$ state with initial position $\mathbf{r}$ and initial velocity $\mathbf{v}$. For a laser pulse of length t_{laser}, the contribution to the spectrum from such an atom is proportional to the probability of the atom being in the $2S$ state at the end of the pulse, $\rho_{2S,2S}(\nu, \mathbf{r}, \mathbf{v}, t_{laser})$. This is found by numerically integrating Eq. 4.28 and Hamilton's equations for classical motion of an atom in the trap. The photo-excitation spectrum for the entire sample is found by numerically integrating over all initial conditions

$$S(\nu) = \int d^3r\ d^3p\ f(\mathbf{r}, \mathbf{v}) \rho_{2S,2S}(\nu, \mathbf{r}, \mathbf{v}, t_{laser}). \tag{4.31}$$

Equation 4.31 is a six-dimensional integral over the solution to coupled first order differential equations. Fortunately, proper use of symmetries and approximations can reduce the calculation time significantly. Further details of the numerical analysis are presented in App. B.

4.4.2 Cold Collision Frequency Shift

A shift in the transition level spacing which is linear in sample density has been observed (Chap. 5). This effect probes the quantum mechanical properties of the gas (See Sec. 6.3), so it is not possible to correctly include it in the semiclassical simulation of the spectrum. An approximate treatment of the shift's effect on the spectrum is obtained by including a local level shift in the Hamiltonian,

$$\Delta E_{coll}(\mathbf{r}) = h\chi n_{1S}(\mathbf{r}) \tag{4.32}$$

where $n_{1S}(\mathbf{r})$ is the local density of $1S$ atoms and $\chi = -3.8 \pm 0.8 \times 10^{-10}$ Hz cm^3.

An atom's energy levels are shifted due to interactions with neighboring atoms. The interactions can be represented by a mean field energy or through collision

based formalism and the result for a noncondensed, homogeneous sample is $\Delta E_{coll} = \frac{8\pi\hbar^2}{m} n_{1S} (a_{1S-2S} - a_{1S-1S})$, where a_{1S-2S} and a_{1S-1S} are the s-wave elastic triplet scattering lengths for $1S$-$2S$ and $1S$-$1S$ collisions. The theory is discussed in Chap. 6.

A broadening is predicted to accompany the shift (App. C). It arises from dephasing collisions which for a homogeneous system occur at a rate $\gamma_{coll} = 8\pi a_{1S-2S}^2 \sqrt{2}\bar{v}n$, where $\bar{v}$ is the thermal average velocity, $\sqrt{8k_BT/\pi m}$. The broadening at the sum frequency is $\gamma_{coll}/2\pi \approx 7 \times 10^{-9}\ n\sqrt{T}$ Hz/$\sqrt{\text{K}}$cm^{-3}. The importance of the broadening decreases with decreasing temperature. At 100 μK, $\Gamma_{coll}/2\pi = 6.9 \times 10^{-11}\ n$ Hz/cm^{-3}, which is small compared to other linewidths in the spectrum. There is presently no experimental observation of the broadening.

The experimental observations and simulations of spectra which are dominated by the effects of collisions are described in Chap. 5.

4.4.3 Additional Sources of Spectral Broadening

In this section we briefly describe additional sources of spectral broadening which can be included in the effective two-level Hamiltonian.

Laser Linewidth

The laser linewidth is 1 kHz or below at 243 nm and is usually unimportant. However, it does set the lower bound to the width of any feature in the spectrum. For very cold samples, when the time-of-flight linewidth becomes similar to or less than the laser linewidth, it is not possible to use the width to measure sample temperature[10] and the spectrum reflects the laser frequency spectrum (See Sec. 4.3.2).

Photoionization

A laser photon can excite an atom from the $2S$ state to the continuum, leading to photoionization. In the laser beam, this one-photon process can proceed rapidly because we produce a high laser intensity for the two-photon excitation. From the calculated photoionization cross section $\sigma_{photo} = 7.9 \times 10^{-18}$ cm^2 [83], one finds the

photoionization rate

$$\gamma_{photo}(\mathbf{r}) = 9.7[I_1(\mathbf{r}) + I_2(\mathbf{r})] \text{ s}^{-1}(\text{W/cm}^2)^{-1}. \tag{4.33}$$

Typical laser intensities in the beam focus can exceed 100 W/cm^2, for which $\gamma_{photo}(\mathbf{r}) \approx$ 2000 s^{-1}. This limits the lifetime of a $2S$ atom to 500 μs if the atom is in the laser focus during the entire laser pulse. Since most atoms spend a significant amount of time out of the laser beam, photoionization is suppressed and it only serves to reduce the spectral contribution from the lowest energy atoms, rounding out the peak on center of the time-of-flight spectrum.

AC Stark Shift

Since the electric dipole Hamiltonian associated with the photon-atom interaction connects the S and P states, there is a significant transition frequency shift associated with the AC Stark effect. The shift can be found from an extension of the analysis in Sec. 4.1.2. One must calculate the level shifts that arise from transitions $1S \rightarrow nP \rightarrow 1S$ and $2S \rightarrow nP \rightarrow 2S$ [79], which were neglected. The result is

$$\Delta E_{\text{AC Stark}}(\mathbf{r})/h = 3.34\sqrt{I_1(\mathbf{r})I_2(\mathbf{r})} \text{ Hz } (\text{W/cm}^2)^{-1}. \tag{4.34}$$

In these experiments, this can shift the resonance hundreds of Hz at the laser focus.

2S Radiative Decay and the DC Stark Effect

In the absence of any perturbations, the natural $2S \rightarrow 1S$ radiative decay channel[66] is via two photons at a rate of $\gamma_{2S} = 8.23$ s^{-1} [84]. The resulting natural linewidth of the transition is 1.31 Hz at 122 nm.

A DC electric field, $\mathcal{E}$, mixes the $2S$ level with P levels just as an AC field does. When the excited state wave function has some P character, it can decay to the $1S$ state via the emission of one 122 nm Lyman-alpha photon. This reduces the lifetime

to[85]

$$\tau_{2S}(\mathcal{E}) = \tau_{2P}\ (475/\mathcal{E})^2(\mathrm{V/cm})^2, \tag{4.35}$$

where $\tau_{2P} = 1.6$ ns is the $2P$ lifetime. In a metal-coated trapping cell, it was shown [10] that the $2S$ lifetime could be comparable to $\tau_{2S}^0 = 121.5$ ms, but the cell which was used for the experiments described in this thesis was made of plastic and the $2S$ lifetime was typically a few milliseconds, indicating the presence of stray electric fields of about 0.5 V/cm.

There is also a small shift of the $1S$-$2S$ transition frequency associated with the DC Stark mixing [59],

$$\Delta E_{\text{DC Stark}}/h = 3600\ \mathcal{E}^2\ \mathrm{Hz}\ (\mathrm{V/cm})^{-2}. \tag{4.36}$$

Residual Zeeman Shift

The energies of the $1S$ and $2S$ states shift strongly with magnetic field. This provides the trapping potential for the atoms, and for a sample at temperature T, d state atoms are confined by fields of $B \approx k_B T/\mu_B = 1.47\ T$ T/K. Normally this makes high resolution spectroscopy impossible for magnetically trapped neutral particles because of the large Zeeman shift and broadening of the spectrum. The $1S$ and $2S$ $F = 1$, $m_F = 1$ states, however, shift identically with field, except for a small relativistic correction [85]. The residual Zeeman shift for the $1S - 2S$ transition in a magnetic trap is

$$\Delta E_{\text{zeeman}}(\mathbf{r})/h = B(\mathbf{r})\alpha^2\mu_B/4h = 1.8 \times 10^5\ B(\mathbf{r})\ \mathrm{Hz/T}. \tag{4.37}$$

This effect is negligible at present. For example, for a 100 μK sample the trapping fields are about 1.5×10^{-4} T, and the resulting frequency shift is about 30 Hz at 122 nm.

4.4.4 Numerical Calculation of the Time of Flight Lineshape

A check of the numerical simulation of the spectrum is to derive the experimentally important time-of-flight lineshape. For this we restrict ourselves to the regime in which there are no significant broadenings or shifts other than the finite transit-time broadening. When the laser waist is much smaller than the sample radius, and the length of a laser pulse, t_{laser}, is such that an atom makes one complete pass through the Gaussian laser beam during the excitation, the probability of exciting the atom to the $2S$ state should have the same form as the analytic expression, Eq. 4.23,

$$\rho_{2S,2S}(\nu, z, v, t_{laser}) \approx \Omega_0^2(0)\frac{w_0^2}{v^2}\exp\left[-\frac{(2\pi)^2(\nu - \frac{\nu_{1S-2S}}{2})^2 w^2(z)}{v^2}\right]. \tag{4.38}$$

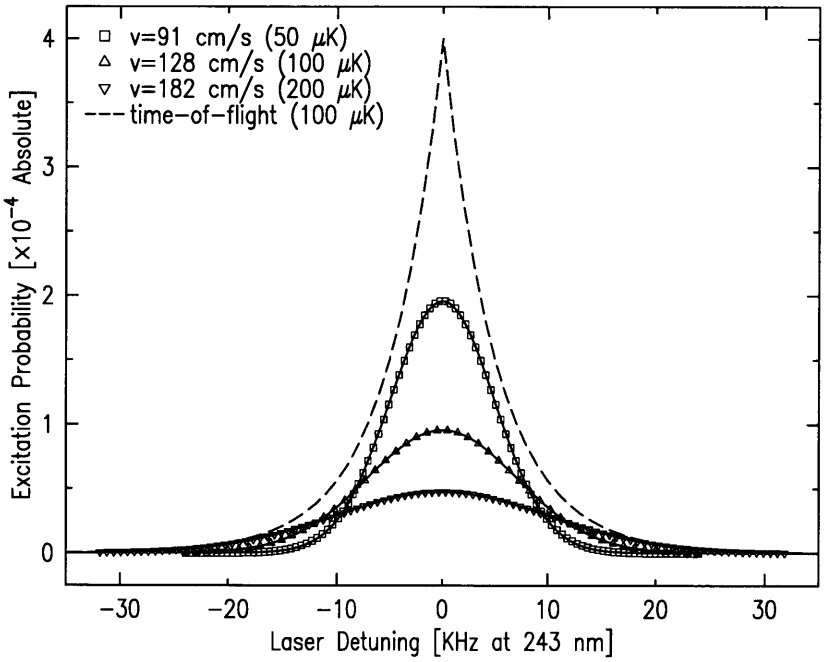

Figure 4-5: Probability for excitation to the $2S$ state for atoms which start outside the laser beam and make one pass through the beam with zero impact parameter. The velocities quoted in the figure refer to the velocity of the atom as it passes the origin, and the temperature is given for which this velocity is the most probable thermal velocity, $\sqrt{2k_BT/m}$. The data points are the results of the numerical simulation for a laser beam waist of 20 μm, 1 mW laser power, and atomic motion in the trapping potential. The solid lines are Gaussian fits. The dashed line is the time-of-flight lineshape for a 100 μK sample.

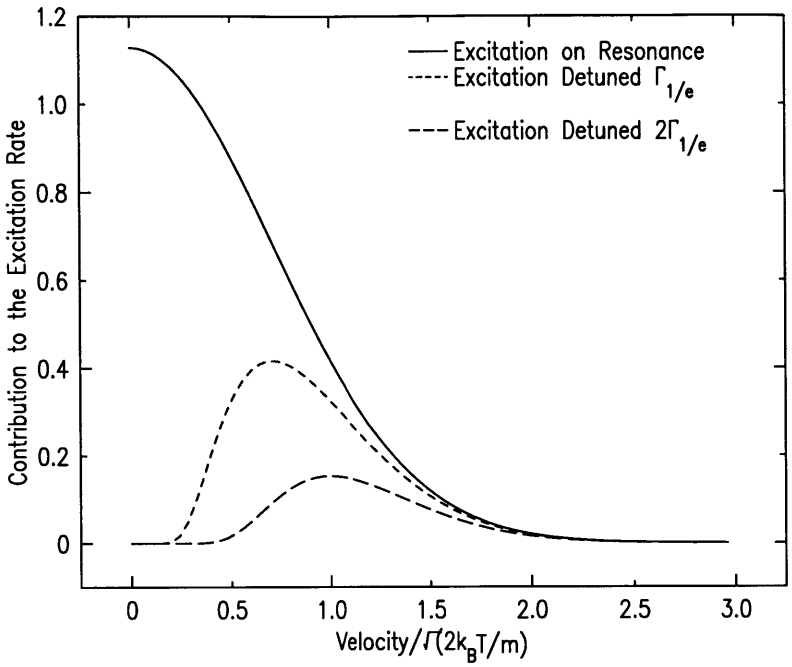

Figure 4-6: Contribution to the excitation rate from all the atoms with a given atomic velocity in the laser beam, for various detunings from resonance. The total excitation rate for a given detuning is found by integrating the area under the curve. The curves are normalized to unity excitation rate for zero detuning. The $1/e$ halfwidth is denoted $\Gamma_{1/e}$.

Here, ν is the laser frequency, and z and v are the atom's axial position and velocity when it passes through the beam.

Figure 4-5 shows the behavior of the numerically calculated $\rho_{2S,2S}(\nu, z, v, t_{laser})$ for atoms which are in the trap and make one pass through the laser at $z = 0$. At the high atomic energies used, the velocity is nearly constant as the atom passes through the laser. The numerical result for the excitation spectrum is described exactly by Eq. 4.38 including the values of the width and height. The exponential time-of-flight lineshape for a 100 μK sample, which is the weighted sum of Gaussian curves, is also shown. The dominant contribution on line center comes from atoms with energy substantially below k_BT.

The contribution to the excitation rate, as a function of atomic energy, or peak velocity, is shown in Fig. 4-6 for various detunings from resonance. The flux of atoms passing through the laser with a given velocity is approximately proportional to the three-dimensional Maxwell-Boltzmann velocity distribution, $\sim v^2 \exp\left[-(v^2/u^2)\right]$ (Eq.

4.24, Eq. B.14). This distribution function vanishes at zero velocity, which implies that for zero detuning, a large fraction of the signal comes from a relatively small number of low energy atoms which are in the laser for a long time.

4.4.5 Coherence Effects

When the atoms pass in and out of the laser beam more than once during one laser pulse, the spectrum can be much different. The collision cross-section for hydrogen is so small that there are essentially no collisions during the excitation pulse and atoms maintain coherence with the laser beam as they oscillate in the trap. This produces interference fringes, or sidebands on the spectrum, as observed in 1995 [10]. Numerical simulations illustrating the effect are shown in Fig. 4-7.

One can describe the excitation as a form of Ramsey separated oscillatory fields spectroscopy [86] in which an atom passes through an interaction region at regular time intervals. The fringe width is the inverse of the total time between the first and last pass. The fringes lie under the time-of-flight envelope whose width is the inverse of the time to pass through the laser once.

Another way to explain the fringes [60] is to quantize the motional states of atoms in the trap. This picture emphasizes the analogy with sidebands observed in the absorption spectra of trapped ions [87] and in the spectrum of scattered light from neutral atoms in optical lattices [88]. When an atom make an electronic transition from $1S$ to $2S$, its trap state can change if it gets a momentum kick from the momentum in the Fourier transform of the spatial profile of the laser beam. The spectrum takes the form of a carrier with sidebands. For a harmonic trap, the resonance condition is satisfied for $2h\nu = h\nu_{1S,2S} + 2ph\nu_{trap}$ where ν_{trap} is the frequency of the atoms orbital motion and p is an integer. Because of the cylindrical symmetry of the system, the initial and final harmonic oscillator quantum numbers must differ by an even number of quanta. At the laser frequency, the sideband spacing is equal to the trap oscillation frequency. The width of the individual peaks is given by the inverse of the shortest coherence time in the system. This time may be the inverse of the laser linewidth, the length of the laser pulse, or the time between collisions, for example.

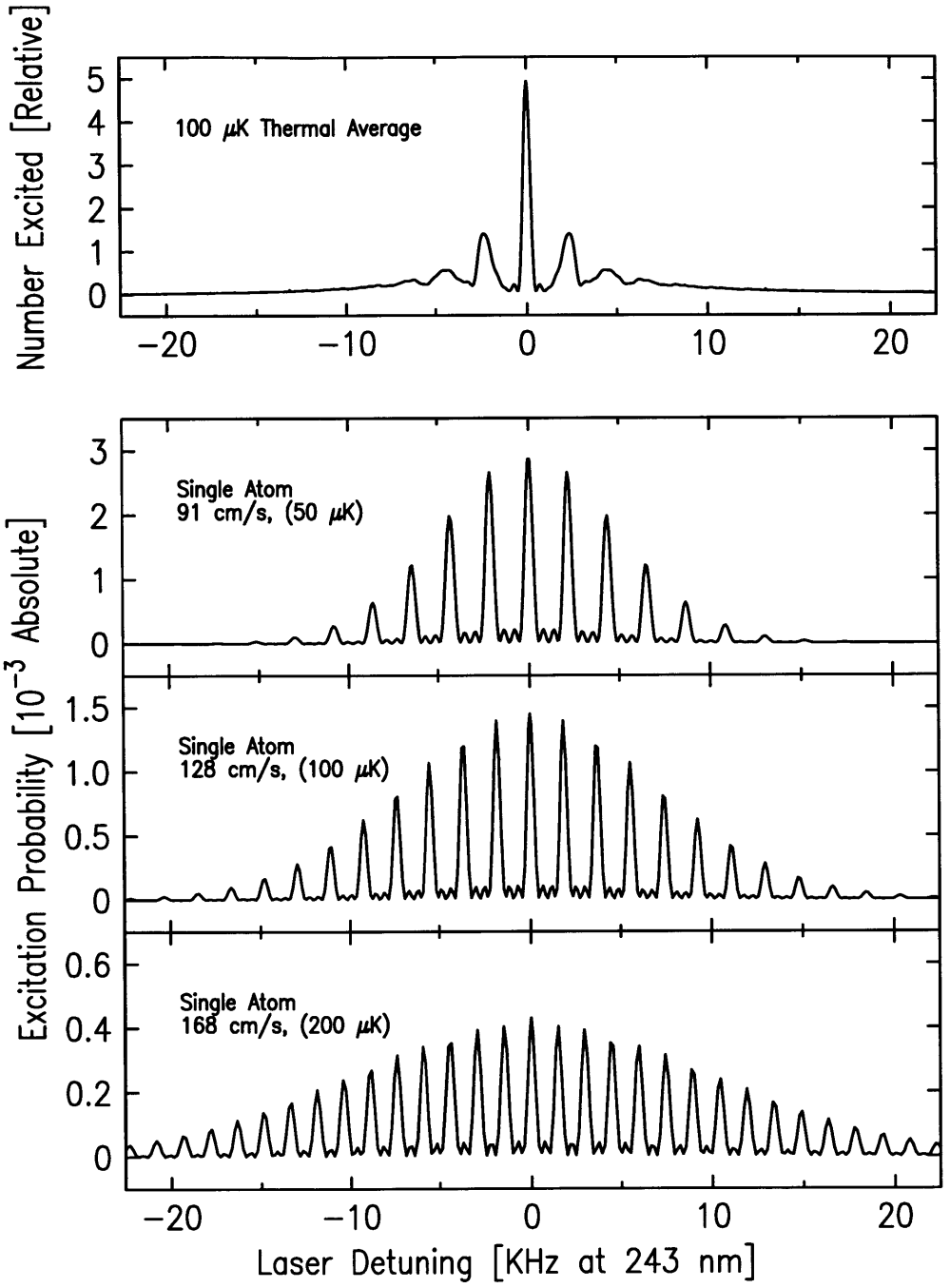

Figure 4-7: Numerical calculation of the probability for excitation to the $2S$ state after a 1 ms laser pulse. Atoms move at $z = 0$ in the trapping potential and pass through the laser beam multiple times, giving rise to interference fringes in the excitation probability. The fringe separations are equal to the atom oscillation frequencies. The widths result from the finite length of the laser pulse. The envelopes of the curves are the Gaussians (Fig. 4-5) observed for the spectrum after one pass through the laser. The velocity quoted in the figure refers to the velocity of the atom as it passes through the origin, and the temperature is given for which this velocity is the most probable thermal velocity, $\sqrt{2k_BT/m}$. The upper trace is the excitation spectrum for a 100 μK sample which is the weighted sum of curves such as the ones shown in the lower three traces. The laser beam waist is 20 μm, and the power is 1 mW.

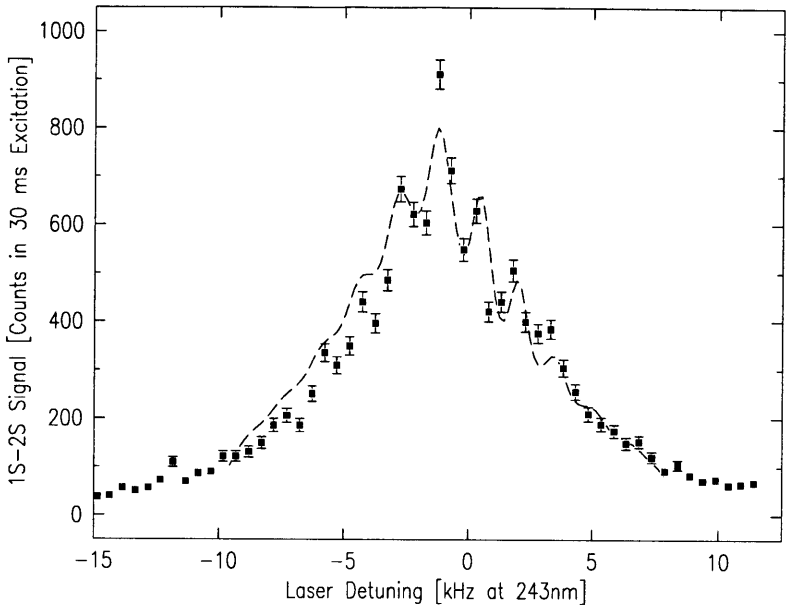

Figure 4-8: Spectrum of a 275 μK sample showing coherence sidebands. The asymmetry arises from the cold collision frequency shift associated with the inhomogeneous density. Peak sample density is around 10^{13} cm^{-3}. The cold collision frequency shift, laser linewidth of about 1 kHz, and variation of trap oscillation frequency with atom motional energy and axial position reduce the contrast of the fringes. The dashed line is the result of the numerical calculation of the spectrum which takes these effects into account.

To understand all the details of Fig. 4-7, it is helpful to discuss the atomic motion in more detail. We can neglect the axial motion, so each atom is associated with a z position for which the profile of the trap along r is $U(r) = \mu\sqrt{B_0(z)^2 + (rB')^2}$ (Sec. 2.2.1). $U(r)$ is nearly harmonic for $r < B_0/B'$ and approximately linear in r at greater distances. Thus low energy atoms exhibit simple harmonic motion with frequency $\nu_{trap}(0) = \sqrt{\mu/mB_0}\ B'/2\pi$. Higher energy atoms exhibit periodic motion, but with an increasing period. The frequency for passing through the laser approaches $\nu_{trap}(E) \approx \mu B'/(4\sqrt{2mE})$ for high energy. To provide axial confinement, $B_0(z)$ varies with z, so $\nu_{trap}(0)$ also varies in the trap.

Since ν_{trap} varies, so does the sideband spacing. This is evident in the calculated spectra for various atomic energies with z=0 (Fig. 4-7). The spacing decreases for higher energy atoms and this dispersion washes out the sidebands in the spectrum for the thermal sample. Additional dispersion, not shown in the figure, arises because a

real spectrum has contributions from various values of z. The cold collision frequency shift can also obscure the sideband structure because atoms with different trajectories in the trap see different densities and experience different shifts (Chap. 5).

Experimental Observation

In order to resolve the sidebands, their spacing must be greater that the spectral resolution, which is ultimately limited by the laser linewidth ($\sim$ 1 kHz), and the dispersion of the spacing must not be too great. Typically, for traps for samples with temperature below 200 μK, the frequency $\nu_{trap}(0)$ is between 1 and 4 kHz.

The best resolved sideband spectrum to date is shown in Fig. 4-8. The variation of ν_{trap} along z and the cold collision frequency shift make the experimental spectrum less clean than Fig. 4-7. With a narrower laser linewidth, one could use a more harmonic trap and tolerate the lower $\nu_{trap}(0)$. With greater fluorescence detection efficiency, one could work with lower density. These improvements should increase the contrast of the fringes in the spectrum.

Recently, the group of T. Hänsch observed similar $1S$-$2S$ spectra using time-domain Ramsey spectroscopy of the $1S$-$2S$ transition in an atomic beam [64].

As a final note on the subject, when the atoms are confined by the trap to within the laser beam, there are no sidebands, just as the time-of-flight linewidth vanishes as discussed in Sec. 4.3.2.

Chapter 5

Cold Collision Frequency Shift: Observations

When the peak sample density, n_0, is greater than about 10^{13} cm^{-3}, the cold collision shift of the transition frequency is clearly visible in the spectrum. Figure 5-1 shows spectra for a sample with an initial $n_0 = 5.0 \times 10^{13}$. This chapter contains data on the cold collision frequency shift observed in the Doppler-free $1S$-$2S$ transition, along with simulations of the spectra and a detailed description of how we calibrate the shift for a given density and derive the $1S$-$2S$ triplet scattering length. The result for the scattering length is compared with a recent theoretical calculation, and the usefulness of $1S$-$2S$ spectroscopy as a probe of trapped hydrogen is discussed.

5.1 Data

5.1.1 Experimental Procedure

Hydrogen atoms are trapped and evaporatively cooled as described in Sec. 2. For identically prepared samples, the reproducibility of n_0 immediately after the forced evaporation ends is on the order of a few percent and it is measured using the bolometer as described in Sec. 2.5.2.

A representative sample and trap has $\sim 10^{11}$ atoms with $T = 120$ μK and $n_0 \sim$

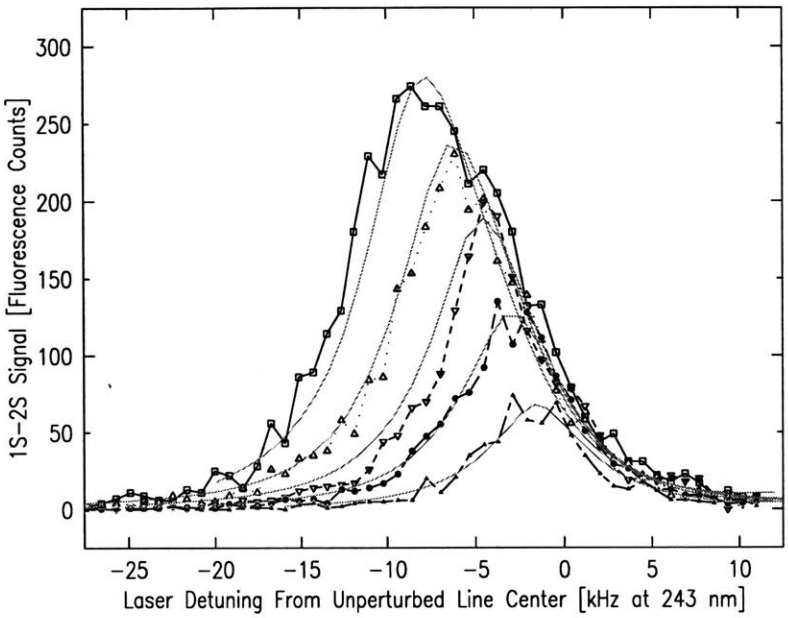

Figure 5-1: Spectra of a 120 μK sample with an initial peak sample density of $n_0 = 5.0 \times 10^{13}$ cm^{-3}. The furthest red-shifted line was recorded first. The signal becomes less intense and the shift decreases as the sample density drops. Each data point represents 30 ms of laser excitation. Approximately 45 seconds elapses between the first and last scan shown. The origin of the frequency axis is the unperturbed transition frequency. The smooth lines are the results of numerical simulations of the lineshape.

5×10^{13} cm^{-3}. The axial bias field is 0.4×10^{-4} T and the axial oscillation frequency is 10 Hz. The radial linear field gradient is 229×10^{-4} T/cm. The radial oscillation frequency near the trap minimum is 4000 Hz. The thermal energy equals the confining potential at characteristic dimensions of the sample, $z_{thermal} = \pm 3.8$ cm and $r_{thermal} = 100$ μm. The laser beam waist radius is $w_0 = 45$ μm and the divergence length is $z_0 = 3.0$ cm.

Spectra are recorded as described in Sec. 3, beginning within a few seconds after the forced evaporation ends. While the laser illuminates the gas, helium gas evaporates off the retroreflecting mirror at the bottom of the cell and knocks atoms out of the trap. The sample decays with a $\sim$ 10 second time constant. For typical samples, about one second is required to record a spectrum with a sufficient signal-noise ratio to determine the line center to $\sim$ 100 Hz. With a single load of the trap and evaporation, up to 30 useful spectra are recorded.

The first scan after the forced evaporation ends probes the highest density and shows the greatest red-shift. For subsequent scans, as the density drops, the shift decreases. The time scale of the measurement is short compared to the time scale for drift of the reference cavity mode to which the laser is locked (Sec. A.2.1), so the later, low density spectra, provide the unperturbed transition frequency. Thus one can determine the value of the frequency shift for a given spectrum without knowing the absolute frequency of the line center.

5.1.2 Data Analysis

An example of the data analysis is shown in Fig. 5-2 for a 120 μK sample with an initial density of 6.6×10^{13} cm^{-3}. The upper left graph shows the integrated signal for each sweep and the fit to a model of a one body loss rate. Using this fit and the initial sample density measured with the bolometer, one can assign a density to each sweep. The first sweep is typically discarded from the analysis because the laser is not well aligned during that time.

The upper right graph shows the $1/e$ halfwidths of double exponential fits to the lines. The high density spectra are broadened due to the inhomogeneous density distribution. This point will be discussed in Sec. 5.1.3. A phenomenological model is fit to the curve of linewidth versus sweep number. The low density limit of the fit gives the time-of-flight linewidth, which, along with the energy distribution measured with the bolometer (Sec. 2.5.1) and the thermodynamic model of heating and cooling [24], is used to determine the sample temperature and monitor the effective laser beam waist (Sec. 4.3.2).

The center frequency of each sweep, measured with respect to a transmission mode of the optical Fabry-Perot reference cavity, is plotted in the lower left graph. The frequencies have been corrected for drift of the frequency of the transmission mode (Sec. A.2.1) due to fluctuating light power in the cavity and long term relaxation of the cavity mirror spacing. The scatter in the data is greater than the statistical errors for the determination of the line centers, and may arise from laser power fluctuations, changes in the laser beam alignment, or shifts in offsets in the frequency control

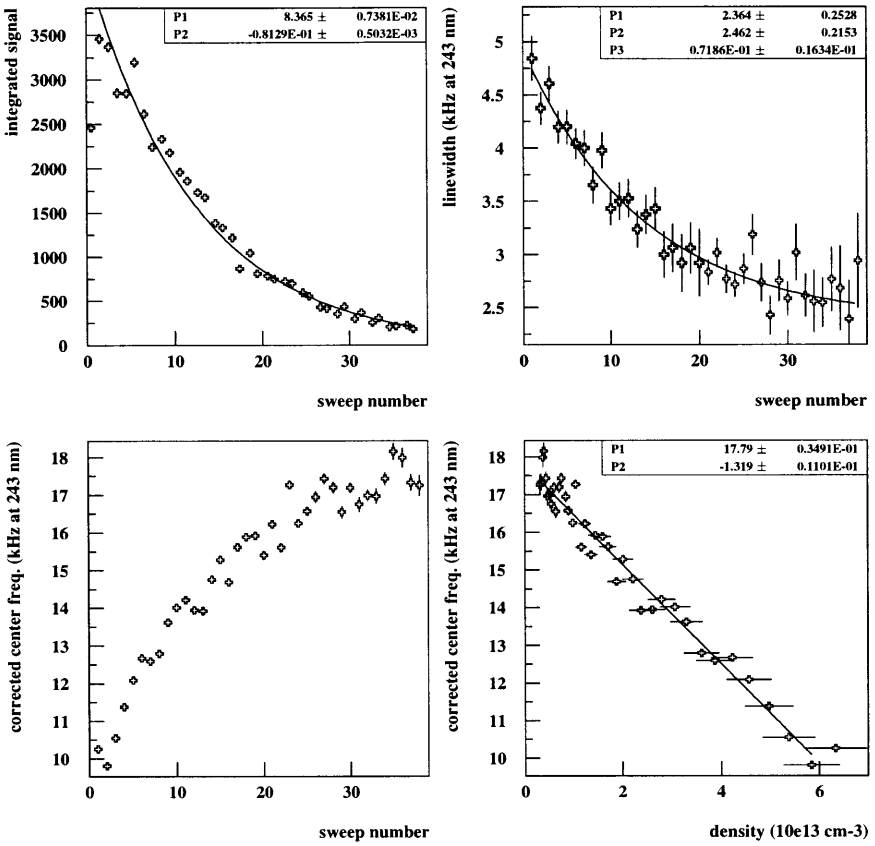

Figure 5-2: Analysis of spectra from a 120 μK sample with an initial density of 6.6×10^{13} cm^{-3}. *Upper left:* The integrated signal of each sweep. *Upper right:* The $1/e$ halfwidth of a fit of a double exponential to each spectrum. *Lower left:* The center frequency of each sweep, measured with respect to a transmission mode of the optical Fabry-Perot reference cavity. *Lower right:* Line center as a function of the sample density. The slope of this linear fit is $k = -1.32$ kHz/(10^{13} cm^{-3}).

electronics. The scatter is not a limitation at present, but one could probably control these parameters more carefully to improve the quality of the measurement.

Finally, the line centers are plotted against the sample density obtained from the fit of the integrated signal. We make a linear fit to this data. The slope of this line is a measurement of k, the proportionality between the observed shift of the line center at 243 nm and the peak sample density.

5.1.3 Inhomogeneous Broadening and Shift

If the region sampled by the laser were small on the length scale of density variations in the trap, the line shape would not change as the density dropped; it would only shift. In actuality, however, the laser samples a distribution of densities in the trap and the lineshape and k depend on the trap geometry and sample temperature.

The effect of the inhomogeneous density distribution is evident in the plot of the linewidths in Fig. 5-2. As discussed in Sec. C.4, the homogeneous broadening associated with the cold collision frequency shift is small; the observed broadening is inhomogeneous. Different atoms in the laser beam see different average densities and experience different shifts of their resonance frequency.

The physically interesting cold collision shift parameter is χ, which is defined by the local mean field relation between the level shift and the local density, $\Delta E_{1S-2S}(\mathbf{r}) = h\chi n(\mathbf{r})$. The relation between χ and k is $\chi = 2k/\alpha$, where the factor of two refers the shift to the $1S$-$2S$ energy level spacing at 122 nm, and α, which varies with the experimental geometry, corrects for the inhomogeneous density distribution in the trapped gas. For every trap and sample configuration, α is determined by numerically calculating the spectrum (Sec. 4.4), including the cold collision frequency shift and the density distribution and laser spatial profile. Then, for every k, one can extract a measurement of χ.

The smooth curves in Fig. 5-1 are the results of simulations and demonstrate that in this regime the calculation agrees with experiment reasonably well. It is found that for a given trap and sample temperature, the shift of the line center is a constant fraction (α) of the shift associated with the peak sample density, independent of the peak density. For different magnetic trap profiles and temperatures, the fraction ranged from 0.7 to 0.8. For a discussion of some the limitations of the numerical simulation of the spectrum, see Sec. 6.3.

5.1.4 Systematic Uncertainties

The statistical uncertainties are small for an individual measurement of χ. There are significant possible systematic errors however.

Density Calibration

As discussed in Sec. 2.5.2, we determine n_0 by measuring the dipolar decay rate through bolometric detection of the atoms after they are released from the trap. The dominant uncertainty in density measurements arises from imperfect knowledge of our trapping fields on the 10^{-4} T level due to trapped fluxes in our large superconducting coils and fringe fields from the 4 T field in the discharge region. This produces systematic errors of about of 10-20%.

Any error in the calculated value of g would also be reflected in the value of χ.

$n_0(10^{13}\ \mathrm{cm}^{-3})$	$T(\mu\mathrm{K})$	$k(\mathrm{kHz}/(10^{13}\ \mathrm{cm}^{-3}))$	α	$\chi = 2k/\alpha(\mathrm{kHz}/(10^{13}\ \mathrm{cm}^{-3}))$
3.1 ± 0.3	490	-1.59 ± 0.16	0.79	-4.02 ± 0.80
3.1 ± 0.3	490	-1.45 ± 0.15	0.79	-3.67 ± 0.73
3.1 ± 0.3	490	-1.66 ± 0.17	0.79	-4.20 ± 0.84
3.1 ± 0.3	490	-1.75 ± 0.18	0.79	-4.43 ± 0.88
5.5 ± 0.6	250	-1.22 ± 0.12	0.7	-3.49 ± 0.70
4.5 ± 0.9	250	-1.20 ± 0.24	0.7	-3.43 ± 1.03
4.5 ± 0.9	250	-1.11 ± 0.22	0.7	-3.17 ± 0.95
4.5 ± 0.9	260	-1.84 ± 0.37	0.79	-4.66 ± 1.40
4.5 ± 0.9	260	-1.85 ± 0.37	0.79	-4.68 ± 1.40
4.5 ± 0.9	260	-1.71 ± 0.34	0.79	-4.33 ± 1.30
3.2 ± 0.6	110	-1.69 ± 0.34	0.79	-4.28 ± 1.28
3.2 ± 0.6	110	-1.66 ± 0.33	0.79	-4.20 ± 1.26
6.6 ± 0.7	120	-1.25 ± 0.13	0.8	-3.13 ± 0.62
6.6 ± 0.7	120	-1.46 ± 0.15	0.8	-3.65 ± 0.73
6.6 ± 0.7	120	-1.32 ± 0.13	0.8	-3.30 ± 0.66
6.6 ± 0.7	120	-1.51 ± 0.15	0.8	-3.78 ± 0.76
7.1 ± 1.4	120	-1.36 ± 0.27	0.8	-3.40 ± 1.02

Table 5.1: Data for determining the cold collision frequency shift. The symbols are defined in the text. Errors in k are from the errors in n_0. Uncertainties for χ are the sum of a 10% uncertainty arising from α and the uncertainty coming from k.

Geometry Correction Factor α

The calculation of α for a given trap is most sensitive to the assumed position of the laser focus with respect to the atom cloud. Radially, the atoms are overlapped with the laser experimentally by monitoring the $1S$-$2S$ signal while varying magnet currents to move the cloud. Axially, it is difficult to move the cloud and there is an uncertainty in relative position on the order of two centimeters. By performing calculations for various reasonable laser focus positions, it was determined that for a given sample there is a 10% uncertainty in α.

5.1.5 Measured Value of χ

To examine the sensitivity to systematic effects, χ was measured in different trap configurations, with sample temperatures between 110 and 500 μK and initial maximum densities in the range $(2 \sim 7) \times 10^{13}$ cm^{-3} (Tab. 5.1). For a given measurement, the uncertainties are systematic, rather than statistical, so, to be conservative, we add

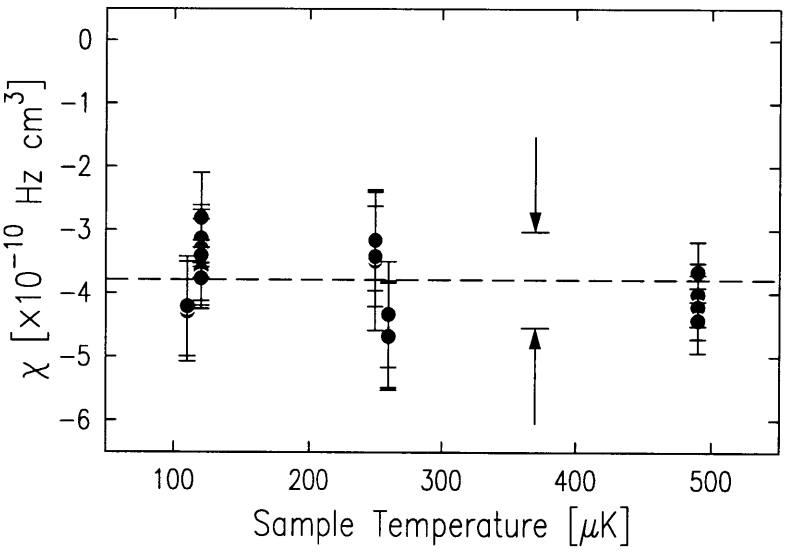

Figure 5-3: The frequency shift parameter χ, determined as described in the text for various trap configurations. No significant dependence on sample temperature is observed. The error bars reflect systematic uncertainties in the magnetic trapping fields and laser geometry. The dashed line is the weighted mean of all measurements, $\chi = -3.8 \pm 0.8 \times 10^{-10}$ Hz cm^3. and the quoted uncertainty is indicated by the double arrows.

them linearly, rather than in quadrature.

In Fig. 5-3, the various measurements are plotted versus sample temperature. We observe no significant temperature dependence of the shift, consistent with theory. Any significant nonlinear density dependence of the shift would manifest itself in data such as the lower right graph in Fig. 5-2, but none is evident.

From a weighted average of the various measurements, we find $\chi = -3.8 \pm 0.8$ kHz/(10^{13} cm^{-3}). Under the worst case scenario, the systematic errors could all be of the same sign, so we give the uncertainty in χ as the average of the systematic uncertainties of the individual measurements. In an apparatus optimized for spectroscopy, rather than achieving BEC, the magnetic field and laser geometries could be better known, and the uncertainty in χ could be greatly reduced.

5.2 The $1S$-$2S$ S-Wave Triplet Scattering Length

5.2.1 Experimental Value of the $1S$-$2S$ Scattering Length

For a homogeneous sample and excitation, assuming the observed frequency shift arises entirely from elastic collisions, χ is given by (See Chap. 6),

$$\chi = (a_{1S-2S} - a_{1S-1S})\frac{4\hbar n_{1S}}{m}, \tag{5.1}$$

From this, we derive $a_{1S-2S} = -1.4 \pm 0.3$ nm. We have used the theoretical value of $a_{1S-1S} = 0.0648$ nm[89], which constitutes only a small contribution to χ.

The sample is not homogeneous, however, and possible implications of this fact for the expression for χ are discussed in Chap. 6. Since the theory for the frequency shift in an inhomogeneous system is not completely understood, the measurement of a_{1S-2S} should be viewed as preliminary. Further experiment and theory are needed.

It is safe to neglect contributions to the shift from inelastic processes. The most important of these effects would be collisional hyperfine transitions and quenching of the $2S$ state. Hyperfine transitions in the spin-polarized sample arise only through weak magnetic dipole interactions[42], and in our experiment we observe no evidence

for collisional quenching on a millisecond time scale. Thus it is reasonable to neglect inelastic processes when describing the observed density-dependent frequency shift.

5.2.2 Comparison with Theory

Jamieson *et al.*[90] calculated $a_{1S-2S} = -2.3$ nm. No uncertainty was attached to this value, but a rough estimate[91] is about $\pm$ 30%. With this uncertainty, the calculation is in fair agreement with experiment.

Excited $2S$ atoms in the spin-polarized sample interact with $1S$ atoms on the $e^3\Sigma_u^+$ potential. The theoretical result for the scattering length was based on a potential derived from several *ab initio* calculations [92, 93] for small interatomic separations and an attractive van der Waals potential for large separations. The authors comment that the scattering length is particularly difficult to calculate because the potential is only slightly too shallow to support an additional bound level. In addition, they cautioned that the potentials do not mesh smoothly and somewhat arbitrary interpolations are required. Different interpolation methods produced $1S$-$2S$ scattering lengths which varied by 15%. Extension of the *ab intio* potentials could reduce the uncertainty in the calculation. A possible way to determine the potential to high precision is to perform photoassociative spectroscopy of bound states of the $e^3\Sigma_u^+$ potential.

5.3 Using the Cold Collision Frequency Shift as a Probe of the Trapped Gas

5.3.1 Noncondensed Gas

With the calibration of the cold collision frequency shift, one can use the Doppler-free $1S$-$2S$ spectrum of the noncondensed gas to determine sample density. This proves particularly useful for colder and more compressed traps for which bolometric determination of the density becomes unreliable due to decreasing signal strength and increasing uncertainty in the shape of the magnetic trap. When the sample radius

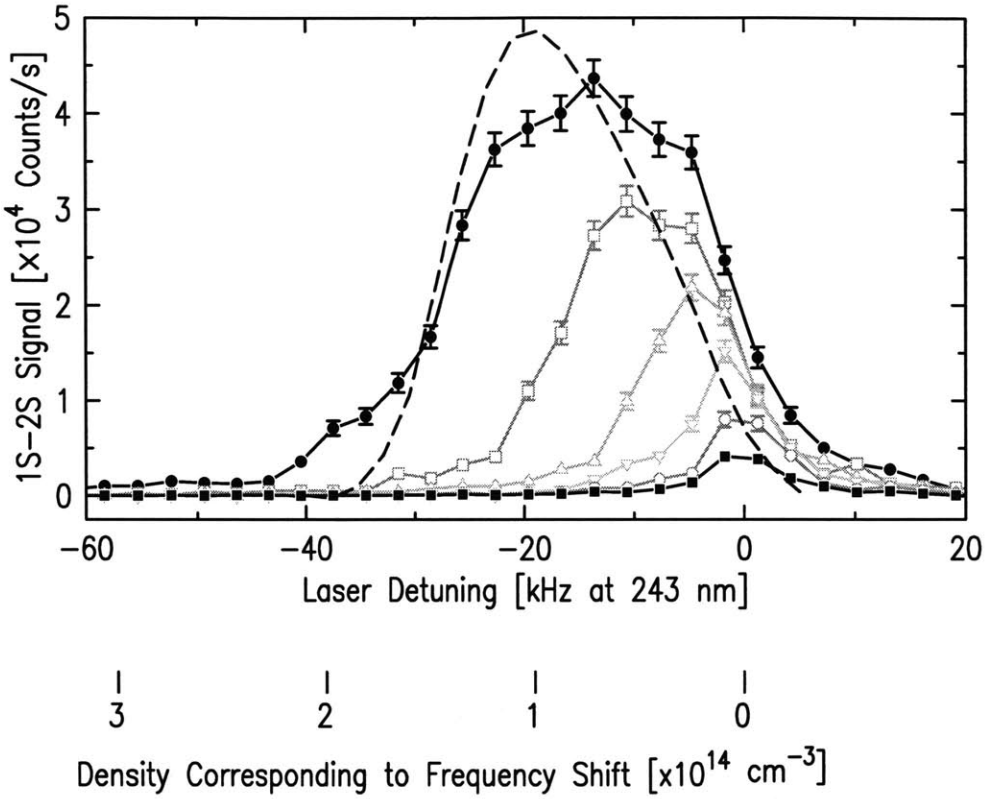

Figure 5-4: Spectra of a 55 μK sample (trap depth = 350 μK) with initial peak sample density of between $(1 \sim 2) \times 10^{14}$ cm^{-3}. The most intense spectrum was recorded first and the signal strength and density are lower for subsequent traces. The time-of-flight $1/e$ halflinewidth, measured from the low density spectra, is 2.2 kHz and is much smaller than the widths of the high density spectra, which arise from the inhomogeneous density sampled by the laser. The unperturbed center frequency of the low density sweeps is taken as zero detuning. The density which corresponds to a given frequency shift ($n = 2\Delta\nu/\chi$), is indicated below the graph. Each data point corresponds to 12 ms of laser excitation. The dashed line is a crude simulation of the spectrum (Eq. 5.2) for a sample with $n_0 = 1.5 \times 10^{14}$ cm^{-3}

is greater than the laser beam radius, which holds for all but the lowest accessible temperatures and strongest magnetic trap compressions, the $1S$-$2S$ signal intensity varies as the sample density. The bolometer signal, however, varies as the number of trapped atoms. As the sample is evaporatively cooled, the atom number decreases so the bolometer signal intensity drops, but the peak density generally increases as atoms settle into the trap, so the $1S$-$2S$ signal strength increases.

Figure 5-4 shows spectra of a 55 μK sample (trap depth = 350 μK). The lineshape is dominated by the cold collision frequency shift. Numerical simulations of the

spectra are not particularly illuminating because uncertainties in the trap and laser geometry are significant for such a cold sample and the semiclassical calculation of the lineshape is not expected to be accurate when the cold collision frequency shift dominates (Sec. 6.3).

For a high density sample, a simple approximate calculation of the lineshape is instructive. If one interprets the spectrum as a histogram of densities in the laser beam, the spectrum is approximated by

$$S(\nu) \sim \int d^3r \; F\left(\nu - \frac{\chi}{2} n(\mathbf{r}); \gamma\right) n(\mathbf{r}) I^2(\mathbf{r}), \tag{5.2}$$

where $I(\mathbf{r})$ is the laser intensity profile and $F(\nu;\gamma)$ is a lineshape function with width γ, centered on $\nu = 0$. The convolution enforces the resonance condition and allows inclusion of a laser linewidth. By allowing γ to depend on local density, one can incorporate the broadening due to $1S$-$2S$ collisions. Such a calculation neglects atomic motion.

The result of such a calculation is shown in Fig. 5-4. It does not reproduce the detailed shape of the data, but as a simple approximation, it shows that the histogram interpretation is not too far off. Because the experimental lineshape is not yet well understood (Sec. 6.3), however, a discussion of the discrepancy between data and the simple calculation is not possible.

The initial peak sample density can be estimated from the peak shift observed in the first recorded spectrum. One must allow for transit-time broadening, laser linewidth, and broadening due to the $1S$-$2S$ collisions, so the initial peak sample density determined from the spectrum is between $(1 \sim 2) \times 10^{14}$ cm^{-3}. In an apparatus with less uncertainty in the magnetic field and laser-atom overlap, study of such low temperature, high density spectra could provide a great deal of information on the cold collision frequency shift in an inhomogeneous system.

5.3.2 Bose-Einstein Condensation

Spectroscopy of the $1S$-$2S$ transition has proven to be an invaluable tool for studying Bose-Einstein condensation in hydrogen. Section 6.2 derives the condensate $1S$-$2S$ spectrum. The large density in the condensate shifts the resonance far to the red (Fig. 6-6), and the shape of the spectrum can provide valuable information on the distribution of densities and the condensate wave function. Experimental results are discussed in more detail in Chap. 7.

Chapter 6

Cold Collision Frequency Shift: Mean Field Theory

The pressure shift and broadening of an atomic spectrum arises because an atom's energy levels are perturbed due to interactions, or collisions, with neighboring atoms [14]. The thermal average phase shift per collision is $\phi = 2\pi a/\lambda_T$, where a is the s-wave scattering length for the collision and $\lambda_T = \sqrt{h^2/2\pi m k_B T}$ is the thermal de Broglie wavelength. When $\phi \ll 1$ only s-waves are involved in the collisions and the effect on the spectrum is often called the cold collision frequency shift.

Theory for the shift in the low temperature regime, based on the Boltzmann transport equation (App. C), has been developed to explain observations in cryogenic hydrogen masers [15] and laser cooled atomic fountains[18, 16]. These calculations assume a homogeneous sample and excitation and find the shift resulting from elastic collisions for a coherent, weak excitation in a two-level system is

$$2\pi\Delta\nu_{coll} = \frac{8\pi\hbar}{m}(a_{1-2} - a_{1-1})n_1, \tag{6.1}$$

where state 1(2) is the ground(excited) state, n_1 is the density of the sample, and $a_{\alpha-\beta}$ is the s-wave scattering length for $\alpha - \beta$ collisions. There is also a broadening of the transition, $\Gamma/2\pi = n_1 4a_{1-2}^2\langle v_{relative}\rangle$ (assuming $|a_{1-2}| \gg |a_{1-1}|$), which arises from dephasing collisions. For an atom in state 2, Γ is the normal collision rate with

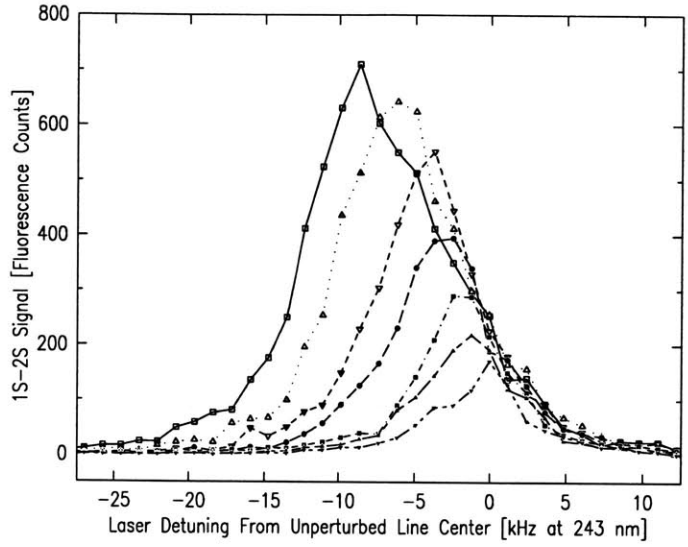

Figure 6-1: Doppler-free spectra of noncondensed trapped hydrogen, showing the cold collision frequency shift. The sample temperature is 120 μK and the furthest red shifted line corresponds to a peak density of $\sim 6.6 \times 10^{13}$ cm^{-3}. Sample density is proportional to the integrated area under a given trace. The small extra broadening of the high density traces is inhomogeneous, arising from the inhomogeneous density distribution in the trap. Each data point represents 30 ms of laser excitation and the line center of the low density trace is taken as the frequency origin.

atoms in state 1, assuming the cross section is $\sigma = 8\pi a^2$ as would be the case for collisions between identical particles. The broadening is equal to $\sqrt{2}\phi$ times the shift. If ϕ is large, then the line is mostly broadened. If ϕ is small, however, as is the case for the cold collision frequency shift, the atom's oscillating dipole retains its phase relation with the electric field for many collisions and the resonance is mostly shifted.

We have observed the cold collision frequency shift in the $1S$-$2S$ spectrum of trapped atomic hydrogen [11] for both a noncondensed sample (Fig. 6-1) and a Bose-Einstein condensate (BEC) [13]. The atomic motion and the inhomogeneous trap make it nontrivial to quantitatively explain the observations by generalizing the Boltzmann transport equation treatment. To gain some insight, and to derive expressions for the frequency shift which are appropriate to these new experimental conditions, we present a simple calculation based on a mean field interaction. We specifically consider Doppler-free $1S$-$2S$ excitation of trapped hydrogen, but the basic results should

apply for any excitation scheme so long as the momentum imparted to the atoms by the light does not change the spatial distribution of the particles appreciably during the time of the excitation.

To illustrate some of the concepts, we will first consider a simple homogeneous system, both for a noncondensed and condensed gas. Then we will consider the more realistic situation of an inhomogeneous system.

6.1 Mean Field Description for a Spatially Homogeneous System

The gas is assumed to be homogeneous and dilute ($na^3 \ll 1$), where n is the density and a is the s-wave scattering length, and one can neglect interactions between more than two particles. Also, $a \ll \lambda_T$, which in hydrogen is satisfied below a temperature of about 1 K [94], so interactions arise only through s-wave collisions. For s-wave collisions, the interatomic potential can be replaced by a shape independent pseudopotential[95] corresponding to a phase shift per collision of ka, where $\hbar\mathbf{k}$ is the momentum of each of the colliding particles in the center of mass frame. In this regime, the cold collision frequency shift can be described with mean field theory[96].

The important scattering lengths are the triplet scattering lengths, a_{1S-1S} and a_{1S-2S}. We neglect $2S$-$2S$ scattering because the excitation rate is assumed low (in the experiment typically 10^{-4} of the atoms are excited), so the background gas is essentially pure $1S$. Collisions between $1S$ and $2S$ atoms produce the dominant effect and the observed shift is to the red.

Inelastic collisions, such as collisions in which the hyperfine level of one or both of the colliding partners changes, will contribute additional shifts which are not easily explained in this formalism, but these effects are small in the experiment.

We consider a gas of N particles. The translational states of the atoms are plane wave states with periodic boundary conditions in a box of volume V. As $N, V \to \infty$, physical observables do not depend on the boundary conditions. We identify N/V as

the particle density.

The wave vectors of the atoms form an ordered set of motional quantum numbers $\mathbf{k}_i$. For a spatially homogeneous sample and excitation profile, the probability of an atom being promoted to the $2S$ state is independent of its motional state. This is not a good approximation of the real experimental situation but would describe excitation in, for instance, a hydrogen maser bulb, where the density and excitation rate are homogeneous in the sample.

6.1.1 State Vectors

Before laser excitation, the system consists of N particles in the $1S$ state. For the case of a noncondensed gas, with no two atoms in the same motional state, the normalized state vector before excitation is

$$|\Psi_{norm}^{N;0}\rangle = \mathcal{S}\ |1S, \mathbf{k}_1; 1S, \mathbf{k}_2; ...1S, \mathbf{k}_N\rangle. \tag{6.2}$$

We define $\mathcal{S}$ as the operator which creates a normalized state which is symmetric with respect to particle label. For state 6.2, $\mathcal{S} = \frac{1}{\sqrt{N!}} \sum_Q Q$, where the sum runs over all $N!$ permutations Q of the particle labels. For the state vector, we use the ket notation ($|...\rangle$), in which the entry in the first slot is the state of atom 1, the second entry is the state of atom 2, etc.

For a condensate at $T = 0$ with N particles, all $\mathbf{k}_i = 0$, where 0 denotes the motional ground state of the system. The normalized state vector before excitation is

$$|\Psi_{BEC}^{N;0}\rangle = |\underbrace{1S, 0; ...1S, 0}_{\text{N terms}}\rangle. \tag{6.3}$$

To form the normalized state vector of the excited state, we note that during Doppler-free excitation of a homogeneous system by a spatially homogeneous laser profile, an atom's motional state is left unchanged (See Sec. 4.4.5 and [60]). Assuming a monochromatic laser, the internal state evolves unitarily [97]. If the amplitude of excitation for each atom is r, and the amplitude for remaining $1S$ is t, where

$t^2 + r^2 = 1$, then $|1S, \mathbf{k}_i\rangle \Rightarrow t|1S, \mathbf{k}_i\rangle + r|2S, \mathbf{k}_i\rangle$, and the excited state vector is

$$|\Xi_x^e\rangle = \sum_{n=0}^{N} t^{N-n} r^n \sqrt{\frac{N!}{n!(N-n)!}} |\Psi_x^{N-n;n}\rangle \tag{6.4}$$

The normalized state $|\Psi_x^{N-n;n}\rangle$ describes a gas with $N-n$ $1S$ atoms and n $2S$ atoms, where x can either refer to the normal or condensed gas,

$$\begin{aligned} |\Psi_{norm}^{N-n;n}\rangle &= \mathcal{RS}|2S, \mathbf{k}_1; ...2S, \mathbf{k}_n; 1S, \mathbf{k}_{n+1}; ...1S, \mathbf{k}_N\rangle \\ |\Psi_{BEC}^{N-n;n}\rangle &= \mathcal{S}|\underbrace{2S, 0; ...2S, 0;}_{\text{n terms}} \underbrace{1S, 0; ...1S, 0}_{\text{N−n terms}}\rangle. \end{aligned} \tag{6.5}$$

Here, as before, $\mathcal{S} = \frac{1}{\sqrt{N!}} \sum_Q Q$ for the normal gas. For BEC, $\mathcal{S} = \sqrt{\frac{n!(N-n)!}{N!}} \sum_Q' Q$, where $\sum_Q'$ runs over the $N!/n!(N-n)!$ permutations which create distinct arrangements of the particle labels. The new operator, $\mathcal{R}$, symmetrizes the state vector with respect to the motional states, $\mathbf{k}_i$, which are excited to the $2S$ level. For example, for $N = 3$ and $n = 1$,

$$\begin{aligned} |\Psi_{norm}^{2,1}\rangle &= \mathcal{RS}|2S, \mathbf{k}_1; 1S, \mathbf{k}_2; 1S, \mathbf{k}_3\rangle \\ &= \mathcal{S}\frac{1}{\sqrt{3}} [|2S, \mathbf{k}_1; 1S, \mathbf{k}_2; 1S, \mathbf{k}_3\rangle + |2S, \mathbf{k}_2; 1S, \mathbf{k}_3; 1S, \mathbf{k}_1\rangle \\ &\quad + |2S, \mathbf{k}_3; 1S, \mathbf{k}_1; 1S, \mathbf{k}_2\rangle], \end{aligned} \tag{6.6}$$

and $\mathcal{S}$ then symmetrizes with respect to particle label.[1]

In $|\Xi_x^e\rangle$, the number of atoms in the $2S$ state is not a good quantum number. However, the probability distribution is strongly peaked around $\bar{n} = r^2 N$ $2S$ atoms, and the excited state vector can be approximated by $|\Xi_x^e\rangle \approx |\Psi_x^{N-\bar{n};\bar{n}}\rangle$. This is illustrated in Fig. 6-2 for a sample with $N = 10^7$.

Both states $|\Psi_{norm}^{N;0}\rangle$ and $|\Psi_{norm}^{N-\bar{n};\bar{n}}\rangle$ are symmetric with respect to exchange of any momentum state labels $\mathbf{k}_i$ and $\mathbf{k}_j$. When all atoms are $1S$ this is required by the statistics for identical bosons, but nature does not require the state vector to be

[1] One is not required to exchange the particle labels of $1S$ and $2S$ atoms, but the physical observables of the system are unaffected by this and it is mathematically simpler.

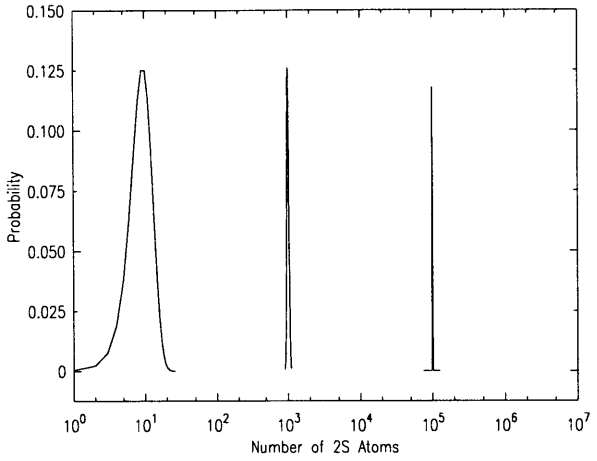

Figure 6-2: Probability distributions of the number of atoms in the $2S$ state for a total of 10^7 atoms and various fractions of atoms excited. The left most distribution is for each atom having a 10^{-6} probability of being excited ($r = .001$), the middle is 10^{-4} ($r = .01$.) and is multiplied by 10, and the right most is 10^{-2} ($r = .1$) and is multiplied by 100. The sum of the probabilities for each case is 1. Note that the distribution is quite narrow except for very small excitation probabilities. In our experimental situation we typically have a 10^{-3} to 10^{-4} excitation probability for each atom.

symmetric under exchange of the motional states of a $1S$ atom and a $2S$ atom. The momentum exchange symmetry of $|\Psi_{norm}^{N-\bar{n};\bar{n}}\rangle$ is particular to our assumption that the excitation probability is equal for all motional states and reflects the homogeneity of the system.

6.1.2 Hamiltonian and Mean Field Energies

The total many-body Hamiltonian is

$$H = \sum_{i=1}^{N} \left(\frac{\tilde{P}_i^2}{2m} + H_i^{int} \right) + H', \tag{6.7}$$

where $\tilde{\mathbf{P}}_i$ is the momentum operator for particle i, H_i^{int} is the Hamiltonian for the internal state of atom i, and H' is the operator for the two-body interaction which contains the effects of $1S$-$1S$ and $1S$-$2S$ elastic collisions. Using pseudopotential

formalism [95, 96] H' is written

$$\begin{aligned} H' &= \frac{4\pi\hbar^2}{m}\sum_{1\le i<j}^{N}\delta(\tilde{\mathbf{r}}_i-\tilde{\mathbf{r}}_j)\left\{a_{1S-1S}\mathcal{P}_i^{1S}\mathcal{P}_j^{1S}+a_{1S-2S}\left[\mathcal{P}_i^{1S}\mathcal{P}_j^{2S}+\mathcal{P}_i^{2S}\mathcal{P}_j^{1S}\right]\right\} \\ &\equiv \sum_{1\le i<j}^{N} w_{i,j}. \end{aligned} \tag{6.8}$$

The sum is over $N(N-1)/2$ distinct terms. Here, $\tilde{\mathbf{r}}_i$ is the operator for the position of atom i. The operator $\mathcal{P}_i^x = (|x\rangle\langle x|)_i$, where $x = 1S$ or $2S$, projects the internal state of atom i onto state $|x\rangle$. Note there are no terms of the form $(|1S\rangle\langle 2S|)_i(|2S\rangle\langle 1S|)_j$, which would involve excitation exchange [98] – a distinct process from those described in 6.8. This process could take place in the sample, but we neglect it here [99].

The energy before laser excitation (N $1S$ atoms and 0 $2S$ atoms) is

$$E^{N;0} = \sum_{i=1}^{N}\frac{\hbar^2 k_i^2}{2m} + E'^{N;0}, \tag{6.9}$$

where $E'^{N;0}$ is the interaction energy (See Sec. D.2),

$$\begin{aligned} E'^{N;0} &= \langle\Psi^{N;0}|H'|\Psi^{N;0}\rangle \\ &= \frac{2\pi\hbar^2 a_{1S-1S}}{m}\frac{N^2}{V}g^{(2)}(0), \end{aligned} \tag{6.10}$$

where $g^{(2)}(\mathbf{x})$ is the density-normalized second order spatial correlation function of the gas [100, 101] before excitation (See Sec. D.1),

$$g^{(2)}(\mathbf{x}) = \frac{1}{V}\int d^3r\ \left\{\sum_{i\neq j}\langle\Psi^{N;0}|\delta(\tilde{\mathbf{r}}_i-\mathbf{r})\delta(\tilde{\mathbf{r}}_j-\mathbf{r}-\mathbf{x})|\Psi^{N;0}\rangle/[n(\mathbf{r})]^2\right\}. \tag{6.11}$$

The correlation function expresses the statistics of the system. It shows antibunching for identical fermions ($g^{(2)}(0) = 0$), bunching for incoherent identical bosons ($g^{(2)}(0) = 2$), and classical behavior for coherent identical bosons ($g^{(2)}(0) = 1$).

The interaction energy $E'^{N;0}$ has the form of a mean field energy in which the individual pair-wise interactions have been replaced by an average over the distribution of atomic positions in the sample.

The total energy of the system in the excited state, $|\Psi^{N-\bar{n};\bar{n}}\rangle$, is

$$E^{N-\bar{n};\bar{n}} = \bar{n}E_{1S-2S} + \sum_{i=1}^{N} \frac{\hbar^2 k_i^2}{2m} + E'^{N-\bar{n};\bar{n}}. \tag{6.12}$$

As discussed in greater detail in Sec. 6.3, the excited state is one state in a manifold of states with $\bar{n}$ $2S$ atoms. The manifold is degenerate in the absence of H' and one must use degenerate perturbation theory to find the interaction energy, $E'^{N-\bar{n};\bar{n}}$. Fortunately, the state excited by the laser (Eq. 6.5) is an eigenstate of H', and the interaction energy of the excited state is given by (Sec. D.3)

$$\begin{aligned} E'^{N-\bar{n};\bar{n}} &= \langle \Psi^{N-\bar{n};\bar{n}} | H' | \Psi^{N-\bar{n};\bar{n}} \rangle \\ &= \frac{2\pi\hbar^2}{m} \frac{N(N-\bar{n})}{V(N-1)} \left[(N-\bar{n}-1)a_{1S-1S} + 2\bar{n}a_{1S-2S} \right] g^{(2)}(0). \end{aligned} \tag{6.13}$$

For $N \gg \bar{n}$, the energy to excite $\bar{n}$ atoms to the $2S$ state is

$$E^{N-\bar{n};\bar{n}} - E^{N;0} \approx \bar{n} \frac{4\pi\hbar^2}{m} \frac{N}{V} (a_{1S-2S} - a_{1S-1S}) g^{(2)}(0) + \bar{n}E_{1S-2S}. \tag{6.14}$$

For a nondegenerate Bose gas, $g^{(2)}(0) = 2$. From this it follows that the energy supplied by two laser photons to excite an atom out of a normal gas is

$$\frac{E^{N-\bar{n};\bar{n}}_{norm} - E^{N;0}_{norm}}{\bar{n}} \equiv \frac{8\pi\hbar^2}{m} \frac{N}{V} (a_{1S-2S} - a_{1S-1S}) + E_{1S-2S}. \tag{6.15}$$

For a condensate, $g^{(2)}(0) = 1$, and the energy required for excitation is

$$\frac{E^{N-\bar{n};\bar{n}}_{BEC} - E^{N;0}_{BEC}}{\bar{n}} \equiv \frac{4\pi\hbar^2}{m} \frac{N}{V} (a_{1S-2S} - a_{1S-1S}) + E_{1S-2S}. \tag{6.16}$$

6.1.3 Discussion

We interpret the transition energy shifts in Eq. 6.15 and 6.16 as arising from mean field shifts of the energy levels, as shown in Fig. 6-3. Spectroscopy of the $1S$-$2S$ transition measures the separation of the perturbed levels.

In Eq. 6.14 for the transition energy shift, the term arising from $1S$-$2S$ interactions

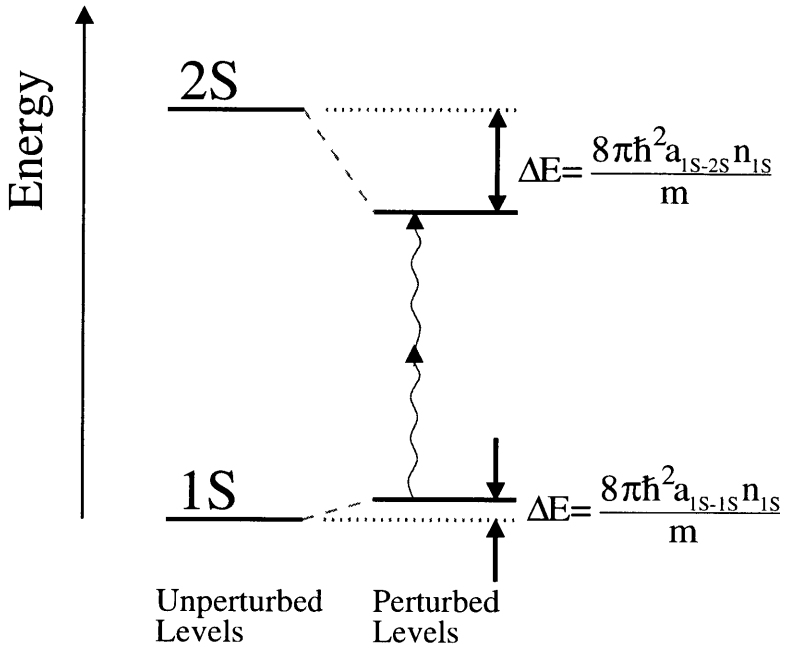

Figure 6-3: $1S$-$2S$ energy level diagram for a noncondensed, homogeneous sample, showing the density-dependent level shift which gives rise to the cold collision frequency shift.

depends on the $1S$-$1S$ correlation function $g^{(2)}(0)$ in the same way that the $1S$-$1S$ interaction term does. In quantum mechanics, $2S$ particles are considered distinguishable from $1S$ particles and one might not expect such exchange effects to appear in the $1S$-$2S$ interaction. In other words, for a given $1S$ density, one might expect the same shift due to the $1S$-$2S$ interactions in a condensate or normal gas. The dependence on $g^{(2)}(0)$ for the $1S$-$2S$ interaction arises in this case from the special form of the excited state given by Eq. 6.5. Since all motional states in the original system are equally likely to be excited, the $2S$ excitation is equally shared by every atom. Consequently, in addition to the direct contribution to the $1S$-$2S$ interaction energy from terms of the form $\langle 2S, \mathbf{k}_1; 1S, \mathbf{k}_2 | H' | 2S, \mathbf{k}_1; 1S, \mathbf{k}_2 \rangle$, because of the extra symmetry in the state vector, there is also an equal contribution from exchange terms like $\langle 2S, \mathbf{k}_1; 1S, \mathbf{k}_2 | H' | 2S, \mathbf{k}_2; 1S, \mathbf{k}_1 \rangle$ ($\mathbf{k}_1$ and $\mathbf{k}_2$ have been switched in the ket.). This can be interpreted as implying that the motion of the excited $2S$ atoms is correlated to the motion of the $1S$ atoms, and it is a purely quantum mechanical effect. This correlation can be seen in the state vector for the excited state of the normal gas, Eq.

6.5, which is the coherent sum of state vectors of many configurations of the system. If in one configuration, a $2S$ atom is found in motional state $\mathbf{k}_i$, then in almost every other configuration, there is a $1S$ atom in state $\mathbf{k}_i$.

If one were to measure the interaction energy of a $2S$ particle introduced to the sample from far away, its motion would not be correlated with the motion of the $1S$ atoms. There would be no exchange contribution, and the energy would be $4\pi\hbar^2 a_{1S-2S} n_{1S}/m$.

6.2 Mean Field Description for a Bose Condensed Gas in a Magnetic Trap

If one makes a local density approximation, in which the excitation of a given atom takes place in a small region in space where the shift is given by Eq. 6.16, with N/V replaced by the local density, then the spectrum for the condensate is given by

$$S(\nu) \propto \int d^3r \; n^N_{BEC}(\mathbf{r}) \delta \left[\nu - \frac{\left(E_{1S-2S} + 4\pi\hbar^2 (a_{1S-2S} - a_{1S-1S}) \; n^N_{BEC}(\mathbf{r})/m \right)}{2h} \right]. \tag{6.17}$$

This expression turns out to be correct, but it does not provide much insight into the excitation process. For instance, how can one make a local approximation when the condensate wave function extends over a large region of space? We present a more rigorous derivation of the spectrum which explicitly calculates the state vector and energy of the system before and after excitation.

When the system is Bose condensed, the density becomes so high that the interaction energy significantly modifies the wave functions for an inhomogeneous system. In this case one cannot treat the interaction as a perturbation as was done in the previous section.

The Hamiltonian for the system is now

$$H = \sum_{i=1}^{N} \left(\frac{\tilde{P}_i^2}{2m} + U(\tilde{\mathbf{r}}_i) + H_i^{int} \right) + H', \tag{6.18}$$

where $U(\mathbf{r})$ is the trapping potential, which for a magnetic trap is effectively the same for $1S$ and $2S$ atoms. H' is given in Eq. 6.8. We treat the condensate in the $T = 0$ limit and leave finite temperature effects for a future study. We specialize to the case of $a_{1S-1S} > 0$ and $a_{1S-2S} < 0$.

6.2.1 System before Excitation

At $T = 0$ all the atoms are in the condensate, and the condensate state vector before excitation is

$$|\Psi_{BEC}^{N;0}\rangle = |\underbrace{1S, 0^{N,1S}; ...1S, 0^{N,1S}}_{\text{N terms}}\rangle. \tag{6.19}$$

where $|0^{N,1S}\rangle$ is the single particle motional state of a $1S$ atom in a condensate with N atoms. It is important to note that by writing the condensate state vector as Eq. 6.19, we have set $g^{(2)}(0) = 1$. For the system to have $g^{(2)}(0) \neq 1$, the state vector for the "condensate" would have to involve more than one motional state.

One finds $|0^{N,1S}\rangle$ by minimizing $E_{BEC}^{N;0} = \langle \Psi_{BEC}^{N;0} | H | \Psi_{BEC}^{N;0} \rangle$ under the constraint of there being N total particles. The constrained minimization leads to the Gross-Pitaevskii, or nonlinear Schrödinger equation [102, 103, 104] for the single particle BEC wave function, $\psi_{BEC}^{N}(\mathbf{r}) = \langle \mathbf{r} | 0^{N,1S} \rangle$. The kinetic energy is small and can be neglected. This leads to the Thomas-Fermi wave function,

$$\begin{aligned} \psi_{BEC}^{N}(\mathbf{r}) &= \sqrt{\frac{n_{BEC}^{N}(\mathbf{r})}{N}} \\ &= \begin{cases} N^{-1/2} \left(n_{BEC}^{N}(0) - U(\mathbf{r})/\tilde{U} \right)^{-1/2} & U(\mathbf{r}) \leq n_{BEC}^{N}(0)\tilde{U} \\ 0 & \text{otherwise} \end{cases}, \end{aligned} \tag{6.20}$$

where $n_{BEC}^{N}(\mathbf{r})$ is the density distribution in the condensate, $n_{BEC}^{N}(0)$ is the peak density, and $\tilde{U} = 4\pi\hbar^2 a_{1S-1S}/m$. It can be shown for a cylindrically symmetric trap

that

$$n^N_{BEC}(0) = 0.118\left(Nm^3w_r^2w_z/\hbar^3a_{1S-1S}^{3/2}\right)^{2/5}, \tag{6.21}$$

where w_r and w_z are the frequencies in rad/s for small radial and axial oscillations at the bottom of the trap. One can interpret $\psi^{N*}_{BEC}(\mathbf{r}_i)\psi^N_{BEC}(\mathbf{r}_i)$ as the probability of finding condensate particle i at position $\mathbf{r}_i$. For a harmonic trap, $\psi^{N*}_{BEC}(\mathbf{r}_i)\psi^N_{BEC}(\mathbf{r}_i)$ varies as an inverted parabola along any trap axis (See Fig. 6-4).

In the Thomas-Fermi approximation, the Lagrange multiplier enforcing particle conservation in the constrained minimization is the chemical potential,

$$\mu_N = \frac{\hbar\omega_r}{2}\left[15Na_{1S-1S}\left(\frac{m\omega_r}{\hbar}\right)^{1/2}\frac{\omega_z}{\omega_r}\right]^{2/5} = \tilde{U}n^N_{BEC}(0), \tag{6.22}$$

and because $\mu_N = \partial E^{N;0}_{BEC}/\partial N$, the energy of the ground state before laser excitation is

$$E^{N;0}_{BEC} = \frac{5}{7}N\mu_N. \tag{6.23}$$

6.2.2 System after Excitation

We consider a homogeneous excitation, which is a good approximation for the hydrogen experiment because the laser is uniform over the region of the condensate.

When p condensate atoms are excited to the $2S$ state, $\psi^N_{BEC}(\mathbf{r})$ is no longer the single particle wave function which minimizes the energy of the condensate atoms.[2] For a weak excitation ($p \ll N$), we can neglect the small perturbation of the BEC wave function due to the presence of the $2S$ atoms, and the new equilibrium condensate many body state vector is given by $|\Psi^{N-p;0}_{BEC}\rangle$, as defined as in Eq. 6.19 and 6.20.

The $2S$ atoms interact strongly with the $1S$ atoms in the dense condensate. To find the effective potential in which $2S$ atoms move, we will see that one adds the $1S$-$2S$ interaction, $\Delta E(\mathbf{r}) = (4\pi\hbar a_{1S-2S}/m)n^{N-p}_{BEC}(\mathbf{r})$, to the magnetic trapping potential.

[2]The interesting problem of determining the relaxation time of the wave function [105, 106] after excitation is left to future study and we assume the excitation is slow enough that the excited state is in equilibrium.

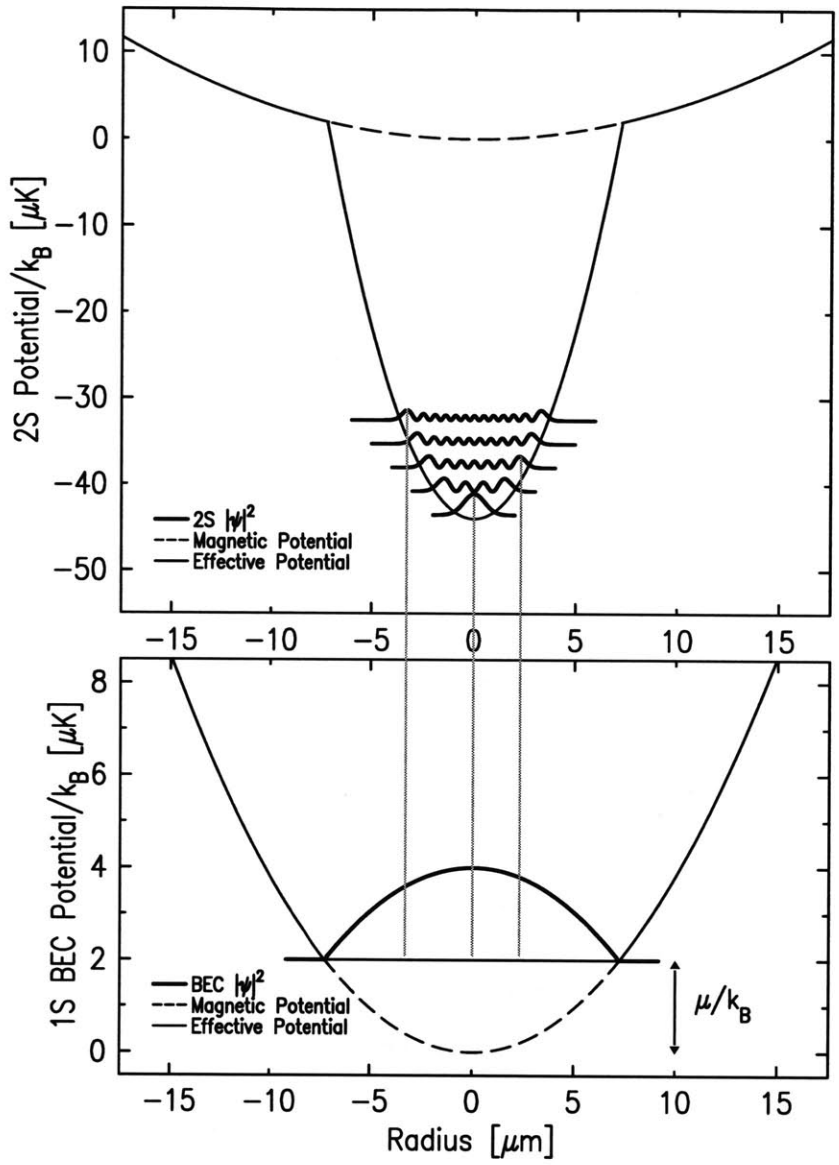

Figure 6-4: Radial potentials and single particle wave functions for $1S$ atoms in the condensate and $2S$ atoms trapped in the condensate interaction well. The dashed line is the magnetic trapping potential $U(\mathbf{r})$, which is identical for $1S$ and $2S$ atoms. The solid line is the effective potential in which atoms move, which includes the mean field interaction energy. Note the different energy scales. The heavy solid lines represent probability density distributions for atoms in various states. For the $2S$ states, every third state in the BEC interaction well is shown, up to the twelfth. The light solid lines indicate allowed Doppler-free transitions from the condensate, which must preserve mirror symmetry. The radial potentials and condensate wave function are for a peak condensate density of 5×10^{15} cm^{-3} ($\mu_N/k_B \approx 2$ μK), and a radial trap oscillation frequency of 4 kHz, which are characteristic conditions for the MIT hydrogen BEC experiment. The scattering lengths used in the calculations are $a_{1S-1S} = 0.0648$ nm and $a_{1S-2S} = -1.4$ nm. The $2S$ wave functions shown are one-dimensional simple harmonic oscillator wave functions. The bound $2S$ levels form a near continuum of motional states in a realistic anisotropic three dimensional trap.

This forms a deep potential well in which $2S$ motional states are trapped. At a given laser frequency, the condensate atoms are excited to one of the states in the well (See Fig. 6-4).

The energy of the excited state after laser excitation, and the $2S$ motional wave functions, are found by minimizing the energy functional,

$$E_{BEC}^{N-p;p,i} = \langle \Psi_{BEC}^{N-p;p,i} | H | \Psi_{BEC}^{N-p;p,i} \rangle, \tag{6.24}$$

where[3]

$$|\Psi_{BEC}^{N-p;p,i}\rangle = \mathcal{S}| \underbrace{2S, k_i^{N-p,2S}; ...2S, k_i^{N-p,2S}}_{\text{p terms}}; \underbrace{1S, 0^{N-p,1S}; ...1S, 0^{N-p,1S}}_{\text{N-p terms}} \rangle, \tag{6.25}$$

and $k_i^{N-p,2S}$ is the $2S$ motional state which is resonantly excited. Using Eq. 6.18, the energy functional reduces to (See Sec. D.4)

$$\begin{aligned} E_{BEC}^{N-p;p,i} &= E_{BEC}^{N-p;0} \\ &\quad + p\langle 2S, k_i^{N-p,2S}| \left[H^{int} + \frac{\tilde{P}^2}{2m} + U(\tilde{\mathbf{r}}) + \frac{4\pi\hbar^2 a_{1S-2S}}{m}\, n_{BEC}^{N-p}(\tilde{\mathbf{r}}) \right] |2S, k_i^{N-p,2S}\rangle \\ &= E_{BEC}^{N-p;0} + p(E_{1S-2S} + \varepsilon_i), \end{aligned} \tag{6.26}$$

where $E_{BEC}^{N-p;0}$ is defined in Eq. 6.23.

Finding the $2S$ motional states which minimize this functional, with the requirement that the $2S$ motional states form an orthonormal basis, is equivalent to finding the eigenstates of the effective $2S$ Hamiltonian

$$H_{eff}^{2S} = \frac{\tilde{P}^2}{2m} + U(\tilde{\mathbf{r}}) + \frac{4\pi\hbar^2 a_{1S-2S}}{m}\, n_{BEC}^{N-p}(\tilde{\mathbf{r}}), \tag{6.27}$$

and the eigenvalue for state $k_i^{N-p,2S}$ is ε_i. The effective potential and some $2S$ motional states are depicted in Fig. 6-4.

Inside the BEC potential well, using the Thomas-Fermi BEC density distribution,

[3]The excited state has a distribution in the number of $2S$ atoms, as discussed in Sec. 6.1.1, but we assume p is large enough that the distribution is narrow and peaked around a well defined number.

the eigenstates and eigenvalues are approximately those of a three dimensional harmonic oscillator with spring constants larger than those of the magnetic trap alone by a factor of $\sqrt{1 - a_{1S-2S}/a_{1S-1S}}$. States near the top and outside of the BEC interaction well are more complicated.

6.2.3 Discussion

From Eq. 6.23 and 6.26, the energy supplied by two photons to drive the transition, for $p \ll N$, is given by

$$\begin{aligned} 2h\nu &= \frac{E_{BEC}^{N-p;p,i} - E_{BEC}^{N;0}}{p} = \frac{p(E_{1S-2S} + \varepsilon_i) + E_{BEC}^{N-p;0} - E_{BEC}^{N;0}}{p} \\ &\approx E_{1S-2S} + \varepsilon_i - \mu_N. \end{aligned} \tag{6.28}$$

We have used $(E_{BEC}^{N;0} - E_{BEC}^{N-p;0})/p \approx \partial E_{BEC}^{N;0}/\partial N = \mu_N$ for small p. Note that $\varepsilon_i < 0$ for states bound in the BEC interaction well. Since there are many $2S$ motional levels which may be excited (See Fig. 6-4), there will be a distribution of excitation energies which extends from $2h\nu \approx E_{1S-2S}$ on the high frequency side, to $2h\nu \approx E_{1S-2S} + 4\pi\hbar^2 a_{1S-2S}\, n_{BEC}^N(0)/m - \mu_N$ on the low side, where ν is the laser frequency. The lowest frequency is for transitions to the lowest state in the interaction well. The spectrum dies off above E_{1S-2S} because states outside the well have negligible overlap with the condensate and are essentially inaccessible by laser excitation.

The excitation rate when the laser is resonant with $2S$ motional states with energy ε, $S[2h\nu = (E_{1S-2S} + \varepsilon - \mu_N)]$, is proportional to $\sum_{i,\varepsilon_i=\varepsilon} |\langle k_i^{N-p,2S}|0^{N,1S}\rangle|^2$ or

$$S(2h\nu) = \frac{\pi\hbar\Omega_0^2(0)}{2} \sum_i |\langle k_i^{N-p,2S}|0^{N,1S}\rangle|^2\, \delta(2h\nu - E_{1S-2S} - \varepsilon_i + \mu_N) \tag{6.29}$$

where the delta function enforces the resonance condition. The Rabi frequency for Doppler-free excitation in a standing wave is denoted (Eq. 4.17)

$$\Omega_0(\mathbf{R}) = 2M_{2S,1S}^{12} \left(\frac{\alpha}{2R_\infty}\right)^3 \frac{1}{3\pi^2\hbar c} I(\mathbf{R}), \tag{6.30}$$

where $I(\mathbf{r})$ is the laser intensity profile.

An interesting result of this calculation is that the broadening of the Doppler-free BEC spectrum is homogeneous. Since all atoms are initially in the same quantum state, the spectrum of every atom is identical. Recall that the Doppler-free excitation spectrum of the normal gas is inhomogeneously broadened by the frequency shift and the density distribution (Sec. 5.1.3 and 6.3).

Because the $2S$ single particle wave function $\psi_{\mathbf{k}_i^{N-p,2S}}(\mathbf{r}) = \langle \mathbf{r}|k_i^{N-p,2S}\rangle$ oscillates rapidly, the overlap integral, $\langle k_i^{N-p,2S}|0^{N,1S}\rangle$, will be most sensitive to the value of $\psi_{BEC}^N(\mathbf{r}) = \langle \mathbf{r}|0^{N,1S}\rangle$ at the classical turning points, which is approximately $\psi_{BEC}^N(\mathbf{r}_{turn}) = \sqrt{n_{BEC}^N(\mathbf{r}_{turn})\ /N}$. Intuitively, the sum over states at energy ε integrates the condensate density in a shell at the equipotential surface defined by $\mathbf{r}_{turn}^{\varepsilon}$, the turning points of $2S$ atoms with motional energy ε. Because the turning points satisfy $\varepsilon = 4\pi\hbar^2 a_{1S-2S}\ n_{BEC}^N(\mathbf{r}_{turn}^{\varepsilon})/m + U(\mathbf{r}_{turn}^{\varepsilon})$, this implies that the shape of the spectrum is approximately given by

$$\begin{aligned} S(2h\nu) &= \frac{\pi\hbar\Omega_0^2(0)}{2}\int d^3r\ \psi_{BEC}^{*N}(\mathbf{r})\psi_{BEC}^N(\mathbf{r}) \\ &\quad \times\delta\left[2h\nu - \left(E_{1S-2S} + \frac{4\pi\hbar^2 a_{1S-2S}\ n_{BEC}^N(\mathbf{r})}{m} + U(\mathbf{r}) - \mu_N\right)\right] \\ &= \frac{\pi\hbar\Omega_0^2(0)}{2}\int d^3r\ n_{BEC}^N(\mathbf{r}) \\ &\quad \times\delta\left[2h\nu - \left(E_{1S-2S} + \frac{4\pi\hbar^2(a_{1S-2S} - a_{1S-1S})\ n_{BEC}^N(\mathbf{r})}{m}\right)\right], \end{aligned} \tag{6.31}$$

which is identical to Eq. 6.17. In the last line we have used the fact that in the Thomas-Fermi approximation, $\mu_N - U(\mathbf{r}) = 4\pi\hbar^2 a_{1S-1S}\ n_{BEC}^N(\mathbf{r})/m$.

Numerical calculation of the overlap integrals in Eq. 6.29 for a spherically symmetric harmonic trap confirms Eq. 6.31 (Fig. 6-5). The integral over the BEC density distribution can also be motivated by noting that when a Lyman-alpha fluorescence photon is detected at a given frequency in the spectrum of the condensate, it is recording the fact that a $1S$ atom was found at a position which had a $1S$ density which brought that atom into resonance with the laser. The rate of detection of such photons is proportional to the probability of finding a condensate atom in a region

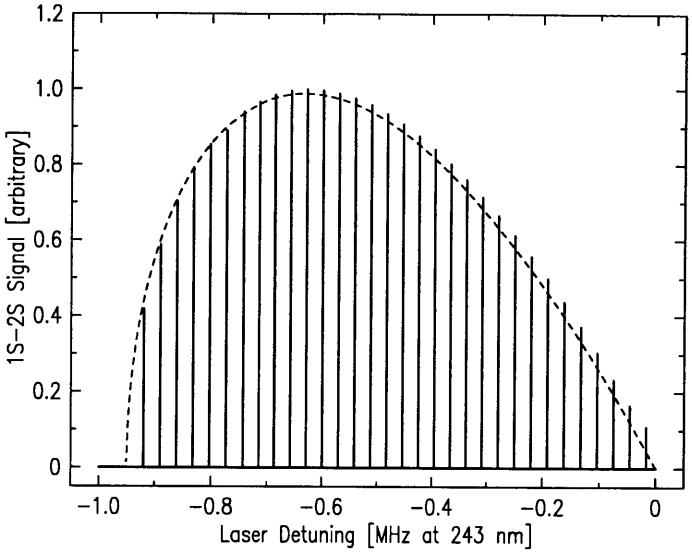

Figure 6-5: Theoretical Doppler-free spectrum of a condensate at $T = 0$ in a three-dimensional harmonic trap. The dashed curve (Eq. 6.32) follows from the integral over the BEC density distribution, Eq. 6.31, using the Thomas-Fermi density distribution for a peak condensate density of 5×10^{15} cm^{-3}, assuming $a_{1S-1S} = 0.0648$ nm and $a_{1S-2S} = -2.9$ nm. The stick spectrum results from the sum over the transition amplitudes expressed in Eq. 6.29 for the same conditions. In the overlap integrals, wave functions for an infinite harmonic trap were used for the $2S$ motional states. These deviate from the actual motional states near the top of the BEC interaction well, so the deviation between the dashed curve and the quantum mechanical stick spectrum nearer zero detuning is not surprising.

with the correct density.

For a Thomas-Fermi distribution (Sec. 6.2.1) in a three dimensional harmonic trap, Eq. 6.31 reduces to

$$S(2h\nu) = \frac{15\pi\hbar\Omega_0^2(0)N\ (E_{1S-2S} - 2h\nu)}{8\left[\frac{4\pi\hbar^2(a_{1S-2S}-a_{1S-1S})\ n_{BEC}^N(0)}{m}\right]^2}\left[1 - \frac{2h\nu - E_{1S-2S}}{\frac{4\pi\hbar^2(a_{1S-2S}-a_{1S-1S})\ n_{BEC}^N(0)}{m}}\right]^{1/2} \tag{6.32}$$

for $4\pi\hbar^2(a_{1S-2S} - a_{1S-1S})\ n_{BEC}^N(0)/m < 2h\nu - E_{1S-2S} < 0$, and otherwise $S(\nu) = 0$. The number of atoms in the condensate, N, is related to $n_{BEC}^N(0)$ through Eq. 6.21. Note that this result is independent of the oscillation frequencies and is valid for spherically symmetric, as well as asymmetric traps.

Theory and experimental data are compared in Fig. 6-6. The statistical error bars

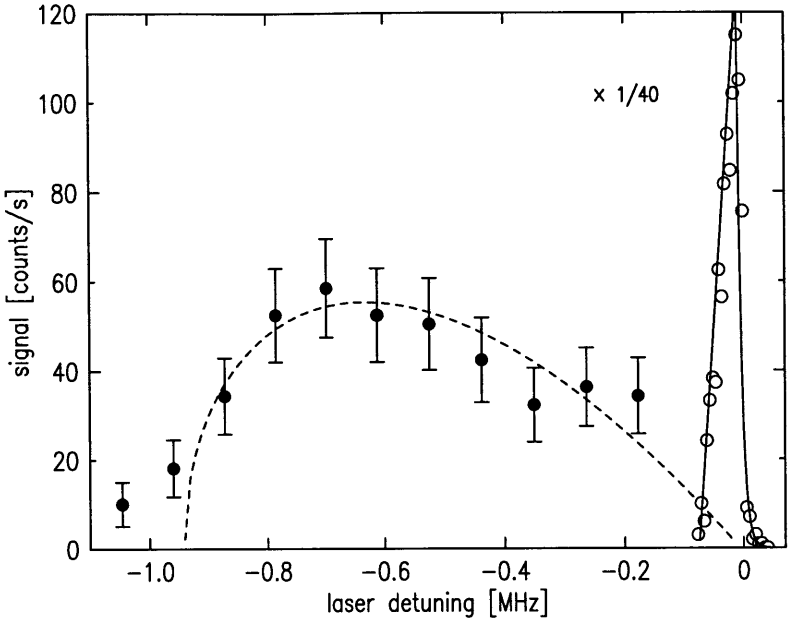

Figure 6-6: Doppler-free spectrum of a condensate: comparison of theory and experiment. The narrow feature near zero detuning is the spectral contribution from the noncondensed atoms. The broad feature is the spectrum of the condensate. The dashed curve is the semiclassical expression for the spectrum using the Thomas-Fermi density distribution for a harmonic trap (Eq. 6.32), a peak condensate density of 1×10^{16} cm^{-3} and the measured value of $a_{1S-2S} = -1.4$ nm. The spectrum is discussed in more detail in Chap. 7.

for the data are large due to the small number of counted photons, but the theoretical BEC spectrum for a condensate at $T = 0$ describes the shape of the data reasonably well. We have used the value for a_{1S-2S} found in Sec. 5.2.1 from the spectrum of a noncondensed gas, and a peak condensate density of $1.0 \pm 0.2 \times 10^{16}$ cm^{-3}.

It is worth noting that the description of the BEC spectrum given by Eq. 6.29 is quite general. If the $1S$-$2S$ interaction were repulsive, this would simply modify the effective $2S$ Hamiltonian, Eq. 6.27, and the form of the motional states excited by the laser would change. Raman spectroscopy has recently been used to excite atoms out of alkali metal condensates [107, 108]. In the regime where mean field effects dominate, the formalism presented here should explain the excitation spectrum for this process as well.

6.3 Cold Collision Frequency Shift for an Arbitrary System

In an arbitrary geometry, the density distribution and the excitation may be inhomogeneous. This implies that at a given laser frequency, the probability that an atom is excited may depend on its motional state (See, for example, Sec. 4.3.2.). Also, if the laser is not spatially homogeneous, the motional state of an atom can change as it is excited to the $2S$ state, as discussed in Sec. 4.4.5 in the context of coherence sidebands on the spectrum. This complicates the derivation of an expression for the shift which would be analogous to Eq. 6.14.

6.3.1 Sum Rule for the Mean Frequency Shift in the Spectrum

L. Levitov[109] has recently derived a sum rule which relates the mean frequency shift, weighted by the spectrum intensity, to an average mean field shift in the sample, weighted by the local density and excitation rate (Fig. 6-7). This is

$$\frac{\int d\nu\ (2h\nu - E_{1S-2S})S(\nu)}{\int d\nu\ S(\nu)} = \frac{4\pi\hbar^2(a_{1S-2S} - a_{1S-1S})}{m} \frac{\int d^3r\ I^2(\mathbf{r})[n(\mathbf{r})]^2 G(\mathbf{r},0)}{\int d^3r\ I^2(\mathbf{r})n(\mathbf{r})}. \quad (6.33)$$

Here, $S(\nu)$ is the signal at laser frequency ν, $I(\mathbf{r})$ is the laser intensity profile, and $G(\mathbf{r},0)$ is the normalized density-density correlation function for zero separation at position $\mathbf{r}$ in the inhomogeneous sample[100],

$$G(\mathbf{r},0) = \sum_{i\neq j}^{N} \langle \Psi^{N;0}|\delta(\tilde{\mathbf{r}}_i - \mathbf{r})\delta(\tilde{\mathbf{r}}_j - \mathbf{r})|\Psi^{N;0}\rangle / [n(\mathbf{r})]^2. \quad (6.34)$$

For a noncondensed system in thermal equilibrium $G(\mathbf{r},0) = 2$ and for a Bose-condensed system at $T = 0$, $G(\mathbf{r},0) = 1$. $G(\mathbf{r},0)$ is well defined for any arbitrary thermodynamic state, even one which is not in thermal equilibrium, and in principle $G(\mathbf{r},0)$ can vary with $\mathbf{r}$.

For a homogeneous system, $G(\mathbf{r},0) = g^{(2)}(0)$ and Eq. 6.33 reduces to Eq. 6.14. The

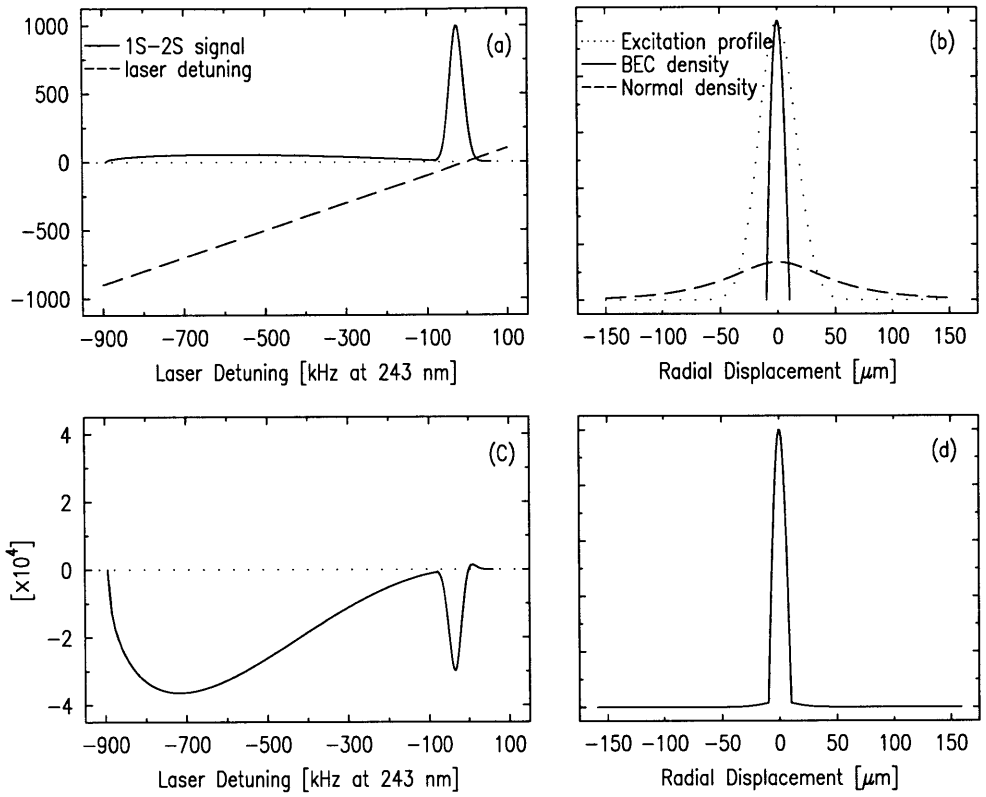

Figure 6-7: Graphical depiction of the sum rule. Plot (a) represents a typical Doppler-free spectrum of a Bose condensate and the noncondensed atoms. (See Fig. 6-6 and Chap. 7 for more discussion of the spectrum.) The mean frequency in the spectrum, weighted by the spectral intensity, is proportional to an integral over all space of the product of the square of the total density and the excitation probability (Eq. 6.33). These factors are shown in plot (b). Plots (c) and (d) display the appropriate products which form the integrands for the numerators on each side of the sum rule equation (Eq. 6.33), showing that the condensate dominates the expression.

sum rule agrees with the result that for the same density, the shift in a noncondensed gas is twice the shift in a pure condensate.

Derivation of the Sum Rule

Equation 6.33 is a powerful relation for analyzing the spectrum, but what is the physics it contains? We can derive this relationship in the context of an explicit calculation of the spectrum for an arbitrary system, and this will give us some insight.

To calculate the spectrum, we consider the cold collision frequency shift and motional effects. By implicitly allowing the motional states of atoms to change during

the excitation, we include effects such as time-of-flight broadening or coherence sidebands. We neglect the AC Stark shift, laser linewidth, and all relaxation processes such as photoionization and radiative decay of the $2S$ state. For the collisional interaction, we use the Hamiltonian, H', given in Eq. 6.8. We know that the frequency shift is dominated by the $1S$-$2S$ interaction, so to a good approximation, we can set $a_{1S-1S} = 0$. This will greatly simplify the analysis. For the state of the system before excitation, we take a general state with N $1S$ atoms, denoted by $|\Psi^{N;0}\rangle$. This state could describe bosons, fermions, or even classical particles [110], in any thermodynamic state.

We saw in Sec. 6.1 that for weak excitation the transition frequency shift is independent of the number of $2S$ atoms, so, for simplicity, for the state after laser excitation we consider only configurations of the system with 1 $2S$ atom and $N-1$ $1S$ atoms. Note that these configurations form a manifold of states of the system. In each configuration, the $2S$ excitation is associated with different single-particle motional states. In the absence of H', this manifold is degenerate, and the energy is about equal to E_{1S-2S} (neglecting kinetic energy). The interaction breaks this degeneracy, and one can then think of the laser exciting the system to one or a distribution of the eigenstates of H', as shown in Fig. 6-8. We denote the eigenstates as $|v_i\rangle$, and $H'|v_i\rangle = E'_i|v_i\rangle$.

The states and energies are not determined until we specify the trap geometry, but we can write the expression for the spectrum,

$$S(2h\nu) = \sum_i \frac{2\pi}{\hbar} |\langle v_i|H_{las}|\Psi^{N;0}\rangle|^2 \delta(2h\nu - E_{1S-2S} - E'_i). \tag{6.35}$$

The overlap matrix element is calculated with the atom-laser Hamiltonian, which can be written (Eq. 4.8)

$$H_{las} = \sum_{j=1}^{N} \frac{\hbar\Omega_0(\tilde{\mathbf{r}}_j)}{2} (|2S\rangle\langle 1S|)_j. \tag{6.36}$$

We can show that Eq. 6.35 implies the sum rule, Eq. 6.33. We start with

$$2h \int d\nu \; (2h\nu - E_{1S-2S}) S(2h\nu) =$$

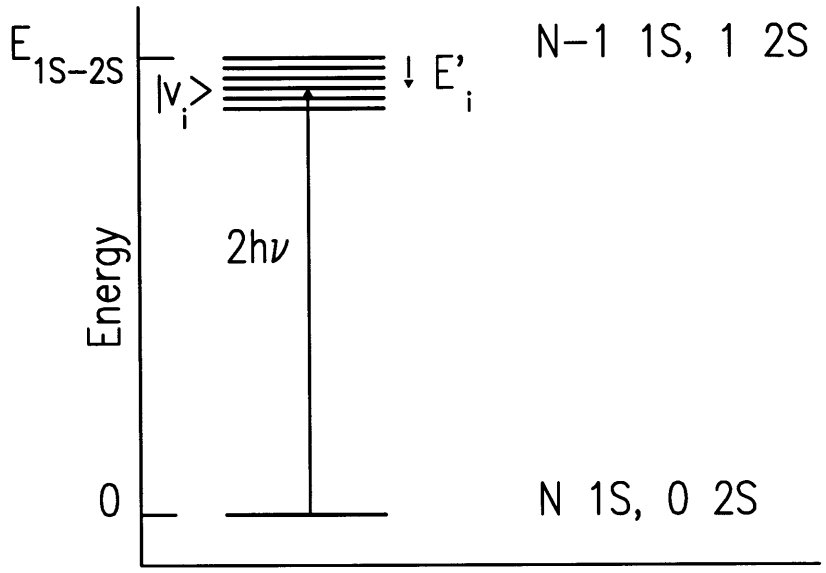

Figure 6-8: Excitation of the system to excited state $|v_i\rangle$. The states with energy around E_{1S-2S} are the eigenstates of H' with 1 $2S$ atom. The distribution of states which can be excited by the laser leads to inhomogeneous broadening of the $1S$-$2S$ spectrum.

$$
\begin{aligned}
&= 2h \int d\nu \; (2h\nu - E_{1S-2S}) \sum_i \frac{2\pi}{\hbar} |\langle v_i | H_{las} | \Psi^{N;0} \rangle|^2 \delta(2h\nu - E_{1S-2S} - E_i') \\
&= \sum_i \frac{2\pi}{\hbar} E_i' \langle \Psi^{N;0} | H_{las}^\dagger | v_i \rangle \langle v_i | H_{las} | \Psi^{N;0} \rangle \\
&= \sum_i \frac{2\pi}{\hbar} \langle \Psi^{N;0} | H_{las}^\dagger H' | v_i \rangle \langle v_i | H_{las} | \Psi^{N;0} \rangle .
\end{aligned}
$$

The eigenstates $|v_i\rangle$ are a complete orthonormal basis for the Hilbert space connected to $|\Psi^{N;0}\rangle$ by H_{las}, so the expression further simplifies to

$$
\begin{aligned}
&\frac{2\pi}{\hbar} \langle \Psi^{N;0} | H_{las}^\dagger H' H_{las} | \Psi^{N;0} \rangle \\
&= \frac{4\pi\hbar^2 a_{1S-2S}}{m} \int d^3r \; \frac{\pi\hbar\Omega_0^2(\mathbf{r})}{2} [n(\mathbf{r})]^2 G(\mathbf{r}, 0). \qquad (6.37)
\end{aligned}
$$

In the last line we have inserted the form of H_{las} and H' and identified the correlation function $G(\mathbf{r}, 0)$. The details of this calculation are given in Sec. D.5.

Using the same techniques, one can show (Sec. D.5)

$$2h \int d\nu \; S(2h\nu) \;\; =$$

$$
\begin{aligned}
&= 2h \int d\nu \sum_i \frac{2\pi}{\hbar} |\langle v_i | H_{las} | \Psi^{N;0} \rangle|^2 \delta(2h\nu - E_{1S-2S} - E_i') \\
&= \sum_i \frac{2\pi}{\hbar} \langle \Psi^{N;0} | H_{las}^\dagger | v_i \rangle \langle v_i | H_{las} | \Psi^{N;0} \rangle \\
&= \frac{2\pi}{\hbar} \langle \Psi^{N;0} | H_{las}^\dagger H_{las} | \Psi^{N;0} \rangle = \int d^3r \, \frac{\pi\hbar\Omega_0^2(\mathbf{r})}{2} n(\mathbf{r}). \qquad (6.38)
\end{aligned}
$$

Taking the ratio of Eq. 6.37 and 6.38 and recalling that $\Omega_0(\mathbf{R}) \propto I(\mathbf{R})$ (Eq. 4.17) proves Eq. 6.33 within the approximation that $a_{1S-1S} = 0$. It is straightforward to include $a_{1S-1S} \neq 0$ in the proof.

Discussion of the Sum Rule

The calculation in the previous section shows that Eq. 6.33 is reminiscent of other sum rules in atomic physics, such as the Thomas-Reiche-Kuhn sum rule for the oscillator strengths in electronic transitions in an atom [111, 112]. The physics in Eq. 6.33 is that if the degeneracy in a manifold of states is lifted by a two-body interaction like H', then there is a relation between the mean frequency in the spectrum for excitation into that manifold and a weighted spatial average of a local expression for the interaction. In this case, we identify the local expression as $\Delta E_{coll}(\mathbf{r}) = (4\pi\hbar^2 a_{1S-2S}/m) G(\mathbf{r}, 0) n(\mathbf{r})$, and the weighted average is

$$
\frac{\int d^3r \Omega_0^2(\mathbf{r}) n(\mathbf{r}) \Delta E_{coll}(\mathbf{r})}{\int d^3r \Omega_0^2(\mathbf{r}) n(\mathbf{r})}. \qquad (6.39)
$$

It is important to note that the sum rule says nothing about the shape of the excitation spectrum. In principle, the recipe implied in the expression for the spectrum given in Eq. 6.35 can be used to calculate the lineshape, but diagonalizing the interaction Hamiltonian and finding the overlap integrals for a realistic system is a daunting task. For a homogeneous system this can be done, which is essentially the calculation in Sec. 6.1. In an inhomogeneous system, however, the motional state of a particle can change when it is excited to the $2S$ state, and the number of configurations which must be included in the interaction Hamiltonian becomes too large to handle for even a few hundred particles.

Accuracy of the Semiclassical Calculation Used to Model Spectra and Experimentally Calibrate the Cold Collision Frequency Shift

The sum rule implies that the cold collision frequency shift probes the quantum nature of the system. This is evident from the appearance of G(**r**,0). For a system in thermal equilibrium with a given density profile and excitation profile, the mean frequency shift in the spectrum for classical particles (G(**r**,0))=1) is one half of the mean shift for noncondensed bosons (G(**r**,0))=2)[4].

This calls into question the validity of the semiclassical calculation of the lineshape (Sec. 4.4) which is used in Chap. 5 to analyze the data for the cold collision frequency shift. For that calculation, a local shift of the level spacing,

$$\Delta E_{coll}(\mathbf{r}) = (8\pi\hbar^2/m)\,(a_{1S-2S} - a_{1S-1S})\,n(\mathbf{r}), \tag{6.40}$$

is included in the Hamiltonian which is used to numerically calculate the contribution to the Doppler-free $1S$-$2S$ spectrum for an atom which moves in the trap. Particles are treated classically in this calculation. It is not possible to include the effects of bosonic symmetry which are essential for making (G(**r**,0))=2) and producing the exchange contribution to the cold collision frequency shift (See Sec. 6.1.3).

It seems that setting $\Delta E_{coll}(\mathbf{r}) = (4\pi\hbar^2/m)(a_{1S-2S} - a_{1S-1S})n(\mathbf{r})$ and using the semiclassical numerical calculation of the lineshape accurately calculates the spectrum for a classical gas. The mean frequency shift will then be one half of the mean frequency shift observed for a Bose gas with the same density distribution and excitation geometry. In Chap. 5, we calculated the spectrum semiclassically, but used $\Delta E_{coll}(\mathbf{r}) = (8\pi\hbar^2/m)(a_{1S-2S} - a_{1S-1S})n(\mathbf{r})$, so the mean of the calculated spectrum should equal the mean of the spectrum for the experimentally observed Bose system.

The calibration of the cold collision frequency shift, and the extracted value of a_{1S-2S} given in Chap. 5, utilizes the semiclassical spectrum calculation to account for the inhomogeneous density distribution. It would seem to be better to use the sum

[4]Far from quantum degeneracy, the difference between the Bose distribution and Boltzmann distribution is negligible.

rule to analyze the data and calibrate the shift, but, since the calibration is most sensitive to the mean shift in the spectrum, the above arguments imply that both approaches should give the same answer.

For a given density and laser profile, it is found that the mean frequency shift in the calculated spectrum is systematically ~5% larger than the value found from the right hand side of the sum rule, Eq. 6.33. Allowing for the approximations used in the numerical calculation (Sec. B.2), this agreement is satisfactory and seems to confirm that the numerical calculation adequately reproduces the mean frequency shift in the spectrum. The 5% difference is small compared to other uncertainties in the calibration of the shift, and thus it is not worthwhile to reanalyze the data for the shift using the sum rule.

Potential Applications of the Sum Rule

If spectra are recorded carefully so that the entire lineshape is scanned and the background count rate can be taken into account, it is straightforward to determine the mean shift in the experimental spectrum. The sum rule can then be used to extract quantitative information from the data even when the lineshape is not well understood (see, for example, Sec. 7.5).

One must still know the laser and trap geometry to evaluate the required integrals for the sum rule, but these calculations require little computational time compared to the semiclassical calculation of the lineshape which has been used (Sec. 4.4). In the future, the sum rule should be a useful analytic tool.

6.4 Conclusion

Presently, there is no accurate and computationally executable model for the *shape* of the spectrum for a noncondensed Bose gas at very high density. There is no reason to expect that the semiclassical calculation of the spectrum, with twice the classical frequency shift, accurately reproduces the lineshape. For an accurate simulation, one might need to perform a fully quantum mechanical calculation (Eq. 6.35). In the

regime where the lineshape is not dominated by the cold collision frequency shift, good agreement is found between the data and the semiclassical calculation (Fig. 5-1), but simulations for spectra recorded at higher density have not been successful (Fig. 5-4). Uncertainties in the trap and laser geometry make a detailed study of the lineshape difficult at this time, but if these uncertainties can be reduced (Chap. 8), such a study could prove interesting in the future.

Improved accuracy in the theoretical calculation of a_{1S-2S} and the experimental measurement of the proportionality between the density and frequency shift could give more insight into the shape of the spectrum for the noncondensed gas. Further theoretical investigation of the cold collision frequency shift would also be beneficial.

There are of course other questions regarding the mean field treatment of the frequency shift. Hydrogen atoms can receive a small momentum kick when excited Doppler-free due to the spatial profile of the laser beam (Sec. 4-8). A recent calculation [109] indicates that this will add a small additional shift and a broadening to the spectrum. Also, we have ignored collisional diffusion of the excited $2S$ atoms. This is a reasonable first attempt, however, at a mean field theory of the effects of collisions on the Doppler-free $1S$-$2S$ spectrum of trapped hydrogen.

Chapter 7

Spectroscopic Studies of a Quantum Degenerate Hydrogen Gas

An exciting new application of $1S$-$2S$ spectroscopy is in the study of Bose-Einstein condensation. A general discussion of BEC in hydrogen is found in D. Fried's PhD thesis [23]. Here, we emphasize the utility of $1S - 2S$ spectroscopy for studying the condensate and point out some of the new physics probed with the two-photon transition.

The appearance of two new features on the $1S$-$2S$ spectrum provides the clearest indication that the BEC phase transition has been crossed. Figure 7-1 shows these features, which, for the particular loading conditions and evaporative cooling path used, appear when the sample is cooled below about 70 μK. These new features arise from excitation of condensate atoms.

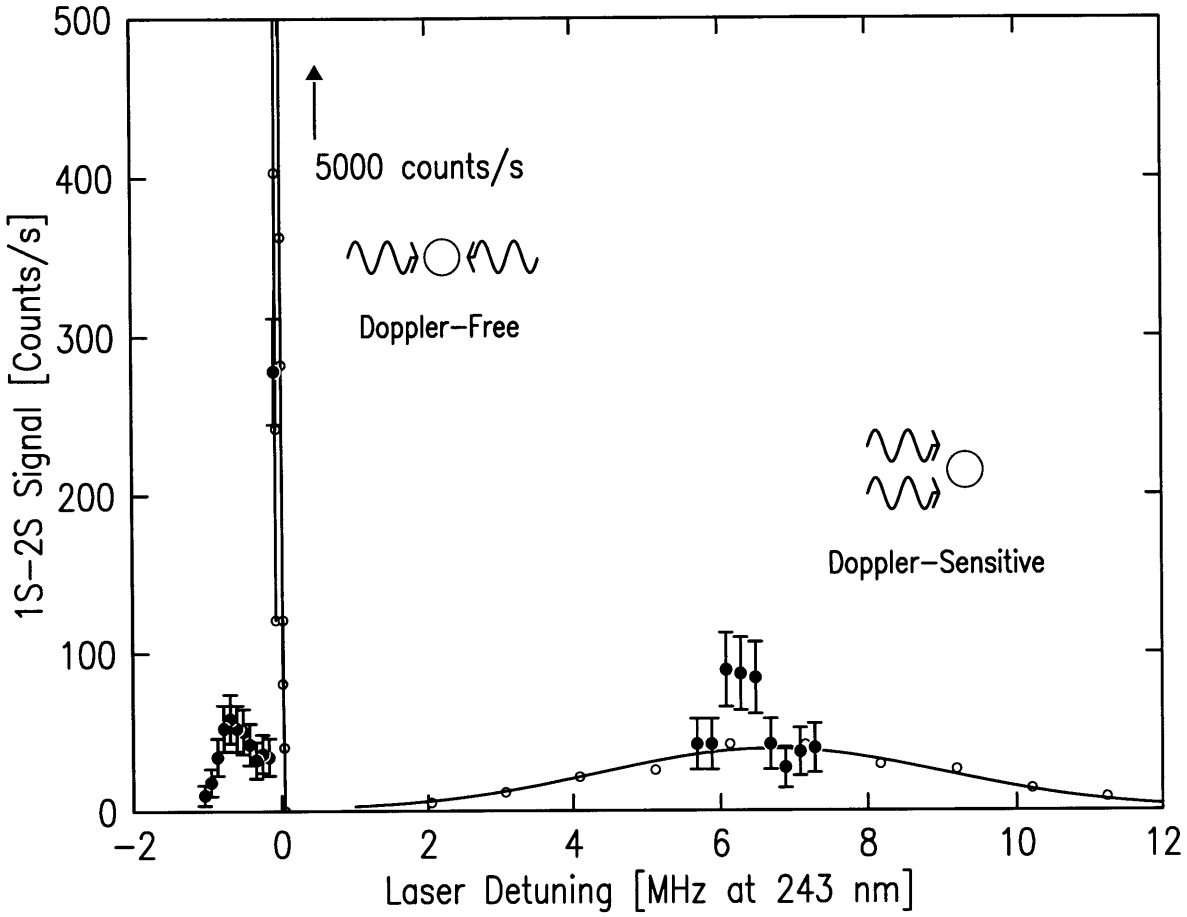

Figure 7-1: Composite $1S$-$2S$ two-photon spectrum of trapped hydrogen. ○–spectrum of sample without a condensate; •–additional features due to presence of a condensate. The intense, narrow peak arises from Doppler-free absorption of counter-propagating photons by the normal gas. The Doppler-free contribution from the Bose-Einstein condensate is shifted to the red and broadened due to atom-atom interactions in the high density region. The wide, low feature on the right is from Doppler-sensitive absorption of co-propagating photons. The fact that the condensate contribution near the center of the Doppler-sensitive line is narrower than the broad signal from the normal gas confirms the condensation in momentum space expected with BEC, although like the Doppler-free BEC signal, the Doppler-sensitive contribution is shifted and broadened due to interactions.

7.1 Spectroscopic Signature of Bose-Einstein Condensation

Turning first to the broad Doppler-sensitive peak, recall (Sec. 4.2) that this feature is shifted 6.7 MHz from the unperturbed $1S$-$2S$ frequency by momentum recoil, and

the lineshape maps the axial momentum distribution. The condensate feature near the center of the line is narrower than the contribution from the normal fraction, showing the condensation in momentum space. In the absence of interactions, the width of this feature would be determined by the axial momentum distribution in the condensate, which is approximately given by the position-momentum uncertainty relation, $\Delta p_z \approx \hbar/\Delta z$, where Δz is the axial extent of the condensate. This would correspond to a spectral width of less than a kHz. However, because of the cold collision frequency shift, the BEC feature has a width of about 1 MHz and is shifted from line center.

The Doppler-free contribution to the spectrum can be seen in Fig. 7-1 near $\nu = 0$. The shoulder at large red-shift results from excitation of condensate atoms. It is red-shifted from the intense narrow Doppler-free spectrum of the normal fraction by the cold collision frequency shift, and is evidence of the high density which results from condensation in position space, as expected in a trapped gas.

7.2 Doppler-Free Spectrum of the Condensate

Figure 6-6 shows the Doppler-free spectrum of the largest observed condensate. Section 6.2 discusses in detail how the spectral lineshape can be related to the distribution of densities in the condensate. Because the cold collision frequency shift dominates lineshape, the spectrum essentially is a histogram of density in the condensate. Using the value of a_{1S-2S} found from spectroscopy of the normal gas (Sec. 5.2.1), and describing the condensate with the equilibrium system at $T = 0$ for which $2h\Delta\nu_B \approx 4\pi\hbar^2(a_{1S-2S} - a_{1S-1S})n_{1S}/m$ (Sec. 6.2), the peak shift in the spectrum implies that the peak condensate density is $n_{peak}^{BEC} = 1.0 \pm 0.2 \times 10^{16}$ cm^{-3}.

One should consider the possibility of extra broadening or shift of the resonance in the BEC spectrum because the cold collision frequency shift was calibrated at densities two orders of magnitude lower than those encountered in the condensate. Nonlinear effects due to collisions between three or more particles should still be negligible even for excitation of condensate atoms, because the parameter governing the importance

of higher order collisions, $a_{1S-2S}n_{1S}^{1/3}$, is always small. ($a_{1S-2S}n_{1S}^{1/3} = 0.03$ for $n_{1S} = 10^{16}$ cm^{-3}.) One cannot rule out the existence of other higher order effects which are not governed by this perturbation parameter, but as will be discussed below, there is no sign of such an effect.

7.3 Condensate Fraction

7.3.1 Theoretical Limit of the Condensate Fraction in Hydrogen

For N particles in an infinite harmonic trap [113, 114], the critical temperature for Bose condensation is $T_c = \hbar\bar{\omega}[N/1.202]^{1/3}$, where $\bar{\omega}$ is the geometric mean of the trap frequencies. At a temperature $T \leq T_c$, the fraction of atoms in the condensate, neglecting interactions, is

$$f = N_B/(N_N + N_B) = 1 - (T/T_c)^3, \tag{7.1}$$

where the subscripts B and N refer to BEC and normal, respectively. For Rb and Na atoms, it is possible to evaporatively cool to $T \ll T_c$ and achieve condensate fractions as high as 75%[106] in a purely magnetic trap. Hydrogen behaves differently, however.

The group of Walraven *et al.*[115] calculated the dynamics of trapped hydrogen at $T \leq T_c$ under conditions essentially identical to those in the experiments discussed here. For an evaporatively cooled system in thermal equilibrium which crosses T_c at a density of $\sim 10^{14}$ cm^{-3}, they concluded that the maximum condensate fraction should not exceed a few percent.

Below T_c, the high density in the condensate, even for a low condensate fraction, produces a very high dipolar loss rate from the condensate. The condensate is fed through collisions in the normal gas, which are infrequent because of the small hydrogen scattering length. This implies a limit for the condensate fraction at which condensate atoms are lost as fast as they can be replenished. One could say that trying to evaporate from $T = T_c$ to $T \ll T_c$ is thwarted in hydrogen because the time

scale for the evaporation, set by the low elastic collision rate, is longer than the time scale for the destruction of the condensate due to dipolar decay. Essentially, T_c drops as fast as T drops, so T is always close to T_c. In Rb[116] and Na[117], the collision cross section is more than 1000 times the hydrogen cross section, and the evaporation time from $T = T_c$ to $T \ll T_c$ is much shorter than the decay time of the condensate.

It is also instructive to consider the balance between heating and evaporative cooling in the sample, which determines the temperature. For the hydrogen experiment, this has been investigated by D. Fried [23]. In an elastic collision between two normal atoms which results in one atom entering the condensate, the condensate atom carries no kinetic energy, while the normal atom takes away all the energy initially in the collision. Thus a net flux of atoms from the normal gas into the condensate, for instance when the condensate is forming and growing or holding constant in size against the ever present dipolar decay, increases the average energy per atom in the normal gas. This imposes a large heat load on the normal gas which must be balanced by evaporative cooling. The finite evaporative cooling power limits the attainable temperature for a given number of trapped atoms, and thus limits the condensate faction.

In the hydrogen experiment, the condensate fraction can be determined in two independent ways. We will discuss each method separately.

7.3.2 Spectroscopic Determination of the Condensate Fraction

One can determine the condensate fraction by comparing the areas under the normal and BEC contributions to the Doppler-free spectrum. It is experimentally difficult to record both features simultaneously, but the trapping and cooling is reproducible enough on short time scales to compare spectra of identically prepared samples.

To account for different experimental conditions, one must consider that the signal, $S_x(\nu_i)$, is recorded at discrete frequency points, ν_i, with spacing $\Delta\nu_x$, where x is either B or N. The excitation time per point is τ_x. The geometric overlap of the laser and the atoms is accounted for by a parameter β_x. If the laser beam is well aligned, the

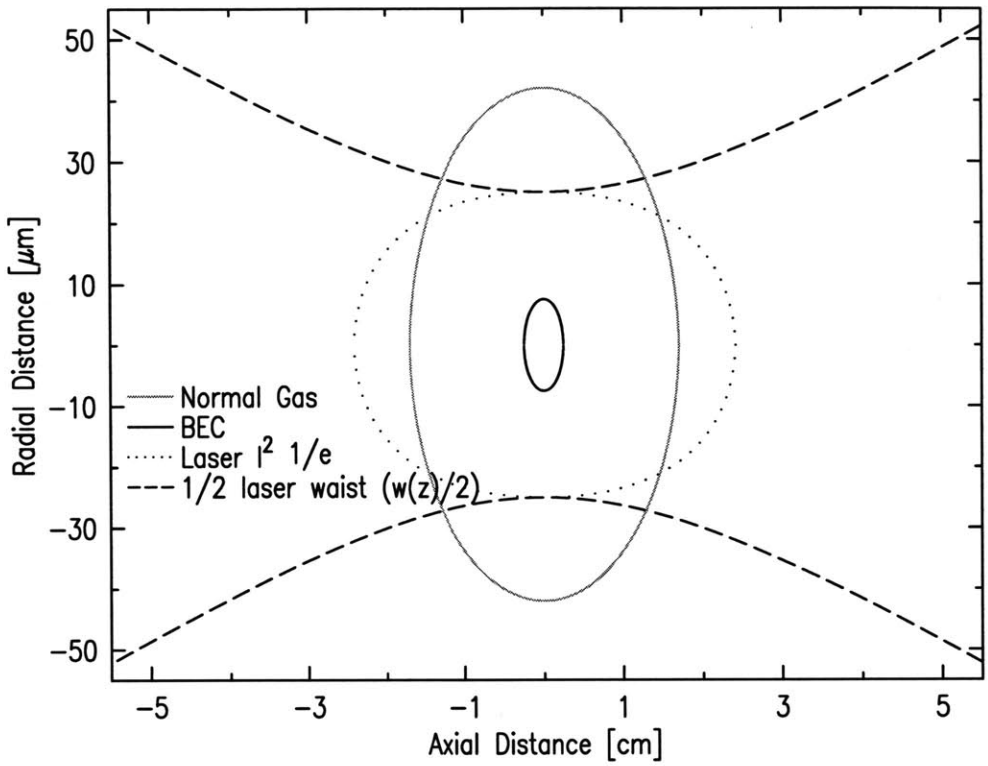

Figure 7-2: Typical laser and sample geometry at the BEC transition. The magnetic trap is described in Sec. 5.1.1, and the sample temperature is 45 μK. The contour is plotted where the density of the normal gas is 1/e of its peak value. The extent of the Thomas-Fermi density distribution for a condensate with 10^9 atoms is shown. The excitation rate goes as the laser intensity squared, $I^2(\mathbf{r}) = [2P/\pi w^2(z)]^2 \exp[-4r^2/w^2(z)]$, where P is the laser power, $w(z) = w_0\sqrt{1+(z/z_0)^2}$ is the characteristic radius of the laser beam, and $z_0 = \pi w_0^2/\lambda$ is the divergence length or Rayleigh length. The contour where I^2 is $1/e$ of its peak value is plotted, along with $w(z)/2$. Note the different scales for each axis. The sample's axial length is about 400 times its diameter.

condensate is entirely within the laser focus and $\beta_B \approx 1$, but the laser focus is smaller than the thermal cloud (Fig. 7-2). Through numerical calculation (Sec. D.5), β_N can be found. It is defined as the ratio of the integral of the signal using the actual experimental geometry to the integral of the signal with an infinite laser radius. It can be interpreted as the effective fraction of noncondensed atoms which are illuminated by the laser.

Assuming that in the laser the excitation probability is the same on resonance for a condensate and normal atom, the number of atoms in component x is proportional to the normalized integral of the contribution of component x to the spectrum,

$\sum_i S_x(\nu_i)\Delta\nu_x/(\beta_x\tau_x)$. The condensate fraction is given by

$$f = \frac{\sum_i S_B(\nu_i)\Delta\nu_B/(\beta_B\tau_B)}{\sum_i S_B(\nu_i)\Delta\nu_B/(\beta_B\tau_B) + \sum_i S_N(\nu_i)\Delta\nu_N/(\beta_N\tau_N)}. \tag{7.2}$$

We calculate f for the data shown in Fig. 7-3 and the results are given in Fig. 7-4. The time evolution of the observed condensate and normal gas will not be identical in this data set because there is significant loss due to laser excitation when on resonance with the normal gas (Sec. 4.3.2). Thus only the calculated condensate fraction immediately after the end of the forced evaportion will be reliable.

Corrections for Laser and Sample Geometry, and Uncertainties in the Measurement

The value of β_N is sensitive to the laser beam and sample geometry. The time-of-flight linewidth observed for low density spectra implies that the effective laser beam waist was ~ 45 μm when this data was recorded (See Sec. 4.3.2.) This is close to the beam waist for which the optical layout was designed, adding confidence that the laser geometry is well understood. The axial overlap of the laser and atoms is still in question, however, the signals from the condensate and normal gas are both sensitive to this in similar fashion, reducing the sensitivity of the fraction measurement to this factor.

Because the thermal cloud is larger than the laser beam radius, β_N is also sensitive to temperature. The most reliable measure of temperature in this regime is the Doppler-sensitive spectrum. When the condensate is present, Bose statisics must be taken into account to understand the shape of the Doppler-sensitive line [23], and the data indicates that the average sample temperature is approximately 60 μK while the condensate exists, but there are large error bars for this measurement and it is unclear if the sample temperature is changing while the condensate is present. Presently, the time required to make this measurement is too long to use it to monitor the changing temperature while the condensate exists. The temperature diagnostics must be improved in order to measure condensate parameters accurately (Chap. 8),

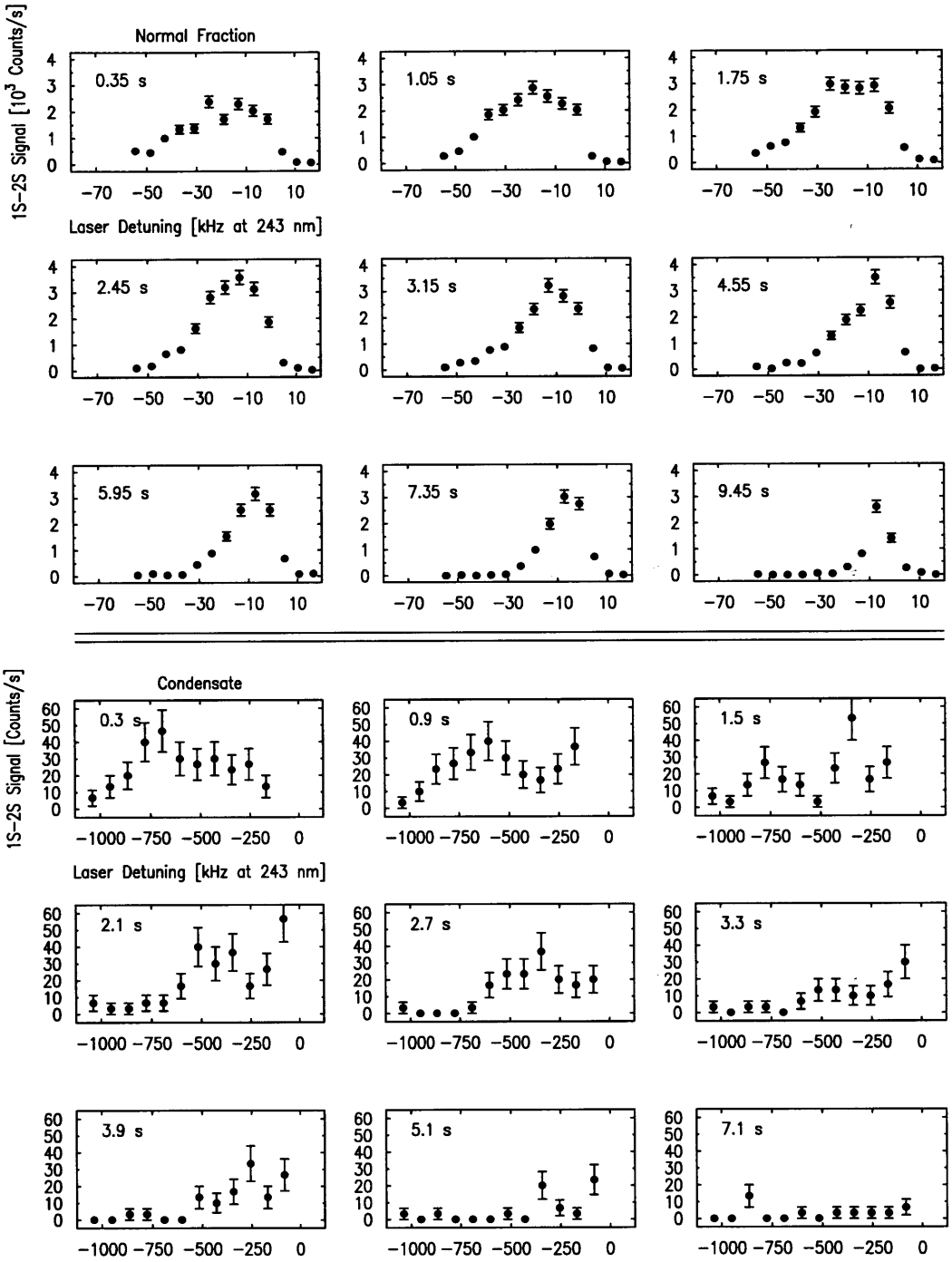

Figure 7-3: Doppler-free spectra of normal gas (each data point represents 50 ms of excitation) and condensate (each data point represents 300 ms of excitation). Samples are identically prepared and the trap depth at the end of the forced evaporation is 280 μK. The time quoted is the time of the midpoint of the scan, measued from the end of the forced evaporation. The laser power in the trapping region is about 5 mW. The effective beam waist is 45 μm, and is determined from the time-of-flight linewidths of the later, low density spectra of the normal gas.

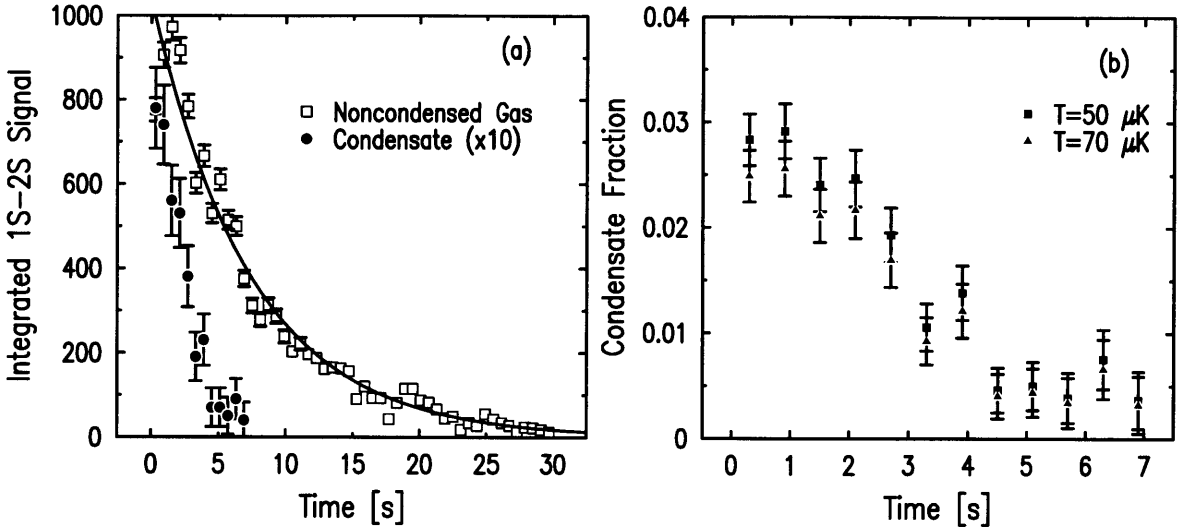

Figure 7-4: Spectroscopic determination of the condensate fraction. (a) Total counts in one scan for the data shown in Fig. 7-3. The quoted time for each sweep is the mean time after the end of the forced evaporation. Error bars are statistical, but additional uncertainties due to variations in laser power and alignment are indicated by the spread in the data from smooth curves. As discussed in the text, only the initial condensate and normal gas spectra can be compared directly because the loss rate due to excitation is significant when on resonance with the normal gas. (b) Condensate fraction determined as described in the text. To calculate the fraction, one must know the sample temperature. The temperature is expected to be about 60 μK. The error bars represent statistical uncertainty only. Only the $t = 0$ measurement is reliable. If data could be taken in such a way that the time evolution of the sample is identical when recording both the condensate and normal gas spectra, than the time evolution of the condensate fraction could be measured in this way.

and the time dependence of the sample temperature in the presence of the condensate is not yet well understood.

Assuming thermal equilibrium of the normal gas and using a nontruncated bose particle distribution, $\beta_N = 1/8$ for $T = 50$ μK and $\beta_N = 1/12$ for $T = 70$ μK. Using the actual truncated distribution in which no atoms with energy above the trap threshold are present [23], the factors are $\beta_N \approx 1/7$ for $T = 50$ μK and $\beta_N \approx 1/8$ for $T = 70$ μK. Using the latter values, the condensate fraction immediately after the end of the forced evaporation, calculated from the ratio of the spectral areas, is $f \approx 3^{+3}_{-2}\%$, where the errors are chiefly due to uncertainties in the experimental geometry and sample temperature. The larger positive error reflects the difficulty in ensuring that the laser is perfectly aligned over the condensate. Experimentally, it

is seen that slight misalignment can decrease the condensate signal by as much as 50%. The number of atoms in the condensate implied by this measurement is very sensitive to the temperature of the sample, but a conservative estimate is greater than 10^9 atoms.

7.3.3 Determination of the Condensate Fraction from the Peak Shift in the Doppler-Free Spectrum

If the condensate is well modelled by an equilibrium system at $T = 0$, then the density distribution is given by the square of the Thomas-Fermi condensate wave function (See Sec. 6.2.1), and the number of atoms in the condensate is given by

$$N = \frac{2^{9/2}\pi\tilde{U}^{3/2}(n_{peak}^{BEC})^{5/2},}{15m^{3/2}w_r^2 w_z} \tag{7.3}$$

where $\tilde{U} = 4\pi\hbar^2 a_{1S-1S}/m$. Using calculated and measured trap parameters, a peak condensate density of $n_{peak}^{BEC} = 1.0 \pm 0.2 \times 10^{16}$ cm^{-3} corresponds to $6 \pm 3 \times 10^9$ condensate atoms, where the uncertainty reflects only uncertainty in n_{peak}^{BEC}, not in the trap parameters.

If the system is in thermal equilibrium, the number of atoms in the normal phase, N_N, is determined if the temperature and trap are known and $T \leq T_c$. N_N varies approximately as T^{-3} [23], and as discussed above, the temperature is difficult to determine. Assuming thermal equilibrium of the entire sample at a temperature of about 60 μK, this condensate density corresponds to about a 9% condensate fraction [23] with error bars of at least a factor of 2 arising from uncertainty in temperature and n_{peak}^{BEC}.

7.3.4 Implications of the Measurement of the Condensate Fraction

The spectroscopic determination of the condensate fraction is independent of how one models the condensate. Thus the reasonable agreement between the two methods is

a check that the equilibrium $T = 0$ model describes the BEC wavefunction well. This should only be viewed as a preliminary result, however, because there are such large uncertainties for these measurements. The dominant errors in the parameters which determine the condensate fraction, either from the ratio of spectral areas or the peak shift of the condensate spectrum, are systematic, not statistical. They arise from imprecise knowledge of the sample temperature and the geometry of the sample and laser beam. It is difficult to assign uncertainties to these parameters and large systematic errors would obviously confuse the analysis. Improvements in the experimental apparatus (Chap. 8) are required to minimize the possibilities for large errors.

Evidence for Spatial Correlation in the Condensate

One can interpret the reasonable agreement between the two calculations as the first evidence of local second order spatial coherence in the hydrogen condensate because the equilibrium model assumes $g^{(2)}(0) = 1$. If coherence is lacking, $g^{(2)}(0) = 2$ and the shape of the spectrum and the relation between the frequency shift and condensate density would be different (See Sec. 6.1.3).

The study of phase coherence and spatial correlation in condensates in dilute gases is a subject which has inspired much debate (See the discussion in [118]). A brief review of the experimental evidence for coherence and correlation in alkali metal condensates is found in [101]. Long range first order spatial correlation ($g^{(1)}(\mathbf{r}) = 1$) in a Na condensate was established by the observation of interference fringes in the spatial distribution of atoms in two overlapping condensates[118]. The most direct measurement of local second order spatial correlation ($g^{(2)}(0) = 1$) comes from observations of the ballistic expansion of Na[119, 101] and Rb[120, 114] condensates. Such data determines the condensate's interaction energy, which depends on the s-wave scattering length, density, and $g^{(2)}(0)$. One could also take the agreement between theories and experiments on collective excitations[121, 122], sound propagation [123], component separation in mixtures of condensates[106, 124], and the limited condensate number in the negative scattering length Li BEC [22], as evidence that $g^{(2)}(0) = 1$. All of these

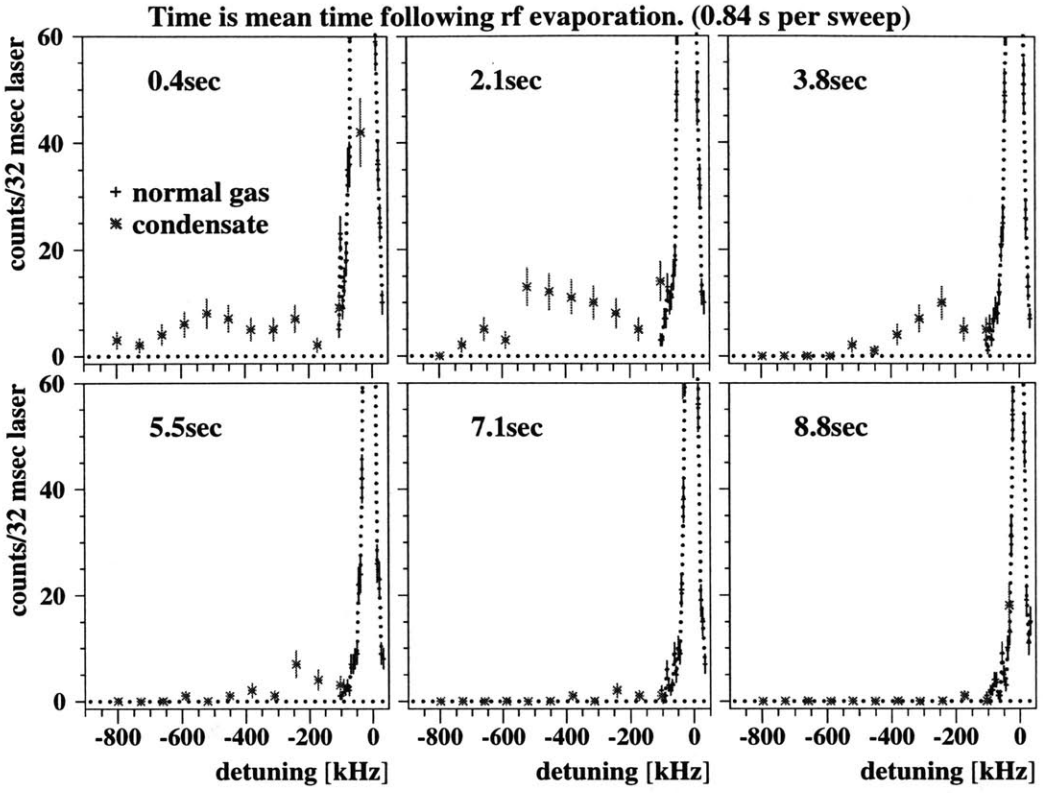

Figure 7-5: Time evolution of the Doppler-free spectrum of a single condensate. The trap depth is held at 280 μK. The time quoted is the time of the midpoint of the scan, measured from the end of the forced evaporation. The condensate appears stable in peak density and atom number for 2-3 seconds, and then decays away over the next few seconds.

effects probe the interactions between condensate particles, and thus probe $g^{(2)}(0)$, and the theoretical models all assume an equilibrium condensate with local second order spatial correlation. Local third order spatial correlation ($g^{(3)}(0) = 1$) in a Rb condensate was demonstrated by comparing the three-body decay rates in condensed and noncondensed samples[125].

Because spatial correlation is the rule in Na and Rb condensates it would be surprising if second order spatial correlation were absent in H, but there are differences which make its existence nontrivial. Dipolar decay from a H condensate with 10^9 atoms causes the condensate to decay with a time constant of about 1 second. The observed lifetime of about 3 seconds (Fig. 7-5) implies that the condensate is con-

stantly being replenished by new atoms from the thermal cloud, so coherence must be reestablished continually. The loss rate in the H condensate is much higher than that observed in the Rb and Na condensates because the density in the H condensate is more than an order of magnitude greater.

One might suspect that coherence is established slowly because of the low hydrogen elastic collision rate. (As pointed out before, the elastic collision cross section is 1000 times smaller in H than in Na and Rb.) The time scale for *formation* of the condensate will be governed by this rate [126, 127], but forming a condensate and establishing coherence or correlation are two different processes. It has been suggested[127] that once the condensate forms, the establishment of coherence is fast, occurring on a time scale of $\tau_{coherence} = \hbar/(4\pi\hbar^2 a_{1S-2S} n^{BEC}/m)$. This is on the order of milliseconds for hydrogen, which implies that coherence is established quickly on the time scale of H loss processes.

7.4 Phase Diagram

Because the normal gas and the condensate contributions to the Doppler-free spectrum are well resolved, one can study the hydrogen phase diagram near the BEC phase transition (Fig. 7-6). The shift of the resonance in the normal gas is used to measure the density through an analysis similar to that in Sec. 5.1.2. The data shows that as the sample is evaporatively cooled, the atoms settle into the trap and the peak density increases until the BEC phase transition is reached. At lower temperatures, the normal gas density is pinned at $n_c(T)$. The critical density limits the population in the normal gas and atoms which cannot be accommodated form the condensate.

Figure 7-6 shows that the largest condensate and condensate density is found shortly after the transition is crossed. This is very different from the behavior observed in Rb and Na condensates (see, for example, [114]), for which the condensate size continues to increase as the sample is cooled. In hydrogen, the fast dipolar decay and slow evaporative cooling, as discussed above in the context of the condensate fraction, precludes penetration far into the BEC regime.

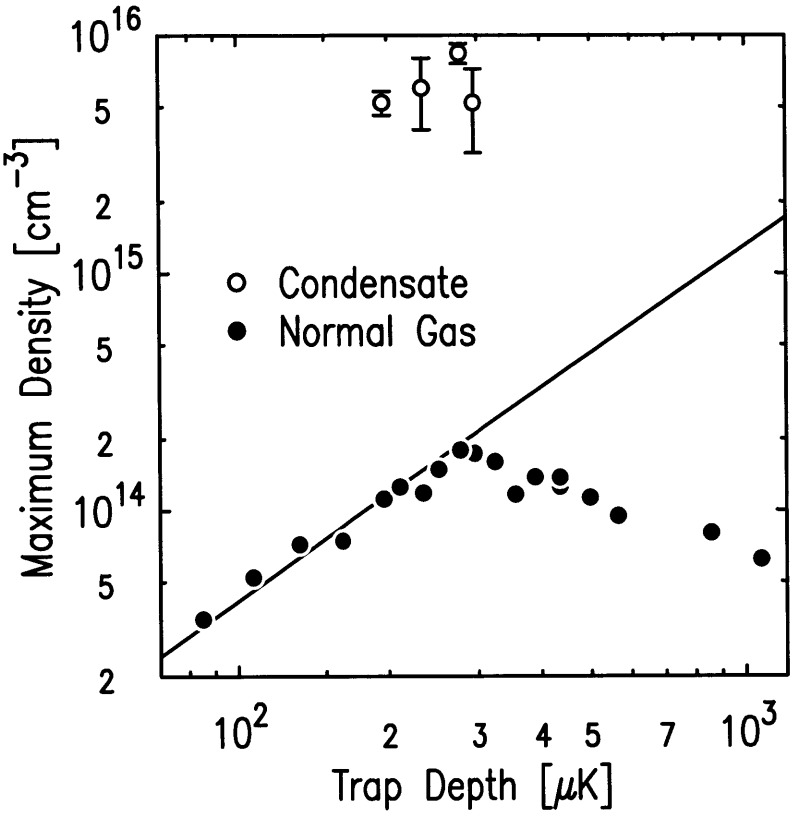

Figure 7-6: BEC phase diagram of hydrogen and a typical evaporative cooling path. Each data point represents a different load of the trap. The solid line is the BEC phase transition, $n_c(T) = 2.612(2\pi m k_B T)^{3/2}/h^3$, assuming the sample temperature is one sixth of the trap depth. The density of the condensate and normal fraction is measured with the Doppler-free spectrum and the phase separation is clearly signalled by the appearance of the shoulder at large red-shift as described in Fig. 7-1. The scatter of the data for the normal fraction reflects the typical uncertainty in the measurement.

7.5 Spectrum of the Normal Fraction in the Degenerate Regime

Inspection of the Doppler-free spectra of the normal gas which were used to construct Fig. 7-6 reveals some surprising behavior (Fig. 7-7). When the BEC threshold is crossed, the spectrum qualitatively changes shape and has contributions at large red-shift. Some shape change is expected when the chemical potential approaches zero and the shape of the Bose density distribution ceases to be well approximated by the Maxwell-Boltzmann distribution. However, much of the integrated signal intensity is further red-shifted than the shift corresponding to the critical density. The volume

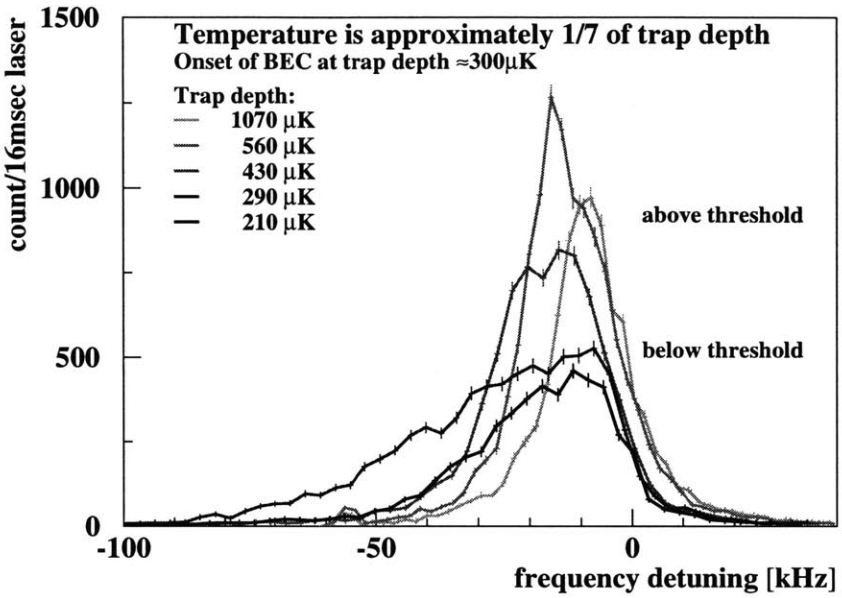

Figure 7-7: Doppler-free spectrum of the normal fraction immediately after the end of the forced evaporation. The signal in the presence of a condensate (trap depth < 300 μK) stretches to larger red-shift than expected for a static system in thermal equilibrium.

of the condensate is about 10^{-3} of the volume of the thermal cloud, so it is surprising that the condensate appears to affect the spectrum of the normal gas so much.

In order to quantitatively analyze the spectrum, one would need improved temperature diagnostics, knowledge of the trap and laser geometry, and theoretical understanding of the lineshape for the normal gas. However, the strange shape may imply that the sample is far from equilibrium near the transition, so the critical density may not be well defined. The sample's thermodynamic properties are changing rapidly in the first few seconds after crossing the BEC threshold, as discussed in the context of Fig. 7-4, and the large aspect ratio of the trap and the fast dipolar loss rates could impede thermalization. Since the sample is always close to the critical temperature, there may also be large fluctuations in the number of atoms in the condensate [128]. The data indicates that the degenerate hydrogen gas is a dynamic system and further study is required to understand its kinetic properties and explain the interesting

shape of the Doppler-free spectrum of the normal gas.

7.6 $1S$-$2S$ Spectroscopy as a Probe of BEC

High resolution spectroscopy is a powerful new way to study Bose condensation. It already has been used to detect the condensate and study its momentum and density distributions and its coherence properties. The frequency shifts provide information on how impurity $2S$ atoms interact with the condensate and there is much to explore in this area, such as collisional de-excitation. The spectrum should help to understand the dynamic nature of the hydrogen condensate, such as the dipolar decay and the feeding of the condensate from the thermal cloud.

Chapter 8

Future Prospects

$1S$-$2S$ spectroscopy of trapped atomic hydrogen has progressed dramatically since the signal was first observed in 1995 [10]. It is now a valuable probe of sample temperature and density and has been used to study atom-atom interactions and BEC. The technology is still evolving rapidly however, and there is promise for major improvements.

The weak signal strength is presently a limitation when studying the condensate or the Doppler-sensitive excitation of the normal gas. Shot noise due to the small number of photons counted is the major source of error for these features: nearly a second is required to record a useful spectrum. This makes study of dynamics and thermalization very difficult.

A factor of 10 improvement in Lyman-alpha detection efficiency could be realized by moving the atoms closer to the MCP detector to improve the solid angle for collection of the fluorescence. Another factor of 6 improvement is available by replacing the Lyman-alpha filter above the MCP with a MgF_2 window. As discussed in Sec. 3.4, the filter blocks scattered laser photons so that the MCP is not saturated. If the filter were removed, to avoid MCP saturation the MCP gain could be reduced when the laser is present, and restored on a time scale shorter than a millisecond in order to detect the signal. Experiments have shown that switching the high voltage on the MCP assembly can change the gain on a fast enough time scale. A possible concern is that long-lived fluorescence from materials excited by the laser scatter (Sec. 3.3)

may produce a large background count rate if the filter is removed.

With greater signal to noise it should be possible to study the thermal equilibration of the sample near the BEC phase transition and to quantitatively compare the condensate spectrum with the spectrum predicted by the Thomas-Fermi density distribution. This should help to resolve the questions surrounding the strange appearance of the Doppler-free spectrum of the normal fraction near the transition and improve understanding of transport properties in the quantum gas. Deviations from the Thomas-Fermi prediction may provide imformation on finite temperature effects, for instance.

In addition, a new trap geometry in which the atoms are moved away from the large superconducting magnets before performing spectroscopy, could greatly reduce the uncertainty in the trap and laser geometry. These uncertainties are the limiting factors in the measurement of the cold collision frequency shift and the $1S$-$2S$ scattering length, and in using the frequency shift to study the density distribution of the sample. With better understanding of the trap shape it might be possible to quantitatively compare the dipolar decay of a condensed and noncondensed gas and directly measure the second order spatial correlation function, $g^{(2)}(0)$.

While the laser illuminates the gas, helium atoms evaporate off the retroreflecting mirror at the bottom of the cell and knock atoms out of the trap. This causes the sample to decay with a $\sim$ 10 second time constant. One would like to observe the sample for longer and in a less destructive fashion. A helium film pump in the cell [23] can be used to remove most of the liquid ^{4}He from the trapping region and reduce the helium flux. This tool has not yet been used to its full potential, but preliminary results in a previous experiment indicate that it increases the sample lifetime by a factor of three to five.

Stray electric fields in the plastic cell used in the experiments described here limit the lifetime of the excited $2S$ atoms to a few milliseconds, but in a metal cell the lifetime approached the 122 ms natural lifetime [10]. It should be possible to coat the inside of the plastic cell with a thin conductive layer to provide DC electric field shielding without causing too much eddy current heating during the RF evaporation.

This will allow studies of the $2S$ lifetime in the condensate which may give more insight into the interactions of these impurity atoms with the condensate.

A long $2S$ lifetime is essential for higher resolution spectroscopy of the $1S$-$2S$ transition. Straightforward application of available technology in laser frequency stabilization should improve the laser linewidth to 100 Hz or less. The production of cold atoms which suffer less than 10 Hz residual Zeeman broadening is now feasible with RF evaporation and adiabatic expansion of the cloud. With improved detection efficiency, there would be no prohibition to working at densities below 10^{10} cm^{-3} where the cold collision frequency shift becomes unimportant. The path seems clear to achieving a spectral resolution at least an order of magnitude better than the best results from atomic beam experiments. This use of the $1S$-$2S$ transition in trapped hydrogen as a frequency standard seems promising.

Another avenue which has not been explored is the excitation of transitions from the $2S$ state. When excited Doppler-free, the $2S$ atoms are trapped and are at approximately the same temperature as the $1S$ atoms. Powerful techniques for imaging in the visible wavelength region have been developed to observe small numbers of alkali metal condensate atoms. In a 1 ms laser pulse, up to 10^6 $2S$ atoms can be excited. This number of atoms can easily be detected with absorptive or dispersive imaging on the 656 nm Balmer-alpha transition, for example. This could prove to be a useful alternative method for monitoring the $1S$-$2S$ excitation rate, but it also could lead to new experimental measurements, such as the determination of numerous scattering lengths for collisions between $1S$ atoms and more highly excited states than $n = 2$.

This is just a short list of the many improvements and experiments for $1S$-$2S$ spectroscopy of trapped atomic hydrogen. The results are already impressive, but they promise to be even more so in the near future.

Appendix A

High Resolution Spectroscopy

The two-photon $1S$-$2S$ transition in a cold, trapped sample has great potential for high resolution spectroscopy. This goal has not yet been aggressively pursued at MIT because achievement of BEC has been the primary objective. Even with the present apparatus, however, the resolution is comparable to the best results from atomic beam experiments[64, 9]. $1S$-$2S$ spectroscopy in an atomic beam is limited by the finite interaction time of atoms with the laser, and by the second order Doppler shift of the frequency. A trap provides long interaction times and a low enough temperature that the second order Doppler shift is negligible.

A.1 Best Achieved Resolution

A.1.1 Time-of-Flight Broadened Lines

Figure A-1 shows successive scans of a cold (<40 μK), low density ($<10^{13}$ cm^{-3}) hydrogen sample. A simple model for the spectrum incorporating the time-of-flight lineshape and some additional broadening implies that the spectrum is still dominated by the time-of-flight shape. Additional broadening, most likely arising from the laser frequency spectrum, cold collision frequency shift, and photoionization, contributes about 1 kHz FWHM to the width. The relative importance of each broadening mechanism was not determined.

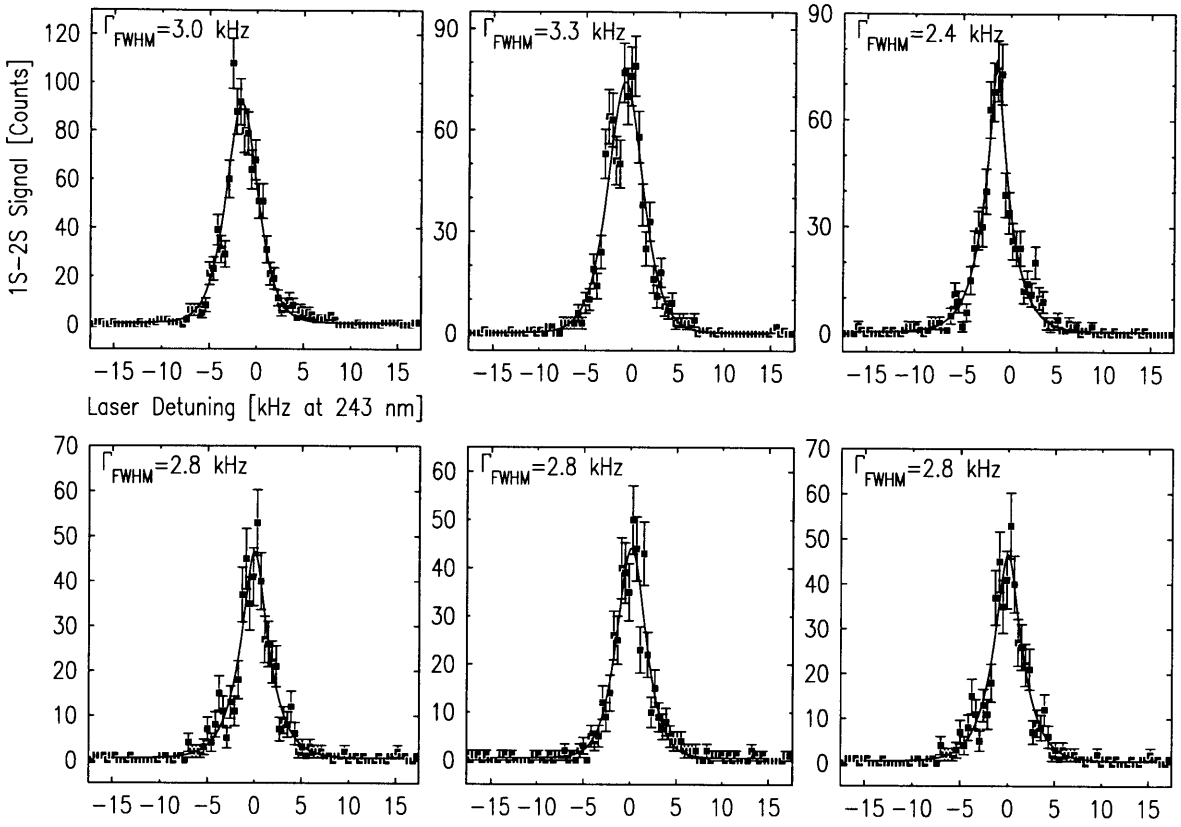

Figure A-1: Spectroscopy of a single cold (<40 μK) low density (<10^{13} cm^{-3}) hydrogen sample. The sample was created by evaporating to a temperature of about 150 μK and then adiabatically expanding the magnetic trap. Each data point represents 25 ms of laser excitation, and each successive sweep was recorded in 5 s. The excitation laser power was about 5 mW. The error bars are statistical and the solid lines are the results of a simple model which incorporates the time-of-flight lineshape and additional broadening mechanisms. The resulting linewidths are about 3 kHz FWHM.

On the time scale of about one second, the laser linewidth is below 1 kHz, but on a longer time scale, the laser shows more instability. For instance, between the third and fourth sweep the spectrum shifts about 1.5 kHz.

For spectroscopy of trapped hydrogen, the signal rate is quite high. It is currently possible to determine the line center to better than 100 Hz in one second. The high signal rate and signal-noise ratio for trapped hydrogen is an important consideration when comparing its potential as a frequency standard with that of trapped ions or the low velocity tail of a hydrogen atomic beam.

A.1.2 Coherence Effects

Time-of-flight broadening dominates the linewidths in Fig. A-1. As discussed in Sec. 4.4.5, in a tightly confined trap the frequency for periodic atomic motion is high enough that atoms maintain coherence with the laser as they repeatedly pass through the excitation region. This produces interference fringes on the spectrum which are narrower than the time-of-flight linewidth [10, 60]. The envelope of the line is given by the time-of-flight lineshape and the central fringe arises mostly from excitation of very low energy atoms which are in the laser for a long time.

Presently, the width of the fringes is limited by the resolution limit of the apparatus, ~ 1 kHz under ideal conditions. Figures 4-8 and A-2 show examples of spectra exhibiting motional sidebands.

A.2 Laser Frequency Stability Limitations

By using the $1S$-$2S$ signal as our absolute frequency reference we were able to study many systematics which affect the frequency stability of our laser system. Two important effects are discussed below. This section is intended to be useful for future operators of the MIT laser system, and a familiarity with the system is assumed.

A.2.1 Reference Cavity Shift with Light Power

The frequency of the reference cavity transmission modes was found to vary with the circulating light power in the reference cavity. The circulating power is monitored by measuring the transmitted light after it passes through a 25/75 beam splitter. The weaker beam falls on a DT-25 photodiode with a 1 kΩ load which is amplified by 50 in the frequency servo electronics box. This signal is used to determine if the laser frequency is locked to the cavity mode, which is important for the redundant cavity locking scheme. Including the amplification, the calibration is about 0.4 volts per 100 μW of cavity transmission. The stronger beam falls on an FND-100Q photodiode which has a 22 kΩ load and is amplified by 10 by a simple op-amp circuit. The

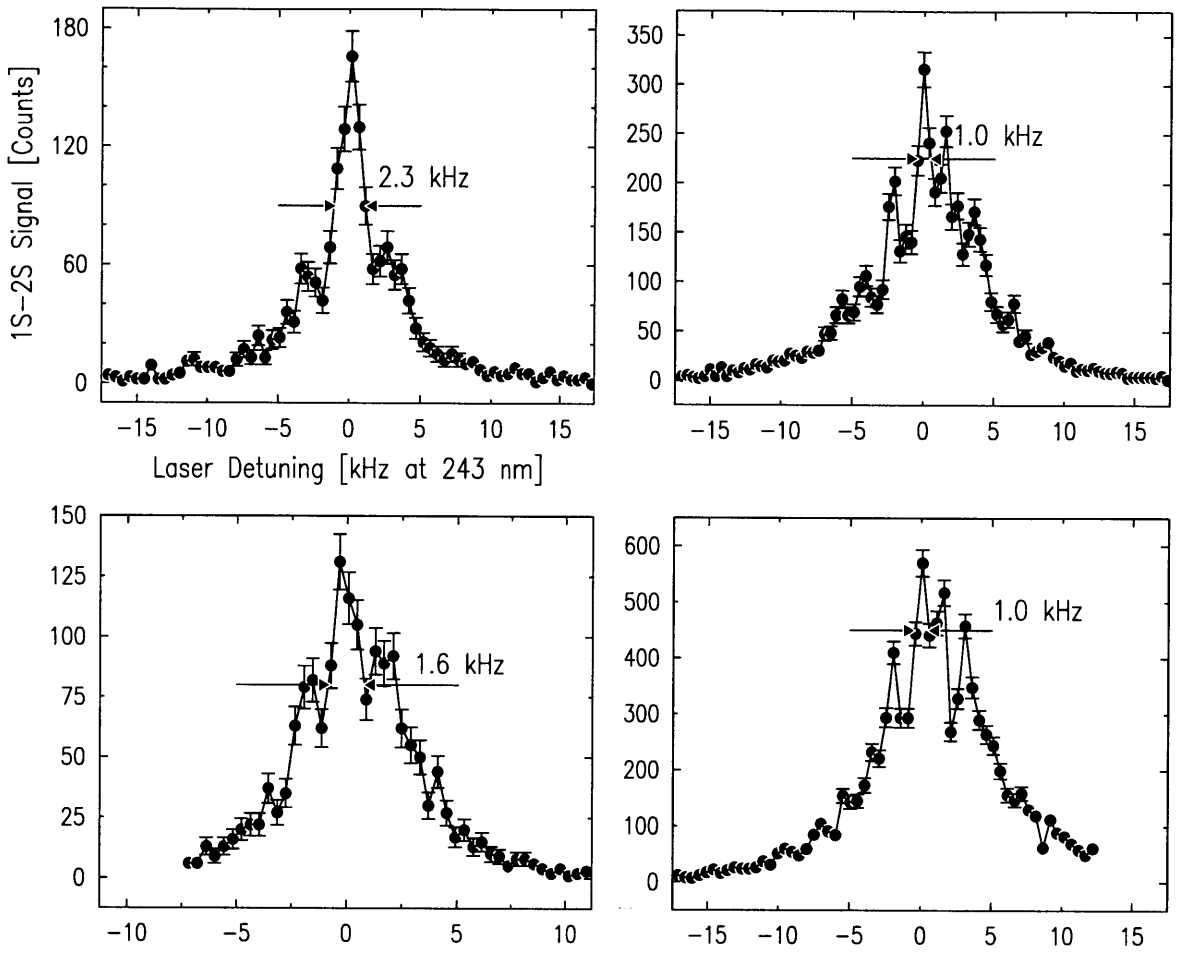

Figure A-2: Spectra showing motional sidebands. Conditions vary, but typically, each point represents 25 ms of laser excitation and a single laser pulse was 430 μs or greater. The width of the central fringe is indicated in each plot, and under ideal conditions the best resolution is about 1 kHz, which corresponds to 1 part in 10^{-12}. Error bars are statistical and do not include uncertainty arising from variation in laser power and alignment. The solid lines are meant to guide the eye.

calibration for this signal is 4 volts per 100 μW transmission.

We see 100 μW transmission for about 4 mW of incident power when each EOM sideband has 30% of the power of the carrier. When the cavity was constructed [59], the mirror transmission was measured to be about 0.1%. This implies about 100 mW circulating in the cavity, which translates into an enhancement in the cavity of 50, assuming about one half of the incident power is coupled into the cavity. In the absence of any scattering or absorption at the mirrors, the enhancement would be $\frac{F}{\pi} \approx 640$, where F is the cavity finesse. A 0.3% absorption or scatter, which is not

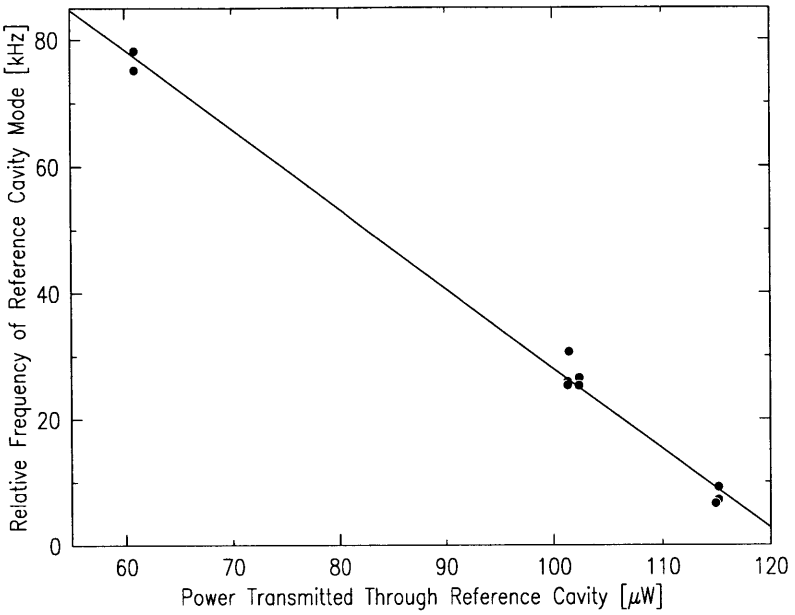

Figure A-3: Reference cavity transmitted power as measured by the FND-100Q photodiode/amplifier circuit. The relative frequency is found by comparing the mode frequency to the 1S-2S transition frequency. The line is a linear fit which yields a -1.3 kHz/μW shift of the mode frequency. Long term drift of about 8 kHz/hour is taken into account.

unreasonable, would reduce the enhancement by an order of magnitude[129].

Figure A-3 shows the sensitivity of the cavity mode frequency to circulating power. We found that the mode frequency shifts by -1.3 kHz per μW change in transmitted power. The data was taken over the course of a few hours and for each data point the power in the reference cavity was changed approximately 10 minutes before the data was taken. Our interpretation of this shift is that there are local heating effects on the mirror coatings which change the effective length of the cavity. The time constant for this effect is on the order of 100 ms, as shown in figure A-4.

The light level in the cavity varies due to laser power fluctuations and angular displacements of the laser beam which change the coupling efficiency. If not controlled, this would significantly broaden the laser spectrum. For the majority of data discussed in this thesis, the power incident on the reference cavity was stabilized by varying the RF power on an acousto-optic modulator (AOM). This reduced much of the frequency shift, but even with an optical fiber between the laser and the reference cavity, there were still slow drifts of the beam alignment which led to variations of

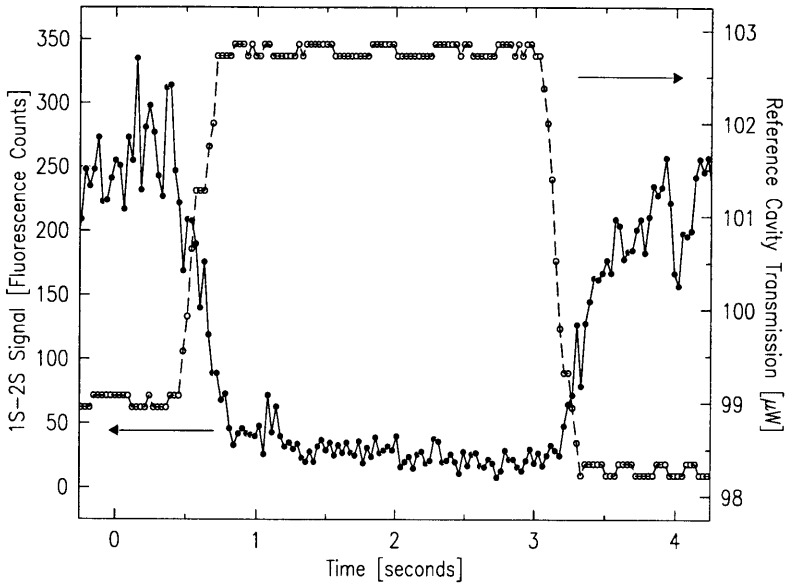

Figure A-4: Response of the reference cavity mode frequency to a sudden change in light level. The frequency offset of the laser from the reference cavity transmission mode was held fixed and the $1S$-$2S$ excitation rate was monitored as the light power in the cavity was changed. Each data point represents about 30 ms of time with 50% duty cycle laser excitation. 250 counts per point represents the peak count rate on line center. The lower count rate corresponds to the wing of the line about 5 kHz from resonance. The $1S$-$2S$ excitation rate, and thus the cavity mode frequency, responds to the change in light power with about a 100 ms time constant.

circulating power. Stabilizing the transmitted power is superior, and we now follow this procedure.

We also see a shift of the mode frequency with a time constant of hours or more if the light level is changed or when light is first put into the reference cavity, which we interpret as a temperature change of the zerodur cavity mirror spacer. This effect can be larger than the long term drift of the cavity of about -3 MHz per month.

A.2.2 Doppler-Shifts Along the Beam Path

As shown in Fig. 3-4, the laser system is about 30 m away from the hydrogen trap. There are advantages and disadvantages to this arrangement. The dilution refrigerator generates significant noise and vibrations, which are not conducive to frequency stabilization of a laser, so it is helpful to move the laser away. The laser beam must still journey to the trapping apparatus, however, and at present no optical fibers

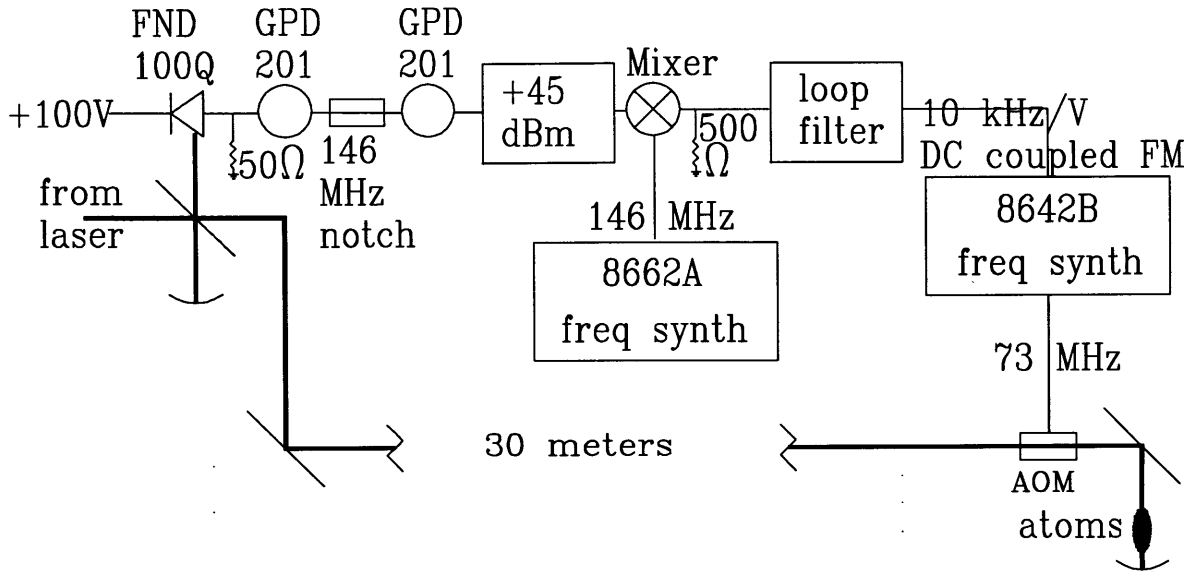

Figure A-5: Schematic of the Doppler servo system. The heavy black line shows the laser beam path, which is in an interferometer configuration to generate a beatnote at 146 MHz on the FND-100Q photodiode. The beatnote is amplified (GPD-201 is a +30 dBm RF amplifier) and then mixed with a clean 146 MHz signal to generate an error signal. The loop filter is a simple op-amp circuit with a 10 kΩ input impedance, gain of 1420 at DC, and a single pole at 8.4 Hz.

exist for 243 nm. Thus the beam bounces off mirrors mounted to the ceiling and, eventually, the vibrating cryostat.

When a laser beam bounces off a moving mirror, its frequency is Doppler-shifted by about $2\mathbf{k} \cdot \mathbf{v}$, where $\mathbf{k}$ is the wave vector of the light and $\mathbf{v}$ is the velocity of the mirror. To investigate the size of this effect in the present experiment, the spectrum of the light after it has traveled to the cryostat and returned to the optics table is measured by interfering it with a beam which has not left the table (A-5). To move the beatnote away from DC, an AOM frequency shifter is placed in the beam path. Since the coherence time of the laser beam on the optics table, equal to the inverse of the linewidth, is long compared to the travel time, the beatnote measures the spectral broadening suffered by the laser beam along its path.

The beatnote after the mixer and its Fourier transform are shown in Fig. A-6. The width of the spectrum is about 10 kHz. Since the laser is in a standing wave geometry, and the atomic sample is essentially at the retro-reflecting mirror, the width of the laser when it excites the atoms is about half of the width measured by the beatnote,

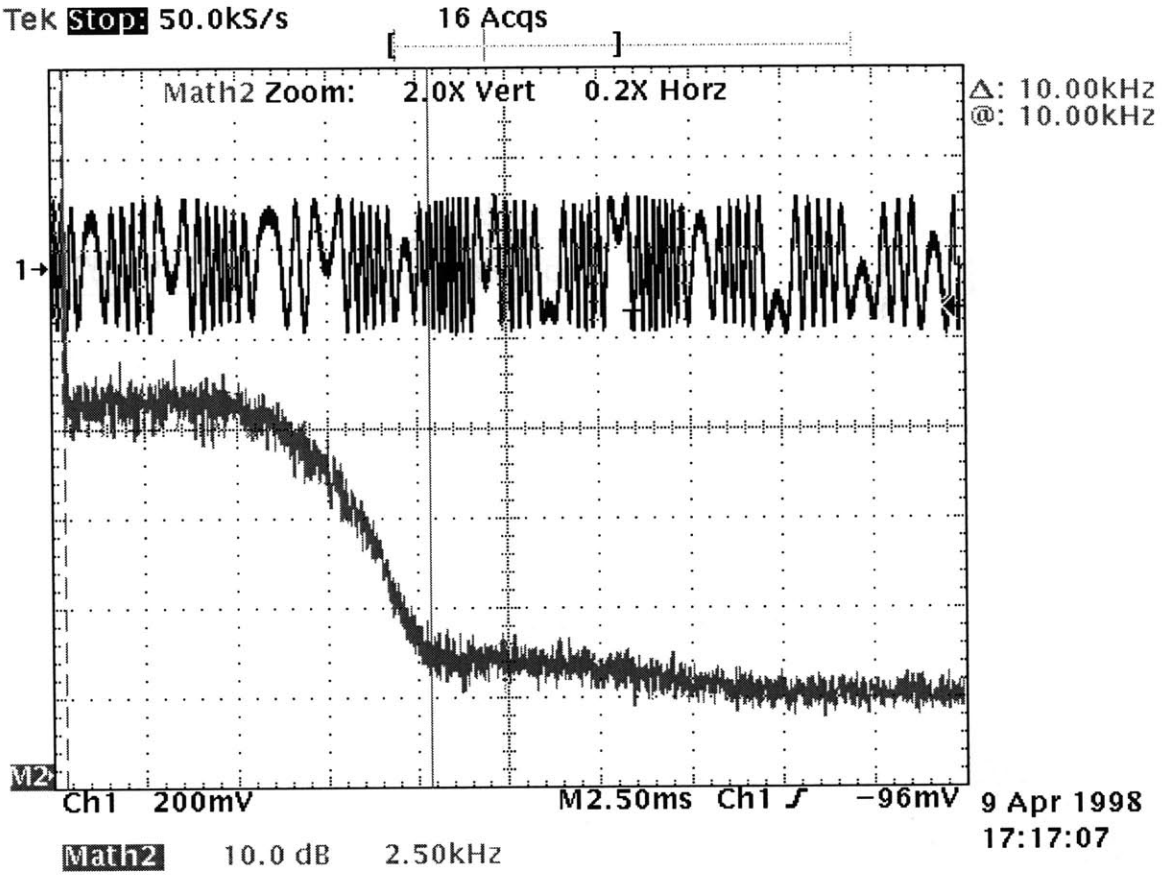

Figure A-6: Beatnote of Doppler servo system. The dark trace shows the beatnote after the mixer. The scales are 200 mV/div and 2.5 ms/div. The light trace is the fast Fourier transform, after subtracting the 146 MHz AOM shift, of the difference frequency between the return laser beam and a laser beam which has not left the optics table. The scales are 10 dB/div and 2.5 kHz/div. The implied FWHM of the return beam laser spectrum is about 10 kHz.

and Doppler-jitter should limit the resolution of the experiment.

A control loop was built to vary the frequency of the AOM so as to lock the beatnote to a radio frequency synthesizer. The schematic is shown in Fig. A-5. The loop locks well with a 0 dBm beatnote before the mixer, and it acquires in less than 50 μs when the laser is chopped at about 1 kHz. When the loop is locked, the beatnote width is less than 3 Hz. Since the laser beam passes through the AOM twice, to a good approximation this scheme also produces a clean laser frequency spectrum in the excitation region. Any jitter introduced by the retro-mirror will not be corrected.

Most of the data in Fig. A-1 and A-2 was recorded with the Doppler servo. A systematic study was not done to determine the actual resolution limitation due to

the Doppler-jitter, or how much the Doppler servo helped. In most of the studies described in this thesis the linewidth is greater than 4-5 kHz and can be accounted for by the time-of-flight broadening and the cold collision frequency shift, and the trap oscillation frequency is not high enough to resolve the sidebands. From the width of the spectrum in Fig. A-6, it is still surprising that the Doppler-jitter limit is not more clearly evident. In fact, on rare occasions the spectrum has very high resolution without the Doppler servo, such as in Fig. 4-8 and the lower right hand plot in Fig. A-2. Clearly, when high resolution spectroscopy is pursued more vigorously, this effect will require further study.

A.3 Prospects for Improving the Frequency Stability

At present, the resolution of the spectrum is limited by the laser linewidth ($\sim$ 1 kHz at 243 nm), the low signal rate, and the cold collision frequency shift (One needs to work at relatively high densities to obtain spectra with sufficient signal/noise). Laser stabilization to Fabry-Perot optical resonators has progressed dramatically since the current laser system was constructed [59]. A 1 Hz laser linewidth for an integration time of over a minute has been achieved by J. Bergquist at NIST, Colorado [130], and cryogenic optical resonators [131] are a recent advance which shows great promise. As discussed in Chap. 8, the signal rate can be increased dramatically by improving the detection efficiency for fluorescence – making it feasible to record spectra at much lower densities.

Appendix B

$1S$-$2S$ Spectroscopy Appendix

This appendix gives a more detailed derivation of the effective two-level Hamiltonian and discusses the numerical simulation of the spectrum.

B.1 Effective Two-Level Hamiltonian

The present treatment of the photo-excitation spectrum begins with time-dependent perturbation theory[78], with the perturbing Hamiltonian

$$\tilde{H}' = -e\tilde{\mathbf{r}} \cdot \mathbf{E}(\tilde{\mathbf{R}}, \tilde{\mathbf{r}}, t). \tag{B.1}$$

The operators are $\tilde{\mathbf{R}}$, the center of mass of the atom, and $\tilde{\mathbf{r}}$, the position of the electron with respect to the nucleus. The charge of the electron is $e < 0$, and we represent our standing wave laser as a classical monochromatic electric field of the the form

$$\mathbf{E}(\tilde{\mathbf{R}}, \tilde{\mathbf{r}}, t) = \frac{1}{2}\hat{\epsilon}_1 E_1(\tilde{\mathbf{R}}) e^{i\mathbf{k}_1\cdot(\tilde{\mathbf{R}}+\tilde{\mathbf{r}})-i\omega_1 t} + \frac{1}{2}\hat{\epsilon}_2 E_2(\tilde{\mathbf{R}}) e^{i\mathbf{k}_2\cdot(\tilde{\mathbf{R}}+\tilde{\mathbf{r}})-i\omega_2 t} + c.c. \tag{B.2}$$

E_1 and E_2 are taken to be real and they contain the slow spatial variations of the beam profiles. The laser is applied at time t_0.

For an electric dipole-allowed transition, the excitation rate is found from the first

order coefficient of the excited state,

$$C^{(1)}_{2S,\mathbf{p}_2}(t) = -\frac{i}{\hbar}\int_{t_0}^{t} dt'' \langle 2S,\mathbf{p}_2 \mid \tilde{H}'(t'') \mid 1S,\mathbf{p}_1\rangle e^{-i\omega_{2S,\mathbf{p}_2-1S,\mathbf{p}_1}(t''-t_0)}. \tag{B.3}$$

As is well known, $\langle 2S,\mathbf{p}_2 \mid H'(t'') \mid 1S,\mathbf{p}_1\rangle = 0$, since parity conservation forbids a one-photon $\Delta l = 0$ transition, so $C^{(1)}_{2S,\mathbf{p}_2}$ vanishes.

We turn to the second order coefficient of the $2S$ state,

$$\begin{aligned} C^{(2)}_{2S,\mathbf{p}_2}(t) &= -\frac{1}{\hbar^2}\int_{t_0}^{t} dt'' \int_{t_0}^{t''} dt' \sum_{n,\mathbf{p}'_n} \langle 2S,\mathbf{p}_2 \mid \tilde{H}'(t'') \mid nP,\mathbf{p}'_n\rangle e^{-i\omega_{2S,\mathbf{p}_2-nP,\mathbf{p}_n}(t''-t_0)} \\ &\quad \times \langle nP,\mathbf{p}'_n \mid \tilde{H}'(t') \mid 1S,\mathbf{p}_1\rangle e^{-i\omega_{nP,\mathbf{p}_n-1S,\mathbf{p}_1}(t'-t_0)}. \end{aligned} \tag{B.4}$$

The sum extends over all P states, including the continuum, and center of mass momenta. We can recast this expression in the form

$$C^{(2)}_{2S,\mathbf{p}_2}(t) = -\frac{i}{\hbar}\int_{t_0}^{t} dt'' V_{2S,\mathbf{p}_2;1S,\mathbf{p}_1}(t'') e^{-i\omega_{2S,\mathbf{p}_2-1S,\mathbf{p}_1}(t''-t_0)}, \tag{B.5}$$

which is in the form of Eq. B.3. Once we have done this, we can forget about many of the complications that arise from the two-photon nature of the transition.

To derive Eq. B.5 from Eq. B.4, we make the rotating wave approximation and the adiabatic approximation [79] ($|\mathrm{d}E_i(\mathbf{R})/\mathrm{dt}| \ll |\omega_i E_i(\mathbf{R})|$). Using the electric dipole approximation, we set $e^{i\mathbf{k_i}\cdot\tilde{\mathbf{r}}}$ to unity, but we leave $e^{i\mathbf{k_i}\cdot\tilde{\mathbf{R}}}$ since it contains important information on momentum exchange during the excitation. We also specialize to the case of a standing wave laser field, for which $\mathbf{k}_1 = -\mathbf{k}_2 = \mathbf{k}_{\text{laser}}$, and $\omega_1 = \omega_2 = \omega_{\text{laser}}$, and $\hbar|\omega_{\text{laser}} + \omega_{1S,nP}| \gg |\frac{\mathbf{p}_1^2}{2m} - \frac{\mathbf{p}_n^2}{2m}|$

After some lines of calculations, this gives

$$\begin{aligned} C^{(2)}_{2S,\mathbf{p}_2}(t) &= -\frac{e^2}{4\hbar^2}\int_{t_0}^{t} dt'' \langle 2S,\mathbf{p}_2 \mid \sum_{n,\mathbf{p'}_n} \frac{1}{i(\omega_{\text{laser}} + \omega^0_{1S-nP})} \\ &\quad \times [E_1(\tilde{\mathbf{R}})e^{-i\mathbf{k}_{\text{laser}}\cdot\tilde{\mathbf{R}}}\ \tilde{\mathbf{r}}\cdot\hat{\epsilon}_1 \mid nP,\mathbf{p'}_n\rangle\langle nP,\mathbf{p'}_n \mid \tilde{\mathbf{r}}\cdot\hat{\epsilon}_1\ E_1(\tilde{\mathbf{R}})e^{-i\mathbf{k}_{\text{laser}}\cdot\tilde{\mathbf{R}}} \\ &\quad + E_1(\tilde{\mathbf{R}})e^{-i\mathbf{k}_{\text{laser}}\cdot\tilde{\mathbf{R}}}\ \tilde{\mathbf{r}}\cdot\hat{\epsilon}_1 \mid nP,\mathbf{p'}_n\rangle\langle nP,\mathbf{p'}_n \mid \tilde{\mathbf{r}}\cdot\hat{\epsilon}_2\ E_2(\tilde{\mathbf{R}})e^{i\mathbf{k}_{\text{laser}}\cdot\tilde{\mathbf{R}}} \\ &\quad + 1 \to 2] e^{2i\omega_{\text{laser}}t''} \mid 1S,\mathbf{p}_1\rangle e^{-i\omega_{2S,\mathbf{p}_1-1S,\mathbf{p}_2}(t''-t_0)}. \end{aligned} \tag{B.6}$$

To simplify the matrix elements in Eq. B.6, it is important to recall that $e^{i\mathbf{k}_i\cdot\tilde{\mathbf{R}}}$ is the operator for a translation in momentum space by $\hbar\mathbf{k}_i$. It ensures that the atom takes up the momentum of the photon. One can expand $E_i(\tilde{\mathbf{R}})$ in spatial Fourier components, each of which causes momentum translation [60] as well. The latter effect we will neglect in consideration of the matrix elements of Eq. B.6. It is equivalently treated by viewing $E_i(\mathbf{R})$ as a c-number whose amplitude varies in time as the particle moves along the trajectory, $\mathbf{R}(t)$.

We can now write,

$$\langle 2S,\mathbf{p}_2 \mid E_i(\mathbf{R})e^{-i\mathbf{k}_{\rm laser}\cdot\tilde{\mathbf{R}}}\,\tilde{\mathbf{r}}\cdot\hat{\epsilon}_i \mid nP,\mathbf{p}_n\rangle\langle nP,\mathbf{p}_n \mid \tilde{\mathbf{r}}\cdot\hat{\epsilon}_j\; E_j(\mathbf{R})e^{i\mathbf{k}_{\rm laser}\cdot\tilde{\mathbf{R}}} \mid 1S,\mathbf{p}_1\rangle =$$
$$E_i(\mathbf{R})E_j(\mathbf{R})\;\mathbf{r}_{2S,nP}\cdot\hat{\epsilon}_i\;\mathbf{r}_{nP,1S}\cdot\hat{\epsilon}_j\;\delta_{\mathbf{p}_2,\mathbf{p}_1+\hbar\mathbf{k}_i+\hbar\mathbf{k}_j}, \tag{B.7}$$

where $\mathbf{r}_{i,j}$ is the dipole matrix element between states i and j and the Kronecker delta function ensures momentum conservation. We arrive at the central result of this section,

$$\begin{aligned} V_{2S,1S}(t) &= \hbar\left(\frac{\alpha}{2R_\infty}\right)^3\frac{1}{3\pi^2\hbar c}\{[I_1(\mathbf{R})\delta_{\mathbf{p}_2,\mathbf{p}_1+2\hbar\mathbf{k}_{\rm laser}}+I_2(\mathbf{R})\delta_{\mathbf{p}_2,\mathbf{p}_1-2\hbar\mathbf{k}_{\rm laser}}]M^{11}_{2S,1S}/2 \\ &\quad+\sqrt{I_1(\mathbf{R})I_2(\mathbf{R})}\delta_{\mathbf{p}_2,\mathbf{p}_1}M^{12}_{2S,1S}\}e^{2i\omega_{\rm laser}t}, \end{aligned} \tag{B.8}$$

where $I_i=\frac{1}{2}\varepsilon_0 c|E_i(\mathbf{R})|^2$ is the intensity of beam i. The sums over dipole matrix elements are reduced to

$$M^{ij}_{2S,1S} =$$
$$\left(\frac{2R_\infty}{\alpha}\right)^3\frac{3\pi^3e^2}{\varepsilon_0 2h}\sum_n\frac{1}{(\omega_{\rm laser}+\omega_{1S-nP})}(\mathbf{r}_{2S,nP}\cdot\hat{\epsilon}_i\;\mathbf{r}_{nP,1S}\cdot\hat{\epsilon}_j+\mathbf{r}_{2S,nP}\cdot\hat{\epsilon}_j\;\mathbf{r}_{nP,1S}\cdot\hat{\epsilon}_i). \tag{B.9}$$

The term proportional to $M^{12}_{2S,1S}$ gives rise to Doppler-free absorption of two counter-propagating photons, for which there is no momentum transfer and thus no recoil shift. The term proportional to $M^{11}_{2S,1S}$ gives rise to recoil-shifted Doppler-sensitive absorption of two Jo-propagating photons. The photons can come from either of the

two laser beams. In our particular experimental arrangement, $\hat{\epsilon}_1 = \hat{\epsilon}_2$ and $\omega_1 = \omega_2 = \omega_{laser} = \omega^0_{2S-1S}/2$, and $M^{12}_{2S,1S} = M^{11}_{2S,1S} = 11.78$ [80].

The AC Stark shift, $\Delta E_{\text{AC Stark}} = \hbar(\Delta\omega_{2S} - \Delta\omega_{1S})$, is found from an extension of this analysis. One must calculate the level shifts that arise from transitions $1S \rightarrow nP \rightarrow 1S$ and $2S \rightarrow nP \rightarrow 2S$ [79], which we have neglected here. For our purposes, it suffices to know that the transition frequency is shifted by $\Delta E_{\text{AC Stark}}/h = 3.34\sqrt{I_1 I_2}$ Hz W^{-1} cm^2.

We now have all the pieces of the effective two level Hamiltonian, which is similar in form to the interaction for a one-photon transition.

$$H'_{\text{eff}} = \begin{pmatrix} \hbar\Delta\omega_{2S} & V_{2S,1S} \\ V^*_{2S,1S} & \hbar\Delta\omega_{1S} \end{pmatrix}. \tag{B.10}$$

B.2 Numerical Calculation of the Spectrum

The numerical calculation of the spectrum, Eq. 4.31, can be simplified through symmetry arguments and approximations. Because of the axial symmetry of the problem, spatially, ρ only depends on the initial axial position, z, and distance from the z axis (which we call r instead of ρ to avoid confusion with the density matrix). Also, typically the laser pulse length is set to 400-500 μs. In this time the atoms in our evaporatively cooled sample move a maximum of a few millimeters. The axial length scale for variation of the laser waist or sample density is centimeters, so we can neglect the axial velocity.

There is another symmetry in the problem. Axial angular momentum, L, is conserved in our trap, so we can describe the motion in r through the effective potential

$$V_{eff}(r) = \frac{L^2}{2mr^2} + U(r). \tag{B.11}$$

which includes the centrifugal barrier, $L^2/2mr^2$, and the magnetic trapping potential, $U(r) = \mu\sqrt{B_0^2 + (r\partial_r B)^2}$. Here, μ is the Bohr magneton, B_0 is the axial bias field and $\partial_r B$ is the linear radial field gradient produced by the quadrupole magnets. (B_0

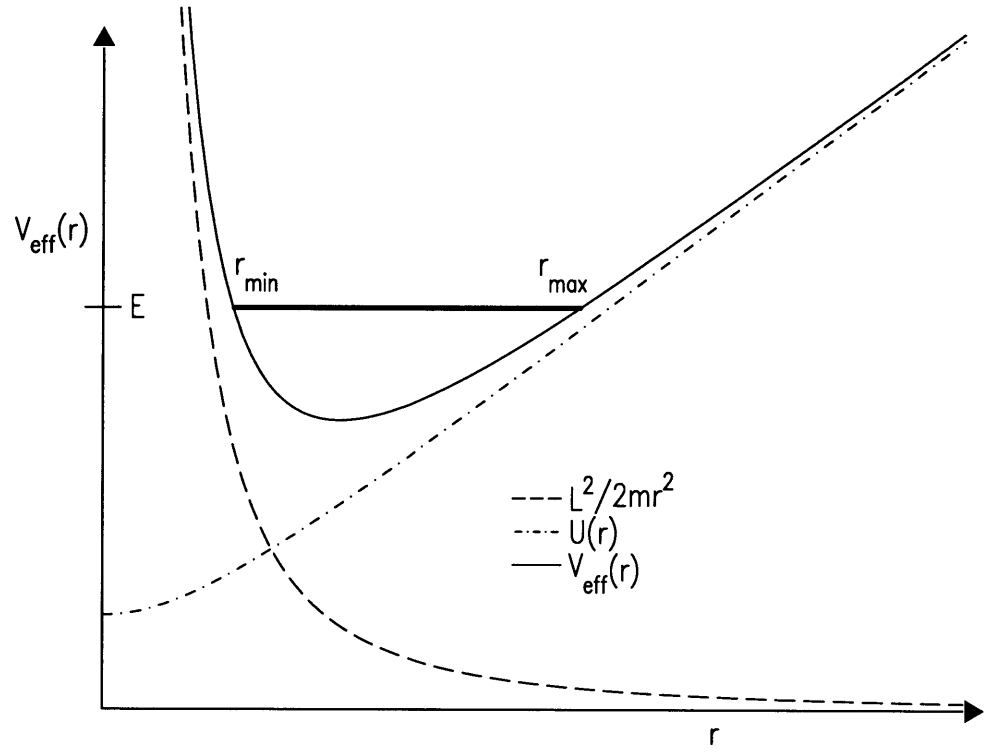

Figure B-1: Energy diagram for radial motion of an atom in the magnetic trap including the centrifugal potential, $L^2/2mr^2$. The magnetic trapping potential is $U(r) = \mu\sqrt{B_0^2 + (r\partial_r B)^2}$. Here, μ is the Bohr magneton, B_0 is the axial bias field and $\partial_r B$ is the linear radial field gradient produced by the quadrupole magnets. For a given motional energy, the particle moves between the turning points at r_{min} and r_{max}.

is really quadratic in z to provide axial confinement, but it is not important to the discussion.) The effective potential for r motion is shown in Fig. B-1. For a given L and total motional energy E, the particle moves between the turning points at r_{max} and r_{min}. The evolution of the density matrix, described by Eq. 4.28, only depends on r. For a given z, all atoms on radial orbits with a given total energy and axial orbital momentum contribute equally provided that the laser pulse is long compared to the radial period of oscillation for atoms in the trap. (Typically, the period for radial oscillation is a few hundred microseconds, and the laser pulse is 400 microseconds or more, so the approximation is not so bad.) We can parameterize the orbits by E and L or, equivalently, the axial distance r_0 at which the radial velocity vanishes, and the tangential velocity at that point, v_0. (This double counts orbits because the radial

velocity vanishes twice in any orbit, but this is just an overall normalization.) Then

$$S(\nu) = \int_{-\infty}^{\infty} dz \int_0^{\infty} 2\pi dr_0 \; r_0 \int_0^{\infty} dv_0 \; g(r_0, v_0) \; n_0(z) \mathrm{e}^{-\frac{U(r_0,z)}{k_B T}} \mathrm{e}^{-\frac{m v_0^2}{2 k_B T}} \times \rho_{2S,2S}(\nu, r_0, z, v_0, T_{laser}), \qquad \text{(B.12)}$$

where we have put in the Maxwell-Boltzmann weighting of an orbit, which should only depend on the energy of the orbit and can be related to the initial position and velocity. We must determine $g(r_0, v_0)$, the relative density of orbits at v_0 and r_0. If we let $\rho_{2S,2S} = 1$ for all orbits, then the integral over all orbits must equal the number of atoms in the sample, which implies

$$S(\nu) = \int_{-\infty}^{\infty} dz \int_0^{\infty} 2\pi dr_0 \; r_0 \int_0^{\infty} dv_0 \; v_0 \frac{m}{k_B T} \; n_0 \mathrm{e}^{-\frac{U(r_0,z)}{k_B T}} \mathrm{e}^{-\frac{m v_0^2}{2 k_B T}} \times \rho_{2S,2S}(\nu, r_0, z, v_0, T_{laser}). \qquad \text{(B.13)}$$

This expression gives the number of $2S$ atoms at the end of a laser pulse at frequency ν. With a 333 MHz Pentium II microprocessor, the code used for this thesis takes about 24 hours to calculate 20 to 30 frequency points. This recipe must be followed when the atom cloud is not much larger than the laser beam waist.

When the thermal radius of the sample is much greater than the laser beam radius, the calculation can be further simplified. For all but a negligible number of atoms, the variation of the trapping potential is insignificant in the region of the laser beam. The trajectories of atoms which contribute to the spectrum can be described by the impact parameter r, and the velocity when passing near the origin, v. This does not allow for angular momentum, but atoms with significant angular momentum do not pass through the laser and thus do not contribute to the spectrum. The contributions from different impact parameters all have the same spectral shape as discussed when describing the analytic derivation of the time-of-flight lineshape in Sec. 4.3.2. So the spectrum is found from looking at the flux of atoms with a given velocity at the origin, rather than integrating over initial conditions of orbits. This leads to an expression

similar to Eq. 4.24,

$$S(\nu) \approx 4w_0 n_0 \int_{-\infty}^{\infty} dz \int_0^{\infty} dv\ v^2 \frac{m}{k_B T} \mathrm{e}^{-\frac{U(r=0,z)}{k_B T}} \mathrm{e}^{-\frac{mv^2}{2k_B T}} \times \rho_{2S,2S}(\nu, z, v, T_{laser}) \frac{T_{osc}(v)}{T_{laser}}, \tag{B.14}$$

where $\rho_{2S,2S}(\nu, z, v, T_{laser})$ is found for an atom initially at $r = 0$ with velocity v.

$T_{osc}(v)$ is the period of the radial motion for an atom with peak velocity v. The factor of $\frac{T_{osc}(v)}{T_{laser}}$ is necessary because the integral counts the flux of atoms with a given velocity, and during the numerical integration to find $\rho_{2S,2S}(\nu, z, v, T_{laser})$, the same atom passes through the laser beam $T_{laser}/T_{osc}(v)$ times. As written, Eq. B.14 gives the number of excitations per second of laser exposure. This simulation program requires an order of magnitude less computation time than Eq. B.13. The advantage of Eq. B.14 over Eq. 4.24 is that the former can account for the effects of repeated passes through the laser and any additional spectral broadenings or shifts, even if they vary spatially.

Appendix C

Boltzmann Transport Equation Derivation of the Cold Collision Frequency Shift

One can explain the cold collision frequency shift from a collisional, rather than mean field approach, using the formalism developed for cold collision frequency shifts in hydrogen masers [15] and more recently applied to observations in atomic fountain clocks [16, 17, 18]. This gives additional insight into the collision events and is more easily expanded to include inelastic processes. This section is not meant to offer a derivation from first principles; instead it applies the results of the group of B. J. Verhaar (Eindhoven University, The Netherlands) to the $1S$-$2S$ transition in hydrogen. It is not clear how to apply this formalism to a condensate or a inhomogeneous system, so we restrict ourselves to the case of a homogeneous non-degenerate gas.

C.1 Evolution of the Single Atom Density Matrix

One starts with the equation of motion for the density matrix, ρ,

$$\dot{\rho} = \frac{1}{i\hbar}[H, \rho] + \frac{d}{dt}\rho \mid_{coll} + \frac{d}{dt}\rho \mid_{rel} .$$

Where $\frac{d}{dt}\rho\mid_{coll}$ contains the effects of collisions and $\frac{d}{dt}\rho\mid_{rel}$ contains all other relaxation effects. (From now on we will drop the relaxation term since it is not relevant to the discussion.) The Hamiltonian, after making the dipole and rotating wave approximations, can be expressed as

$$H = \frac{\hbar}{2}\begin{bmatrix} \omega_0 & \Omega_{Rabi}(\mathbf{r})e^{-i\omega_{laser}t} \\ . & -\omega_0 \end{bmatrix}. \tag{C.1}$$

We have restricted ourselves to a two level system consisting of the $F = 1, m_F = 1$ states of the 2S and 1S levels and $\hbar\omega_0$ is the level spacing. (One could easily include other hyperfine levels which would be required to handle inelastic collisions.) For the off diagonal coherence term we obtain

$$\dot{\rho}_{1S,2S} = \frac{1}{i\hbar}(\hbar\omega_0)\rho_{1S,2S} - \frac{i}{2}(\rho_{1S,1S} - \rho_{2S,2S})\Omega_{Rabi}(\mathbf{r})e^{i\omega_{laser}t} + \frac{d}{dt}\rho_{1S,2S}\mid_{coll}. \tag{C.2}$$

When $\frac{d}{dt}\rho\mid_{coll}= 0$, one normally makes the ansatz of $\rho_{1S,2S} = \rho^0_{1S,2S}e^{i\omega_0 t}$. This gives

$$\dot{\rho}^0_{1S,2S} = -\frac{i}{2}(\rho_{1S,1S} - \rho_{2S,2S})\Omega_{Rabi}(\mathbf{r})e^{i(\omega_{laser}-\omega_0)t}. \tag{C.3}$$

From this one sees that if $\omega_{laser} = \omega_0$, the fast time dependence of the differential equation is satisfied and $(\rho_{1S,1S} - \rho_{2S,2S})\Omega_{Rabi}$ drives an oscillating dipole moment ($\sim \mathrm{Im}(\rho_{1S,2S})$) which, in the equation for $\dot{\rho}_{2S,2S}$, drives population into the 2S state.

In anticipation of a frequency shift and broadening arising from $\frac{d}{dt}\rho_{1S,2S}\mid_{coll}$, we instead set $\rho_{1S,2S} = \rho^0_{1S,2S}e^{i(\omega_0+\delta\omega i\Gamma)t}$. This yields

$$\begin{aligned}\dot{\rho}^0_{1S,2S} &= -i(\delta\omega + i\Gamma)\rho^0_{1S,2S} - \frac{i}{2}(\rho_{1S,1S} - \rho_{2S,2S})\Omega_{Rabi}(\mathbf{r})e^{i[\omega_{laser}-(\omega_0+\delta\omega+i\Gamma)]t} \\ &\quad + e^{-i(\omega_0+\delta\omega+i\Gamma)t}\frac{d}{dt}\rho_{1S,2S}\mid_{coll}\end{aligned} \tag{C.4}$$

Then to resonantly create an oscillating dipole moment, we set $\omega_{laser} = \omega_0 + \delta\omega$, and we can identify the shift and broadening through $(i\delta\omega - \Gamma)\rho_{1S,2S} = \frac{d}{dt}\rho_{1S,2S}\mid_{coll}$.

C.2 Quantum Boltzmann Transport Equation

The collision term can be found from the Bogoliubov-Born-Green-Kirkwood-Yvon hierarchy[132] for the quantum Boltzmann transport equation[15].

$$\frac{d}{dt}\rho_{1S,2S} \mid_{coll} = (i\delta\omega - \Gamma)\rho_{1S,2S} =$$

$$\rho_{1S,2S}\sum_{\nu} n_\nu \sum_{\mu}[(1+\delta_{1S,\mu})(1+\delta_{2S,\mu})(1+\delta_{1S,\nu})(1+\delta_{2S,\nu})]^{1/2}\langle v\sigma_{(1S,2S),(\nu\to\mu)}\rangle. \quad \text{(C.5)}$$

Brackets refer to a thermal average over velocity, $v = (\frac{\hbar k}{m})$. k is the momentum of each particle of mass m in the center of mass frame. This is a local equation, so n_ν is the local density of atoms in internal atomic state ν. It inherently assumes that the relative populations in the states don't depend on atomic velocity. $\sigma_{(1S,2S),(\nu\to\mu)}$ is the "cross section" for an atom in a superposition of 1S and 2S to collide with an atom which makes a transition from $\nu \to \mu$. This is given by

$$\sigma_{(1S,2S),(\nu\to\mu)} = \frac{\pi}{k^2}\sum_{l}(2l+1)[S^l_{[1S,\mu],[1S,\nu]}S^{l*}_{[2S,\mu],[2S,\nu]} - \delta_{\mu\nu}].$$

$S^l_{[1S,\mu],[1S,\nu]}$ is the l-wave scattering matrix for the collision between the properly symmetrized wave functions for the incoming state of two atoms, $[1S,\mu]$, and the outgoing state, $[1S,\nu]$.

C.3 Application to the $1S$-$2S$ Transition in Trapped Hydrogen

Now we can specialize to our experimental situation. We restrict ourselves to s-wave collisions, and the only nonvanishing density is that of the $1S$ atoms, so ν is set to $1S$. Inelastic collisions contribute through cross sections such as

$$\sigma_{(1S,2S),(1S\to\mu)} = \frac{\pi}{k^2}[S^0_{[1S,\mu],[1S,1S]}S^{0*}_{[2S,\mu],[2S,1S]} - 1]$$

where μ ranges over the 1S hyperfine levels, a, b, and c, but no relevant inelastic collision cross sections have been calculated. The collision term arises from

$$\sigma_{(1S,2S),(1S\rightarrow 1S)} = \frac{\pi}{k^2}[S^0_{[1S,1S],[1S,1S]}S^{0*}_{[2S,1S],[2S,1S]} - 1]. \tag{C.6}$$

This yields

$$\frac{d}{dt}\rho_{1S,2S}\mid_{coll} = (i\delta\omega - \Gamma)\rho_{1S,2S} = \rho_{1S,2S}n_{1S}2\left\langle\left(\frac{2\hbar k}{m}\right)\sigma_{(1S,2S),(1S\rightarrow 1S)}\right\rangle. \tag{C.7}$$

In the zero temperature limit, the s-wave elastic scattering matrices are given by $S^0_{[1S,1S],[1S,1S]} = exp[-2ika_{1S,1S}]$ and $S^0_{[2S,1S],[2S,1S]} = exp[-2ika_{2S,1S}]$. This implies that

$$\frac{d}{dt}\rho_{1S,2S}\mid_{coll} = (i\delta\omega - \Gamma)\rho_{1S,2S} =$$

$$\rho_{1S,2S}n_{1S}2\left\langle\left(\frac{2\hbar k}{m}\right)\left(\frac{\pi}{k^2}\right)[(1-2ika_{1S,1S})(1+2ika_{2S,1S}-4k^2a^2_{2S,1S})-1]\right\rangle$$

$$= \rho_{1S,2S}\left[i\left(\frac{8\pi\hbar n_{1S}}{m}\right)(a_{2S,1S}-a_{1S,1S}) - n_{1S}8\pi a^2_{2S,1S}\left\langle\left(\frac{2\hbar k}{m}\right)\right\rangle\right]. \tag{C.8}$$

C.4 Discussion

We can identify the frequency shift in the first term in Eq. C.8 as $\delta\omega = (8\pi\hbar n_{1S}/m)\,(a_{2S,1S}-a_{1S,1S})$, which is identical to the expression found using the mean field approach for a homogeneous gas with homogeneous excitation probability. The second term is the next higher order term in ka, which contributes to the broadening, $\Gamma = n_{1S}8\pi a^2_{2S,1S}\langle v_{relative}\rangle$. The broadening is equal to the normal collision rate for atoms in the 2S state with $1S$ atoms assuming $\sigma = 8\pi a^2_{1S-2S}$ as is the case for collisions between identical particles. $1S$ and $2S$ particles are distinguishable, but somewhere buried in the quantum Boltzmann equation is the same $1S$-$2S$ exchange effect described in Sec. 6.1.3. Evidently, the formalism assumes all motional states are equally excited, so it may need to be modified to describe an inhomogeneously excited sample.

We can gain some intuition from these expressions. If the phase shift per collision

is large, then the line is mostly broadened. The phase of the oscillating dipole is randomized in every collision, so the atom cannot determine the frequency of the radiation to better than Γ. If the phase shift per collision is small, however, the dipole never completely loses memory of its phase relation with the electric field. The net effect of the collisional phase shifts is to decrease or increase the natural frequency of revolution of the dipole, depending upon the sign of the scattering length, which changes the resonant frequency. The shift in this case is larger than the broadening.

The thermal average of ka_{1S-2S} is $2\pi a_{1S-2S}/\lambda_T$, where the thermal deBroglie wavelength is $\lambda_T = h/\sqrt{2\pi m k_B T}$. For a typical trapped hydrogen sample, $T \approx$ 100 μK, λ_T = 123 nm and the broadening is around 0.18 of the shift. The importance of the broadening decreases with decreasing temperature. It is small compared to other linewidths in the spectrum, but not entirely negligible.

It is important to note that the equations for the time evolution of the single particle density matrix, which form the basis of the numerical simulations described in Sec. 4.4, are the same whether one includes a mean field energy shift in the Hamiltonian or the collisional term $\frac{d}{dt}\rho_{1S,2S}\mid_{coll}$.

Appendix D

Details of the Mean Field Theory Calculation of the Cold Collision Frequency Shift

This appendix provides detailed calculations of some of the results stated in the cold collision frequency shift theory chapter. For ease of calculation, more explicit notation is often used.

D.1 Correlation Functions for a Homogeneous System

The notation is described in Sec. 6.1. The normalized second order spatial correlation function of the gas, $g^{(2)}(\mathbf{x})$, as defined in Eq. 6.11, is

$$g^{(2)}(\mathbf{x}) = \frac{1}{V}\int d^3r \left\{ \sum_{i\neq j}^{N} \langle \Psi^{N;0} | \delta(\tilde{\mathbf{r}}_i - \mathbf{r})\delta(\tilde{\mathbf{r}}_j - \mathbf{r} - \mathbf{x}) | \Psi^{N;0} \rangle / [n(\mathbf{r})]^2 \right\}, \qquad \text{(D.1)}$$

where $n(\mathbf{r})$ is the density at position $\mathbf{r}$,

$$n(\mathbf{r}) = \sum_{i=1}^{N} \langle \Psi^{N;0} | \delta(\tilde{\mathbf{r}}_i - \mathbf{r}) | \Psi^{N;0} \rangle, \qquad \text{(D.2)}$$

and the state vector for N $1S$ particles, $|\Psi^{N;0}\rangle$, for a noncondensed and condensed gas, is given in Eq. 6.2 and 6.3.

For the case of particles in a box of volume V, the motional states can be taken as plane waves with periodic boundary conditions, $\langle \mathbf{r}|\mathbf{k}\rangle = \exp(-i\mathbf{k}\cdot\mathbf{r})/\sqrt{V}$, so

$$\langle \mathbf{k}_1\mathbf{k}_2|\delta(\tilde{\mathbf{r}}_1 - \tilde{\mathbf{r}}_2)|\mathbf{k}_3\mathbf{k}_4\rangle = \frac{1}{V}\delta_{\mathbf{k}_1+\mathbf{k}_2,\mathbf{k}_3+\mathbf{k}_4}, \tag{D.3}$$

and $n(\mathbf{r}) = N/V$. Equation D.1 then reduces to

$$g^{(2)}(\mathbf{x}) = \frac{V}{N^2}\sum_{i\neq j}^{N}\langle\Psi^{N;0}|\delta(\tilde{\mathbf{r}}_i - \tilde{\mathbf{r}}_j + \mathbf{x})|\Psi^{N;0}\rangle. \tag{D.4}$$

The state vectors are symmetric with respect to particle label, so

$$g^{(2)}(\mathbf{x}) = \frac{V(N-1)}{N}\langle\Psi^{N;0}|\delta(\tilde{\mathbf{r}}_1 - \tilde{\mathbf{r}}_2 + \mathbf{x})|\Psi^{N;0}\rangle. \tag{D.5}$$

We now specialize to a non-condensed gas with no state doubly occupied. For $\mathbf{x} = 0$, the correlation function reduces to

$$g^{(2)}_{norm}(0) = \frac{V(N-1)}{NN!}\sum_{Q,R}\langle\mathbf{k}_{Q(1)}\mathbf{k}_{Q(2)}|\delta(\tilde{\mathbf{r}}_1 - \tilde{\mathbf{r}}_2)|\mathbf{k}_{R(1)}\mathbf{k}_{R(2)}\rangle\prod_{i=3}^{N}\delta_{\mathbf{k}_{Q(i)},\mathbf{k}_{R(i)}} \tag{D.6}$$

For all $i \geq 3$, for every nonzero contribution to $g^{(2)}(0)$, $\mathbf{k}_{Q(i)} = \mathbf{k}_{R(i)}$ due to the Kronecker delta functions. Thus, for each permutation Q, 2 R's contribute - a direct term, $\langle\mathbf{k}_{Q(1)}\mathbf{k}_{Q(2)}|\delta(\tilde{\mathbf{r}}_1 - \tilde{\mathbf{r}}_2)|\mathbf{k}_{Q(1)}\mathbf{k}_{Q(2)}\rangle$, and a momentum exchange term, $\langle\mathbf{k}_{Q(1)}\mathbf{k}_{Q(2)}|\delta(\tilde{\mathbf{r}}_1 - \tilde{\mathbf{r}}_2)|\mathbf{k}_{Q(2)}\mathbf{k}_{Q(1)}\rangle$. Thus

$$\begin{aligned} g^{(2)}_{norm}(0) &= \frac{V(N-1)}{NN!}\sum_{Q}(\langle\mathbf{k}_{Q(1)}\mathbf{k}_{Q(2)}|\delta(\tilde{\mathbf{r}}_1 - \tilde{\mathbf{r}}_2)|\mathbf{k}_{Q(1)}\mathbf{k}_{Q(2)}\rangle \\ &\quad +\langle\mathbf{k}_{Q(1)}\mathbf{k}_{Q(2)}|\delta(\tilde{\mathbf{r}}_1 - \tilde{\mathbf{r}}_2)|\mathbf{k}_{Q(2)}\mathbf{k}_{Q(1)}\rangle) \\ &= \frac{V(N-1)}{NN!}\sum_{Q}\frac{2}{V} = \frac{2(N-1)}{N}. \end{aligned} \tag{D.7}$$

For a condensate

$$g^{(2)}_{BEC}(0) = \frac{V(N-1)}{N}\langle \mathbf{k}_1 = 0\ \mathbf{k}_2 = 0|\delta(\tilde{\mathbf{r}}_1 - \tilde{\mathbf{r}}_2)|\mathbf{k}_1 = 0\ \mathbf{k}_2 = 0\rangle \prod_{i=3}^{N} \delta_{\mathbf{k}_i=0,\mathbf{k}_i=0}$$
$$= \frac{V(N-1)}{NV} = \frac{(N-1)}{N}. \tag{D.8}$$

D.2 Interaction Energy for a Homogeneous System before Excitation

The interaction Hamiltonian, H', is defined in Eq. 6.8. The interaction energy, $E'^{N;0}$, for a condensed or noncondensed homogeneous gas, as stated in Eq. 6.10, is given by

$$\begin{aligned} E'^{N;0} &= \langle \Psi^{N;0}|H'|\Psi^{N;0}\rangle \\ &= \langle \Psi^{N;0}|\sum_{1\le i<j}^{N} \frac{4\pi\hbar^2 a_{1S-1S}}{m}\delta(\tilde{\mathbf{r}}_i - \tilde{\mathbf{r}}_j)|\Psi^{N;0}\rangle \\ &= \frac{2\pi\hbar^2 a_{1S-1S}}{m}\langle \Psi^{N;0}|\sum_{i\neq j}^{N}\delta(\tilde{\mathbf{r}}_i - \tilde{\mathbf{r}}_j)|\Psi^{N;0}\rangle \\ &= \frac{2\pi\hbar^2 a_{1S-1S}}{m}\frac{N^2}{V}g^{(2)}(0). \end{aligned} \tag{D.9}$$

D.3 Interaction Energy for a Homogeneous System after Excitation

For a homogeneous system, the state vectors after excitation for a noncondensed and condensed gas are given in Eq. 6.5. The calculation of the interaction energy is simpler if they are expressed, for both a condensed and noncondensed gas, as

$$|\Psi^{N-\bar{n};\bar{n}}\rangle = \sqrt{\frac{\bar{n}!(N-\bar{n})!}{N!}}\sum_{\{\sigma\}}(|2S\rangle\langle 1S|)_{\sigma_1}(|2S\rangle\langle 1S|)_{\sigma_2}...(|2S\rangle\langle 1S|)_{\sigma_{\bar{n}}}|\Psi^{N;0}\rangle. \tag{D.10}$$

The operator $(|2S\rangle\langle 1S|)_i$ changes atom i from a $1S$ to a $2S$ atom while leaving its motional state unchanged, and $\{\sigma\}$ refers to an allowed set of σ_i's, $(1 \le \sigma_1 < \sigma_2... <$

$\sigma_n \leq N$). The sum over all $\{\sigma\}$ reflects the fact that we are equally likely to excite any atom, and it produces a state which is totally symmetric with respect to particle label and the motional states of the $2S$ atoms.

Using Eq. D.10 and 6.8, we can write the interaction energy as

$$\begin{aligned}
E'^{N-\bar{n},\bar{n}} &= \langle \Psi^{N-\bar{n},\bar{n}} | H' | \Psi^{N-\bar{n},\bar{n}} \rangle = \frac{\bar{n}!(N-\bar{n})!}{N!} \\
&\quad \times \left[\sum_{\{\sigma\}} \langle \Psi^{N;0} | (|1S\rangle\langle 2S|)_{\sigma_1} (|1S\rangle\langle 2S|)_{\sigma_2} \ldots (|1S\rangle\langle 2S|)_{\sigma_{\bar{n}}} \right] |H'| \\
&\quad \left[\sum_{\{\kappa\}} (|2S\rangle\langle 1S|)_{\kappa_1} |2S\rangle\langle 1S|)_{\kappa_2} \ldots |2S\rangle\langle 1S|)_{\kappa_{\bar{n}}} |\Psi^{N;0}\rangle \right] \\
&= \frac{\bar{n}!(N-\bar{n})!}{N!} \sum_{\{\sigma\},\{\kappa\}} \langle \Psi^{N;0} | (|1S\rangle\langle 2S|)_{\sigma_1} (|1S\rangle\langle 2S|)_{\sigma_2} \ldots (|1S\rangle\langle 2S|)_{\sigma_{\bar{n}}} \\
&\quad \left| \sum_{1 \leq l < m}^{N} w_{l,m} \right| (|2S\rangle\langle 1S|)_{\kappa_1} |2S\rangle\langle 1S|)_{\kappa_2} \ldots |2S\rangle\langle 1S|)_{\kappa_{\bar{n}}} |\Psi^{N;0}\rangle \\
&= \frac{\bar{n}!(N-\bar{n})!}{N!} \\
&\quad \times \sum_{1 \leq l < m}^{N} \sum_{\{\sigma\},\{\kappa\}} \langle \Psi^{N;0} | \left[\prod_{i \leq 1}^{\bar{n}} (|1S\rangle\langle 2S|)_{\sigma_i} \right] |w_{l,m}| \left[\prod_{j \leq 1}^{\bar{n}} (|2S\rangle\langle 1S|)_{\kappa_j} \right] |\Psi^{N;0}\rangle .
\end{aligned} \tag{D.11}$$

Because $w_{l,m}$ is diagonal in the internal states of atoms l and m, only terms with $\{\sigma\} = \{\kappa\}$ are nonzero. The sum over $\{\sigma\}$ and $\{\kappa\}$ reduces to a sum over the $\binom{N}{n} = \frac{N!}{\bar{n}!(N-\bar{n})!}$ different $\{\sigma\}$'s.

$$\begin{aligned}
E'^{N-\bar{n},\bar{n}} &= \frac{\bar{n}!(N-\bar{n})!}{N!} \\
&\quad \times \sum_{1 \leq l < m}^{N} \sum_{\{\sigma\}} \langle \Psi^{N;0} | \left[\prod_{i \leq 1}^{\bar{n}} (|1S\rangle\langle 2S|)_{\sigma_i} \right] |w_{l,m}| \left[\prod_{j \leq 1}^{\bar{n}} (|2S\rangle\langle 1S|)_{\sigma_j} \right] |\Psi^{N;0}\rangle
\end{aligned} \tag{D.12}$$

For a given l and m, there are four classes into which the various $\{\sigma\}$ fall. There are $\binom{N-2}{\bar{n}} = \frac{(N-2)!}{\bar{n}!(N-2-\bar{n})!}$ permutations for which no σ_i takes the value l or m and the interaction is $1S$-$1S$. There are $\binom{N-2}{\bar{n}-1} = \frac{(N-2)!}{(\bar{n}-1)!(N-2-(\bar{n}-1))!}$ permutations for which

one σ_i takes on the value l, and none are m, and there are $\binom{N-2}{\bar{n}-1}$ permutations for which one σ_i takes the value m, and none are l. For both these cases the interaction is $1S$-$2S$. Finally, there are $\binom{N-2}{n-2} = \frac{(N-2)!}{(\bar{n}-2)!(N-2-(\bar{n}-2))!}$ permutations for which one σ_i takes the value l, and a $\sigma_{j\neq i}$ is m, and the interaction is $2S$-$2S$ and vanishes. This implies

$$\begin{aligned} E'^{N-\bar{n},\bar{n}} &= \frac{\bar{n}!(N-\bar{n})!}{N!}\sum_{1\leq l<m}^{N}\left[\frac{(N-2)!}{\bar{n}!(N-2-\bar{n})!}\langle\Psi^{N;0}|w_{l,m}|\Psi^{N;0}\rangle\right. \\ &+\frac{(N-2)!}{(\bar{n}-1)!(N-1-\bar{n})!}\langle\Psi^{N;0}|(|1S\rangle\langle 2S|)_1\,|w_{l,m}|\,(|2S\rangle\langle 1S|)_1|\Psi^{N;0}\rangle \\ &\left.+\frac{(N-2)!}{(\bar{n}-1)!(N-1-\bar{n})!}\langle\Psi^{N;0}|(|1S\rangle\langle 2S|)_2\,|w_{l,m}|\,(|2S\rangle\langle 1S|)_2|\Psi^{N;0}\rangle\right] \end{aligned} \tag{D.13}$$

We can insert the form of $w_{l,m}$ from Eq. 6.8 and evaluate the matrix elements of the internal states to find

$$\begin{aligned} E'^{N-\bar{n},\bar{n}} &= \frac{\bar{n}!(N-\bar{n})!}{N!}\left[\frac{(N-2)!}{\bar{n}!(N-2-\bar{n})!}a_{1S-1S}+2\frac{(N-2)!}{(\bar{n}-1)!(N-1-\bar{n})!}a_{1S-2S}\right] \\ &\times \sum_{1\leq l<m}^{N}\langle\Psi^{N;0}\left|\frac{4\pi\hbar^2}{m}\delta(\tilde{\mathbf{r}}_l-\tilde{\mathbf{r}}_m)\right|\Psi^{N;0}\rangle \\ &= \frac{2\pi\hbar^2}{m}\frac{(N-\bar{n})}{N(N-1)}\left[(N-\bar{n}-1)a_{1S-1S}+2\bar{n}a_{1S-2S}\right] \\ &\times \sum_{l\neq m}^{N}\langle\Psi^{N;0}\,|\delta(\tilde{\mathbf{r}}_l-\tilde{\mathbf{r}}_m)|\,\Psi^{N;0}\rangle \\ &= \frac{2\pi\hbar^2}{m}\frac{N(N-\bar{n})}{V(N-1)}\left[(N-\bar{n}-1)a_{1S-1S}+2\bar{n}a_{1S-2S}\right]g^{(2)}(0). \end{aligned} \tag{D.14}$$

This result was stated in Eq. 6.13.

D.4 Derivation of the Energy Functional for the Excited State of a Condensed Gas in a Trap

In this section we derive the energy functional for the excited state of a condensed gas in a trap, Eq. 6.26. See Sec. 6.2.1 for a full description of the notation.

The energy of the excited state after laser excitation, and the $2S$ motional wave functions, are found by minimizing the energy functional,

$$E_{BEC}^{N-p;p,i} = \langle \Psi_{BEC}^{N-p;p,i} | H | \Psi_{BEC}^{N-p;p,i} \rangle, \tag{D.15}$$

where

$$|\Psi_{BEC}^{N-p;p,i}\rangle = \mathcal{S}| \underbrace{2S, k_i^{N-p,2S}; ...2S, k_i^{N-p,2S}}_{\text{p terms}}; \underbrace{1S, 0_i^{N-p,1S}; ...1S, 0^{N-p,1S}}_{\text{N-p terms}} \rangle, \tag{D.16}$$

and $k_i^{N-p,2S}$ is the $2S$ motional state which is resonantly excited. The symmetry operator is $\mathcal{S} = \sqrt{\frac{p!(N-p)!}{N!}} \sum_Q' Q$, where the sum runs over the $\frac{N!}{p!(N-p)!}$ particle label permutations which produce unique kets.

The Hamiltonian is defined in Eq. 6.18 and the energy functional is

$$\begin{aligned}
E_{BEC}^{N-p;p,i} &= \langle \Psi_{BEC}^{N-p;p,i} | H | \Psi_{BEC}^{N-p;p,i} \rangle \\
&= \langle \Psi_{BEC}^{N-p;p,i} | \sum_{j=1}^{N} \left(\frac{\tilde{P}_j^2}{2m} + U(\tilde{\mathbf{r}}_\mathbf{j}) + H_j^{int} \right) + H' | \Psi_{BEC}^{N-p;p,i} \rangle \\
&= (N-p) \langle 1S, 0^{N-p,1S} | \left(\frac{\tilde{P}^2}{2m} + U(\tilde{\mathbf{r}}) + H^{int} \right) | 1S, 0^{N-p,1S} \rangle \\
&\quad + p \langle 2S, k_i^{N-p,2S} | \left(\frac{\tilde{P}^2}{2m} + U(\tilde{\mathbf{r}}) + H^{int} \right) | 2S, k_i^{N-p,2S} \rangle \\
&\quad + \langle \Psi_{BEC}^{N-p;p,i} | H' | \Psi_{BEC}^{N-p;p,i} \rangle.
\end{aligned} \tag{D.17}$$

We will break this into pieces and evaluate the interaction part,

$$\langle \Psi_{BEC}^{N-p;p,i} | H' | \Psi_{BEC}^{N-p;p,i} \rangle = \langle ... | \mathcal{S} H' \mathcal{S} | ... \rangle$$

$$= \langle ...|H'\mathcal{S}\mathcal{S}|...\rangle = \langle ...|H'\mathcal{S}|...\rangle, \tag{D.18}$$

where we have used the fact that H' is diagonal in the space of the internal states of the atoms, and $\mathcal{S}\mathcal{S} = \mathcal{S}$. Inserting H', we find,

$$\langle ...|\frac{4\pi\hbar^2}{m}\sum_{1\le i<j}^{N}\delta(\tilde{\mathbf{r}}_i-\tilde{\mathbf{r}}_j)\left\{a_{1S-1S}\mathcal{P}_i^{1S}\mathcal{P}_j^{1S}+a_{1S-2S}\left[\mathcal{P}_i^{1S}\mathcal{P}_j^{2S}+\mathcal{P}_i^{2S}\mathcal{P}_j^{1S}\right]\right\}\mathcal{S}|...\rangle. \tag{D.19}$$

Of the permutations in $\mathcal{S}$, $\frac{(N-2)!}{p!(N-p-2)!}$ of them result in a $1S-1S$ interaction, $\frac{2(N-2)!}{(p-1)!(N-p-1)!}$ of them result in a $1S-2S$ interaction, and the rest result in a $2S-2S$ interaction which vanishes. The expectation value of H' reduces to

$$\begin{aligned}
&\frac{p!(N-p)!}{N!}\frac{N(N-1)}{2}\frac{4\pi\hbar^2}{m}\\
&\left(\frac{(N-2)!}{p!(N-p-2)!}a_{1S-1S}\langle 0^{N-p,1S};0^{N-p,1S}|\delta(\tilde{\mathbf{r}}_1-\tilde{\mathbf{r}}_2)|0^{N-p,1S};0^{N-p,1S}\rangle\right.\\
&\left.+\frac{2(N-2)!}{(p-1)!(N-p-1)!}a_{1S-2S}\langle k_i^{N-p,2S};0^{N-p,1S}|\delta(\tilde{\mathbf{r}}_1-\tilde{\mathbf{r}}_2)|k_i^{N-p,2S};0^{N-p,1S}\rangle\right)\\
&=\frac{2\pi\hbar^2}{m}(N-p)(N-p-1)a_{1S-1S}\langle 0^{N-p,1S};0^{N-p,1S}|\delta(\tilde{\mathbf{r}}_1-\tilde{\mathbf{r}}_2)|0^{N-p,1S};0^{N-p,1S}\rangle\\
&+\frac{4\pi\hbar^2}{m}p(N-p)a_{1S-2S}\langle k_i^{N-p,2S};0^{N-p,1S}|\delta(\tilde{\mathbf{r}}_1-\tilde{\mathbf{r}}_2)|k_i^{N-p,2S};0^{N-p,1S}\rangle.
\end{aligned} \tag{D.20}$$

Inserting this result into Eq. D.17, we find the energy functional is

$$\begin{aligned}
E_{BEC}^{N-p;p,i} &= E_{BEC}^{N-p;0}\\
&\quad +p\langle 2S,k_i^{N-p,2S}|\left[H^{int}+\frac{\tilde{P}^2}{2m}+U(\tilde{\mathbf{r}})+\frac{4\pi\hbar^2a_{1S-2S}}{m}\,n_{BEC}^{N-p}(\tilde{\mathbf{r}})\right]|2S,k_i^{N-p,2S}\rangle\\
&= E_{BEC}^{N-p;0}+p(E_{1S-2S}+\varepsilon_i),
\end{aligned} \tag{D.21}$$

where $E_{BEC}^{N-p;0}$, as defined in Eq. 6.23, is

$$\begin{aligned}
E_{BEC}^{N-p;0} &= (N-p)\langle 1S,0^{N-p,1S}|\left(\frac{\tilde{P}^2}{2m}+U(\tilde{\mathbf{r}})+H^{int}\right)|1S,0^{N-p,1S}\rangle\\
&\quad +\frac{2\pi\hbar^2}{m}(N-p)(N-p-1)a_{1S-1S}\\
&\quad \times\langle 0^{N-p,1S};0^{N-p,1S}|\delta(\tilde{\mathbf{r}}_1-\tilde{\mathbf{r}}_2)|0^{N-p,1S};0^{N-p,1S}\rangle,
\end{aligned} \tag{D.22}$$

and

$$n_{BEC}^{N-p}(\mathbf{r}) = \langle 0^{N-p,1S}|\delta(\tilde{\mathbf{r}}_1 - \tilde{\mathbf{r}})|0^{N-p,1S}\rangle \tag{D.23}$$

is the density in the condensate for $N-p$ condensate atoms.

D.5 Details of Elements of the Proof of the Sum Rule for the Mean Frequency of the Spectrum for an Arbitrary System

In Sec. 6.3 we proved a sum rule (Eq. 6.33) for the cold collision frequency shift of the spectrum for an arbitrary system. Here we provide more detailed calculations of some of the intermediate results. Refer to Sec. 6.3 for a complete explanation of the notation.

For the collisional interaction, we use the Hamiltonian, H', given in Eq. 6.8, except we set $a_{1S-1S} = 0$. H' is written

$$H' = \frac{4\pi\hbar^2 a_{1S-2S}}{m} \sum_{m\neq n}^{N} \delta(\tilde{\mathbf{r}}_m - \tilde{\mathbf{r}}_n)\mathcal{P}_m^{2S}\mathcal{P}_n^{1S}. \tag{D.24}$$

For the state of the system before excitation, we take a general state with N $1S$ atoms, denoted by $|\Psi^{N,0}\rangle$. This state could describe bosons, fermions, or even classical particles [110], in any thermodynamic state.

For the state after laser excitation we consider all configurations of the system with 1 $2S$ atom and $N-1$ $1S$ atoms. In the absence of H', this manifold of states is degenerate, with energy about equal to E_{1S-2S} (neglecting kinetic energy). H' lifts some of the degeneracy, and one can then think of the laser exciting the system to one or a distribution of the eigenstates of H', as shown in Fig. 6-8. We denote the eigenstates as $|v_i\rangle$, and $H'|v_i\rangle = E_i'|v_i\rangle$.

We can write an expression for the spectrum,

$$S(2h\nu) = \sum_i \frac{2\pi}{\hbar} |\langle v_i | H_{las} | \Psi^{N;0} \rangle|^2 \delta(2h\nu - E_{1S-2S} - E_i'), \tag{D.25}$$

where the sum runs over all eignestates $|v_i\rangle$. The overlap matrix element is found from the atom-laser Hamiltonian which can be written (Eq. 4.8)

$$H_{las} = \sum_{j=1}^{N} \frac{\hbar\Omega_0(\tilde{\mathbf{r}}_j)}{2} (|2S\rangle\langle 1S|)_j, \tag{D.26}$$

where $\Omega_0(\mathbf{r})$ is defined in Eq. 4.17 and the sum runs over the N particles.

We can show that the spectrum given by Eq. D.25 obeys the sum rule, Eq. 6.33. We start with

$$\begin{aligned}
&\int 2h d\nu (2h\nu - E_{1S-2S}) S(2h\nu) = \\
= &\int 2h d\nu (2h\nu - E_{1S-2S}) \sum_i \frac{2\pi}{\hbar} |\langle v_i | H_{las} | \Psi^{N;0} \rangle|^2 \delta(2h\nu - E_{1S-2S} - E_i') \\
= &\sum_i \frac{2\pi}{\hbar} E_i' \langle \Psi^{N;0} | H_{las}^\dagger | v_i \rangle \langle v_i | H_{las} | \Psi^{N;0} \rangle \\
= &\sum_i \frac{2\pi}{\hbar} \langle \Psi^{N;0} | H_{las}^\dagger H' | v_i \rangle \langle v_i | H_{las} | \Psi^{N;0} \rangle.
\end{aligned}$$

The eigenstates $|v_i\rangle$ are a complete orthonormal basis for the Hilbert space connected to $|\Psi^{N;0}\rangle$ by H_{las}, so the expression further simplifies to

$$\begin{aligned}
&\frac{2\pi}{\hbar} \langle \Psi^{N;0} | H_{las}^\dagger H' H_{las} | \Psi^{N;0} \rangle \\
= &\frac{2\pi}{\hbar} \langle \Psi^{N;0} | \sum_{j=1}^{N} \frac{\hbar\Omega_0(\tilde{\mathbf{r}}_j)}{2} (|1S\rangle\langle 2S|)_j \\
&\times \frac{4\pi\hbar^2 a_{1S-2S}}{m} \sum_{m\neq n}^{N} \delta(\tilde{\mathbf{r}}_m - \tilde{\mathbf{r}}_n) \mathcal{P}_m^{2S} \mathcal{P}_n^{1S} \sum_{i=1}^{N} \frac{\hbar\Omega_0(\tilde{\mathbf{r}}_i)}{2} (|2S\rangle\langle 1S|)_i | \Psi^{N;0} \rangle \\
= &\frac{2\pi}{\hbar} \frac{4\pi\hbar^2 a_{1S-2S}}{m} \sum_{m\neq n}^{N} \langle \Psi^{N;0} | \frac{\hbar\Omega_0(\tilde{\mathbf{r}}_m)}{2} (|1S\rangle\langle 2S|)_m \\
&\times \delta(\tilde{\mathbf{r}}_m - \tilde{\mathbf{r}}_n) \mathcal{P}_m^{2S} \mathcal{P}_n^{1S} \frac{\hbar\Omega_0(\tilde{\mathbf{r}}_m)}{2} (|2S\rangle\langle 1S|)_m | \Psi^{N;0} \rangle
\end{aligned}$$

$$
\begin{aligned}
&= \frac{2\pi}{\hbar}\frac{4\pi\hbar^2 a_{1S-2S}}{m}\sum_{m\neq n}^{N}\langle\Psi^{N;0}|\frac{\hbar\Omega_0(\tilde{\mathbf{r}}_m)}{2}\delta(\tilde{\mathbf{r}}_m-\tilde{\mathbf{r}}_n)\frac{\hbar\Omega_0(\tilde{\mathbf{r}}_m)}{2}|\Psi^{N;0}\rangle \\
&= \frac{2\pi}{\hbar}\frac{4\pi\hbar^2 a_{1S-2S}}{m}\int d^3r_1\ d^3r_2\ \sum_{m\neq n}^{N}\langle\Psi^{N;0}|\frac{\hbar\Omega_0(\tilde{\mathbf{r}}_m)}{2}(|\mathbf{r}_1\rangle\langle\mathbf{r}_1|)_m \\
&\quad\times\delta(\tilde{\mathbf{r}}_m-\tilde{\mathbf{r}}_n)\frac{\hbar\Omega_0(\tilde{\mathbf{r}}_m)}{2}(|\mathbf{r}_1\rangle\langle\mathbf{r}_1|)_n|\Psi^{N;0}\rangle \\
&= \frac{2\pi}{\hbar}\frac{4\pi\hbar^2 a_{1S-2S}}{m}\int d^3r_1\ \left[\frac{\hbar\Omega_0(\mathbf{r}_1)}{2}\right]^2\sum_{m\neq n}^{N}\langle\Psi^{N;0}|(|\mathbf{r}_1\rangle\langle\mathbf{r}_1|)_m(|\mathbf{r}_1\rangle\langle\mathbf{r}_1|)_n|\Psi^{N;0}\rangle \\
&= \frac{2\pi}{\hbar}\frac{4\pi\hbar^2 a_{1S-2S}}{m}\int d^3r_1\ \left[\frac{\hbar\Omega_0(\mathbf{r}_1)}{2}\right]^2\sum_{m\neq n}^{N}\langle\Psi^{N;0}|\delta(\tilde{\mathbf{r}}_m-\mathbf{r}_1)\delta(\tilde{\mathbf{r}}_n-\mathbf{r}_1)|\Psi^{N;0}\rangle \\
&= \frac{4\pi\hbar^2 a_{1S-2S}}{m}\int d^3r\ \frac{\pi\hbar\Omega_0^2(\mathbf{r}_1)}{2}[n(\mathbf{r})]^2 G(\mathbf{r},0). \qquad \text{(D.27)}
\end{aligned}
$$

In the last line we have identified the correlation function, $G(\mathbf{r},0)$, defined in Eq. 6.34.

We also need to calculate

$$
\begin{aligned}
\int 2hd\nu S(2h\nu) &= \\
&= \int 2hd\nu\sum_i\frac{2\pi}{\hbar}|\langle v_i|H_{las}|\Psi^{N;0}\rangle|^2\delta(2h\nu-E_{1S-2S}-E_i') \\
&= \sum_i^N\frac{2\pi}{\hbar}\langle\Psi^{N;0}|H_{las}^\dagger|v_i\rangle\langle v_i|H_{las}|\Psi^{N;0}\rangle \\
&= \frac{2\pi}{\hbar}\langle\Psi^{N;0}|H_{las}^\dagger H_{las}|\Psi^{N;0}\rangle \\
&= \frac{2\pi}{\hbar}\langle\Psi^{N;0}|\sum_{j=1}^{N}\frac{\hbar\Omega_0(\tilde{\mathbf{r}}_j)}{2}(|1S\rangle\langle 2S|)_j\sum_{i=1}^{N}\frac{\hbar\Omega_0(\tilde{\mathbf{r}}_i)}{2}(|2S\rangle\langle 1S|)_i|\Psi^{N;0}\rangle \\
&= \frac{2\pi}{\hbar}\sum_{i=1}^{N}\langle\Psi^{N;0}|\frac{\hbar\Omega_0(\tilde{\mathbf{r}}_i)}{2}(|1S\rangle\langle 2S|)_i\frac{\hbar\Omega_0(\tilde{\mathbf{r}}_i)}{2}(|2S\rangle\langle 1S|)_i|\Psi^{N;0}\rangle \\
&= \frac{2\pi}{\hbar}\sum_{i=1}^{N}\langle\Psi^{N;0}|\left[\frac{\hbar\Omega_0(\tilde{\mathbf{r}}_i)}{2}\right]^2|\Psi^{N;0}\rangle \\
&= \frac{2\pi}{\hbar}\int d^3r\ \sum_{i=1}^{N}\langle\Psi^{N;0}|\left[\frac{\hbar\Omega_0(\tilde{\mathbf{r}}_i)}{2}\right]^2(|\mathbf{r}\rangle\langle\mathbf{r}|)_i|\Psi^{N;0}\rangle \\
&= \frac{2\pi}{\hbar}\int d^3r\ \left[\frac{\hbar\Omega_0(\mathbf{r})}{2}\right]^2\sum_{i=1}^{N}\langle\Psi^{N;0}|(|\mathbf{r}\rangle\langle\mathbf{r}|)_i|\Psi^{N;0}\rangle \\
&= \frac{2\pi}{\hbar}\int d^3r\ \left[\frac{\hbar\Omega_0(\mathbf{r})}{2}\right]^2\langle\Psi^{N;0}|\sum_{i=1}^{N}\delta(\tilde{\mathbf{r}}_i-\mathbf{r})|\Psi^{N;0}\rangle
\end{aligned}
$$

$$= \int d^3r \, \frac{\pi\hbar\Omega_0^2(\mathbf{r})}{2} n(\mathbf{r}). \tag{D.28}$$

Taking the ratio of Eq. D.27 and D.28 and recalling that $\Omega_0(\mathbf{R}) \propto I(\mathbf{R})$ (Eq. 4.17) proves the sum rule, Eq. 6.33, within the approximation that $a_{1S-1S} = 0$. It is straightforward to include a_{1S-1S} in this proof.

Appendix E

$^{130}Te_2$ Reference Spectroscopy

This appendix describes the $^{130}Te_2$ reference spectrometer used to locate the frequency of the two-photon $1S$-$2S$ $F = 1$ transition within a few hundred kHz. The $^{130}Te_2$ cells were obtained from Opthos Instruments, Rockville, MD, (301)926-0589.

E.1 Introduction

Detecting the two-photon 1S–2S $F = 1$ signal in this experiment remains a challenging endeavor even though it has developed into a working tool. The search, especially the first time attempted during a cool down, is in a phase space with many parameters. Laser frequency and spatial overlap of the laser and the atom cloud must be right, and the many components of the experiment must all function (and be turned on).

We typically search for the signal in a low compression trap, which makes laser-atom overlap easier to obtain. We also use a sample with a temperature of around 20 mK so that the sample preparation time is minimized due to the short evaporation route. The 1S–2S Doppler-free line is still only 20–30 kHz wide at 243 nm, even in this warm trap. The best commercial wavemeters can only fix the frequency to a few hundred MHz, which leaves a large search range. The solution to this problem is to utilize the well-studied absorption spectrum of $^{130}Te_2$ as a reference. The frequencies of many lines in the 486 nm region have been determined to an accuracy of about 1 MHz[133, 134] because of the interest in 1S–2S spectroscopy of hydrogen, deuterium,

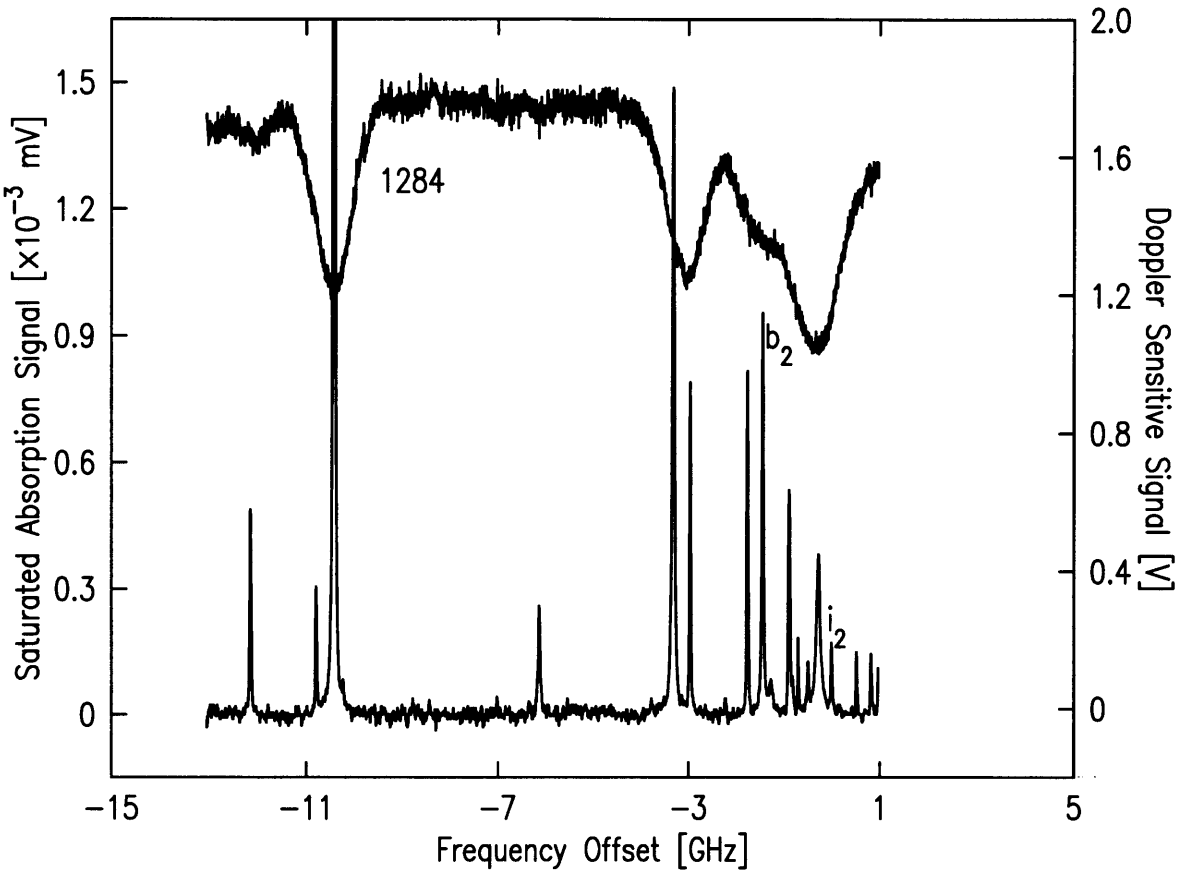

Figure E-1: Doppler-sensitive spectrum of $^{130}Te_2$ - upper trace. Saturated absorption spectrum of same region - lower trace. The Doppler-broadened line 1284 is often used to calibrate sample temperature. Lines b_2 and i_2 are important references for 1S–2S hydrogen spectroscopy.

muonium and positronium. Relative measurement of the difference frequency between a $^{130}Te_2$ line and a particular 1S–2S line can be substantially better[135].

Spectroscopy of $^{130}Te_2$ is relatively easy. The substance is a gray metal at room temperature, but has a substantial vapor pressure at around 500 °C.

The simplest method to interrogate the spectrum is with direct absorption of a probe beam[136]. This yields Doppler-broadened lines of the form

$$S(\Delta\nu) \sim e^{-1/2\frac{mc^2}{k_B T}(\frac{\Delta\nu}{\nu_0})^2}, \tag{E.1}$$

where ν_0 is the transition frequency. The resulting linewidth, FWHM, is about 760 MHz at 486 nm. It is very difficult to derive line centers from such features

with 1 MHz accuracy, especially when there are many spectral lines contributing to a single Doppler feature, as is often the case. Figure E-1 shows an example of Doppler sensitive spectroscopy of Tellurium. One can avoid the limitation of the Doppler width by performing saturated absorption spectroscopy, as is also shown in the figure.

E.2 Saturated Absorption Spectroscopy

The full theory of the sub-Doppler technique, saturated absorption spectroscopy, is complicated[137], but a simple model will suffice here. A pump beam along the z-axis of the sample burns a hole in the z velocity distribution of the ground state by exciting atoms which are at the velocity which is brought into resonance by the Doppler shift. (Complete saturation of the transition reduces the population to 1/2 its value.) The width of this feature in the velocity distribution is nominally $\gamma_{\text{natural}}/k$ where $\gamma_{\text{natural}}/2\pi$ is the natural linewidth of the transition in Hz (typically 10-20 MHz) and k is the wavevector of the laser, although the feature can be broadened a bit by power broadening. For a few mW of power, this feature is much narrower than width of the entire 500 K distribution. The Doppler sensitive absorption of a counter-propagating probe beam essentially maps out the z velocity distribution of the sample. It shows the normal Doppler profile, except for a decrease in absorption corresponding to the velocity class excited by the pump beam. This dip in absorption is the saturated absorption signal.

Normally, both pump and probe are derived from the same laser, so the frequencies of both are scanned simultaneously. In this configuration, the saturated absorption feature has a width equal to half the natural linewidth.

The presence of the dip on the probe absorption indicates that both beams are interacting with the same velocity class. Atoms in this class have z velocity within $\sim \gamma_{\text{natural}}/k$ of v_z, where v_z must satisfy $\nu_0 = \nu_{\text{pump}} - k v_z/2\pi$ and $\nu_0 = \nu_{\text{probe}} + k v_z/2\pi$. This implies $\nu_{\text{probe}} + \nu_{\text{pump}} = 2\nu_0$. This shows how the Doppler effect cancels and also that the signal arises from only a small fraction of the atoms in the laser beam,

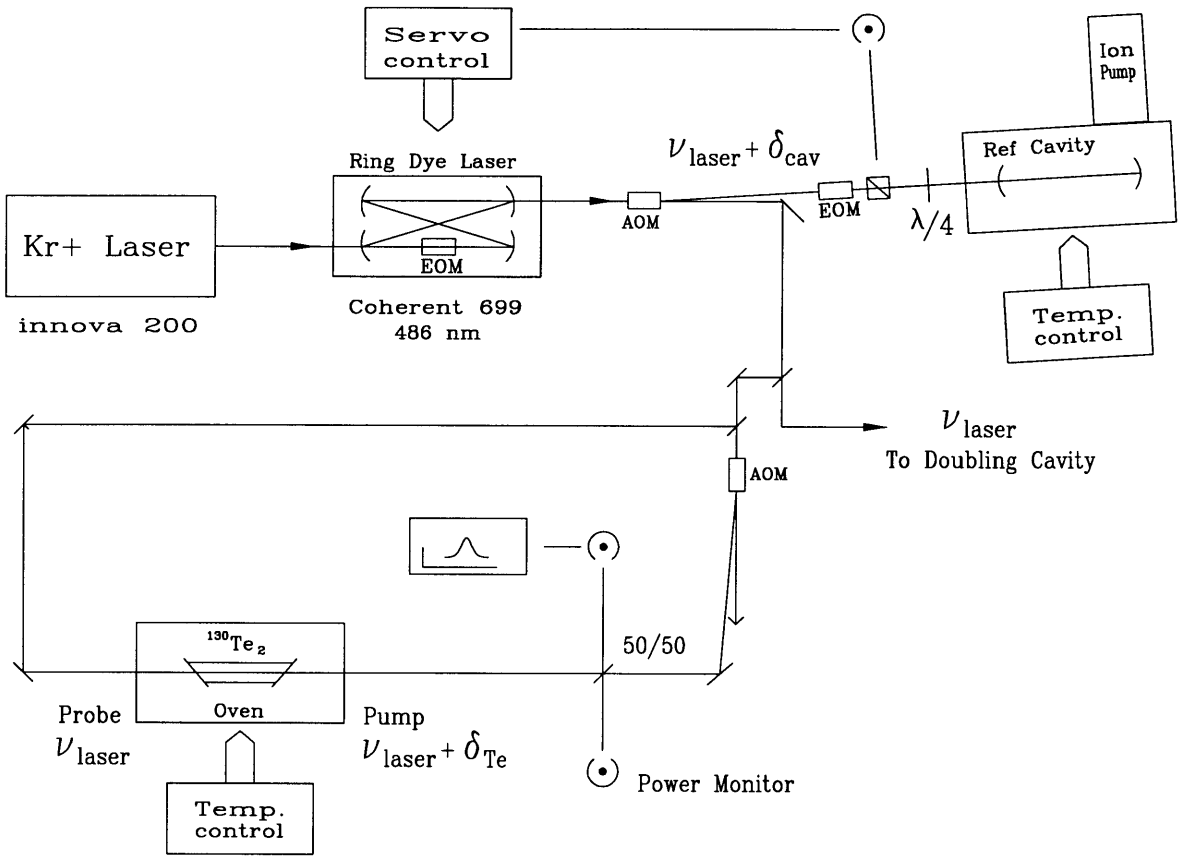

Figure E-2: Components of the laser system which are important for Tellurium spectroscopy. Beam splitters are 4% surface reflections unless otherwise noted.

$\sim \gamma_{natural}/\gamma_{Doppler}$, as opposed to the signal from Doppler-free 1S–2S spectroscopy, which arises from all the atoms. In practice, the pump beam is amplitude modulated, which modulates the saturated absorption feature. One can then use lock-in detection to pick the small saturated absorption signal out of the large Doppler background.

E.2.1 Laser System

The optical layout is shown in Fig. E-2. The frequency of the dye laser can be controlled by its commercial optical cavity, producing a 1 MHz linewidth and allowing scans of up to 30 GHz. Alternatively, it can be locked to a mode of the stable reference cavity. The linewidth is then less than 1 kHz. The frequency of the cavity modes are fixed, so the frequency of the laser in this configuration is scanned by scanning δ_{cav}, the frequency of the AOM which splits off the beam that goes to the reference cavity.

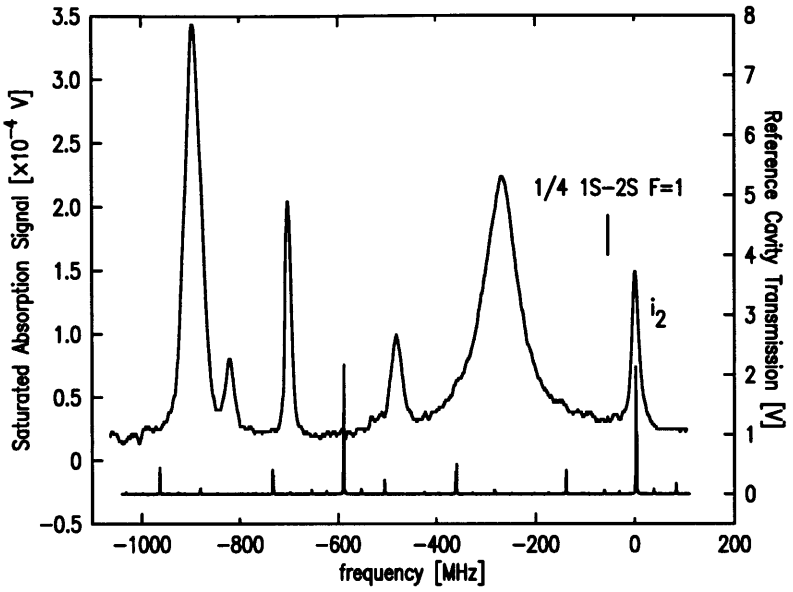

Figure E-3: Saturated absorption spectrum near 1/4 of the hydrogen 1S–2S $F = 1$ transition. The lower trace is the transmission of the reference cavity which provides the frequency calibration.

Because the first-order AOM deflected beam must remain aligned with the reference cavity optics, the tuning range when locked to the cavity is limited to 20 MHz.

The pump beam is frequency shifted by δ_{Te} from the laser frequency, ν_{laser}. This makes it easy to modulate the pump beam at 20 kHz and allows offsetting of center frequency of the saturated absorption signal. As the laser frequency is scanned, the center of the saturated absorption signal is at $\nu_{\mathrm{laser}} = \nu_0 - \delta_{\mathrm{Te}}/2$. The pump beam has a waist radius of 500 μm in the tellurium cell, and a peak power of 30 mW. The probe beam has a waist of 400 μm and a power of 5 mW. After passing through the cell, the probe beam falls on a fast photodiode. The saturated absorption signal is extracted by a Stanford Research Systems lock-in which demodulates the photodiode signal at 20 kHz with a time constant of 300 ms or shorter.

E.2.2 $1S$-$2S$ $F = 1$ Reference Transition, i_2

The most useful $^{130}\mathrm{Te}_2$ line for 1S–2S spectroscopy of hydrogen is labeled i_2 in Fig. E-3. This spectrum was recorded by locking the laser to the commercial cavity and scanning with the Coherent 699 internal scan. The location of the hydrogen line is

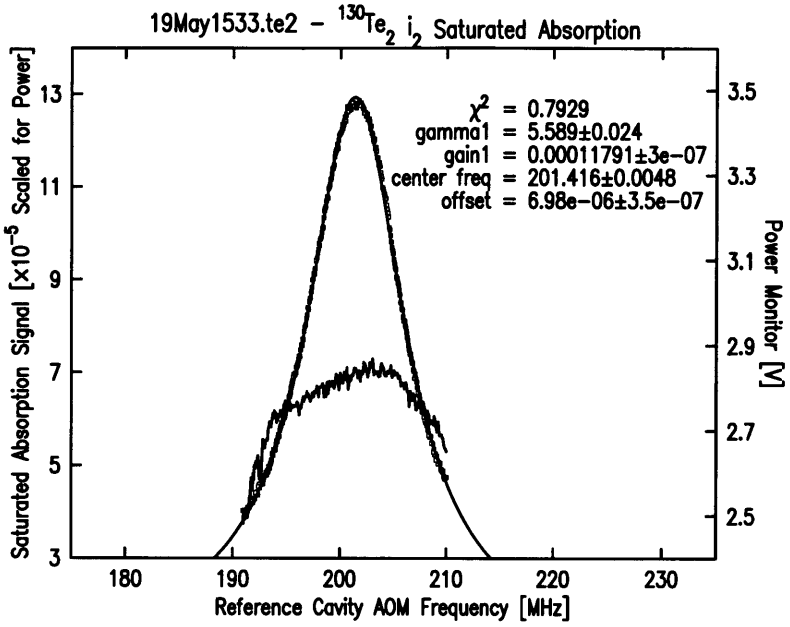

Figure E-4: High resolution saturated absorption spectrum of the i_2 line in $^{130}Te_2$. For this spectrum, the laser frequency was locked to the external reference cavity. The signal is normalized by the square of the pump power, and parameters of the Lorentzian fit are given.

indicated. Figure E-4 is a high resolution scan of i_2 obtained by locking the laser frequency to the reference cavity and scanning with the reference cavity AOM. The latter procedure is our standard way of recording the spectrum. We fit the line to a Lorentzian and can split a given line to about 10 kHz. The quoted width in the fit is HWHM. Unfortunately, the maximum scan range is only about 2 full linewidths.

The absolute frequency of i_2 is known to better than 1 MHz[133, 134]. More useful than the absolute frequency, however, is the relative separation between i_2 and the Doppler-free hydrogen line. This can be found with RF accuracy, and in practice we tune δ_{Te} so that we are on resonance with the Tellurium line and 1/4 of the hydrogen line frequency at the same value of δ_{cav}. McIntyre[135] found the frequency of i_2 to lie 57.1(4) MHz above 1/4 of the $F = 1$, 1S–2S transition in hydrogen. Unfortunately, the frequency of the line has a large temperature dependence, and impurities in the cell can produce cell to cell variations of as much as 1 MHz. These systematics must be controlled if the i_2 line is to be useful as a sub-MHz frequency standard.

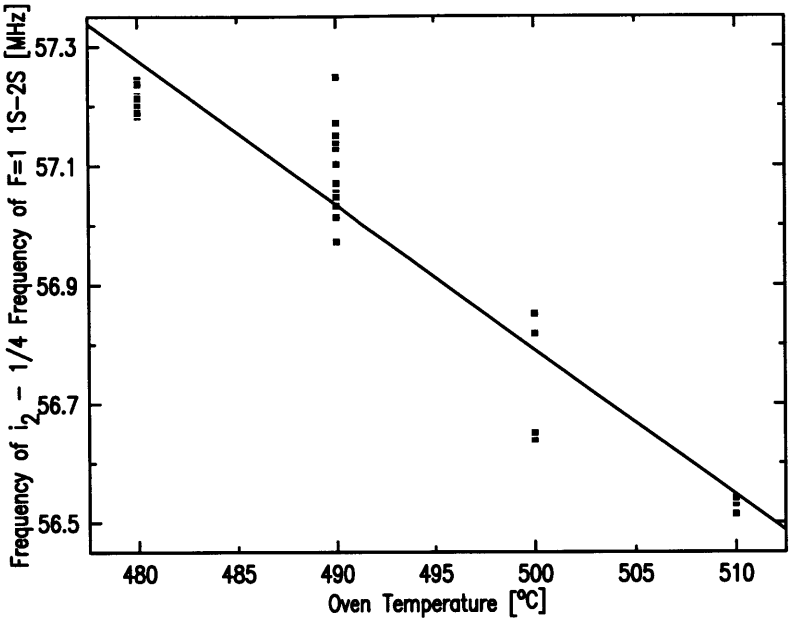

Figure E-5: Temperature dependence of the frequency of the i_2 line in $^{130}Te_2$ at saturated vapor pressure. The frequency is referenced to 1/4 of the $F = 1$ 1S–2S Doppler-free hydrogen frequency.

E.3 Systematics of i_2 Frequency Stability

E.3.1 Temperature

McIntyre found that the i_2 frequency varied by -30 kHz/°C, which corresponds to -1.10 MHz/torr of saturated vapor pressure. The standard condition for which the frequency is quoted is 513(5) °C or 0.89(11) T. The cell temperature is difficult to measure and it may not even be uniform. In our case, we have an uncalibrated thermocouple gauge in the oven, a few centimeters from the cell. The temperature of the thermocouple is controlled by a commercial servo-system, but this probably only controls the cell temperature to about ±5 °C. Once we were able to detect the $F = 1$ 1S–2S Doppler-free signal, we carried out several studies which should make the i_2 line a more reliable reference in the future.

Figure E-5 shows the temperature dependence of the separation of the i_2 and 1S–2S frequencies. We derive -24 kHz/°C for our laboratory definition of temperature, but more importantly, it is clear that we can control the cell temperature to the quoted ±5 °C.

If the thermocouple moves, or if the tellurium cell or the oven configuration must be changed, it is not clear that the thermocouple temperature can reliably set the conditions to determine the frequency within 1 MHz. Fortunately there is a more absolute means of calibrating the temperature.

E.3.2 Column Density

The absorption on the center of a Doppler-sensitive peak is a measure of the integrated column density, which is directly related to temperature through the vapor pressure curve. The absorption of line 1284, shown in Fig. E-1, has become a standard reference. McIntyre worked with a 23(2)% absorption in a 7.5 cm cell. We have a 10 cm cell, so the corresponding absorption is 29%. Figure E-6 shows how the absorption varies with oven temperature. The thermal time constant for the oven is on the order of 10 hours, so patience is required to record data such as this. The error in a single absorption measurement is less than 1%, while the scatter at 500 °C, and the overall smoothness of the plot confirms that cell temperature is stable to ±5 °C. The temperature stability is also shown in Fig. E-7, which plots all the frequency measurements made at an oven temperature of 490 °C. The standard deviation is around 100 kHz.

E.3.3 Reliability and Cell to Cell Variation

While the absorption at 513 °C is consistent with what McIntyre quotes, the frequency with respect to 1S–2S differs by about 700 kHz. Our typical working temperature is 490 °C, which gives an average frequency separation of about 57.1 MHz and an absorption on line 1284 of 17%.

In practice, it is good to set the temperature so that the absorption on 1284 is about 17% and then check the linewidth of the i_2 line. The linewidth has proven to be a sensitive probe of the purity of the cell.

Figure E-8 shows how the linewidth depends on oven temperature. There is significant scatter in the data, implying some parameter was not well controlled (such

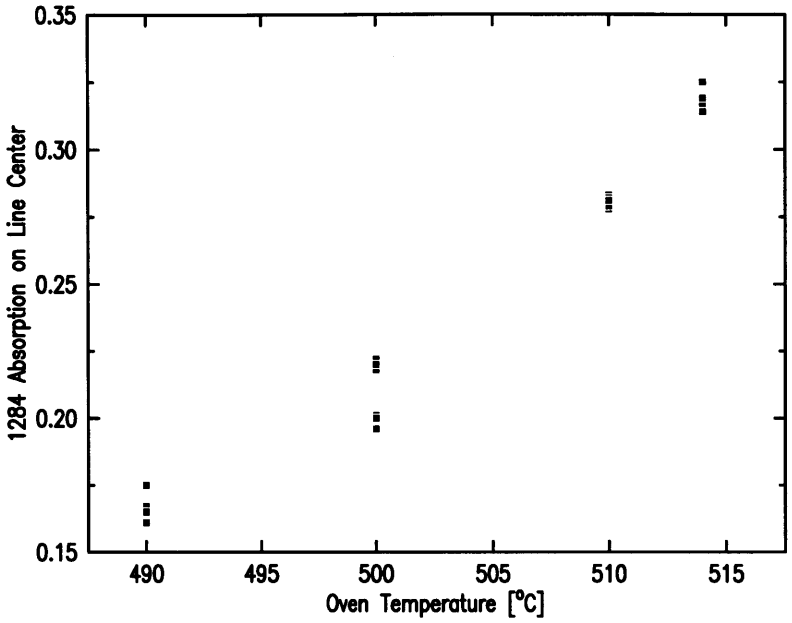

Figure E-6: Absorption on the center of Doppler-broadened line 1284.

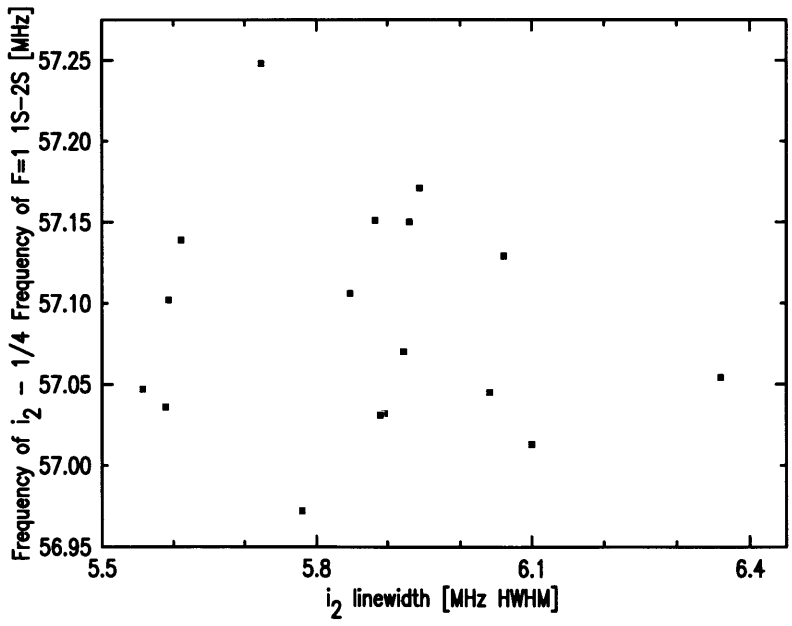

Figure E-7: Frequency of i_2 plotted against linewidth. The oven temperature was controlled at 490 °C and the measurements were taken over a 4 month period.

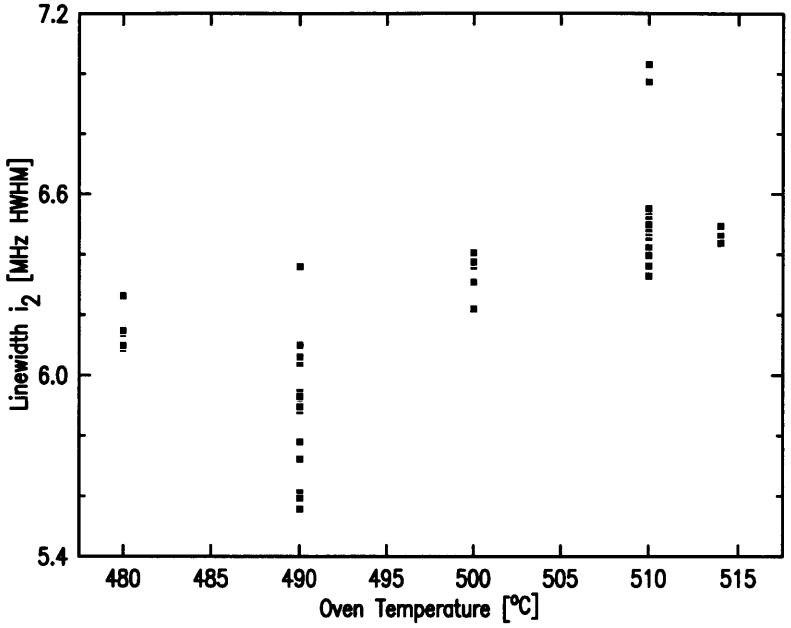

Figure E-8: Linewidth of i_2 versus oven temperature.

as the power broadening), but there is an obvious temperature dependence. For 17% absorption on 1284 and the light powers given above, one should get a linewidth, HWHM of about 5.9–6.0 MHz. If the linewidth deviates from this value, especially if it is too large, the cell should be used with caution because it might have a relatively high level of contaminants.

For a previous data set with two other tellurium cells, we observed a tight correlation between linewidth and frequency when the oven temperature was set to 490 °C. (See Fig. E-9.) Perhaps parameters were more tightly controlled in this study. One can clearly note that one of the cells consistently had a linewidth which was too large and the frequency is low by about 500 kHz. Considering this data, and the fact that we once received a "$^{130}Te_2$ cell" which actually contained zinc, it is clear that one needs to carefully assess the quality of uncalibrated cells.

E.4 Details of MIT Experimental Procedure

There are a few important procedures to follow in order to use the Tellurium reliably. Always align the beams carefully. It should be possible to obtain a signal by over-

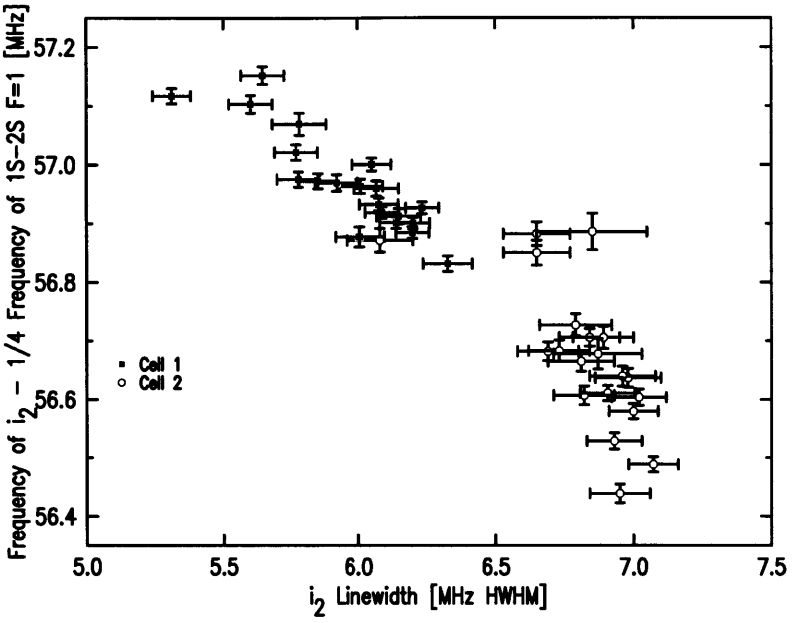

Figure E-9: Frequency of i_2 observed in two other cells, plotted against linewidth. The oven temperature was controlled at 490 °C. Cell 2 appears to have excessive contamination.

lapping the beams by eye, but then peak up the signal by viewing the output of the lock-in on a scope while adjusting the mirrors.

The power levels were given above. McIntyre found that the frequency was insensitive to power, but we have plenty of signal and in general it is good to work at lower powers to reduce any possible power broadening. It might be useful to study how the linewidth varies with power to check if power broadening is contributing to the lack of correlation in Fig. E-7.

As the frequency is swept, the power to the Tellurium spectrometer varies due to the need to keep the power on the reference cavity constant. The power is monitored as shown in Fig. E-2 and Fig E-4. The saturated absorption is a two photon process, so the lockin signal must be normalized by the square of the power to account for the power fluctuations.

The time constant on the lockin should be 300 ms or shorter. A typical scan consists of 300 points across 20 MHz and is recorded in about 5 minutes by a computer and GPIB controller. A longer time constant or faster scan will distort the lineshape enough to move the line center appreciably. A single GPIB measurement requires

about 30 ms. To take advantage of all that potential averaging, the program can record multiple measurements per point. 30 is a reasonable number so that the laser sits at one frequency for about a second. The statistics of the 30 measurements gives one an idea of the noise in the spectrum.

One should worry about the baseline, especially since we do not scan many linewidths and we try to get linewidth information. It should be less than about 5–7% of the amplitude as in Fig. E-4. Check that the baseline goes to zero when either beam is blocked. Note that the Lorentzian fitting function for i_2 includes the effects of the broad line to lower frequency shown in Fig. E-3. This doesn't effect the frequency of the i_2 line that much, but is more important if one is trying to glean information from the the linewidth and baseline. Note that if one changes the order of the AOM beam which goes to the reference cavity, the sweep direction of the spectrum changes as well. The broad line changes from the low frequency side to the high frequency side of i_2. (All the data presented in this thesis is consistent with the broad line being to the low frequency side of i_2.)

In the future, studies of the power dependence of the linewidth and design of a system to allow wider frequency scans while locked to the high finesse cavity would be useful. This could be accomplished for example, by electronically controlling the laser beam alignment into the reference cavity optics. In its present form, however, the Tellurium spectrometer is robust and reliable. Think carefully before changing the oven, thermocouple, or cell. I do not recommend changing the setup unless the hydrogen signal is readily accessible for recalibration.

Good luck!

Bibliography

[1] N. Bohr. *The Theory of Spectra and Atomic Constitution.* Cambridge University Press, 1922.

[2] M. Born. *Atomic Physics*, chapter 5. Dover Publications, Inc., 1989.

[3] G. Gamow. *Thirty Years that Shook Physics*, chapter 6. Dover Publications, 1985.

[4] J. E. Nafe, E.B. Nelson, and I. I. Rabi. *Phys. Rev.*, 71:914, 1947.

[5] J. E. Nafe, E.B. Nelson, and I. I. Rabi. *Phys. Rev.*, 73:718, 1948.

[6] W. E. Lamb and R. C. Retherford. Fine Structure of the Hydrogen Atom. Part I. *Phys. Rev.*, 79:549, 1950.

[7] W. E. Lamb and R. C. Retherford. Fine Structure of the Hydrogen Atom. Part II. *Phys. Rev.*, 81:222, 1951.

[8] K Pachucki, D. Leibfried, M. Weitz, A. Huber, W. König, and T. W. Hänsch. Theory of the Energy Levels and Precise Two-Photon Spectroscopy of Atomic Hydrogen and Deuterium. *J. Phys. B: At. Mol. Opt. Phys.*, 29:177, 1996.

[9] Th. Udem, A. Huber, B. Gross, J. Reichert, M. Prevedelli, M. Weitz, and T. W. Hänsch. Phase-Coherent Measurement of the Hydrogen $1S$-$2S$ Transition Frequency with an Optical Frequency Divider Chain. *Phys. Rev. Lett.*, 79:2646, 1997.

[10] C. L. Cesar, D. G. Fried, T. C. Killian, A. D. Polcyn, J. C. Sandberg, I. A. Yu, T. J. Greytak, D. Kleppner, and J. M Doyle. Two-Photon Spectroscopy of Trapped Atomic Hydrogen. *Phys. Rev. Lett.*, 77:255, 1996.

[11] T. C. Killian, D. G. Fried, L. Willmann, D. Landhuis, S. Moss, T. J. Greytak, and D. Kleppner. Cold Collision Frequency Shift of the $1S$-$2S$ Transition in Hydrogen. *Phys. Rev. Lett.*, 81:3807, 1998.

[12] B. J. Verhaar. Cold Collision Phenomena. In D. J. Wineland, C. E. Wieman, and J. Smith, editors, *Atomic Physics 14: Fourteenth International Conference on Atomic Physics*, page 351, New York, 1995. American Institute of Physics.

[13] D. G. Fried, T. C. Killian, L. Willmann, D. Landhuis, S. Moss, D. Kleppner, and T. J. Greytak. Bose-Einstein Condensation of Atomic Hydrogen. *Phys. Rev. Lett.*, 81:3811, 1998.

[14] C. H. Townes and A. L. Schawlow. *Microwave Spectroscopy*, chapter 13. Dover Publications, Inc., 1975.

[15] B. J. Verhaar, J. M. V. A. Koelman, H. T. C. Stoof, and O. J. Luiten. Hyperfine Contribution to Spin-Exchange Frequency Shifts in the Hydrogen Maser. *Phys. Rev. A*, 35:3825, 1987.

[16] E. Tiesinga, B. J. Verhaar, H. T. C. Stoof, and D. van Bragt. Spin-Exchange Frequency Shift in a Cesium Fountain. *Phys. Rev. A*, 45:R2671, 1992.

[17] K. Gibble and S. Chu. Laser-Cooled Cs Frequency Standard and a Measurement of the Frequency Shift due to Ultracold Collisions. *Phys. Rev. Lett.*, 70:1771, 1993.

[18] S. Ghezali, Ph. Laurent, S. N. Lea, and A. Clairon. An Experimental Study of the Spin-Exchange Frequency Shift in a Laser-Cooled Cesium Fountain Frequency Standard. *Europhys. Lett.*, 36:25, 1996.

[19] M. H. Anderson, J. R. Ensher, M. R. Matthews, C. E. Wieman, and E. A. Cornell. Observation of Bose-Einstein Condensation in a Dilute Atomic Vapor. *Science*, 269:198, 1995.

[20] K. B. Davis, M.-O. Mewes, M. R. Andrews, N. J. van Druten, D. S. Durfee, D. M. Kurn, and W. Ketterle. Bose-Einstein Condensation in a Gas of Sodium Atoms. *Phys. Rev. Lett.*, 75:3969, 1995.

[21] C. C. Bradley, C. A. Sackett, J. J. Tollet, and R. G. Hulet. Evidence of Bose-Einstein Condensation in an Atomic Gas with Attractive Interactions. *Phys. Rev. Lett.*, 75:1687, 1995.

[22] C. C. Bradley, C. A. Sackett, and R. G. Hulet. Bose-Einstein Condensation of Lithium: Observation of Limited Condensate Number. *Phys. Rev. Lett.*, 78:985, 1997.

[23] D. G. Fried. Bose-Einstein Condensation of Atomic Hydrogen. Phd, MIT, 1999.

[24] J. M. Doyle. Energy Distribution Measurements of Magnetically Trapped Spin Polarized Atomic Hydrogen: Evaporative Cooling and Surface Sticking. Phd, MIT, 1991.

[25] C. E. Hecht. The Possible Superfluid Behaviour of Hydrogen Atom Gases and Liquids . *Physica*, 25:1159, 1959.

[26] W. C. Stwalley and L. H. Nosanow. Possible "New" Quantum Systems. *Phys. Rev. Lett.*, 36:910, 1976.

[27] R. D. Etters, J. V. Dugan, and R. W. Palmer. The Ground State Properties of Spin-Aligned Atomic Hydrogen, Deuterium, and Tritium. *J. Chem. Phys.*, 62:313, 1975.

[28] W. Kolos and L. Wolniewicz. Potential Energy Curves for the $X^1\Sigma_g^+$, $b^3\Pi_u^+$, and $C^1\Pi_u$ States of the Hydrogen Molecule. *J. Chem. Phys.*, 43:2429, 1965.

[29] W. Kolos and L. Wolniewicz. Variational Calculation of the Long-Range Interaction between two Ground-State Hydrogen Atoms. *Chem. Phys. Lett.*, 24:457, 1974.

[30] H. A. Bethe and E. E. Salpeter. *Quantum Mechanics of One- and Two-Electron Atoms*, chapter 3. Plenum Publishing Corporation, 1977.

[31] I. F. Silvera and J. T. M. Walraven. *Phys. Rev. Lett.*, 21:164, 1980.

[32] Richard W. Cline, Thomas J. Greytak, and Daniel Kleppner. Nuclear Polarization of Spin-Polarized Hydrogen. *Phys. Rev. Lett.*, 47:1195, 1981.

[33] D. A. Bell, H. F. Hess, G. P. Kochanski, S. Buchman, L. Pollack, Y. M. Xiao, D. Kleppner, and T. J. Greytak. Relaxation and Recombination in Spin-polarized Atomic Hydrogen. *Phys. Rev. B*, 34:7670, 1986.

[34] Harald F. Hess. Evaporative Cooling of Magnetically Trapped and Compressed Spin-Polarized Hydrogen. *Phys. Rev. B*, 34:3476, 1986.

[35] David E. Pritchard. Cooling Neutral Atoms in a Magnetic Trap for Precision Spectroscopy. *Phys. Rev. Lett.*, 51:1336, 1983.

[36] I. D. Setija, H. G. C. Werij, O. J. Luiten, M. W. Reynolds, T. W. Hijmans, and J. T. M. Walraven. Optical Cooling of Atomic Hydrogen in a Magnetic Trap . *Phys. Rev. Lett.*, 70:2257, 1993.

[37] D. S. Zimmerman and A. J. Berlinsky. The Sticking Probability for Hydrogen Atoms on the Surface of Liquid ^{4}He. *Can. J. Phys.*, 61:508, 1983.

[38] B. W. Statt, W. N. Hardy, A. J. Berlinsky, and E. Klein. *J. Low Temp. Phys.*, 61:471, 1985.

[39] J. Helffrich, M. Maley, M. Krusius, and J. C. Wheatley. Hydrogen Dissociation Below 1 K. *J. Low Temp. Phys.*, 66:277, 1987.

[40] H. F. Hess, G. P. Kochanski, J. M. Doyle, T. J. Greytak, and D. Kleppner. Spin-Polarized Hydrogen Maser. *Phys. Rev. A*, 34:R1602, 1986.

[41] V. W. Macalpine and R. O. Schildknecht. Coaxial Resonators with Helical Inner Conductor. In *Proc. IRE*, page 2099, 1959.

[42] H. T. C. Stoof, J. M. V. A. Koelman, and B. J. Verhaar. Spin-Exchange and Dipole Relaxation Rates in Atomic Hydrogen: Rigorous and Simplified Calculations. *Phys. Rev. B*, 38:4688, 1988.

[43] H. F. Hess, G. P. Kochanski, J. M. Doyle, N. Masuhara, D. Kleppner, and T. J. Greytak. Magnetic Trapping of Spin-Polarized Atomic Hydrogen. *Phys. Rev. Lett.*, 59:672, 1987.

[44] R. van Roijen, J. J. Berkhout, S. Jaakkola, and J. T. M. Walraven. Experiments with Atomic Hydrogen in a Magnetic Trapping Field. *Phys. Rev. Lett.*, 61:931, 1988.

[45] A. J. Berlinsky, W. N. Hardy, and B. W. Statt. Theory of Nuclear Spin-Lattice Relaxation of Spin-Polarized Hydrogen on Liquid-Helium-Coated Surfaces due to Magnetic Particles in the Substrate. *Phys. Rev. B*, 35:4831, 1987.

[46] D. G. Friend and R. D. Etters. A Dilute Hard-Sphere Bose-Gas Model Calculation of Low-Density Atomic-Hydrogen Gas Properties. *J. Low Temp. Phys.*, 39:409, 1980.

[47] W. Ketterle and N. J. van Druten. Evaporative Cooling of Trapped Atoms. In B. Bederson and H. Walther, editors, *Advances in Atomic, Molecular, and Optical Physics*, number 37, page 181, San Diego, 1996. Academic Press.

[48] I. A. Yu, J. M. Doyle, J. C. Sandberg, C. L. Cesar, D. Kleppner, and T. J. Greytak. Evidence for Universal Quantum Reflection of Hydrogen from Liquid ^{4}He. *Phys. Rev. Lett.*, 71:1589, 1993.

[49] G. M. Kavoulakis, C. J. Pethick, and H. Smith. Relaxation Processes in Clouds of Trapped Bosons above the Bose-Einstein Condensation Temperature. *Phys. Rev. Lett.*, 81:4036, 1998.

[50] O. J. Luiten, M. W. Reynolds, and J. T. M. Walraven. Kinetic Theory of the Evaporative Cooling of a Trapped Gas. *Phys. Rev. A*, 53:381, 1996.

[51] N. Masuhara, J. M. Doyle, J. C. Sandberg, D. Kleppner, and T. J. Greytak. Evaporative Cooling of Spin-Polarized Atomic Hydrogen. *Phys. Rev. Lett.*, 61:935, 1988.

[52] J. M. Doyle, J. C. Sandberg, I. A. Yu, C. L. Cesar, D. Kleppner, and T. J. Greytak. Hydrogen in the Submillikelvin Regime: Sticking Probability on Superfuid ^{4}He. *Phys. Rev. Lett.*, 67:603, 1991.

[53] P. W. H. Pinske, A. Moske, M. Weidemüller, M. W. Reynolds, T. W. Hijmans, and J. T. M. Walraven. One-Dimensional Evaporative Cooling of Magnetically Trapped Atomic Hydrogen. *Phys. Rev. A*, 57:4747, 1998.

[54] D. E. Pritchard, K. Helmerson, and A. G. Martin. In S. Haroche and J. C. Gay and G. Grynberg, editor, *Atomic Physics 11*, page 179. World Scientific, Singapore, 1989.

[55] I. A. Yu. Ultracold Surface Collisions: Sticking Probability of Atomic Hydrogen on Superfluid ^{4}He. Phd, MIT, 1993.

[56] J. M. Doyle, J. C. Sandberg, N. Masuhara, I. A. Yu, D. Kleppner, and T. J. Greytak. Energy Distributions of Trapped Atomic Hydrogen. *J. of the Opt. Soc. Am. B*, 6:2244, 1989.

[57] O. J. Luiten, H. G. C. Werij, I. D. Setija, M. W. Reynolds, T. W. Hijmans, and J. T. M. Walraven. Lyman-α Spectroscopy of Magnetically Trapped Atomic Hydrogen. *Phys. Rev. Lett.*, 70:544, 1993.

[58] P. W. H. Pinske, A. Moske, M. Weidemüller, M. W. Reynolds, T. W. Hijmans, J. T. M. Walraven, and C. Zimmerman. Resonance Enhanced Two-Photon Spectroscopy of Magnetically Trapped Atomic Hydrogen. *Phys. Rev. Lett.*, 79:2423, 1997.

[59] J. C. Sandberg. Research Towards Laser Spectroscopy of Trapped Hydrogen. Phd, MIT, 1993.

[60] C. L. Cesar. Two-Photon Spectroscopy of Trapped Atomic Hydrogen. Phd, MIT, 1995.

[61] T. W. Hänsch, S. A. Lee, R. Wallenstein, and C. Wieman. Doppler-Free Two-Photon Spectroscopy of Hydrogen $1S$-$2S^*$. *Phys. Rev. Lett.*, 34:307, 1975.

[62] C. J. Foot, B. Couillaud, R. G. Beausoleil, and T. W. Hänsch. Continuous-Wave Two-Photon Spectroscopy of the $1S$-$2S$ Transition in Hydrogen. *Phys. Rev. Lett.*, 54:1913, 1985.

[63] C. Zimmerman, R. Kallenbach, and T. W. Hänsch. High-Resolution Spectroscopy of the Hydrogen $1S$-$2S$ Transition in an Atomic Beam. *Phys. Rev. Lett.*, 65:571, 1990.

[64] B. Gross, A. Huber, M. Niering, M. Weitz, and T. W. Hänsch. Optical Ramsey Spectroscopy of Atomic Hydrogen. *Europhys. Lett.*, 44:186, 1998.

[65] F. Schmidt-Kaler, D. Leibfried, M. Weitz, and T. W. Hänsch. Precision Measurement of the Isotope Shift of the $1S$-$2S$ Transition of Atomic Hydrogen and Deuterium. *Phys. Rev. Lett.*, 70:2261, 1993.

[66] J. H. Tung, X. M. Ye, G. J. Salamo, and F. T. Chan. Two-Photon Decay of Hydrogenic Atoms. *Phys. Rev. A*, 30:1175, 1984.

[67] J. L. Wiza. Microchannel Plate Detectors. *Nuclear Instruments and Methods*, 162:587, 1979.

[68] Galileo Electro-Optics Corporation. Sturbridge, MA. (800)648-1800.

[69] Hamamatsu Corporation. Bridgewater, NJ. (908)231-0960.

[70] Acton Research Corporation. Acton, MA. (508)263-3584.

[71] R. Kallenbach, C. Zimmerman, D. H. McIntyre, and T. W. Hänsch. A blue dye laser with sub-kilohertz stability. *Opt. Comm.*, 70:56, 1989.

[72] A. E. Siegman. *Lasers.* University Science Books, 1986.

[73] R. W. P. Drever, J. L. Hall, F. V. Kowalski, J. Hough, G. M. Ford, A. J. Munley, and H. Ward. Laser Phase and Frequency Stabilization Using an Optical Resonator. *Appl. Phys. B*, 31:97, 1983.

[74] C. Chen, B. Wu, A. Jiang, and G. You. A New-Type Ultraviolet SHG Crystal – β-BaB_2O_4. *Scienta Sinica(Ser. B)*, 28:235, 1985.

[75] T. W. Hänsch and B. Couillaud. Laser Frequency Stabilization by Polarization Spectroscopy of a Reflecting Reference Cavity. *Opt. Comm.*, 35:441, 1980.

[76] C. Borde. Forme de Rai en Spectroscopie a Deux Quanta sans Elargissement Doppler. *C. R. Hebd. Séan. Acad. Sci. B*, 282:341, 1976.

[77] F. Biraben, M. Bassini, and B. Cagnac. Line-Shapes in Doppler-Free Two-Photon Spectroscopy. The Effect of Finite Transit Time. *J. Phys. (Paris)*, 40:445, 1979.

[78] J. J. Sakurai. *Modern Quantum Mechanics.* Addison-Wesley Publishing Company, Inc., 1985.

[79] R. G. Beausoleil and T. W. Hänsch. Ultrahigh-Resolution Two-Photon Optical Ramsey Spectroscopy of an Atomic Fountain. *Phys. Rev. A*, 33:1661, 1986.

[80] F. Bassani, J. J. Forney, and A. Quattropani. Choice of Gauge in Two-Photon Transitions: $1s$-$2s$ Transition in Atomic Hydrogen. *Phys. Rev. Lett.*, 39:1070, 1977.

[81] R. H. Dicke. The Effect of Collisions upon the Doppler Width of Spectral Lines. *Phys. Rev.*, 89:472, 1953.

[82] A. Abragam. *The Mössbauer Effect.* Gordon and Breach, 1964.

[83] A. Burgess. Tables of Hydrogenic Photoionization Cross-Sections and Recombinations Coefficients. *Me. Royal Astron. Soc.*, 69:1, 1965.

[84] S. Klarsfield. Radiative Decay of Metastable Hydrogenic Atoms. *Phys. Lett.*, 30A:38, 1969.

[85] H. A. Bethe and E. E. Salpeter. *Quantum Mechanics of One- and Two-Electron Atoms*, chapter 4. Plenum Publishing Corporation, 1977.

[86] N. F. Ramsey. *Molecular Beams*, chapter 5. Oxford University Press, 1956.

[87] D. J. Wineland, W. M. Itano, J. C. Bergquist, and R. G. Hulet. Laser-Cooling Limits and Single-Ion Spectroscopy. *Phys. Rev. A*, 36:2220, 1987.

[88] M. Gatzke, G. Birkl, P. S. Jessen, A. Kastberg, S. L. Rolston, and W. D. Phillips. Temperature and Localization of Atoms in Three-Dimensional Optical Lattices. *Phys. Rev. A*, 55:R3987, 1997.

[89] M. J. Jamieson, A. Dalgarno, and M. Kimura. Scattering Lengths and Effective Ranges for He-He and Spin-Polarized H-H and D-D Scattering. *Phys. Rev. A*, 51:2626, 1995.

[90] M. J. Jamieson, A. Dalgarno, and J. M. Doyle. Scattering Lengths for Collisions of Ground State and Metastable State Hydrogen Atoms. *Mol. Phys.*, 87:817, 1996.

[91] A. Dalgarno, 1998. Private communication.

[92] J. W. Liu and S. Hagstrom. *J. Phys. B*, 27:L729, 1994.

[93] W. Kolos and J. Rychlewski. *J. Mol. Phys.*, 143:237, 1990.

[94] P. S. Julienne and F. H. Mies. Collisions of Ultracold Atoms. *J. Opt. Soc. Am. B*, 6:2257, 1989.

[95] K. Huang. *Statistical Mechanics*, chapter 10. John Wiley and Sons, 1963.

[96] R. K. Pathria. *Statistical Mechanics*, chapter 10. Pergamon Press, 1972.

[97] M.-O. Mewes, M. R. Andrews, D. M. Kurn, D. S. Durfee, C. G. Townsend, and W. Ketterle. Output Coupler for Bose-Einstein Condensed Atoms. *Phys. Rev. Lett.*, 78:582, 1997.

[98] G. B. Baym. *Lectures on Quantum Mechanics*, chapter 18. Addison-Wesley Publishing Company, 1990.

[99] A. Dalgarno, 1998. Preliminary calculations indicate this effect is small. Private communication.

[100] L. Van Hove. Correlations in Space and Time and Born Approximation Scattering in Systems of Interacting Particles . *Phys. Rev.*, 95:249, 1954.

[101] W. Ketterle and H.-J. Miesner. Coherence Properties of Bose-Einstein Condensates and Atom Lasers. *Phys. Rev. A*, 56:3291, 1997.

[102] V. L. Ginzburg and L. P. Pitaevskii. *Sov. Phys. JETP*, 7:858, 1958.

[103] E. P. Gross. *J. Math. Phys.*, 4:195, 1963.

[104] G. Baym and C. J. Pethick. Ground State Properties of Magnetically Trapped Bose-Condensed Rubidium Gas. *Phys. Rev. Lett.*, 76:6, 1996.

[105] M. R. Mathews, D. S. Hall, D. S. Jin, J. R. Ensher, C. E. Wieman, E. A. Cornell, F. Dalfovo, C. Minniti, and S. Stringari. Dynamical Response of a Bose-Einstein Condensate to a Discontinuous Change in Internal State. *Phys. Rev. Lett.*, 81:243, 1998.

[106] D. S. Hall, M. R. Mathews, J. R. Ensher, C. E. Wieman, and E. A. Cornell. Dynamics of Component Separation in a Binary Mixture of Bose-Einstein Condensates. *Phys. Rev. Lett.*, 81:1539, 1998.

[107] 1998. Recent, unpublished work from the laboratory of W. Ketterle at MIT.

[108] 1998. Recent, unpublished work from the laboratory of W. Phillips at NIST, Gaithersburg. Reported at the DAMOP meeting of the APS.

[109] L. Levitov, 1998. Private communication.

[110] K. Huang. *Statistical Mechanics*, page 182. John Wiley and Sons, 1963.

[111] H. A. Bethe and E. E. Salpeter. *Quantum Mechanics of One- and Two-Electron Atoms*, page 256. Plenum Publishing Corporation, 1977.

[112] J. J. Sakurai. *Modern Quantum Mechanics.* Addison-Wesley Publishing Company, Inc., 1985.

[113] V. Bagnato, D. Pritchard, and D. Kleppner. Bose-Einstein Condensation in an External Potential. *Phys. Rev. A*, 35:4354, 1987.

[114] J. R. Ensher, D. S. Jin, M. R. Mathews, C. E. Wieman, and E. A. Cornell. Bose-Einstein Condensation in a Dilute Gas: Measurement of Energy and Ground-State Occupation. *Phys. Rev. Lett.*, 77:4984, 1996.

[115] T. W. Hijmans, Yu. Kagan, G. V. Shlyapnikov, and J. T. M. Walraven. Bose Condensation and Relaxation in Magnetically Trapped Atomic Hydrogen. *Phys. Rev. A*, 48:12886, 1993.

[116] J. M. Vogels, C. C. Tsai, R. S. Freeland, S. J. J. M. F. Kokkelmans, B. J. Verhaar, and D. J. Heinzen. Prediction of Feshbach Resonances in Collisions of Ultracold Rubidium Atoms. *Phys. Rev. A*, 56:R1067, 1997.

[117] E. Tiesinga, C. J. Williams, P. S. Julienne, K. M. Jones, P. D. Lett, and W. D. Phillips. *J. Res. Natl. Inst. Stand. Technol.*, 101:505, 1996.

[118] M. R. Andrews, C. G. Townsend, H.-J. Miesner, D. S. Durfee, D. M. Kurn, and W. Ketterle. Observation of Interference Between Two Bose Condensates. *Science*, 275:637, 1997.

[119] M.-O. Mewes, M. R. Andrews, N. J. van Druten, D. M. Kurn, D. S. Durfee, and W. Ketterle. Bose-Einstein Condensation in a Tightly Confining dc Magnetic Trap. *Phys. Rev. Lett.*, 78:582, 1997.

[120] M. J. Holland, D. S. Jin, M. L. Chiofalo, and J. Cooper. Emergence of Interactions Effects in Bose-Einstein Condensation. *Phys. Rev. Lett.*, 78:3801, 1997.

[121] M.-O. Mewes, M. R. Andrews, N. J. van Druten, D. M. Kurn, D. S. Durfee, C. G. Townsend, and W. Ketterle. Collective Excitations of a Bose-Einstein Condensate in a Magnetic Trap. *Phys. Rev. Lett.*, 77:988, 1996.

[122] D. S. Jin, J. R. Ensher, M. R. Mathews, C. E. Wieman, and E. A. Cornell. Collective Excitation of a Bose-Einstein Condensate in a Dilute Gas. *Phys. Rev. Lett.*, 77:420, 1996.

[123] M. R. Andrews, D. M. Kurn, H.-J. Miesner, D. S. Durfee, C. G. Townsend, S. Inouye, and W. Ketterle. Propogation of Sound in a Bose-Einstein Condensate. *Phys. Rev. Lett.*, 79:553, 1997.

[124] J. Stenger, S. Inouye, D. M. Stamper-Kurn, H.-J. Miesner, A.P. Chikkatur, and W. Ketterle. Spin Domains in Ground-State Spinor Bose-Einstein Condensates. *Nature*, 396:345, 1998.

[125] E. A. Burt, R. W. Ghrist, C. J. Myatt, M. J. Holland, E. A. Cornell, and C. E. Wieman. Coherence, Correlations, and Collisions: What one Learns about Bose-Einstein Condensates from Their Decay. *Phys. Rev. Lett.*, 79:337, 1997.

[126] H.-J. Miesner, D. M. Stamper-Kurn, M. R. Andrews, D. S. Durfee, S. Inouye, and W. Ketterle. Bosonic Stimulation in the Formation of a Bose-Einstein Condensate. *Science*, 279:1005, 1998.

[127] Yu. M. Kagan, B. V. Svistunov, and G. V. Shlyapnikov. Kinetics of Bose Condensation in an Interacting Bose Gas. *Sov. Phys. JETP*, 75:387, 1992.

[128] S. Giorgini, L. P. Pitaevskii, and S. Stringari. Anomalous Fluctuations of the Condensate in Interacting Bose Gases. *Phys. Rev. Lett.*, 80:5040, 1998.

[129] J. M. Vaughn. *The Fabry-Perot Interferometer: History, Theory, Practice and Applications.* IOP Publishing, Ltd, 1989.

[130] J. C. Bergquist and D. Berkland, 1998. DAMOP meeting of the APS.

[131] S. Seel, R. Storz, G. Ruoso, J. Mlynek, and S. Schiller. Cryogenic Optical Resonators: A New Tool for Laser Frequency Stabilization at the 1 Hz Level. *Phys. Rev. lett.*, 78:4741, 1997.

[132] K. Huang. *Statistical Mechanics*, chapter 3. John Wiley and Sons, 1963.

[133] D. H. McIntyre, W. M. Fairbank, Jr., S. A. Lee, T. W. Hänsch, and E. Riis. Interferometric Frequency Measurement of $^{130}Te_2$ Reference Transitions at 486 nm. *Phys. Rev. A*, 41:4632, 1990.

[134] J. D. Gillaspy and C. J. Sansonetti. Absolute Wavelength Determinations in Molecular Tellurium: New Reference Lines for Precision Laser Spectroscopy. *J. Opt. Soc. Am. B*, 8:2414, 1991.

[135] D. H. McIntyre. High Resolution Spectroscopy of Tellurium and Hydrogen: A measurement of the Rydberg Constant. Phd, Stanford University, 1987.

[136] J. Cariou and P. Luc. *Atlas du Spectre d'Absorption de la Molecule de Tellure.* Laboratoire Aimé Cotton C.N.R.S., Orsay, France, 1980.

[137] S. Haroche and F. Hartman. Theory of Saturated-Absorption Line Shapes. *Phys. Rev. A*, 6:1280, 1972.